

**CONTROL OF DYNAMIC SYSTEM BEHAVIOUR  
BY MAGNETORHEOLOGICAL AND  
VARIABLE ORIFICE DAMPERS**

**A Thesis Submitted to  
the Graduate School of Engineering and Sciences of  
İzmir Institute of Technology  
in Partial Fulfillment of the Requirements for the Degree of**

**DOCTOR OF PHILOSOPHY**

**in Mechanical Engineering**

**by  
Gökçe KINAY**

**July 2013  
İZMİR**

We approve the thesis of **Gökçe KINAY**

**Examining Committee Members:**

---

**Prof. Dr. Serhan ÖZDEMİR**

Department of Mechanical Engineering, İzmir Institute of Technology

---

**Assoc. Prof. Dr. Zeki KIRAL**

Department of Mechanical Engineering, Dokuz Eylül University

---

**Assist. Prof. Dr. H. Seçil ARTEM**

Department of Mechanical Engineering, İzmir Institute of Technology

---

**Assist. Prof. Dr. Barış ERKUŞ**

Department of Civil Engineering, İstanbul Technical University

---

**Assist. Prof. Dr. Özgür ÖZÇELİK**

Department of Civil Engineering, Dokuz Eylül University

**5 July 2013**

---

**Prof. Dr. Serhan ÖZDEMİR**

Supervisor, Department of Mechanical Engineering, İzmir Institute of Technology

---

**Assist. Prof. Dr. Gürsoy TURAN**

Co-Supervisor, Department of Civil Engineering, İzmir Institute of Technology

---

**Prof. Dr. Metin TANOĞLU**

Head of the Department of Mechanical Engineering

---

**Prof. Dr. R. Tuğrul SENGER**

Dean of the Graduate School of Engineering and Sciences

## ACKNOWLEDGEMENTS

I would like to express my deepest gratitude and send my special thanks to my supervisor Asst.Prof.Dr. Gürsoy TURAN for his excellent supervision, help, and guidance he provided throughout my thesis. He light the way for me. This thesis would not exist without his support.

I would like to thank to Prof.Dr. Serhan ÖZDEMİR. I would like to thank to members of the thesis committee Assoc.Prof.Dr. Zeki KIRAL, Asst.Prof. Dr. Seçil ARTEM, Asst.Prof. Dr. Barış ERKUŞ, Asst.Prof. Dr. Özgür ÖZÇELİK, Asst.Prof. Dr. Levent AYDIN, and Prof.Dr. Bülent YARDIMOĞLU.

I would like to thank to Prof.Dr. Hitay ÖZBAY and Assoc.Prof.Dr.Ayhan İRFANOĞLU for their support. Special thanks to Asst.Prof. Dr. Ali Fuat ERGENÇ for discussions on the subjects of systems and control. I would like to thank to Ahmet TAYGUR, the Head of the Advanced Technologies department of BMC, for his support.

I would like to thank the TÜBİTAK Science Fellowships and Grant Programmes Department (BİDEB) for their financial support throughout my thesis.

I would like to thank to Ebru Melek KOÇ and Sinem BEZİRCİLİOĞLU from Academic Writing Center at IZTECH. I could obtain some books and scientific reports from other universities by Librarian Merter İDİN's help. I would like to thank for his kind and helpful manner.

I would like to acknowledge the support of Asst.Prof.Dr. Seçil ARTEM and Levent AYDIN throughout hard times. I am very grateful to Tonguç AKIŞ for his help in some of my social responsibilities and for some of the drawings in the thesis.

Finally, I would like to send my special thanks to my mother, İmren for all her love and wonderful support. I am grateful to the rest of my family Tuğçe, Mehmetcan, Efecan, and Calico who makes me smile. I send my thanks to myself that I did not give up. I would like to send my special thanks to G.G..

Finally, millions of gratitudes to God for everything.

# ABSTRACT

## CONTROL OF DYNAMIC SYSTEM BEHAVIOUR BY MAGNETORHEOLOGICAL AND VARIABLE ORIFICE DAMPERS

Passive and semi-active control devices are widely utilized for response reduction in civil engineering structures subjected to strong earthquakes. These devices absorb energy from the system. They do not add energy into the system being controlled. Therefore, the system stays stable in the sense of bounded-input-bounded-output stability. In the current study, semi-actively controlled devices were investigated: magnetorheological dampers (MRDs) and variable orifice dampers (VODs). Various control schemes were applied to control the seismic response of a three-storey model structure. Some of these control systems were composed of MRDs applied to the bare model structure. Some of them consisted of hybrid application of MRD or VOD to the seismic isolated model structure. The hybrid control, which consisted of passive and semi-active controllers, was studied in order to benefit from advantages of both strategies and to compensate for their weak properties. In the simulations, different controllers were designed depending on the linear quadratic regulator (LQR), sliding mode control,  $H_2/LQG$ , fuzzy logic, and linear quadratic Gaussian (LQG). The effectiveness of the control algorithms and the usefulness of semi-active dampers for response reduction were demonstrated through various numerical examples. Kalman-Bucy filter was designed due to the necessity of an observer in real-world applications with state feedback control. Additional damping at the base level reduced the base velocity directly and decreased the base displacement indirectly at the expense of larger drifts and floor accelerations of the superstructure. The study has shown that the hybrid control system can prevent or significantly reduce structural damage during a seismic event even in case of a frequency overlap of excitation and system. Additionally, vibration response of a truck seat was controlled by three different passive dampers and the MRD. The passive dampers could effectively reduce the oscillations of the truck seat. On the other hand, the capacity of the RD-1005-3 MRD was excessive for the suspension system of the current truck seat.

## ÖZET

### DİNAMİK SİSTEM DAVRANIŞININ MAGNETOREOLOJİK VE DEĞİŞKEN VANA AÇIKLIKLI SÖNÜMLEYİCİLERLE KONTROLÜ

Günümüzde, güçlü depremlere maruz kalan inşaat mühendisliği yapılarının tepkilerinin indirgenmesinde pasif ve yarı-aktif kontrol cihazlarından geniş ölçüde faydalanılmaktadır. Bu cihazlar sistemden enerji sönümlerler. Kontrol edilen sisteme enerji eklemesler. Bundan dolayı sistem sınırlı-girdi-sınırlı-çıkı kararlılığı anlamında kararlı kalır. Mevcut çalışmada yarı-aktif olarak kontrol edilen magnetoreolojik sönümleyicilerle (MRD) ve değişken vana açıklıklı sönümleyicilerle (VOD) ilgilenildi. Üç katlı bir model yapının sismik tepkilerini kontrol etmek için çeşitli kontrol tasarımları uygulandı. Bu kontrol sistemlerinin bazıları çıplak model yapıya uygulanan magnetoreolojik sönümleyicilerden oluştu. Bazıları da sismik izolasyonlu model yapıya magnetoreolojik ya da değişken vana açıklıklı sönümleyicilerin karma uygulanması şeklindeydi. Pasif ve yarı-aktif kontrolcülerden oluşan karma kontrol, iki stratejinin avantajlarından yararlanmak ve zayıf özelliklerini telafi etmek amacıyla kullanıldı. Simulasyonlarda doğrusal karesel düzenleyici (LQR), kayan kipli kontrol,  $H_2/LQG$ , bulanık mantık ve doğrusal karesel Gaussian (LQG) yöntemlerine dayanan farklı kontrolcüler tasarlandı. Kontrol algoritmalarının etkinliği ve yarı-aktif sönümleyicilerin yanıt indirgemedeki kullanışlılığı çeşitli sayısal örneklerle gösterildi. Durum geribeslemeli gerçek uygulamalardaki gözlemleyici ihtiyacından dolayı Kalman-Bucy filtresi tasarlandı. Zemin seviyesinde ilave sönüm, üstyapının katiçi ötelenmelerinin ve kat ivmelerinin artması pahasına, zemin hızını doğrudan ve zemin yerdeğiştirmesini dolaylı olarak azalttı. Mevcut çalışma, tahrik ve sistem frekanslarının çakıştığı bir sismik olay durumunda dahi, karma kontrol sisteminin yapısal zararları önleyebildiğini ya da önemli ölçüde azaltabildiğini göstermiştir. Ayrıca üç pasif ve bir magnetoreolojik sönümleyici ile bir kamyon koltuğunun titreşimleri kontrol edildi. Pasif sönümleyiciler kamyon koltuğunun salınımlarını başarıyla indirgedi. Fakat kullanılan RD-1005-3 magnetoreolojik sönümleyicinin kapasitesi mevcut kamyon koltuğunun süspansiyon sistemi için fazla idi.

*To the memory of  
my grandfather Halil ERAL, grandmothers Mehlika ERAL and Naciye OKLAY*

# TABLE OF CONTENTS

LIST OF FIGURES .....	xi
LIST OF TABLES.....	xviii
CHAPTER 1. INTRODUCTION .....	1
1.1.Overview and Organization of the Thesis .....	2
CHAPTER 2. SEISMIC GROUND EXCITATION DATA .....	5
CHAPTER 3. MODEL SUPERSTRUCTURE.....	17
3.1.Determination of the Damping Matrix .....	19
3.1.1.Measurement of the Modal Damping Ratio $\zeta$ .....	20
CHAPTER 4. CONTROL OF SEISMIC RESPONSE WITH MAGNETORHEOLOGICAL DAMPERS (MRDs) .....	25
4.1.Introduction.....	25
4.2.Literature Review.....	26
4.3.Magnetorheological Dampers.....	28
4.3.1.Modified Bouc-Wen Model for MRDs.....	31
4.3.2.MRD Response to Sinusoidal Excitations for Various Applied Voltage Levels.....	34
4.4.Control of the Seismic Response by MRDs .....	39
4.4.1.Modified Clipped Algorithm.....	40
4.5.Control of the Seismic Response of the Model Superstructure by a MRD .....	42
4.5.1.Model Superstructure Including a MRD .....	42
4.5.2.Steady-State (Infinite-Horizon) Linear Quadratic Regulator.....	44
4.5.3.Sliding Mode Control (SMC).....	46
4.5.4. $H_2$ /LQG Control .....	47
4.5.5.Fuzzy Logic Control .....	48
4.5.6.Simulations.....	51

4.5.6.1. Interpolation of the Seismic Excitation Data .....	51
4.5.6.2. Simulations and Comparison of the Results.....	52
4.6. Comparison of the Responses of a Passively Controlled MRD and a Semi-Actively Controlled MRD.....	58
4.7. Hybrid Control of a Base Isolated Model Structure by MRD .....	65
4.7.1. Base Isolation .....	66
4.7.2. Hybrid-Controlled Building Model.....	68
4.7.3. Current State in the Simulations and Results of the Simulations .....	73

## CHAPTER 5. HYBRID CONTROL OF A BASE ISOLATED MODEL

STRUCTURE WITH A VARIABLE ORIFICE DAMPER (VOD) .....	80
5.1. Overview .....	80
5.2. Literature Review.....	81
5.3. Variable Orifice Damper (VOD) .....	82
5.4. Hybrid-Controlled Building Model .....	86
5.5. Linear Quadratic Gaussian (LQG) Control of the VOD.....	91
5.5.1. Kalman Observer .....	94
5.5.2. Observer Design.....	99
5.5.2.1. Modification of the Kalman-Bucy Observer.....	100
5.5.2.2. Selection of $\mathbf{Q}$ and $\mathbf{R}$ Values by Genetic Algorithms .....	102
5.5.3. Substructured Form of the Building for the Observer Design: Base & Superstructure .....	103
5.5.4. Prewhitening .....	106
5.5.5. Observer of the Superstructure.....	111
5.5.5.1. Diagonalization of the System Equations of the Superstructure .....	112
5.5.5.2. Physical Interpretation of Complex Eigen Quantities.....	114
5.5.5.3. Complex Analysis .....	117
5.5.6. LQR Part of the LQG Control of the VOD.....	119
5.6. Gain Scheduling Control.....	122
5.7. Upper Controller .....	124
5.8. Numerical Simulations.....	127

5.8.1. Interpolation & Synthetic Production of the Seismic Excitation Data .....	127
5.8.2. Current State in the Numerical Simulations.....	130
5.8.3. Block Diagram of the System .....	133
5.8.4. Simulations of the 1940 Imperial Valley Earthquake .....	136
5.8.5. Simulations of the 1999 Düzce Earthquake .....	139
5.8.6. Simulations of the Ground Excitation Data <i>Synthetic1</i> .....	141
5.8.7. Simulations of the Ground Excitation Data <i>Synthetic2</i> .....	144
5.8.8. The Variable <i>PoleRatio</i> in the Observer Design .....	146
5.8.9. Damping Demand of the System .....	148
5.8.10. Maximum Total Shear Forces .....	152
5.8.11. Comparison of the Responses of the Hybrid Controlled Structures with Passive Dampers and VOD .....	153
5.8.12. System Sensitivity with Respect to the Stiffness and Mass of the Structure .....	160
5.8.13. Performance of the Observer Under Arbitrary Initial Conditions .....	164
5.8.14. Filtering Property of the Kalman-Bucy Observer .....	166
5.8.15. Results of the Simulations.....	168
 CHAPTER 6. NUMERICAL STUDIES ON RESPONSE CONTROL OF A TRUCK SEAT .....	169
6.1. Literature Review.....	169
6.2. Truck Seat .....	172
6.3. Mechanical Model of the Truck Seat.....	175
6.4. Frequency Sweep Data .....	176
6.5. Numerical Simulations.....	180
 CHAPTER 7. CONCLUSIONS .....	188
7.1. Conclusions .....	188
7.2. Future Work .....	190
 REFERENCES .....	191

APPENDICES

APPENDIX A. SOLUTION OF THE CONTINUOUS-TIME STATE EQUATION... 204

APPENDIX B. TRANSFORMATION FROM CONTINUOUS TO DISCRETE  
SYSTEMS ..... 206

APPENDIX C. KALMAN FILTER (DISCRETE-TIME FORMULATION)..... 208

APPENDIX D. TRANSFORMATION FROM KALMAN OBSERVER TO  
KALMAN-BUCY OBSERVER ..... 214

APPENDIX E. MATLAB CODE FOR VOD INCLUDING KALMAN-BUCY  
OBSERVER ..... 221

APPENDIX F. UNFORCED RESPONSE OF SECOND-ORDER  
MECHANICAL SYSTEM ..... 223

APPENDIX G. FINITE-TIME LINEAR QUADRATIC REGULATOR..... 226

APPENDIX H. DIAGONALIZATION OF A SQUARE MATRIX..... 234

APPENDIX I. SIGNALS AND RELATED SUBJECTS ..... 236

APPENDIX J. MATLAB CODES FOR MRD INCLUDING LQR, SMC,  
H2/LQG, AND FUZZY CONTROLLERS ..... 240

# LIST OF FIGURES

<b><u>Figure</u></b>	<b><u>Page</u></b>
Figure 2.1.EW component records of the Yarımca station and the İzmit station of the 1999 Kocaeli earthquake.....	7
Figure 2.2.Contour maps of PGA in $\text{cm/s}^2$ from the records of 441 stations of the 1999 Chi-Chi Twain earthquake.....	9
Figure 2.3.Near- and far-fault records of 1999 Kocaeli earthquake for stations located at two different sites in frequency domain (Numbers in the legend are the closest distance to fault rupture and the JB distance).....	11
Figure 2.4.Seismic records in (a) time and (b) frequency domains: N-S component of the El Centro station of the Imperial Valley earthquake (IMP) & E-W component of the Bolu station of the Düzce earthquake (DZC).....	15
Figure 2.5.Synthetic production of the near-fault excitation data .....	16
Figure 3.1.Model superstructure.....	17
Figure 4.1.Magnetorheological Damper.....	25
Figure 4.2.Iron particles in a carrier medium (The arrows indicate the magnetic field direction).....	28
Figure 4.3.Longitudinal cross-section of MRD .....	29
Figure 4.4.Modified Bouc-Wen model.....	31
Figure 4.5.The responses of the MRD to a 5 Hz sinusoidal excitation with an amplitude of 0.01 meters for various applied voltage levels .....	35
Figure 4.6.The responses of the MRD to a 1 Hz sinusoidal excitation with an amplitude of 0.01 meters for various applied voltage levels .....	36
Figure 4.7.The responses of the MRD to a 0.5 Hz sinusoidal excitation with an amplitude of 0.01 meters for various applied voltage levels .....	37
Figure 4.8. Block diagram of the semi-active control system .....	39
Figure 4.9.Graphical representation of modified clipped control algorithm .....	41
Figure 4.10.Graphical representation of the modified clipped control algorithm .....	42
Figure 4.11.Model superstructure including a MRD .....	43
Figure 4.12.Block diagram of semi-active fuzzy control system .....	49
Figure 4.13.Input membership function .....	50
Figure 4.14.Output membership function.....	50

Figure 4.15. Interpolated form of the Imperial Valley earthquake record in (a) time and (b) frequency domains.....	52
Figure 4.16. The response of the first story displacement with respect to the ground due to the Imperial Valley earthquake for different control strategies .....	55
Figure 4.17. Interstory drift of the third floor due to the Imperial Valley earthquake for different control strategies.....	55
Figure 4.18. Absolute acceleration of the first floor due to the Imperial Valley earthquake for different control strategies .....	56
Figure 4.19. Absolute acceleration of the third floor due to the Imperial Valley earthquake for different control strategies .....	56
Figure 4.20. Reduction percentage values of the optimally and passively controlled MRD for the Imperial Valley earthquake .....	61
Figure 4.21. Reduction percentage values of the optimally and passively controlled MRD for the Düzce earthquake .....	62
Figure 4.22. Reduction percentage values of the optimally and passively controlled MRD for the Synthetic1 excitation .....	63
Figure 4.23. Reduction percentage values of the optimally and passively controlled MRD for the <i>Synthetic2</i> excitation .....	64
Figure 4.24. Hybrid-controlled building model (including base isolation and MRD) ....	70
Figure 4.25. Original data of the Imperial Valley event in the frequency domain (The fundamental undamped periods of the fixed-base and isolated structure are marked by the dashed and bold lines).....	73
Figure 4.26. Displacement time histories of the ground, the seismic isolated base and the hybrid controlled base due to the Imperial Valley earthquake (The values of the base are relative to the ground).....	75
Figure 4.27. Interstory drifts of the superstructure due to the Imperial Valley earthquake .....	75
Figure 4.28. Response of the base velocity with respect to the ground due to the Imperial Valley earthquake.....	76
Figure 4.29. Interstory velocities of the superstructure due to the Imperial Valley earthquake .....	77
Figure 4.30. Absolute accelerations due to the Imperial Valley earthquake .....	77
Figure 4.31. Interstory drift of the first floor in frequency domain ((b) is zoomed in vertical axis).....	78

Figure 4.32. Interstory drift of the third floor in frequency domain ((b) is zoomed in vertical axis).....	78
Figure 5.1. Longitudinal section of the utilized semi-active damper .....	83
Figure 5.2. Determination of the critical damping value of the fundamental mode of the system .....	86
Figure 5.3. Hybrid-controlled building model (including base isolation and VOD).....	87
Figure 5.4. Kalman filter (discrete-time) (The equation numbers belong to Appendix C).....	97
Figure 5.5. The first floor responses due to the Imperial Valley event (only superstructure and no control action).....	101
Figure 5.6. The first floor responses due to the Düzce event (only superstructure and no control action) .....	101
Figure 5.7. Substructured configuration of the structure for the observer design– base and superstructure .....	104
Figure 5.8. System augmented by a shaping filter for prewhitening.....	106
Figure 5.9. Base responses (a) prewhitening was not applied to the base and (b) prewhitening was applied to the base (the Imperial Valley earthquake) ...	110
Figure 5.10. Base responses (a) prewhitening was not applied to the base and (b) prewhitening was applied to the base (the Düzce earthquake) .....	110
Figure 5.11. Damped mode shapes of the superstructure (displacement phase angles of the DOFs and damped circular frequencies of the modes are presented).....	115
Figure 5.12. Damped mode shapes of the base isolated structure (the phase angles of the DOFs and the damped circular frequencies of the modes are presented).....	116
Figure 5.13. Supervisory control .....	123
Figure 5.14. Decision of the upper controller .....	126
Figure 5.15. Illustration of the upper controller on a representational displacement graph (the controller is in action along the sections marked by the bold line) .....	126
Figure 5.16. Schematic representation of how the synthetic near-fault data are produced and interpolated.....	127

Figure 5.17.Imperial Valley earthquake and <i>Synthetic1</i> data in frequency domain (The fundamental undamped period of the isolated structure is marked by a thick line) .....	128
Figure 5.18.Düzce earthquake and <i>Synthetic2</i> data in frequency domain (The fundamental undamped period of the isolated structure is marked by a thick line) .....	128
Figure 5.19.Block diagram of the system .....	134
Figure 5.20.Response of the base displacement with respect to the ground due to the Imperial Valley earthquake .....	136
Figure 5.21.Interstory drifts of the superstructure due to the Imperial Valley earthquake .....	137
Figure 5.22.Base velocity response due to the Imperial Valley earthquake .....	137
Figure 5.23.Interstory velocities due to the Imperial Valley earthquake .....	138
Figure 5.24.Absolute accelerations due to the Imperial Valley earthquake .....	138
Figure 5.25.Response of the base displacement with respect to the ground due to the Düzce earthquake .....	139
Figure 5.26.Interstory drifts of the superstructure due to the Düzce earthquake .....	139
Figure 5.27.Base velocity response due to the Düzce earthquake .....	140
Figure 5.28.Interstory velocities due to the Düzce earthquake .....	140
Figure 5.29.Absolute accelerations due to the Düzce earthquake .....	141
Figure 5.30.Response of the base displacement with respect to the ground due to the data <i>Synthetic1</i> .....	142
Figure 5.31.Interstory drifts of the superstructure due to the data <i>Synthetic1</i> .....	142
Figure 5.32.(a) Base velocity and (b) interstory velocities due to the data <i>Synthetic1</i> .....	143
Figure 5.33.Absolute accelerations due to the data <i>Synthetic1</i> .....	143
Figure 5.34.Response of the base displacement with respect to the ground due to the data <i>Synthetic2</i> .....	144
Figure 5.35.Interstory drifts of the superstructure due to the data <i>Synthetic2</i> .....	144
Figure 5.36.(a) Base velocity and (b) interstory velocities due to the data <i>Synthetic2</i> .....	145
Figure 5.37.Absolute accelerations due to the data <i>Synthetic2</i> .....	145
Figure 5.38.Optimum damping values of the VOD and the corresponding damper forces for the Imperial Valley event .....	149

Figure 5.39. Optimum damping values of the VOD and the corresponding damper forces for the <i>Synthetic1</i> excitation.....	149
Figure 5.40. Optimum damping values of the VOD and the corresponding damper forces for the Düzce earthquake .....	150
Figure 5.41. Optimum damping values of the VOD and the corresponding damper forces for the <i>Synthetic2</i> excitation.....	150
Figure 5.42. Maximum absolute values of the simulated base drifts of the hybrid controlled structure .....	154
Figure 5.43. Maximum absolute values of the simulated interstory drifts of the hybrid controlled structure (numbers on the vertical axis indicates the floor numbers).....	155
Figure 5.44. Maximum absolute values of the simulated total accelerations of the hybrid controlled structure (numbers on the vertical axis indicates the floor numbers).....	156
Figure 5.45. Interstory drift of the third floor in frequency domain for the (a) Imperial Valley earthquake, (b) Düzce earthquake, (c) Imperial Valley earthquake zoomed only in vertical axis, and (d) Düzce earthquake zoomed only in vertical axis .....	158
Figure 5.46. Interstory drift of the third floor in frequency domain for the (a) <i>Synthetic1</i> earthquake, (b) <i>Synthetic2</i> earthquake, (c) <i>Synthetic1</i> earthquake zoomed only in vertical axis, and (d) <i>Synthetic2</i> earthquake zoomed only in vertical axis.....	159
Figure 5.47. Responses for the Düzce event with respect to the ground (The stiffness matrix $\mathbf{K}_s$ was increased by 10%) – Best response in the sensitivity analysis .....	163
Figure 5.48. Responses for the Imperial Valley event with respect to the ground (The stiffness matrix $\mathbf{K}_s$ is decreased by 10%) – Worst response in the sensitivity analysis .....	163
Figure 5.49. Floor responses for the Düzce event under the first initial condition set.....	165
Figure 5.50. Floor responses for the Düzce event under the second initial condition set.....	165
Figure 5.51. Magnitudes of the base displacement (with respect to the ground) in the frequency domain for the (a) Düzce earthquake and (b) the Düzce	

earthquake zoomed in vertical axis between periods of 0.004-1 s and scaled in the horizontal axis .....	167
Figure 5.52.Magnitudes of the base displacement (with respect to the ground) in the frequency domain for the (a) <i>Synthetic2</i> excitation and (b) the <i>Synthetic2</i> excitation zoomed in vertical axis between periods of 0.004-1 s and scaled in the horizontal axis .....	167
Figure 6.1.Setup .....	173
Figure 6.2.Front view of the setup .....	173
Figure 6.3.Seat suspension.....	174
Figure 6.4.Seat adjustment buttons.....	174
Figure 6.5. Mechanical model of the truck seat.....	175
Figure 6.6.ISO 7096/2000 Class 2 (a) excitation and (b) base displacement sample...	177
Figure 6.7.Frequency sweep data applied to the base of the truck seat (for the first two seconds of the simulation) .....	179
Figure 6.8.Displacement response of the truck seat relative to the ground in the passive damper application (damping ratio of the damper is 0.8, underdamped case).....	180
Figure 6.9.Velocity response of the truck seat relative to the ground in the passive damper application (damping ratio of the damper is 0.8, underdamped case) .....	181
Figure 6.10.Acceleration response of the truck seat relative to the ground in the passive damper application (damping ratio of the damper is 0.8, underdamped case).....	181
Figure 6.11.Displacement response of the truck seat relative to the ground in the passive damper application (damping ratio of the damper is 1, critically damped case) .....	182
Figure 6.12.Velocity response of the truck seat relative to the ground in the passive damper application (damping ratio of the damper is 1, critically damped case) .....	182
Figure 6.13.Acceleration response of the truck seat relative to the ground in the passive damper application (damping ratio of the damper is 1, critically damped case) .....	183

Figure 6.14. Displacement response of the truck seat relative to the ground in the passive damper application (damping ratio of the damper is 10, overdamped case).....	183
Figure 6.15. Velocity response of the truck seat relative to the ground in the passive damper application (damping ratio of the damper is 10, overdamped case).....	184
Figure 6.16. Acceleration response of the truck seat relative to the ground in the passive damper application (damping ratio of the damper is 10, overdamped case).....	184
Figure 6.17. Displacement response of the truck seat relative to the ground in the MRD application.....	185
Figure 6.18. Velocity response of the truck seat relative to the ground in the MRD application.....	186
Figure 6.19. Acceleration response of the truck seat relative to the ground in the MRD application.....	186
Figure 6.20. Magnitudes of the seat displacement (with respect to the ground) in the frequency domain in the MRD application (the response is displayed in the frequency range of 0-5 Hz).....	187
Figure H.1. The $i$ th eigenvector of the matrix $\mathcal{A}$ in two-dimensional space.....	234
Figure I.1. A signal of 1 Hz is sampled at different frequencies as 2, 3, 4, 10, and 20 Hz (The sampled points and reconstructed signals are indicated by dot and colored lines, respectively) .....	236
Figure I.2.(a) Proper and (b) improper simulation or measurement of the same sine wave.....	238

## LIST OF TABLES

<u>Table</u>	<u>Page</u>
Table 2.1. Geotechnical soil classification according to the geotechnical subsurface characteristics of the station (Third letter of the Geomatrix 3-letter site classification).....	6
Table 2.2. Information about the records of Yarımca and İzmit stations of 1999 Kocaeli earthquake .....	6
Table 2.3. PGA, PGV, and PGD values of four stations of 1999 Kocaeli earthquake emphasizing the amplifying effect of softer soil sites.....	8
Table 2.4. Information about the stations utilized in Figure 2.3.....	11
Table 2.5. Near-fault strong earthquakes in the world ( $M_w > 6.5$ , $d < 10$ km, and $(PGA > 0.5g$ or $PGV > 100\text{cm/s}$ in horizontal direction)) .....	12
Table 2.6. Information about the seismic records utilized in the simulations .....	14
Table 3.1. Undamped periods and frequencies of the 3-story model superstructure.....	18
Table 3.2. Calculation of the proportionality coefficients $\alpha$ and $\beta$ of the Rayleigh damping .....	23
Table 4.1. Parameters for the modified Bouc-Wen model .....	34
Table 4.2. Maximum damping force values of the MRD .....	38
Table 4.3. Fuzzy inference rule .....	51
Table 4.4. Peak responses of the Imperial Valley earthquake for different control strategies.....	57
Table 4.5. Undamped periods and frequencies of the base isolated structure .....	72
Table 5.1. Determination of the critical damping value of the fundamental mode of the system.....	85
Table 5.2. Linear time-variant plant and measurement models.....	96
Table 5.3. Definitions of terms in Table 5.2 .....	96
Table 5.4. Determination of the weighting matrices $Q$ and $R$ for the LQR design .....	121
Table 5.5. System equations utilized in the simulations.....	131
Table 5.6. Gains of the controllers and the observers and <i>PoleRatio</i> of the observers corresponding to the damping values of the VOD .....	147
Table 5.7. Number of under- and over-damped responses .....	152
Table 5.8. Maximum total shear forces at the first floor of the superstructure .....	153

Table 5.9. Ratios of the maximum absolute values of the simulated responses with respect to the responses of the unvaried case as the stiffness matrix $\mathbf{K}_s$ was varied .....	161
Table 5.10. Correlation coefficients between the estimated and simulated responses as the stiffness matrix $\mathbf{K}_s$ of the hybrid controlled structure was varied .....	162
Table G.1. Performance of the controller .....	230

# CHAPTER 1

## INTRODUCTION

Structural control may be utilized to reduce the amount of energy transferred into the structure from the ground motion either by using external energy or absorbing a portion of the seismic energy. There exist passive, semi-active, active, and hybrid structural control systems (Symans & Kelly, 1999). Dampers decrease the response of the structure by absorbing some portion of the mechanical energy of the system and transform it into heat energy.

Semi-active control devices utilized in civil engineering applications are variable orifice dampers, friction controllable braces, friction controllable isolators, variable stiffness devices, and controllable fluid dampers that utilize electrorheological or magnetorheological fluids. Two kinds of semi-active devices are investigated within the context of the present thesis: magnetorheological dampers (MRDs) and variable orifice dampers (VODs).

Semi-active control is an innovation that arises after the passive and active control. The damping properties of passive systems, which are designed to absorb energy during a ground excitation, are constant. They do not need external energy sources. On the other hand, passive controllers are not as effective as semi-active, active, or hybrid ones. Active control strategies, on the other hand, are generally more effective, but they are disadvantageous as they need large amounts of power while they are in action, and they may result in instabilities of the controlled structure. Input power requirements of semi-active control devices are negligible when compared to active devices. Semi-active devices do not add energy into the system being controlled, This property makes semi-active control safer and more reliable than active control during a seismic event, even in case of a power cut. A problem of instability does not occur in the sense of bounded-input-bounded-output stability. Damping of semi-active devices is determined due to the force acting to the structure and can be changed at every time step. The change can be performed by batteries. This fact causes the popularity of semi-active control devices.

## 1.1. Overview and Organization of the Thesis

The present research is mainly two folded as the seismic response reduction of structures by MRDs and VODs, both of which are semiactively controlled devices. The dissertation is organized as explained in the following lines.

In Chapter 2, the parameters considered in choosing the seismic data for the simulations are summarized. The effects of near-fault ground excitation is mentioned. The near-fault strong earthquakes in the world are summarized in a table according to data obtained from PEER. Finally, the seismic records utilized in the current research are presented, and the production of synthetic near-fault seismic excitation data is explained.

Chapter 3 describes the three-storey model structure utilized in the simulations. The subjects of classically and nonclassically damped systems are discussed. The modal damping ratios are determined by means of the measurements performed by Turan and Aydın (2011).

In Chapter 4, the MRD are examined in detail. A literature review on MRDs is provided. Then, the modified Bouc-Wen model is presented to model the behaviour of MRDs. The seismic response of the three-storey model structure in Chapter 3 is controlled by a MRD depending on four different control algorithms: LQR, sliding mode control,  $H_2/LQG$ , and fuzzy controller. The results are compared and interpreted. Additionally, the response control of a hybrid system, which consists of a base isolated building and an MRD, was calculated to benefit from advantages of both strategies and to avoid the yielding of isolators. The fundamental period of the structure is lengthened by adding the base isolator to the bare building. Hence, the structure is affected from the smaller components of excitation and is protected from the detrimental effects of earthquake excitation. The advantages of hybrid application of the two control systems are revealed. The effectiveness of the control algorithm and the usefulness of MRD for response reduction are demonstrated.

The hybrid control of the model structure including a VOD is performed in Chapter 5. Related literature on VODs are reviewed. Quite often it is not practical or possible to measure all the states in real-world applications with full state feedback control. Therefore, the control scheme is designed, depending on the LQG which contains a Kalman-Bucy observer. At the beginning of the studies, the observer cannot

predict the responses successfully. Therefore, Kalman and Kalman-Bucy observers are examined in detail, and some remedies for the observer design are applied: Generally, the disturbances are not sent to the observer. In structural engineering applications, the ground excitation can be recorded and sent to the observer in addition to the measurements during the event. In the present example, the observer is modified by sending the recorded disturbance. In structural engineering applications, the white noise prerequisite of Kalman filter is not fulfilled due to the low-frequency character of ground excitation. Therefore, prewhitening is applied to the base. Hence, the performance of the observer improves within the range of the earthquake-related frequencies. Furthermore, the superstructure is diagonalized to obtain independent subsystems for the observer design. Finally, the observer is designed for the prewhitened base and diagonalized superstructure separately.

In Chapter 5, the control action is mainly governed by an upper controller. The required control force is calculated by LQG, and the VOD is directed to perform the designed control task by gain scheduling control. In the simulations, the system is excited by four different seismic records, two of which are synthetically produced. The chapter concludes with subsections in which the simulation results are discussed within different aspects such as: Damping demand, maximum total shear forces, sensitivity analysis, performance under arbitrary initial conditions, and comparison the responses with those of hybrid systems including passive dampers.

Finally, in Chapter 6, vibrations of a truck seat obtained from a BMC cooperation are controlled by the MRD. The system is excited numerically by a frequency sweep data to monitor the behaviour of the truck seat within the period range of 0.1-2 seconds (the human body is sensitive to the vibrations in the frequency range of the 2-4 Hz).

Important facts utilized within the thesis are presented in the appendices in detail. Appendix I mainly deals with the signal construction and related subjects in the simulations. Information about the LQR is provided in Appendix G. The necessary and sufficient conditions for optimality are discussed briefly. The choice of the weighting matrices in the LQR is discussed. Additionally, the MATLAB code for the system including a MRD is provided in Appendix J.

At the beginning of the VOD studies, not being able to design an appropriate observer has enforced the author to code her own Kalman-Bucy function within MATLAB, instead of utilizing the Kalman function of MATLAB. Therefore, derivation

of the Kalman filter is presented in Appendix C. Transformation from the Kalman observer to the Kalman-Bucy observer is revealed in Appendix B and Appendix D.

The differential equations of the observer of the superstructure have complex coefficients due to the diagonalization. Therefore, its response is calculated by a function coded within MATLAB (see Appendix A for the calculation of the forced response). The details about the diagonalization of the superstructure are displayed in Appendix H.

The system in Chapter 5 exhibits under- and over-damped responses, depending on the selection of damping values of the VOD. Therefore, unforced response of a second-order mechanical system is represented in Appendix F. The MATLAB code for the system including a VOD and Kalman-Bucy observer is provided in Appendix E.

## CHAPTER 2

### SEISMIC GROUND EXCITATION DATA

In the context of the thesis, numerical simulations were performed to investigate the performance of two semi-active dampers as MRD and VOD by different controllers. The parameters that have to be considered while choosing the seismic excitation record were summarized in the following lines (Kalkan & Chopra, 2010; Wang et al., 2002; Katsanos et al., 2010):

1. Magnitude of the earthquake and amplitude of the record
2. Spectrum of the record in frequency domain (should have major components at periods that civil structures are sensitive)
3. Distance from the causative fault
4. Soil profile both at the site of interest and at the station of record
5. Fault rupture directivity (This criterion is usually not taken into account during seismic design although excitation components larger in the strike-normal direction than that in the strike-parallel direction were observed evidently in severe earthquakes (Wang et al., 2002).).
6. Duration of the record

PEER utilizes three soil classifications for stations of the data: USGS, Geomatrix 3-letter, Taiwan CWB. The stations of the earthquakes, utilized in the present research, were classified due to the Geomatrix 3-letter categorization. This classification is displayed in Table 2.1 where  $V_s$  is the average shear wave velocity. The site of the station was classified according to its geotechnical subsurface characteristics. This classification is similar to that of the USGS (PEER, 2000).

In the simulations of the current research, a general comparison of various control designs was performed for a model structure. There was not a certain construction site of interest. In that respect, the seismic data applied to the system had to have a wide frequency range to excite all of the modes of the structure. Therefore, the soil profile of the station of the utilized record had a major effect. The soft soil sites filter out high-frequency components of the ground excitation. On the other hand, records obtained from stations on stiff sites have wider frequency range compared to the

data of stations at softer regions. This case is shown in Figure 2.1 for the 1999 Kocaeli earthquake (see Table 2.2 for additional information for stations).

Table 2.1. Geotechnical soil classification according to the geotechnical subsurface characteristics of the station (Third letter of the Geomatrix 3-letter site classification) (Source: PEER, 2000)

Class	Description	Detailed description
A	Rock	Instrument on rock ( $V_s > 600 \text{ m/s}$ ) or $< 5 \text{ m}$ of soil over rock
B	Shallow (stiff) soil	Instrument on/in soil profile up to $20 \text{ m}$ thick overlying rock
C	Deep narrow soil	Instrument on/in soil profile at least $20 \text{ m}$ thick overlying rock, in a narrow canyon or valley no more than several km wide
D	Deep broad soil	Instrument on/in soil profile at least $20 \text{ m}$ thick overlying rock, in a broad valley
E	Soft deep soil	Instrument on/in deep soil profile with average $V_s < 150 \text{ m/s}$

Table 2.2. Information about the records of Yarımca and İzmit stations of 1999 Kocaeli earthquake (Source: PEER, 2000)

1999 Kocaeli earthquake ( $M_w$ 7.4)		
Station	Yarımca	İzmit
Component	YPT330 (East-West)	IZT090 (East-West)
Site profile	D	A
Distance (km)	2.6 - 2.6	4.8 - 4.8
PGA (g)	0.349	0.220
PGV (cm/s)	62.1	29.8
PGD (cm)	50.97	17.12
Data source	KOERI	ERD
HP (Hz)	0.07	0.1
LP (Hz)	50.0	30.0

In Table 2.2, Yarımca station was placed on a softer soil site while İzmit station was located in a rocky region. The distances are the closest to fault rupture, hypocentral, and the closest to surface projection of rupture (Joyner-Boore distance) in kilometers, respectively. The angle of the station with respect to the North in degrees appears in the file name of the data processed and supplied by PEER (Silva, 2013).

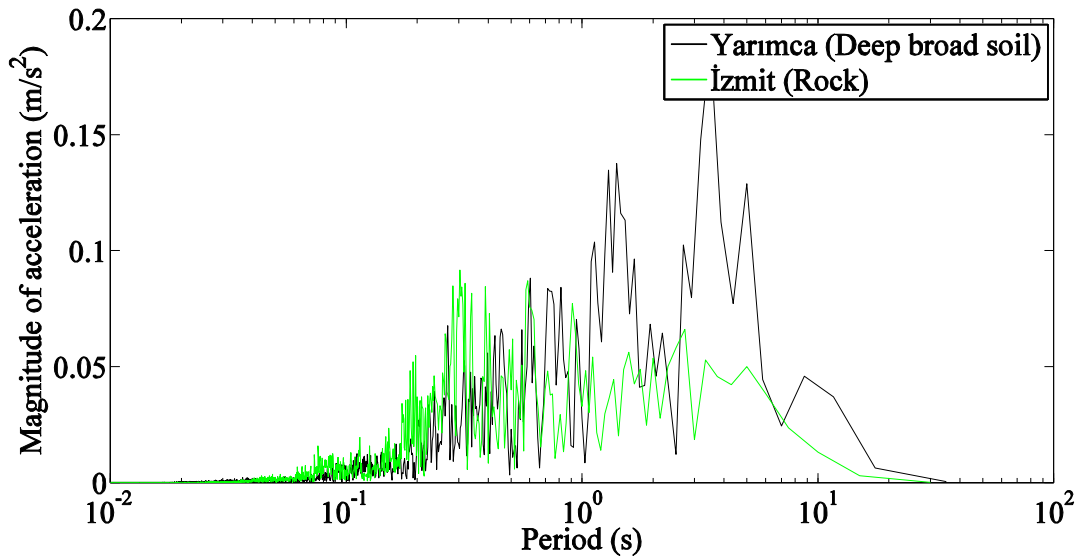


Figure 2.1. EW component records of the Yarımca station and the İzmit station of the 1999 Kocaeli earthquake

The record of the İzmit station, which was placed on a stiffer site, has a wider effective frequency range than the others. The components of the datum on the rock site have almost equally-sized magnitudes, whereas the other datum has components of different magnitudes.

The amplification effect of soft soil sites can be observed in the frequency domain since the data in time domain is composed of different sine waves with various frequencies. The ground accelerations recorded at soft soil sites, like Yarımca station, were amplified compared to those at rock sites. This case can also be shown in time domain by the examples in Table 2.3 for the 1999 Kocaeli earthquake. The distances are the closest to fault rupture, hypocentral, and the closest to surface projection of rupture (Joyner-Boore distance) in kilometers, respectively. The angle of the station with respect to the North in degrees appears in the file name of the data processed and supplied by PEER (Silva, 2013).

In Table 2.3, the closest distances to fault rupture of four stations are approximately similar. If only descending one step in site condition, holding the distance to fault rupture constant, as in Maslak and Zeytinburnu stations, all peak values in horizontal directions are duplicated. As the soil profile of the site gets worse, for instance at Ambarlı station, the horizontal components of all peak values are approximately five times greater than that at Maslak station. The amplification effect of soft soil on the vertical components is not as tremendous as on the horizontal

components. The fact that the soil properties of the sites through which the seismic waves passed to reach the stations approximately 60 km away from the fault rupture has great importance on the recorded data. These properties have to be considered while commenting about the mentioned data sets.

Table 2.3. PGA, PGV, and PGD values of four stations of 1999 Kocaeli earthquake emphasizing the amplifying effect of softer soil sites (Source: PEER, 2000)

1999 Kocaeli earthquake ( $M_w$ 7.4)												
Station	Ambarlı			Ataköy			Zeytinburnu			Maslak		
Site profile	E			D			D			A		
Distance (km)	78.9	-	78.9	67.5	-	67.5	63.1	-	63.1	63.9	-	63.9
Component	UP	000	090	UP	000	090	UP	000	090	UP	000	090
PGA (g)	0.08	0.25	0.18	0.06	0.11	0.16	0.05	0.11	0.11	0.03	0.04	0.04
PGV (cm/s)	8.5	40.0	33.2	7.5	22.4	16.2	7.2	18.5	15.2	5.7	6.6	6.5
PGD (cm)	8.85	30.08	25.83	6.09	23.47	11.59	8.56	12.98	18.2	7.24	6.52	9.24
Data source	KOERI			ITU			ITU			ITU		

Near-field strong ground motions are observed within the diameter of less than 15-20 km from fault rupture (Kalkan et al., 2004). This effect tends to increase the magnitude of the long-period components ( $T > 1$ sec) of the acceleration record. Therefore, it should be taken into account especially for tall or flexible structures, base isolated buildings, and other structures that are sensitive to long-period seismic excitations. Otherwise, the structures in a near-fault region would exhibit harsh nonlinear responses including the possibility of collapse at some parts of the system.

A near-fault ground motion record may contain velocity peaks while having small peak ground displacements. Some portion of displacements might have been removed during a standard processing procedure through filtering or baseline correction (Hall et al., 1995; Kalkan & Kunnath, 2006; Boore, 2001; Boore, 2002). Therefore, special attention should be applied while processing near-field raw records.

The sensitivity of near-field ground motions to variations in the shaking source parameters was studied, and inclusion of directivity effects was recommended while modeling near-fault ground motions (Aagaard et al., 2000). In the literature, different types of pulses are suggested to generate near-fault motions synthetically (Hall et al., 1995; Makris, 1997; Kalkan & Kunnath, 2006).

Wang et al. (2002) constituted iso-PGA maps for the 1999 Chi-Chi earthquake, due to the dense distribution of accelerographs in Taiwan. The distribution of PGAs in three components of 441 stations was presented. It is observed that the contour lines lie along the fault. Their magnitudes decrease as moving away from the fault (see Figure 2.2). Furthermore, it is seen that the ground shaking is effective along the fault rather than around the epicenter.

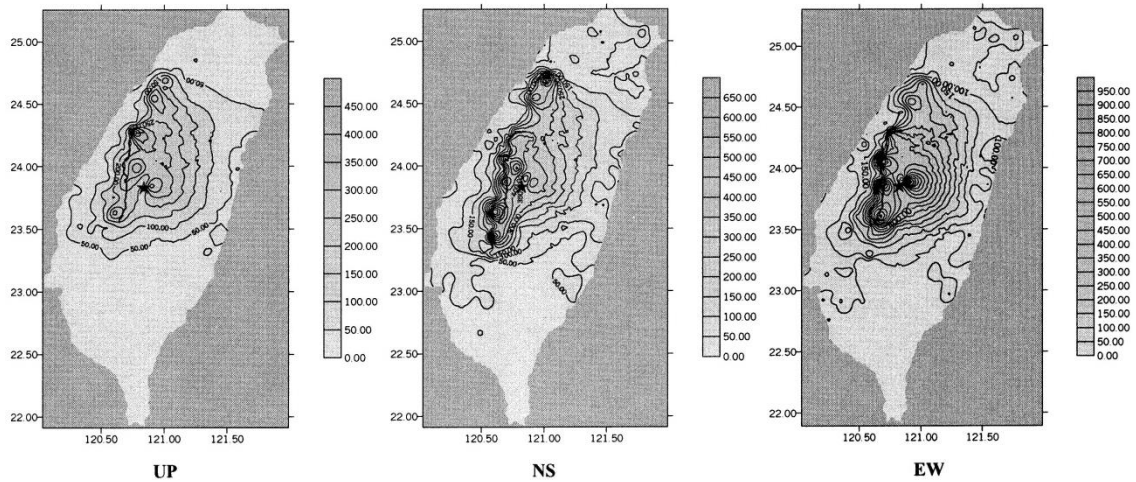


Figure 2.2. Contour maps of PGA in  $\text{cm/s}^2$  from the records of 441 stations of the 1999 Chi-Chi Twain earthquake (Source: Wang et al., 2002)

Chopra and Chintanapakdee (2001) emphasized some important outcomes in case of a near-fault ground motion. The PGA, PGV, and PGD values of the fault-normal component are larger than those of the fault-parallel component for near-field motions (directivity effect). Fault-normal component of a near-fault record displays a long-period pulse in the acceleration time history. Its effect is seen in the velocity and displacement series as compatible pulses. This observation is not valid for far-field records. In most of the near-fault motions, narrower velocity-sensitive regions and wider acceleration- and displacement-sensitive regions are present in the response spectrum. Furthermore, the narrower velocity-sensitive regions are shifted to longer periods. Additional remarks are manifested for inelastic systems.

Two behaviors are observed in near-field records as forward-directivity and fling-step type strong motions. The direction of rupture propagation relative to the site is implied as forward-directivity. Fling-step type motion is observed as a unidirectional large-amplitude velocity pulse and a step-type static permanent displacement history. It occurs in the strike-parallel direction of strike-slip faults and in the strike-normal

direction of dip-slips faults (see (Kalkan & Kunnath, 2006) for details). Records with fling effects activate the fundamental mode of the system. If the forward directivity is dominant without any fling, then higher modes are excited. Therefore, Kalkan and Kunnath (2006) suggested to utilize acceleration and velocity time histories together while examining the effects of near-fault records.

Bolt (2008) provides a brief overview of the history of earthquakes and seismology. The causes and physical properties of seismic activity are explained. Additionally, he recommends leaving the regions close to or on main faults as greenbelts after the field observations of the 1999 Chi-Chi Taiwan earthquake.

The data of four stations of the 1999 Kocaeli earthquake are presented in two graphs of Figure 2.3 to visualize the effect of near-fault records on the amplitude of high period components. In each graph, one pair of near- and far-field records obtained from stations with similar soil conditions is plotted. Hence, the comments can be performed within the content of different soil conditions as stiff soil and softer soil individually. The closest distance to fault rupture is displayed in the legend of the graphs. Other details about the data are presented in Table 2.4. The distances are the closest to fault rupture, hypocentral, and the closest to surface projection of rupture (Joyner-Boore distance) in kilometers, respectively. The angle of the station with respect to the North in degrees appears in the file name of the data processed and supplied by PEER (Silva, 2013). The North-South components of the data were chosen except for the data from Yarımca station. The closest component to the North-South direction was chosen for it as YPT060.

The stations were chosen due to the closest distance to fault rupture and its soil profile. Unfortunately, the distribution of the recorders in Turkey was not as dense as in Taiwan to portrait the near-fault effect of earthquakes. For instance, there is not a station on a soil class of A within the radius of 20-60 km for the 1999 Kocaeli earthquake that affected the most developed regions of Turkey (PEER, 2000) (Near-field strong ground motions are observed within the diameter of less than 15-20 km from fault rupture (Kalkan et al., 2004)). On the other hand, the researchers who investigated the 1999 Chi-Chi Taiwan earthquake could eliminate the data of some stations among those of 441 stations since the data had defects (Wang et al., 2002).

The soil of the station site gets softer from (a) to (b) in Figure 2.3. For each soil profile, the components with higher magnitudes in the high period range can be obviously seen for near-fault records.

It is important to emphasize the fact that most of the seismic record providers supply the data in N-S, E-W, and vertical directions. However, the components larger in the strike-normal direction than those in the strike-parallel direction were observed evidently in severe earthquakes. Therefore, it would be more convenient to supply the angle between the station and the fault together with the data by the data providers. Thus, the seismic data can be rotated.

Table 2.4. Information about the stations utilized in Figure 2.3  
(Source: PEER, 2000)

1999 Kocaeli earthquake ( $M_w$ 7.4)				
Station	Sakarya	Göynük	Yarımca	İznic
Component	SKR090	GYN090	YPT060	IZN090
Site profile	B	B	D	D
Distance (km)	3.1 - 3.1	35.5 - 35.5	2.6 - 2.6	31.8 - 31.8
PGA (g)	0.376	0.119	0.268	0.136
PGV (cm/s)	79.5	10.5	65.7	28.8
PGD (cm)	70.52	3.94	57.01	17.44
Data source	ERD	ERD	KOERI	ERD

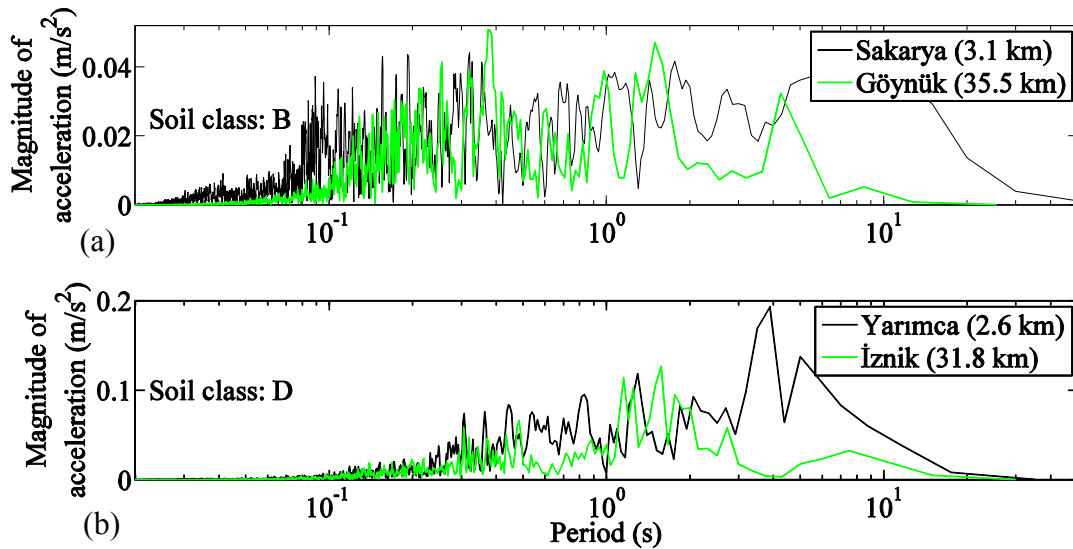


Figure 2.3. Near- and far-fault records of 1999 Kocaeli earthquake for stations located at two different sites in frequency domain (Numbers in the legend are the closest distance to fault rupture and the JB distance)

Some near-fault strong earthquakes of which the moment magnitude  $M_w$  is greater than 6.5 are presented in Table 2.5. The records with PGA value greater than 0.5g or PGV value greater than 100 cm/s were chosen in horizontal direction ( $g$  is the gravitational acceleration). Some records in 1999 Chi-Chi earthquake have relatively small PGA values, whose PGV values are greater than 100 cm/s. The distances are the closest to fault rupture, hypocentral, and the closest to surface projection of rupture (Joyner-Boore distance) in kilometers, respectively. The stations were chosen according to any given distances less than 10 km.

Table 2.5. Near-fault strong earthquakes in the world ( $M_w > 6.5$ ,  $d < 10$  km, and  $(PGA > 0.5g$  or  $PGV > 100\text{cm/s}$  in horizontal direction)) (Source: PEER, 2000)

Earthquake	Mch*	$M_w$	Station	Distance d (km)	Site profile	PGA (g)	PGV (cm/s)	PGD (cm)
Cape Mendocino 1992/04/25	RN	7.1	89005 Cape Mendocino	8.5 - -	A	1.497	127.4	41.0
			89156 Petrolia	9.5 - -	D	0.662	89.7	29.6
Chi-Chi, Taiwan 1999/09/20	RN	7.6	CHY028	7.31 - 7.31	Hard <sup>†</sup>	0.821	67.0	23.3
			CHY080	6.95 - 6.79	USGS B <sup>‡</sup>	0.968	107.5	18.6
			TCU052	0.24 - 0.06	Hard	0.419	118.4	246.2
			TCU065	0.98 - 0.98	Hard	0.814	126.2	92.6
			TCU067	0.33 - 0.33	Hard	0.503	79.5	93.1
			TCU068	1.09 - 0.5	Hard	0.566	176.6	324.1
			TCU071	4.94 - 1.01	Hard	0.655	69.4	49.1
			TCU084	10.39 - 0.01	Hard	1.157	114.7	31.4
			TCU102	1.79 - 1.79	Medium	0.298	112.4	89.2
			TCU129	1.18 - 1.18	Hard	1.01	60.0	50.2
WNT	1.18 - 1.18	Hard	0.958	68.8	31.1			
Duzce, Turkey 1999/11/12	SS	7.1	Duzce	8.2 - 8.2	D	0.535	83.5	51.6
			375 Lamont 375	8.2 - 8.2	B	0.97	36.5	5.5
Erzincan, Turkey 1992/03/13	SS	6.9	95 Erzincan	2.0 - -	D	0.515	83.9	27.4
Gazli, USSR 1976/05/17	RN	6.8	9201 Karakır	- 3.0 -	A	0.718	71.6	23.7

\* Faulting mechanism = RN:Reverse normal, SS:Strike slip, RO:Reverse oblique

<sup>†</sup> For 1999 Chi-Chi earthquake, the site profile is classified according to the Central Weather Bureau (CWB) in Taiwan as *hard*, *medium*, and *soft soil sites*.

<sup>‡</sup> USGS B: Average shear wave velocity to a depth of 30m is 360-750 m/s.

(cont. on next page)

**Table 2.5. (cont.)**

Imperial Valley 1979/10/15	SS	6.5	5054 Bonds Corner	2.5 - 2.6	D	0.775	45.9	14.9
			952 El Centro Array #5	1.0 - 4.0	D	0.519	46.9	35.4
			942 El Centro Array #6	1.0 - 1.3	D	0.439	109.8	65.9
			5028 El Centro Array #7	0.6 - 0.6	D	0.463	109.3	44.7
			958 El Centro Array #8	3.8 - 3.8	D	0.602	54.3	32.3
			6619 SAHOP Casa Flores	11.1 - 8.4	C	0.506	30.9	5.6
Kobe 1995/01/16	SS	6.9	0 KJMA	0.6 - -	B	0.821	81.3	17.7
			0 Takarazuka	1.2 - -	E	0.694	85.3	16.8
			0 Takatori	0.3 - -	E	0.616	120.7	32.7
Landers 1992/06/28	SS	7.3	24 Lucerne	1.1 - -	A	0.721	97.6	70.3
Loma Prieta 1989/10/18	RO	6.9	57007 Corralitos	5.1 - -	B	0.644	55.2	10.9
			16 LGPC	6.1 - -	A	0.563	94.8	41.2
Nahanni, Canada 1985/12/23	RO	6.8	6097 Site 1	6.0 - -	A	1.096	46.1	14.6
Northridge 1994/01/17	RN	6.7	24279 Newhall - Fire Sta	7.1 - 4.5	D	0.59	97.2	38.1
			24514 Sylmar - Olive View Med FF	6.4 - 3.6	D	0.843	129.6	32.7
			24436 Tarzana, Cedar Hill	17.5 - 4.1	B	1.779	113.6	33.2
			0655 Jensen Filter Plant	6.2 - -	D	0.593	99.3	24.0
			00000 LA Dam	2.6 - -	-	0.511	63.7	21.2
			24207 Pacoima Dam (upper left)	8.0 - 8.1	A	1.585	55.7	6.1
			77 Rinaldi Receiving Sta	7.1 - -	C	0.838	166.1	28.8
			0637 Sepulveda VA	8.9 - 0.4	D	0.939	76.6	14.9
			74 Sylmar-Converter Sta	6.2 - 0.2	D	0.897	102.8	47.0
75 Sylmar-Converter Sta East	6.1 - -	D	0.828	117.5	34.2			
San Fernando 1971/02/09	RN	6.6	279 Pacoima Dam	2.8 - -	B	1.226	112.5	35.5
Superstition Hills(B) 1987/11/24	SS	6.7	286 Superstition Mtn.	4.3 - -	A	0.894	42.2	7.3
Tabas, Iran 1978/09/16	RN	7.4	9101 Tabas	- 3.0 -	C	0.852	121.4	94.6

Table 2.5 indicates that there are PGA values greater than 1.0g in earthquakes with moment magnitude of 6.6, 6.7, and 6.8 where  $g$  is the gravitational acceleration (1971 San Fernando, 1994 Northridge, 1985 Nahanni). Very large velocity pulses ( $>1.5$  m/s) were observed in some of the near-field strong ground motions in Table 2.5.

In the present work, the system was excited by two seismic records. These were the North-South component of the El Centro station of the 1940 Imperial Valley event and the East-West component of the Bolu station of the 1999 Düzce earthquake (see Figure 2.4).

Table 2.6. Information about the seismic records utilized in the simulations  
(Source: PEER, 2000)

	1940 Imperial Valley	1999 Düzce
Date	1940/05/19	1999/11/12
Mechanism	Strike slip	Strike slip
Moment magnitude ( $M_w$ )	7.0	7.1
Station	117 El Centro Array #9	Bolu
Component	ELC180 (North-South)	BOL090 (East-West)
Site profile of station	D	D
Distance (km)	8.3 - 12.0	17.6 - 17.6
PGA (g)	0.313	0.822
PGV (cm/s)	29.8	62.1
PGD (cm)	13.32	13.55
Data source	USGS	ERD
HP (Hz)	0.2	0.05
LP (Hz)	15	null

Other details about the records utilized in the present research are presented in Table 2.6. The raw data provider is displayed as the data source, United States Geological Survey (USGS) and Earthquake Research Department (ERD) in Turkey. The processed data were obtained from Pacific Earthquake Engineering Center (PEER). The mechanism was strike slip (SS) in both earthquakes. The angle of the station with respect to the North in degrees appears in the file name of the data processed and supplied by PEER (Silva, 2013). Both stations were located at sites with similar soil profiles. The distances are the closest to fault rupture, hypocentral, and the closest to surface projection of rupture (Joyner-Boore distance) in kilometers, respectively. Peak ground acceleration, velocity, and displacement values are presented respectively where  $g$  is the gravitational acceleration. PGD value is the maximum of the doubly integrated form of the recorded acceleration time series. The cut-off frequencies of high-pass and

low-pass filters were indicated by HP and LP in Hertz, respectively. The data set of the Düzce earthquake was passed through only a high-pass filter. The angle of the station with respect to the North in degrees appears in the file name of the data processed and supplied by PEER (Silva, 2013). The data processed by PEER are presented in time- and frequency-domains for the two seismic events (see Figure 2.4). The two seismic records were plotted together to compare their possible effects on the responses.

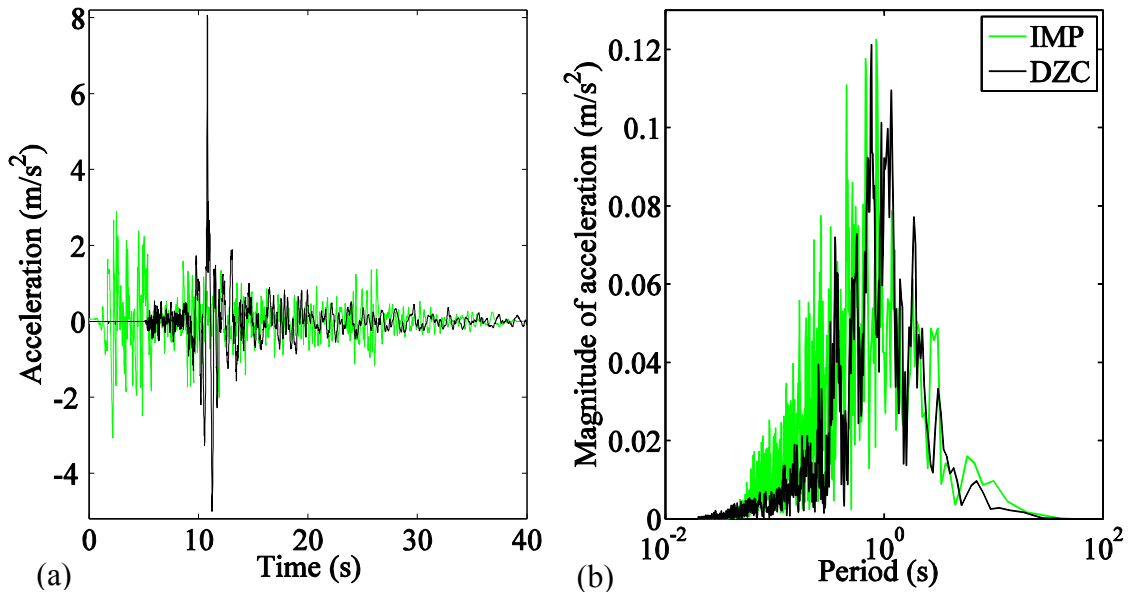


Figure 2.4. Seismic records in (a) time and (b) frequency domains: N-S component of the El Centro station of the Imperial Valley earthquake (IMP) & E-W component of the Bolu station of the Düzce earthquake (DZC)

The Imperial Valley event has a wide frequency range, while the Düzce earthquake consists of low-valued cycling motion together with a single high peak shock at time  $t \approx 12$  s with a value of  $0.8g$  and its neighbor peaks where  $g$  is the gravitational acceleration. The Imperial Valley earthquake affects structures with low periods more intensely compared to the Düzce event.

Seismic records within 15-20 km of an active faulting system are considered as near-field strong motion data (Kalkan et al., 2004). In that respect, the two records in Figure 2.4 can be regarded as near-source data, keeping in mind their difference in distance (see Table 2.6 for the distances of the stations to the fault). On the other hand, the stations of these two seismic records are not as close to the fault as the stations in the 1999 Chi-Chi earthquake, which is a well-known near-fault earthquake (Wang et al., 2002). Therefore, the seismic data of the Imperial Valley and Düzce earthquakes are

shifted to the high-period range in frequency spectrum. The author suggests deeper studies on producing near-fault seismic data synthetically to monitor the effects of fling step and forward directivity on seismic response of controlled structures, especially their effects on flexible structures.

In the context of the present work, two seismic data set were produced synthetically from the Imperial Valley and Düzce earthquakes to investigate the controller performance for near-fault earthquakes. The procedure of seismic data production is illustrated in Figure 2.5.

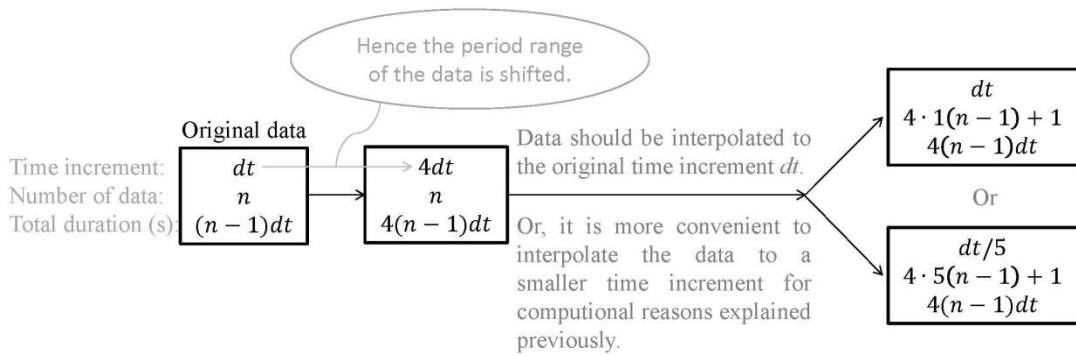


Figure 2.5. Synthetic production of the near-fault excitation data

The original time increment  $dt$  was increased four times, hence the data was shifted to the high-period range in frequency spectrum. At this point, the number of data remained constant, while the total duration of the data was lengthened. The data become sparse and was interpolated to a smaller time increment. The details are presented in Section 4.5.6.1 and Section 5.8.1.

## CHAPTER 3

### MODEL SUPERSTRUCTURE

The model superstructure has three stories (Turan & Aydın, 2011). One of its frames was utilized for calculations. It is a shear frame and is presented in Figure 3.1. The story stiffnesses were modeled by linear springs. Damping of the model superstructure was modeled by proportional viscous damping model and was represented by viscous dashpots.

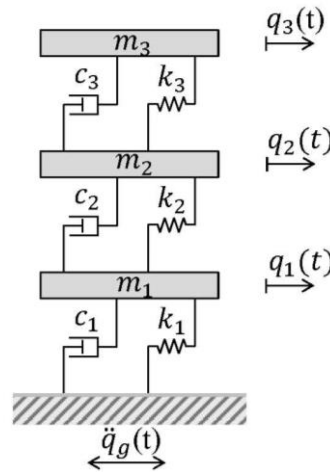


Figure 3.1. Model superstructure

Assuming that the controlled building response remains in the linear region, the equations of motion for the model superstructure was as follows:

$$\mathbf{M}_{ss}\ddot{\mathbf{q}}_{ss}(t) + \mathbf{C}_{ss}\dot{\mathbf{q}}_{ss}(t) + \mathbf{K}_{ss}\mathbf{q}_{ss}(t) = -\mathbf{M}_{ss}\mathbf{h}_{1ss}\ddot{q}_g(t) \quad (3.1)$$

The subscript *ss* stands for the superstructure. The displacements of the floors relative to the ground are presented by the vector

$$\mathbf{q}_{ss}(t) = (q_1(t) \quad q_2(t) \quad q_3(t))^T \quad (3.2)$$

The mass and stiffness matrices of the superstructure are as,

$$\mathbf{M}_{ss} = \begin{bmatrix} 103 & 0 & 0 \\ 0 & 100 & 0 \\ 0 & 0 & 99.5 \end{bmatrix} kg$$

$$\mathbf{K}_{ss} = \begin{bmatrix} 156000 & -78000 & 0 \\ -78000 & 156000 & -78000 \\ 0 & -78000 & 78000 \end{bmatrix} N/m$$
(3.3)

The determination of the damping matrix  $\mathbf{C}_{ss}$  is summarized in Section 3.1.1. The damping matrix is presented in Equation (3.13).  $\mathbf{h}_{1ss}$  is the location matrix of the external excitation. It specifies how the ground excitation  $\ddot{q}_g$  enters into the system. It is presented by

$$\mathbf{h}_{1ss} = (1 \ 1 \ 1)^T$$
(3.4)

indicating that the ground excitation acts to all degrees of freedom since the equation of motion of the system is written with respect to the ground.

The undamped periods and frequencies of the 3-story model structure are presented in Table 3.1. The slowest mode contributes to the response mostly compared to the others since it goes on its response while rapid modes have finished their responses. Therefore, the slowest mode is named the fundamental mode.

Table 3.1. Undamped periods and frequencies of the 3-story model superstructure

	Period (s)	Undamped frequency (Hz)	Undamped circular frequency (rad/s)
First mode	0.51	1.98	12.43
Second mode	0.18	5.50	34.57
Third mode	0.13	7.97	50.09

The damped and undamped circular frequencies obtained from experiments done by Turan and Aydın (2011) are displayed in Table 3.2. The undamped circular frequencies were calculated by means the damped ones.

According to the theory of modeling, the aim of the present research is to uncover the effectiveness of building control by MRDs and VODs. The reaction forces of these dampers are highly dependent on the velocity. In order to relate the outcomes of the present research, the magnitudes of the velocities should be in the same range as

typical building-type structures. Therefore, the period of the model structure was selected to be a typical value of 0.51 seconds and its isolated period as 5.06 seconds (see Section 4.7.1) (the seismic excitation data was not scaled in time domain). Thus, the expected velocities and displacements would be identical to a real structure. If the excitation data had been scaled, then the time increment would have decreased by square root of the scale factor of the structure, and the seismic data would have been pushed to the range of the excitation components with low periods.

### 3.1. Determination of the Damping Matrix

Damping dissipates the mechanical energy of a dynamic system and reduces the amplitude of its oscillations. Most of the dissipated energy is converted to heat energy. Unlike the mass and stiffness properties, in most cases, it is impossible to model damping exactly. There exist different mechanisms of damping (Liang & Lee, 1991; Inman, 2007):

- The energy dissipation, caused by sliding of two dry surfaces under a normal force, is generally represented by the *Coulomb-friction* model.
- In case of frequency-dependent damping, *structural (hysteretic) damping* model is convenient.
- The resisting force in the motion of a body through a liquid is proportional to the velocity of the body and is modeled by the *viscous damping* model.  $F = -c\dot{q}$  where  $F$  is the resisting force, and  $\dot{q}$  is the velocity of the body.  $c$  is a constant of proportionality and is named the *viscous damping coefficient*.

The *classical damping* is a special case of viscous damping, in which the damping coefficient is a linear combination of the mass and the stiffness. In other words, it is *proportionally damped* (Meirovitch, 1989). In multi-degree-of-freedom (MDOF) structures, the damping matrix is assumed to be a classical and a nonclassical one. Chopra (1995) defines: “*Classical damping is an appropriate idealization if similar damping mechanisms are distributed throughout the structure (e.g., a multistory building with a similar structural system and structural materials over its height).*” (p. 417). He also states that: “*The assumption of classical damping is not appropriate if the system to be analyzed consists of two or more parts with significantly different levels of damping.*” (p. 425).

On the other hand, a nonproportionally-distributed damping mechanism is observed in structure-soil, structure-fluid, and seismic isolated systems, and in structures with special energy dissipating devices. The nonclassical damping matrix is formed by assembling the classical damping matrices of subsystems (see Section 5.4).

If the damping ratios of all modes are known somehow (measured or assumed), then the damping matrix can be calculated via the modal damping matrix (in generalized coordinates) whose diagonal elements are  $2\zeta_i\omega_i m_i$ . Here,  $\zeta_i$  is the modal damping ratio,  $\omega_i$  is the natural circular frequency,  $m_i$  is the mass, and  $i = 1, 2, \dots, n$  is the mode number. The damping matrix in physical coordinates is obtained by performing the inverse of the diagonalization (assuming the system is proportionally damped).

On the other hand, if only damping ratios of two modes are known, then Rayleigh damping can be utilized. The damping ratios of other modes are assigned automatically. Additionally, Caughey damping, which is a more general form of Rayleigh damping, can be used (Semblat, 1997). These two procedures form classical damping matrices. Since the mode shapes of undamped and classically-damped systems are the same, a common mode shape that can diagonalize the mass, damping, and stiffness matrices of the system simultaneously exists. Hence,  $n$  uncoupled equations of motion can be formed, and the classical modal analysis can be applied. The applicability of classical modal analysis makes the proportional damping assumption attractive.

On the other hand, for systems with nonclassical damping, the mode shapes of undamped and damped systems are not the same and there is not a common mode shape that can diagonalize every term of the equation(s) of motion. Therefore, the equation(s) of motion cannot be diagonalized and the classical modal analysis cannot be applied (Chopra, 1995; He & Fu, 2001). Furthermore, in a nonproportionally damped system, there are phase differences between various parts of the system leading to complex modes (see Section 5.5.5.2).

### **3.1.1. Measurement of the Modal Damping Ratio $\zeta$**

In an under-damped single-degree-of-freedom (SDOF) system, the damping ratio can be determined via the drop in the amplitude of the response within one cycle of vibration (Meirovitch, 2001). This drop is mainly governed by the magnitude of the

envelope curve  $e^{-\zeta\omega_n t}$  of the unforced response of an under-damped system (see Appendix F).  $\zeta$  is the dimensionless modal damping ratio defined as the fraction of the present damping to the critical damping value, which represents the boundary between the under-damped and over-damped cases.

For a linear MDOF system, every mode can be disturbed by an displacement initial condition in the shape of its mode, and the damping ratio corresponding to the relevant mode can be determined. The unforced responses of an under-damped SDOF system for two successive peaks are presented in Appendix F, as follows

$$\frac{q(t_1)}{q(t_2)} = \frac{\mathbb{C}e^{-\zeta\omega_n t_1} \sin(\omega_d t_1 + \phi)}{\mathbb{C}e^{-\zeta\omega_n t_2} \sin(\omega_d t_2 + \phi)} \quad (3.5)$$

where  $t_2 = t_1 + T_d$ .  $T_d = 2\pi/\omega_d$  and  $\omega_d = \omega_n\sqrt{1-\zeta^2}$  are the period and circular frequency of the damped oscillation, respectively.  $\omega_n$  is the natural circular frequency.  $\zeta$  is the damping ratio.  $\mathbb{C}$  is a constant.  $\phi$  is the phase difference. Then,  $t_2 = t_1 + T_d$  is plugged into Equation (3.5),

$$\frac{q(t_1)}{q(t_2)} = \frac{e^{-\zeta\omega_n t_1} \sin(\omega_d t_1 + \phi)}{e^{-\zeta\omega_n(t_1+T_d)} \sin(\omega_d(t_1 + T_d) + \phi)} \quad (3.6)$$

results in,

$$\frac{q(t_1)}{q(t_2)} = e^{\zeta\omega_n T_d} \frac{\sin(\omega_d t_1 + \phi)}{\sin(\omega_d t_1 + 2\pi + \phi)} = e^{\zeta\omega_n \frac{2\pi}{\omega_d}} \quad (3.7)$$

Finally, the logarithmic decrement  $\delta$  is obtained as:

$$\delta = \ln \frac{q(t_1)}{q(t_2)} = 2\pi \frac{\zeta}{\sqrt{1-\zeta^2}} \quad (3.8)$$

There is only one restriction for Equation (3.8) as the system is under-damped ( $\zeta < 1$ ). The damping ratio  $\zeta$  can be determined via

$$\zeta = \frac{\delta}{\sqrt{4\pi^2 + \delta^2}} \quad (3.9)$$

where the damping ratio  $\zeta$  is not linearly proportional to the logarithmic decrement  $\delta$ . Equation (3.9) is valid for under-damped cases.

The superstructure was manufactured in the Structural Laboratory of IYTE Civil Engineering Department. In the present research, its damping ratios were recalculated by means of the measurements performed previously by Turan and Aydın (2011). The damping ratios were calculated via the logarithmic decrement within successive peaks of the responses. In each case, only the corresponding mode was excited. The maximum values of the responses could not be determined correctly due to the small damping values. Different damping ratios were calculated for every couple of successive peaks. Therefore, a least-squares procedure explained by Meirovitch (2001) was applied. Six successive peak values were read and their natural logarithms were plotted versus measurement number. A line was fitted through a least-squares fit. The slope of the line was negative of the logarithmic decrement  $\delta$ . Six values, which were read from one measurement, were collected by a line fitting procedure to obtain the viscous damping ratio of the excited mode. At this point, it should be noted that the fitted resultant damping ratio was not exactly viscous while the read values were viscous (Meirovitch, 2001).

The damping ratios of the first two modes were calculated as 0.0058 and 0.0038, respectively. But, the damping ratio of the third mode could not be determined since relevant measurements were not reliable. Therefore, the damping matrix was composed via the Rayleigh damping instead of the modal damping matrix whose diagonal elements are  $2\zeta_i\omega_i m_i$ .

Ewins (2000) defines the damping mechanism: “*The actual damping mechanisms are usually found in parallel with the stiffness elements (for damping due to the internal material) or with mass elements (for damping due to friction).*” (p.65). In the light of this opinion, the Rayleigh damping model, which assumes the damping as a combination of mass- and stiffness-proportional components, is utilized in the present research. The viscous damping matrix  $\mathbf{C}_{SS}$  is assumed as

$$\mathbf{C}_{SS} = \alpha \mathbf{M}_{SS} + \beta \mathbf{K}_{SS} \quad (3.10)$$

The subscript *ss* stands for the superstructure in order not to confuse the matrix **K** of the controller with the stiffness matrix of the structure. The damping ratio of the *i*th mode is

$$\zeta_i = \frac{\alpha}{2\omega_i} + \frac{\beta\omega_i}{2} \quad (3.11)$$

The modal damping factors for the two modes were determined and the proportionality coefficients  $\alpha$  and  $\beta$  were calculated via the following formulas:

$$\alpha = \frac{2\omega_1\omega_2(\zeta_2\omega_1 - \zeta_1\omega_2)}{(\omega_1^2 - \omega_2^2)} \quad (3.12)$$

$$\beta = \frac{2(\zeta_1\omega_1 - \zeta_2\omega_2)}{(\omega_1^2 - \omega_2^2)}$$

The derivations of Equations (3.11) and (3.12) are presented in Wood (1995). The undamped circular frequencies were utilized while calculating the proportionality coefficients  $\alpha$  and  $\beta$  in Equation (3.12). Then, the damping ratio of the third mode was obtained automatically by Equation (3.11). The calculation of  $\alpha$  and  $\beta$  are presented in Table 3.2.

Table 3.2. Calculation of the proportionality coefficients  $\alpha$  and  $\beta$  of the Rayleigh damping

	Modal damping ratio $\zeta_i$	Damped circular frequency $\omega_{di}$ (rad/s)	Undamped circular frequency $\omega_{ni}$ (rad/s)	$\alpha$ (rad/s)	$\beta$ (s/rad)
First mode	0.0058	12.0830	12.0832	0.1231	$1.1667 \cdot 10^{-4}$
Second mode	0.0038	34.9066	34.9069		
Third mode		48.3322			

The damping ratios and damped circular frequencies in rad/s were obtained from experiments done by Turan and Aydın (2011). The undamped circular frequencies were calculated by means of the damped circular frequencies. They were very close to the damped ones due to the very low damping levels. The coefficients  $\alpha$  and  $\beta$  were calculated. The numerical difference in the magnitudes of  $\alpha$  and  $\beta$  should be commented in the content of their units.

Then, the damping ratio  $\zeta_3$  of the third mode was calculated as 0.0041 via Equation (3.11). Finally, the damping matrix of the superstructure was obtained by the proportional viscous damping model as

$$\mathbf{C}_{ss} = \alpha \mathbf{M}_{ss} + \beta \mathbf{K}_{ss} = \begin{bmatrix} 30.88 & -9.1 & 0 \\ -9.1 & 30.51 & -9.1 \\ 0 & -9.1 & 21.35 \end{bmatrix} \text{Ns/m} \quad (3.13)$$

The viscous damping model, in which the resisting force was proportional to the velocity difference, was assumed. Then, the viscous damping was determined by the Rayleigh damping model. In this case, it was preferable to express the damping of the structure with mass- and stiffness-proportional elements in Figure 3.1. Modelling the damping by a dashpot in Figure 3.1 was preferred due to the assumption of viscous damping model.

## CHAPTER 4

# CONTROL OF SEISMIC RESPONSE WITH MAGNETORHEOLOGICAL DAMPERS (MRDs)

### 4.1. Introduction

Semi-active control devices have been attractive in recent times since they offer the advantages of passive and active control systems and compensate for weak features of them. The properties of semi-active control devices can be adjusted in real time. Such devices do not add energy into the system being controlled. Magnetorheological dampers (MRDs) are semi-active control devices that utilize MR fluid to produce controllable damping forces.

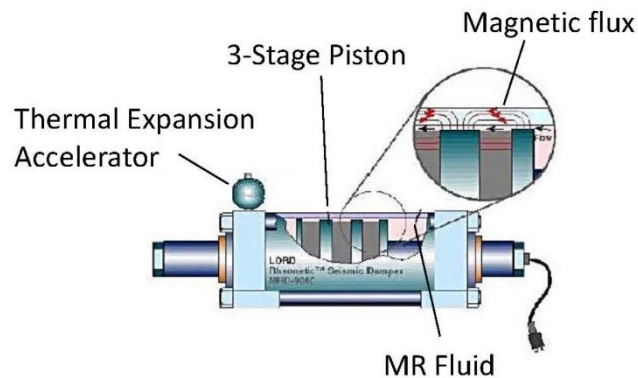


Figure 4.1. Magnetorheological Damper  
(Source: Lord Corporation, 2008)

Magnetorheological dampers are utilized in a variety of real world applications such as semi-active vibration control, sports equipments, and medical prosthesis. MRDs are widely used in suspension system of heavy military vehicles or in seat suspension systems of trucks. Hiemenz et al. applied MRDs to helicopter crew seat suspension system to enhance occupant comfort (2009). In aerospace applications, magnetorheological dampers exhibit benefits of semi-active control of aeromechanical instabilities (Wereley et al., 1999).

The advantages of MRDs are their low power requirements, high yield strength that allows large force capacity, low viscosity, and stable hysteretic behaviour over a wide temperature range. MRDs utilizes MR fluid to produce controllable damping forces (Jung et al., 2002). Jacob Rabinow discovered the MR fluid in 1948-1951 at the US National Bureau of Standards. Although it has been a long time since MR fluid was discovered, they have been utilized in engineering applications recently.

The behaviour of magnetorheological dampers are highly nonlinear. Different phenomenological models exist in the literature for MRDs. In the current work, the modified Bouc-Wen model proposed by Spencer et.al. is utilized (1997). It is composed of Bouc-Wen hysteresis, springs, and dashpots to accurately reproduce the MRD behaviour.

A modified clipped-optimal acceleration feedback control strategy is utilized to control the MRD. The controller consists of a linear optimal control part and a modified clipped algorithm. The effectiveness of the control algorithm and the usefulness of MRDs for response reduction are demonstrated through different numerical examples: First, a single MRD is excited by sinusoidal displacement. Secondly, a model structure including a MRD is excited seismically. Finally, a seismically isolated model structure, which contains a MRD, was controlled.

## **4.2. Literature Review**

Structural control may be utilized to reduce the amount of energy transferred into the structure from the ground motion either by using external energy or by absorbing a portion of the seismic energy. There exist passive, semi-active, active, and hybrid structural control systems (Symans & Kelly, 1999). In that respect, Spencer et al. (1997) states that: *“Semi-active control systems combine the best features of both approaches, offering the reliability of passive devices, yet maintaining the versatility and adaptability of fully active systems. According to presently accepted definitions, a semi-active control device is one that has properties that can be adjusted in real time but cannot input energy into the system being controlled.”* (p.230).

Some advantages of MRDs are their low power requirements, high yield strength that allows large force capacity, low viscosity, and stable hysteretic behavior over a wide temperature range (Spencer et al, 1997). The most attractive property of the

controllable MR fluid is their ability to reversibly change from a free-flowing, linear viscous fluid to a semi-solid with a controllable yield strength in milliseconds when exposed to a magnetic field.

In the literature the damping properties of the MRDs were regulated by different control strategies. Dyke and her co-workers performed acceleration feedback control strategies based on  $H_2$ /LQG methods (1996). Spencer et al. tried frequency domain optimal control strategies by two specific techniques:  $H_2$  and  $H_\infty$  control methods (1994). Various research groups utilized fuzzy logic to control MRDs (Choi et al., 2004; Huang et al., 2009; Schurter & Roschke, 2001; Turan & Kinay, 2009; Wilson, 2005). Dyke and Spencer compared semi-active control strategies for the MRD and concluded that the performance of the control system is highly dependent on the choice of algorithm employed (1997). Instantaneous optimal control with velocity and acceleration feedback was utilized, and additionally the structural stability was guaranteed by using the Lyapunov approach (Ribakov & Gluck, 2002). Sliding mode control was also applied to MR dampers (Kinay & Turan, 2009). Yoshida and Dyke proposed the modified clipped control algorithm, in which the control voltage lies between 0 and  $v_{\max}$  (2004).

JZ20-2NW offshore platform in Bohai Gulf of China is the first offshore platform that is controlled by MRDs in the world (Wu et al., 2010). The dynamic response of the platform against ice and earthquake excitations was tried to be decreased. The control system design and the full-scale real-time hybrid tests of the platform were explained in the mentioned study. Due to the limited number of measurements, a Kalman filter was employed to observe the states from displacement and acceleration measurements. The accuracy of the state estimate in case of an unknown external excitation was not as good as the case, in which the excitation mean value was known. On the contrary, this fact had small effect on the controlled responses.

The response of MRDs that were attached to a three dimensional model structure was investigated by Turan and Kinay (2009). The model structure was excited individually by two horizontal components of the Bolu station of the 1999 Düzce earthquake. The effectiveness of MRDs to control vibrations of three dimensional structures were demonstrated through numerical examples. The floor responses were bounded to the response of a certain node at every story of the superstructure. Four MRDs were attached between the ground and the first floor. The displacement of each

damper was independent of each other. Therefore, their responses were treated separately in the code. The total acceleration values of the first floor were not reduced significantly by the MRDs. This fact may have been due to the existence of the dampers at the first floor level. On the other hand, the absolute acceleration values of the second and third floors provided more correct information with the behavior of the structure since the absolute accelerations of the first floor contained not only the structure's accelerations but also accelerations coming from the damping forces of the MRDs. Acceptable reductions in maximum values of the responses were observed. After the first 8 seconds, the controlled response became very small compared to the uncontrolled one. On the other hand, the improvements in the maximum values of the total accelerations were not as good as those of displacements.

### 4.3. Magnetorheological Dampers

MRDs are widely utilized as supplemental damping strategies for response reduction in civil engineering structures subjected to strong earthquakes and severe winds. They are controllable fluid dampers, which utilize magnetorheological (MR) fluids.

MR fluid is suspension of micron-sized, magnetizable particles randomly dispersed in a carrier medium such as mineral or silicon oil. In the absence of a magnetic field, MR fluid is free-flowing, linear viscous fluids (similar to motor oil). The iron particles form linear chains parallel to the field when exposed to a magnetic field and become a semi-solid behaving as a viscoplastic material.

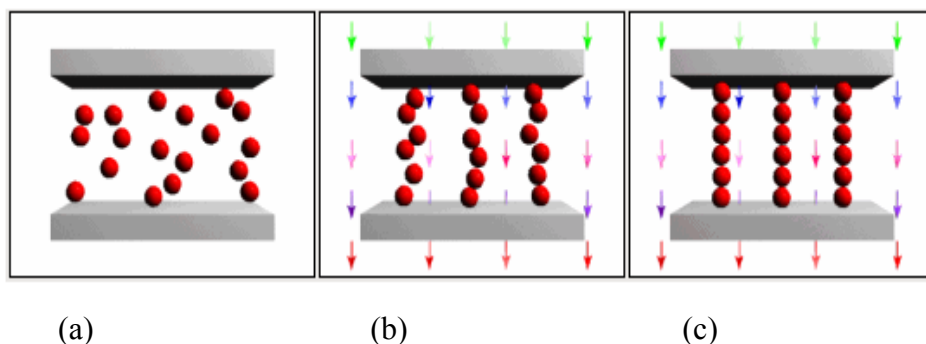


Figure 4.2. Iron particles in a carrier medium (The arrows indicate the magnetic field direction) (Source: Lord Corporation, 2008)

In Figure 4.2(a) the arrangement of iron particles is shown in the absence of a magnetic field. In Figure 4.2(b) and (c) the change of arrangement is presented by increasing the magnetic field. The transition occurs within milliseconds depending on the magnitude of the applied magnetic field. This feature provides the opportunity of construction of devices with high bandwidth.

Semi-active control devices have very low power requirements. This property is very important during seismic events when the main power source to the structure fails. MR fluid can be controlled with a low voltage of ~12-24 Volts, current-driven power supply outputting only ~1-2 amperes. The yield strength of modern MR fluid is at a level of 80 kPa. This feature allows generating high forces which is desired in full-scale applications.

The rise time from 10% to 90% of the final value for the MRD force is a few milliseconds. Some part of this time lag is spent to reach rheological equilibrium of the MR fluid, and the remaining part is associated with the electromagnet's dynamics. A very small time step is required in numerical simulations to reproduce the MRD behaviour correctly.

MR fluid can work over a wide range of operating conditions. Its yield stress varies slightly at temperatures from  $-40$  to  $150^{\circ}\text{C}$ . Additionally, MR fluid is insensitive to impurities, and different additives can be chosen to improve its properties. The additives are utilized to provide homogeneity or to prevent gravitational settling and wear. A small amount of separation between the particle and the carrier fluid occur under common flow conditions.

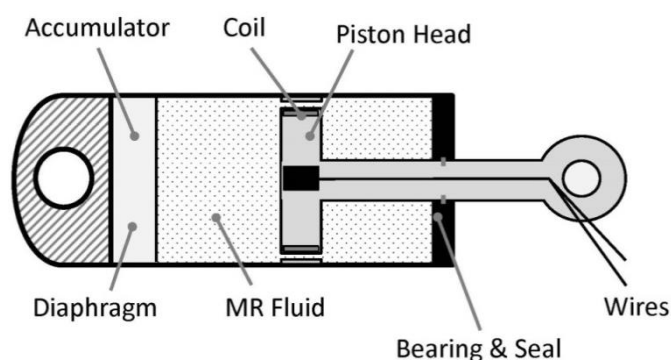


Figure 4.3. Longitudinal cross-section of MRD  
(Source: Dyke et.al., 1996)

A fixed orifice damper filled with MR fluid is presented in Figure 4.3. The input voltage is applied to the wires to the electromagnet. The desired magnetic field is generated by a small electromagnet in the piston head. The coil is placed near the orifice on the piston head. The armature output voltage  $v_A$  in Equations (4.5) and (4.6) occurs on the coil.

An accumulator is placed in the damper in order to prevent cavitation in the fluid during normal operation. Additionally it corresponds to the volume of fluid displaced by the piston rod in the opposite cell and the thermal expansion of the fluid. It consists of a bladder within the main cylinder, which is filled with pressurized gas (see Figure 4.3).

The iron particles in the MR fluid are randomly dispersed in a carrier medium as seen in Figure 4.2. If zero voltage is applied, then magnetic field does not occur, and the MRD behaves as a viscous device. The force-displacement curve is nearly elliptical, and the force-velocity curve is almost linear (see Figure 4.5-Figure 4.7). As the applied voltage increases (or as the current increases), a magnetic field increases by means of the coil, and the force required to yield the fluid increases. MR fluid's behaviour turns into a plastic material in parallel with a viscous damper (Bingham plastic behaviour). The damping force of the MRD is related with the velocity of the fluid while passing along the orifice. As the current increases, iron particles form chains, and the passing velocity decreases. When the iron particles form complete linear chains parallel to the field, the magnetic field may increase, but the fluid flow around the iron particles does not further slow down. An increase in the applied voltage does not affect the passing velocity anymore and the iron particles become stable. Consequently, the damping force of the MRD does not increase anymore. This situation is referred as the saturation of the magnetic field in the MRD. A chain denser than the one in the saturated case can not be obtained. The saturation voltage is the maximum voltage used in the clipped control algorithm.

### 4.3.1. Modified Bouc-Wen Model for MRDs

Magnetorheological dampers are highly nonlinear devices. A mechanical model proposed for a MRD should effectively portray its nonlinear character. Various phenomenological models have been proposed during the development period of behavior model for MR dampers due to their highly nonlinear behaviour.

The Bingham viscoplastic model and a model which is an extension of the Bingham model have been utilized at the beginning of the development of rheological behaviour model for MRDs. As time passed the Bouc-Wen hysteresis model became widely accepted for MRDs. It could exhibit a wide range of hysteretic behaviours. Afterwards, the modified Bouc-Wen hysteresis model was proposed (Yang et al., 2002). This new model could predict the damper response better in the region where the acceleration and velocity have opposite signs, and the magnitude of the velocities are small. Jimenez and Alvarez-Icaza presented the improved LuGre friction model (2005). Yang et.al. (2009) improved the model parameters of the improved LuGre friction model by the gradient-based optimization method and by the least square technique.

In the numerical simulations of the present research, the modified Bouc-Wen model was utilized, which was proposed by Spencer et al. (1997). It is composed of Bouc-Wen hysteresis, springs, and dashpots to accurately reproduce the MRD behavior. The Bouc-Wen hysteresis model is numerically tractable and can exhibit a wide variety of hysteretic behaviour.

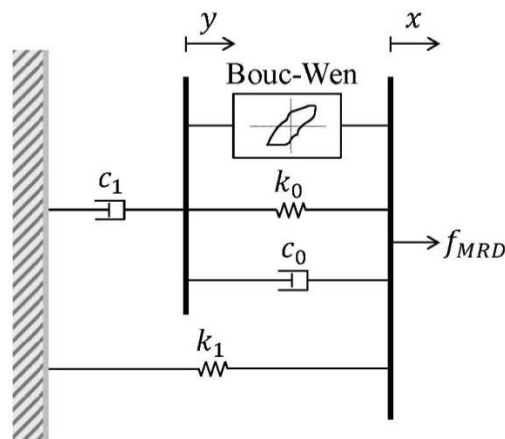


Figure 4.4. Modified Bouc-Wen model  
(Source: Spencer et.al., 1997)

The damping force of the MRD in Figure 4.4 can be calculated from the lower section as,

$$f_{MRD} = c_1\dot{y} + k_1(x - x_0) \quad (4.1)$$

The same force can be calculated from the upper section as follows

$$f_{MRD} = \alpha s + c_0(\dot{x} - \dot{y}) + k_0(x - y) + k_1(x - x_0) \quad (4.2)$$

Solving the two expressions for  $\dot{y}$  results in

$$\dot{y} = \frac{1}{c_0 + c_1} [\alpha s + c_0\dot{x} + k_0(x - y)] \quad (4.3)$$

The evolutionary variable  $s$  of the Bouc-Wen model is governed by

$$\dot{s} = -\gamma|\dot{x} - \dot{y}||s||s|^{n-1} - \beta(\dot{x} - \dot{y})|s|^n + A(\dot{x} - \dot{y}) \quad (4.4)$$

where  $k_1$  is the accumulator stiffness, and  $x_0$  is the initial displacement of spring  $k_1$  associated with the nominal damper force due to the accumulator. The viscous damping observed at high velocities and the viscous damping for the force roll-off at low speeds are represented by  $c_0$  and  $c_1$ , respectively.  $k_0$  is the stiffness at high velocities.  $x$  is the external excitation.  $y$  is the internal variable of the Bouc-Wen model.  $n$  is the shaping parameter of the hysteresis.

The role of the accumulator inside the damper is two folded. First, it accounts for the fluid volume change due to the displacement of the piston rod. Second, it allows volumetric changes of the fluid due to change in temperature. The accumulator in the damper behaves like a spring. Therefore, the spring  $k_1$  is placed in parallel due to the presence of accumulator. The difference between the areas of the piston's both sides, which is due to the presence of piston rod, cause a difference in pressures on the areas. This is modeled by a constant value of an initial displacement  $x_0$  of the spring  $k_1$ .

The values of the characteristic parameters of the model are presented in Table 4.1. The linearity in the unloading region of the force versus velocity graph and the smoothness of the transition from the pre-yield region to the post-yield region can be

controlled by adjusting the characteristic parameters  $\gamma, \beta$ , and  $A$ . The appropriate parameters for the analytical model were obtained by a constrained nonlinear optimization (Spencer et al., 1997). At this point, the aim was to determine parameters for a wide range of operating conditions.

In order to control the model structure's seismic response, the properties of the MRD were varied by the magnetic field. This was performed by applying a voltage to the armature circuit. The MRD is governed by the applied voltage. The parameter  $\alpha$  of the Bouc-Wen model and the viscous damping coefficients  $c_0$  and  $c_1$  are determined for both cases of constant magnetic field and fluctuating magnetic field (i.e. constant and varying applied voltage). The yield stress of the MR fluid depend on the magnetic field strength, therefore the parameter  $\alpha$  is assumed to be directly proportional with the applied voltage. According to Figure 4.5-Figure 4.7, the steady-state yield level varies linearly with the applied voltage and have a nonzero initial value when zero voltage is applied. The reasons of this nonzero initial value are the facts that the fluid is designed in order to have a small yield strength at zero field for stability against gravitational settling and the friction in the piston rod seal. Therefore, the functional dependence of the parameters to the applied voltage presented in Equation (4.5) was proposed by Spencer et. al.:

$$\begin{aligned}\alpha(v_A) &= \alpha_a + \alpha_b v_A \\ c_0(v_A) &= c_{0a} + c_{0b} v_A \\ c_1(v_A) &= c_{1a} + c_{1b} v_A\end{aligned}\tag{4.5}$$

$v_A$  is the armature voltage. It is not possible to measure the armature output voltage  $v_A$ . Therefore, the dynamics of the MR fluid reaching rheological equilibrium are modeled by a first order low-pass filter presented by

$$\dot{v}_A = -\eta(v_A - v)\tag{4.6}$$

where  $v$  is the input voltage sent to the current driver. The mechanical model proposed by Spencer et al. (1997) gives the closest responses to those in the experiments performed within their research. Therefore, the parameters determined by Spencer et al. (1997) were utilized in the response calculations of the MRD (see Table 4.1).

Table 4.1. Parameters for the modified Bouc-Wen model  
(Source: Spencer et al., 1997)

Parameter	Value	Parameter	Value
$c_{0a}$	2100 Ns/m	$\alpha_a$	14000 N/m
$c_{0b}$	350 Ns/m·V	$\alpha_b$	69500 N·V/m
$c_{1a}$	28300 Ns/m	$\gamma$	3630000 m <sup>-2</sup>
$c_{1b}$	295 Ns/m·V	$\beta$	3630000 m <sup>-2</sup>
$k_0$	4690 N/m	$A$	301
$k_1$	500 N/m	$n$	2
$x_0$	0.143 m	$\eta$	190 sec <sup>-1</sup>

#### 4.3.2. MRD Response to Sinusoidal Excitations for Various Applied Voltage Levels

Numerical results of an individual MRD excited by sinusoidal displacement are presented in Figure 4.5-Figure 4.7 for decreasing excitation frequencies. The magnitude was held constant in three excitation cases as the excitation frequencies varied (5 Hz, 1 Hz, and 0.5 Hz). In a loading case, four different constant voltage levels were applied. All the simulations were performed for three full cycle depending on the excitation frequency.

The value of time step increment is a very important issue for the calculations of the MRD response. A large time step causes wrong results, whereas a very small time step results in excessive calculation time. The MRD responses gave results similar to the experimental ones when the simulations run with a maximum time increment of 10<sup>-4</sup> seconds (the experimental responses were obtained from the results of the research done by Spencer et al. (1997)). Time step values smaller than this value yield responses similar to the experimental ones, but increased the computational time unnecessarily. If the time step had been chosen greater than 10<sup>-4</sup> seconds, then the shape of responses completely would have changed.

On the other hand, the other parts of the calculations did not required such a small time increment value (These parts were the calculation of the responses of the structure via the Newmark's linear numerical integration method and the calculation of

the control force via various control methods). Therefore, an inner loop was designed to simulate the response of the MRD at a rate 100 times faster than that of the simulation. An outer loop, in which the responses of the structure were calculated, was run at a rate supplied by the seismic record or by the synthetic seismic excitation.

In the present subsection, a time increment of 0.002 seconds was chosen to coincide with the time increment in the earthquake simulations of the present research. The MRD calculations were run at a rate 100 times faster than that of the simulation. The resultant time increment value for the MRD calculations was  $2 \cdot 10^{-5}$  seconds that was smaller than the limit value ( $10^{-4}$  seconds).

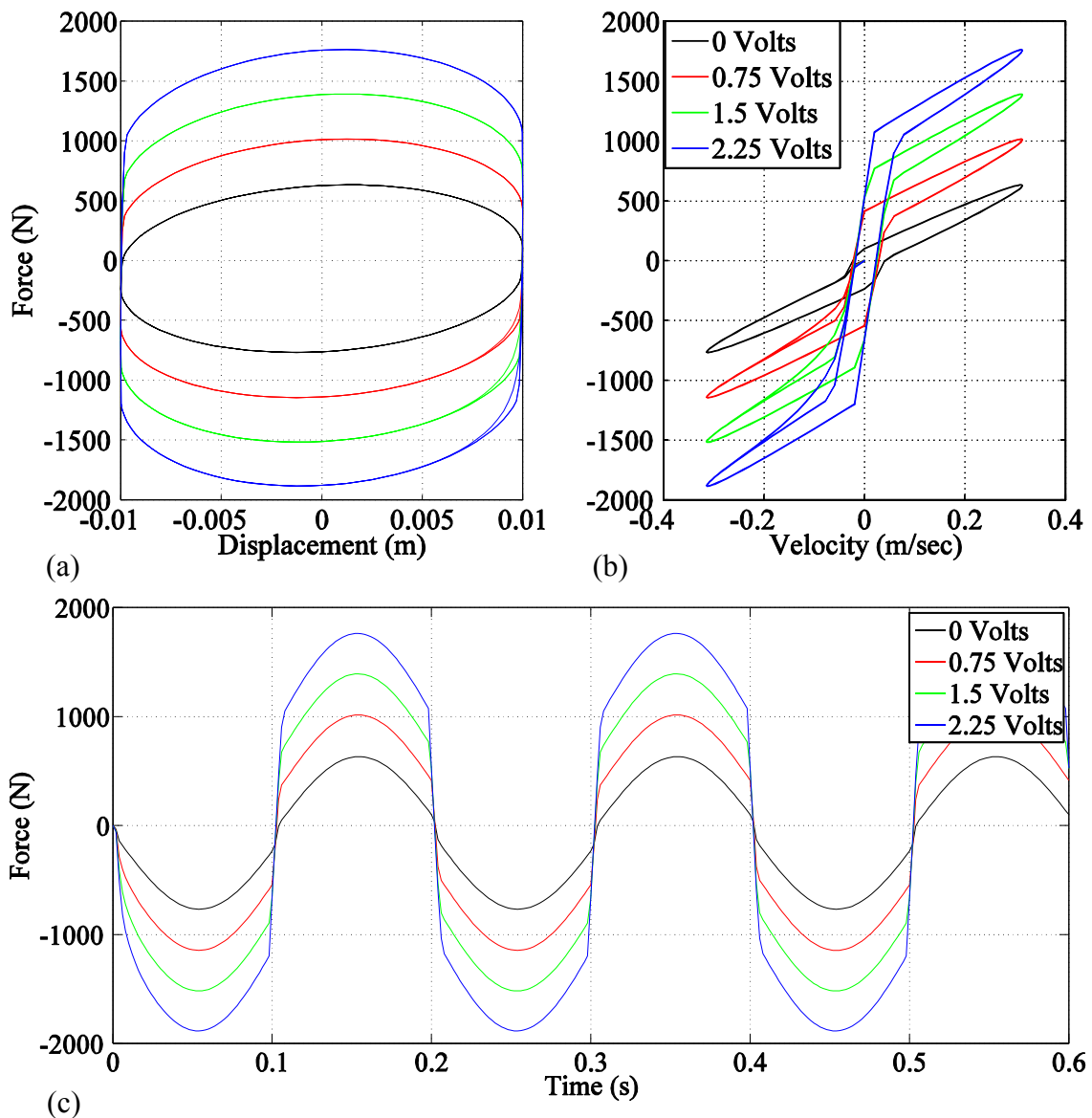


Figure 4.5. The responses of the MRD to a 5 Hz sinusoidal excitation with an amplitude of 0.01 meters for various applied voltage levels

The force versus displacement loops in Figure 4.5-Figure 4.7 progressed in clockwise direction along the path with increasing time. On the other hand, the force versus velocity loops in Figure 4.5-Figure 4.7 progressed in counter-clockwise direction along the path with increasing time.

The accumulator in the MRD was responsible of the nonzero mean force provided by the damper in Figure 4.5(a), Figure 4.6(a), and Figure 4.7(a). It caused an offset in the measured damper force and a small widening of the force-displacement curve and the force-velocity curve through a certain direction of force.

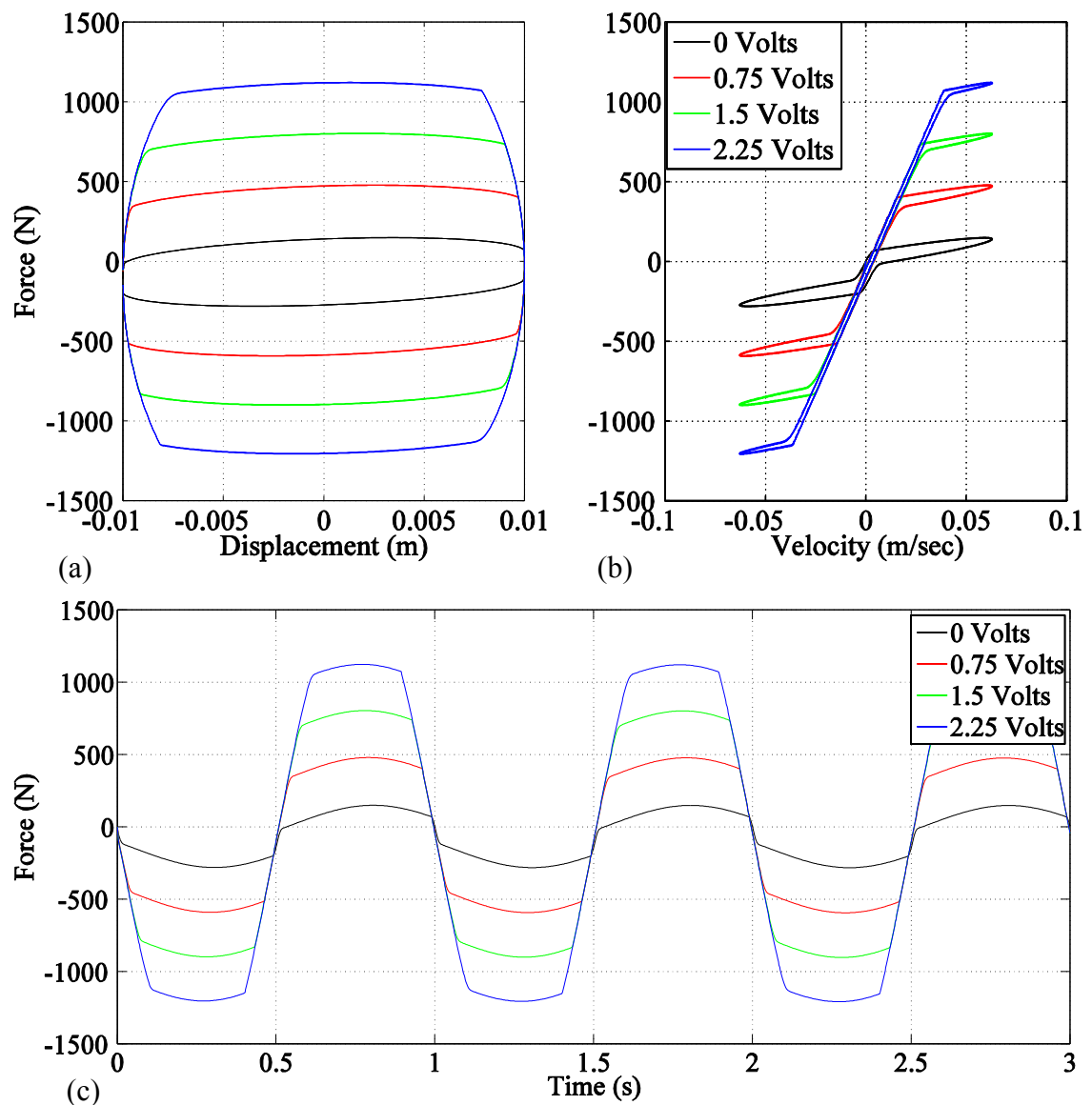


Figure 4.6. The responses of the MRD to a 1 Hz sinusoidal excitation with an amplitude of 0.01 meters for various applied voltage levels

According to the force-velocity curve in Figure 4.5(b), as the command voltage was increased, the maximum damping force of the MRD also increased, and the length of the pre-yield region increased compared to the length of the post-yield region in the force versus velocity loop. This indicates that the yield value increases as the command voltage is increased. The response of the MRD to a 1Hertz sinusoidal displacement is presented in Figure 4.6 for four constant applied voltage levels. Then, the response of the MRD to a 0.5 Hertz sinusoidal displacement is presented in Figure 4.7 for four constant applied voltage levels.

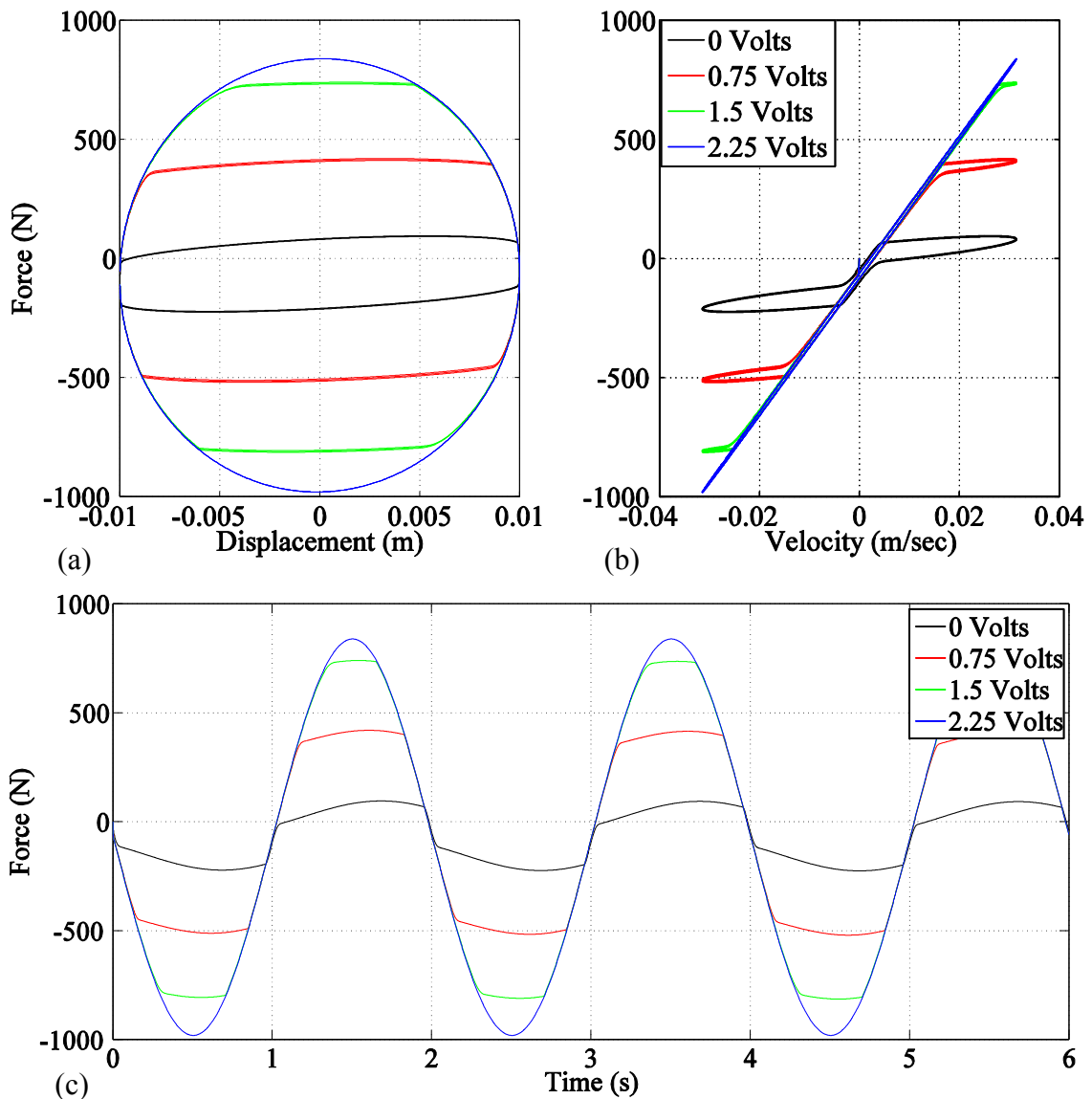


Figure 4.7. The responses of the MRD to a 0.5 Hz sinusoidal excitation with an amplitude of 0.01 meters for various applied voltage levels

As the frequency decreases, which is the case in Figure 4.7, the force versus displacement loop gets the shape of a circle and the force versus velocity curve converges to the elastic case (see the response indicated by blue line in Figure 4.7(b)).

The maximum absolute values of the MRD force are presented in Table 4.2 which corresponds to the applied voltages for three different excitation frequencies. In Table 4.2, one of the voltage values is 2.25 Volts. The results related with this voltage value are presented since it is the maximum allowable voltage value.

Table 4.2. Maximum damping force values of the MRD

Excitation frequency (Hz)	Applied voltage (V)	Maximum MRD force (N)
0.5	0	226
	1	619
	2.25	981
	5	1007
	10	1053
	50	1424
1	0	282
	1	698
	2.25	1208
	5	1942
	10	2035
	50	2776
5	0	768
	1	1271
	2.25	1885
	5	3187
	10	5409
	50	13596

In all of MRD simulations of the current thesis, a conditional loop was present to limit the maximum MRD force by 3000 Newtons if a force value greater than 3000 Newtons was calculated in the MRD functional coded within MATLAB. This conditional loop was removed only for calculations performed for Table 4.2. This case changed only the last three rows of Table 4.2.

According to Table 4.2, as the applied voltage increases, saturation of magnetic field and the upper limit of MRD force can not be observed. The maximum allowable force level of the MRD can not be reached with the maximum allowable voltage level

for tested frequencies and magnitudes of excitations ( $\max|f_{MRD}| = 3000 N$  in Equation (4.1)-(4.2) and  $\max|v| = 2.25 V$  in Equation (4.6)). This case can be observed in the rows of the 2.25 Volts for three different excitation frequencies in Table 4.2.

Consequently, the time step increment mainly influenced the responses of the MRD. In the simulations, two different loops were utilized as inner and outer loops to calculate the responses faster instead of carrying out the calculations within a single loop. Besides, the modified Bouc-Wen model did not reflect saturation of the magnetic field. In the simulations, the MRD force was limited out of the MRD function coded within MATLAB.

#### 4.4. Control of the Seismic Response by MRDs

Different control strategies can be utilized in order to find the control forces required for enhanced structural behaviour. In the optimal control algorithm, control signals that will cause the system to satisfy some physical constraints, and at the same time maximize or minimize a chosen cost function are determined.

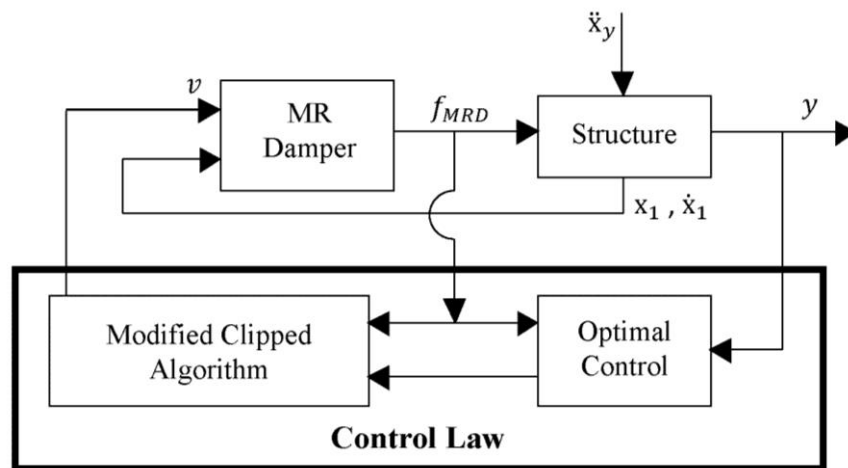


Figure 4.8. Block diagram of the semi-active control system  
(Source: Dyke et.al., 1996)

In the present study, the controller consisted of two stages: a linear optimal control part and a modified clipped algorithm. The required control force  $u$  was calculated by the optimal controller. Then, the voltage to be applied was determined by the modified clipped algorithm by compared the required control force  $u$  and the

damper force  $f_{MRD}$  of the previous time step. The block diagram representation of the system is presented in Figure 4.8.

#### 4.4.1. Modified Clipped Algorithm

The magnetic field in the damper is set to develop damping forces that are equal to those obtained by the optimal control. This is performed by a clipped controller. The output of the feedback block in the block diagram representation in Figure 4.8 is determined by the modified clipped control algorithm.

The MRD is driven by the magnetic field around it, hence it is driven by the voltage applied to the electromagnet. In order to obtain the desired forces by the MRD, the voltage to be applied is set by a clipped algorithm. When the MRD generates the desired control force ( $u = f_{MRD}$ ), the voltage  $v$  should be kept at the present level. If damper force's magnitude is smaller than the desired control force's magnitude, and both forces have the same sign, then maximum voltage should be applied in order to increase the MRD force and to approach the desired control force level. Otherwise, zero voltage should be sent. The algorithm explained above is graphically presented in Figure 4.9, and is stated as

$$v = v_{max} \mathcal{H}\{(u - f_{MRD})f_{MRD}\} \quad (4.7)$$

where  $v$  is the applied voltage,  $v_{max}$  is the maximum voltage, and  $\mathcal{H}\{ \}$  is the Heaviside step function. There is an upper limit of the damping force of the MRD. The upper limit is related with saturation of the magnetic field in the MRD. If the MR fluid saturates, then an increase in the applied voltage will not cause an increase in the damper force. The voltage related with this force upper limit is the maximum voltage.

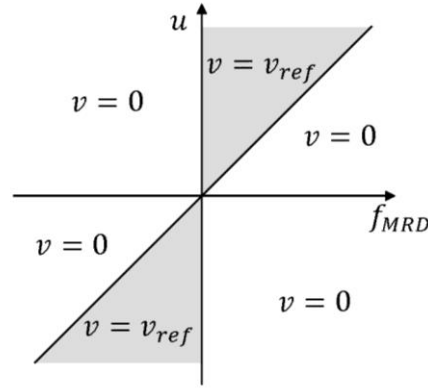


Figure 4.9. Graphical representation of modified clipped control algorithm  
(Source: Dyke et.al., 1996)

In the clipped control strategy, the command voltage is either zero or maximum. During the simulations it is seen that MRD reaches the maximum force level lots of times even if that amount of force is too much for such a kind of system. Thus, the MRD works in a higher force capacity range than the required force capacity. In order to avoid the damper to work at higher force levels, the voltage value is proportioned according to the calculated control force in the modified control algorithm (Yoshida & Dyke, 2004; Yuen et al., 2007). The control voltage can take values between zero and the maximum voltage. In the simulations of Section 4.5, the damper started to work at lower force values and never reached the maximum force level, after the modified clipped algorithm was started to be utilized. The modified clipped algorithm is stated as follows

$$v = v_{ref} \mathcal{H}\{(u - f_{MRD})f_{MRD}\} \quad (4.8)$$

$$v_{ref} = \begin{cases} \frac{u}{\max(f_{MRD})} v_{max}, & \text{for } |u| \leq \max(f_{MRD}) \\ v_{max}, & \text{for } |u| > \max(f_{MRD}) \end{cases} \quad (4.9)$$

where  $v$  is the applied voltage.  $v_{max}$  is the maximum voltage.  $u$  is the desired control force.  $f_{MRD}$  is the damping force of the MRD.  $\max(f_{MRD})$  is the maximum force capacity of MRD. The graphical representation of Equation (4.9) is presented in Figure 4.10.

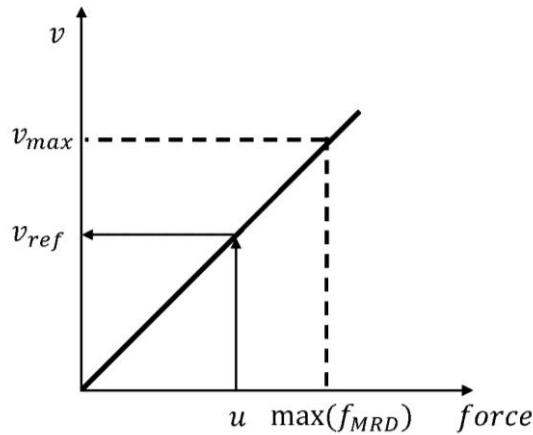


Figure 4.10. Graphical representation of the modified clipped control algorithm

In Figure 4.10, the maximum voltage and the maximum damper force are limited. The applied voltage  $v$  is determined according to the desired control force  $u$ . After application of the voltage  $v$ , the damper force  $f_{MRD}$  can be measured or calculated numerically according to the velocity difference on the damper at the current step.

#### 4.5. Control of the Seismic Response of the Model Superstructure by a MRD

In the present subsection, the seismic response of the three-storey model structure was controlled by four different controllers depending on the LQR, SMC,  $H_2/LQG$ , and fuzzy logic. The system was excited by the data of the Imperial Valley event presented in Figure 2.4. The MRD was attached between the ground and the first floor of the model structure in Figure 3.1. The model structure including the MRD is presented in Figure 4.11.

##### 4.5.1. Model Superstructure Including a MRD

The seismic response of the three-storey single-frame model superstructure in Chapter 3 was controlled by a MRD attached between the ground and the first floor.

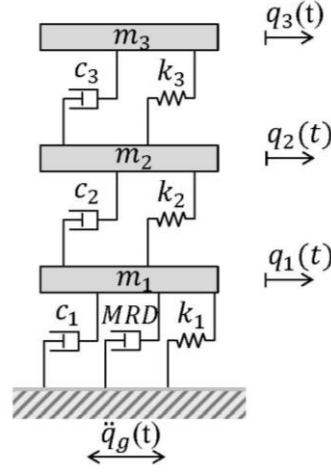


Figure 4.11. Model superstructure including a MRD

The equations of motion for the model superstructure presented by Equation (3.1) was modified for the MRD, as follows

$$\mathbf{M}_{ss}\ddot{\mathbf{q}}_{ss}(t) + [\mathbf{C}_{ss}\dot{\mathbf{q}}_{ss}(t) + \mathbf{h}_{2ss}f_{MRD}(t)] + \mathbf{K}_{ss}\mathbf{q}_{ss}(t) = -\mathbf{M}_{ss}\mathbf{h}_{1ss}\ddot{q}_g(t) \quad (4.10)$$

The subscript  $ss$  stands for the superstructure. The displacement vector of the structure is  $\mathbf{q}_{ss}(t) = (q_1(t) \ q_2(t) \ q_3(t))^T$ . Similarly, the velocity vector of the structure is  $\dot{\mathbf{q}}_{ss}(t) = (\dot{q}_1(t) \ \dot{q}_2(t) \ \dot{q}_3(t))^T$ . The definitions of the variables are presented in Chapter 3.  $f_{MRD}$  is the damping force of the controlled damper. The damper force is assumed as an internal damping. But, for simplicity of presentation and simulation, it is taken from the left-hand-side of the equation of motion to the right-hand-side, as follows

$$\mathbf{M}_{ss}\ddot{\mathbf{q}}_{ss}(t) + \mathbf{C}_{ss}\dot{\mathbf{q}}_{ss}(t) + \mathbf{K}_{ss}\mathbf{q}_{ss}(t) = -\mathbf{M}_{ss}\mathbf{h}_{1ss}\ddot{q}_g(t) - \mathbf{h}_{2ss}f_{MRD}(t) \quad (4.11)$$

$\mathbf{h}_{2ss}$  is the location matrix of the control force. It specifies how the control force  $f_{MRD}$  enters into the system. It is presented by

$$\mathbf{h}_{2ss} = (1 \ 0 \ 0)^T \quad (4.12)$$

indicating that the damping force is present only at the level of the first floor.

In the state-space form of the equations of motion of the model structure, the states  $\mathbf{x}_{ss}(t)$  were chosen as the displacements and velocities of the floors relative to the

ground as  $\mathbf{x}_{ss}(t) = (\mathbf{q}_{ss}(t) \quad \dot{\mathbf{q}}_{ss}(t))^T$ . All the states and the damper force were assumed to be sensed for full state feedback. The process equation is as follows

$$\dot{\mathbf{x}}_{ss}(t) = \mathbf{A}_{ss}\mathbf{x}_{ss}(t) + \mathbf{G}_{ss}w_{ss}(t) + \mathbf{B}_{ss}u_{ss}(t) \quad (4.13)$$

where

$$\begin{aligned} \mathbf{A}_{ss} &= \begin{bmatrix} \mathbf{0} & \mathbf{I} \\ -\mathbf{M}_{ss}^{-1}\mathbf{K}_{ss} & -\mathbf{M}_{ss}^{-1}\mathbf{C}_{ss} \end{bmatrix} \\ \mathbf{G}_{ss} &= \begin{bmatrix} \mathbf{0} \\ -\mathbf{h}_{1,ss} \end{bmatrix} \\ \mathbf{B}_{ss} &= \begin{bmatrix} \mathbf{0} \\ -\mathbf{M}_{ss}^{-1}\mathbf{h}_{2,ss} \end{bmatrix} \end{aligned} \quad (4.14)$$

$u_{ss}(t)$  is the control input.  $w_{ss}(t)$  is the disturbance.  $\mathbf{A}_{ss}$  is the state matrix.  $\mathbf{G}_{ss}$  is the disturbance vector.  $\mathbf{B}_{ss}$  is the control input vector. The definitions of the other variables are presented in Chapter 3.

#### 4.5.2. Steady-State (Infinite-Horizon) Linear Quadratic Regulator

The fundamental aim of the current research is to reduce vibrations of a system during an excitation (ground excitation, mechanical shaking etc.). In other words, the aim is to enforce the system to be as close as possible to an equilibrium state. This task can be performed via a control input. But if a great amount of control effort is spent within in a long time, then this won't be a convenient engineering solution. There should be a balance between the control input amount, the system states, and the time passed, which then leads to an optimum solution. In that respect, Bryson and Ho (1975) defines a regulator as a feedback controller, which forces a stationary system to locate in a reasonable vicinity of a reference zero by spending an admissible amount of control effort.

For a linear regulator, the control input is a linear function of the state vector (Meirovitch, 1989). For an optimal solution, a certain objective function in terms of states, control input, and time passed should be minimized. If the cost function is quadratic, then the problem turns into a linear quadratic regulator (LQR). Its solution

can be obtained via the dynamic programming or via a variational approach. The formulation of the LQR is presented in Appendix G. As time passes, the LQR problem turns into a steady-state (infinite-horizon) LQR design. The derivation of LQ-based control algorithms (LQR, LQG,  $H_2$ /LQG) look like an optimization problem rather than a control design due to the minimization of the performance index.

The constraint cost function in Equation (G.2) is minimized in the finite-horizon LQR design, resulting in the *differential Riccati equation* (DRE) (see Equation (G.13)). As time tends to infinity, the solution  $\mathbf{P}(t)$  to the DRE converges to a finite constant value  $\bar{\mathbf{P}}$  ( $\lim_{t \rightarrow \infty} \mathbf{P}(t) = \bar{\mathbf{P}}$ ). The differential term  $\dot{\mathbf{P}}(t)$  vanishes, and the DRE becomes an *algebraic Riccati equation* (ARE) as below

$$\mathbf{0} = \mathbf{A}^T \bar{\mathbf{P}} + \bar{\mathbf{P}} \mathbf{A} - \bar{\mathbf{P}} \mathbf{B} \mathbf{R}^{-1} \mathbf{B}^T \bar{\mathbf{P}} + \mathbf{Q} \quad (4.15)$$

The state feedback gain  $\mathbf{K}(t) = \mathbf{R}^{-1} \mathbf{B}^T \mathbf{P}(t)$  becomes time-invariant as follows

$$\bar{\mathbf{K}} = \mathbf{R}^{-1} \mathbf{B}^T \bar{\mathbf{P}} \quad (4.16)$$

The optimal state trajectory  $\mathbf{x}^*(t)$  can be obtained via the closed loop state equation as

$$\dot{\mathbf{x}}^*(t) = [\mathbf{A} - \mathbf{B} \mathbf{R}^{-1} \mathbf{B}^T \bar{\mathbf{P}}] \mathbf{x}^*(t) \quad \mathbf{x}(t_0) = \mathbf{x}_0 \quad (4.17)$$

As the final time goes to infinity, the system converges to a steady-state equilibrium state. The terminal penalty term in the constrained cost function disappears since the state vector goes to zero as  $t \rightarrow \infty$ . The constrained performance index becomes

$$\tilde{\mathcal{J}}(\mathbf{z}) = \frac{1}{2} \int_{t_0}^{\infty} \{ \mathbf{x}^T(t) \mathbf{Q} \mathbf{x}(t) + \mathbf{u}^T(t) \mathbf{R} \mathbf{u}(t) + \lambda^T(t) [\mathbf{A} \mathbf{x}(t) + \mathbf{B} \mathbf{u}(t) - \dot{\mathbf{x}}(t)] \} dt \quad (4.18)$$

The free-final-state and fixed-time optimization problem for the finite-horizon case turns into a zero-final-state and infinite-time one. The solution  $\bar{\mathbf{P}}$  of the ARE can be obtained via the Hamiltonian matrix [see the condition for existence of  $\bar{\mathbf{P}}$  in (Williams & Lawrence, 2007; Başar et al., 1998)]. In the current study, its solution is performed via the MATLAB command *care*, which is abbreviated for continuous-time ARE.

The stability of the infinite-horizon LQR problem can be determined via the poles of the closed loop system [see (Anderson & Moore, 1989; Bryson & Ho, 1975) for detailed discussions]. Furthermore, Stengel (1994) discusses the robustness analysis of the LQR in terms of gain and phase margins in detail.

### 4.5.3. Sliding Mode Control (SMC)

The model structure with one MRD is controlled by sliding mode control method. Sliding mode control method is an attractive control strategy due to its robustness against environmental changes. In general, the state equation of the linear time-invariant system being controlled is as

$$\dot{\mathbf{x}}(t) = \mathbf{A}\mathbf{x}(t) + \mathbf{B}\mathbf{u}(t) + \mathbf{E}(t) \quad \mathbf{x}(t_0) = \mathbf{x}_0 \quad (4.19)$$

The definitions of the terms in Equation (4.19) are presented in Table 5.3.  $\mathbf{E}(t)$  is the excitation vector. The the sliding mode control is insensitive to environmental changes. The method aims to design a control rule that forces the response trajectory onto a sliding surface. Sliding surface is a surface, on which the motion is stable. Let  $\mathbf{S}_{SMC} = \mathbf{0}$  be the sliding surface,

$$\mathbf{S}_{SMC}(t) = \mathbf{P}_{SMC}\mathbf{x}(t) \quad (4.20)$$

$\mathbf{S}_{SMC}(t) = [S_1(t) \ S_2(t) \ \dots \ S_{r-1}(t) \ S_r(t)]^T$  is an  $r$ -vector consisting of  $r$  sliding variables  $S_1(t), S_2(t), \dots, S_r(t)$ .  $r$  is the number of controllers.  $\mathbf{P}_{SMC}$  is a  $(r \times 2n)$  matrix, which is determined in such a way that the motion on the sliding surface is stable.  $\mathbf{P}_{SMC}$  is calculated by the LQR.  $\mathbf{P}_{SMC}$  is determined by minimizing the cost function  $J_{SMC}$  as

$$J_{SMC} = \int_0^{\infty} \mathbf{x}^T(t) \mathbf{Q}_{SMC} \mathbf{x}(t) dt \quad (4.21)$$

where  $\mathbf{Q}_{SMC}$  is a  $(2n \times 2n)$  positive definite matrix. The control law is designed to drive the state trajectory into the sliding surface  $\mathbf{S}_{SMC} = \mathbf{0}$ . As a result, the control force is obtained by help of Lyapunov function for a continuous control as

$$\mathbf{u}(t) = \mathbf{G}_{SMC}(t) - \bar{\boldsymbol{\delta}}\boldsymbol{\lambda}(t)^T \quad (4.22)$$

where

$$\boldsymbol{\lambda}(t) = \mathbf{S}_{SMC}(t)^T \mathbf{P}_{SMC} \mathbf{B} \quad (4.23)$$

$$\mathbf{G}_{SMC}(t) = -(\mathbf{P}_{SMC} \mathbf{B})^{-1} \mathbf{P}_{SMC} (\mathbf{A}\mathbf{x}(t) + \mathbf{E}(t)) \quad (4.24)$$

$\delta_i > 0$  is referred to as the sliding margin.  $\bar{\boldsymbol{\delta}}$  is a  $(r \times r)$  diagonal matrix with elements  $\delta_1, \delta_2, \dots, \delta_r$  on the main diagonal. Chattering creates serious problems while determining sliding modes. This formulation is the continuous one that overcomes the chattering phenomenon.

#### 4.5.4. $H_2$ /LQG Control

The  $H_2$  optimal control theory originates from the frequency domain interpretation of the cost function associated with time-domain state-space linear quadratic Gaussian (LQG) control theory. In literature, Safonov et al. (1981), Doyle et al. (1989), and Lu (2001) presented the framework for the LQG method. Ramallo et al. (2002) applied an  $H_2$ /LQG control to a two storey model structure.

The  $H_2$  optimal controller is a combination of a Kalman filter and a full-state feedback gain, both of which are determined in the usual linear quadratic regulator (LQR) manner. The signal  $\mathbf{d}$  contains all external inputs, including disturbances, and sensor noise. The  $H_2$  norm of a transfer function matrix from  $\mathbf{d}$  to  $\mathbf{z}$ ,  $\mathbf{G}_{zd}$  is defined as

$$\|\mathbf{G}_{zd}\|_2 = \sqrt{\text{trace} \left( \frac{1}{2\pi} \int_{-\infty}^{\infty} \mathbf{G}_{zd}(j\omega) \mathbf{G}_{zd}^*(j\omega) d\omega \right)} \quad (4.25)$$

In order to perform a physical interpretation of the  $H_2$  norm, it is important to note that the  $H_2$  norm of a transfer function is equal to the RMS (root mean square) value of its output  $\mathbf{q}$  in case of unit white input. The RMS output vector is defined by

$$\|\mathbf{q}\|_{rms} = \lim_{\tau \rightarrow \infty} \frac{1}{2\tau} \int_{-\tau}^{\tau} \mathbf{q}^T(t) \mathbf{q}(t) dt \quad (4.26)$$

This expression can also be written as

$$\|\mathbf{q}\|_{rms} = \sqrt{\sum_i E[q_i^2(t)]} \quad (4.27)$$

where  $E[\cdot]$  indicates the expected value operator. After the current stage, the problem turns into a LQG algorithm. The LQG optimal controller is simply composed of a Kalman filter (linear quadratic estimator, LQE) with a LQR. The two Riccati equations that come from the optimization of the performance indices are solved for the optimal solution. With appropriate selection of design weights, the  $H_2$  optimal control criteria defined in the frequency domain can be numerically equivalent to the LQG optimal control criteria defined in the time domain (Lu, 2001).

The  $\mathbf{Q}$  and  $\mathbf{R}$  matrices declare the weights (importance) of both the states and the controller. In the LQR design procedure, the  $\mathbf{Q}$  and  $\mathbf{R}$  values were utilized directly whereas in the  $H_2$ /LQG design,  $\mathbf{Q}$  was integrated in matrices  $\mathbf{C}_1$ ,  $\mathbf{D}_{11}$ , and  $\mathbf{D}_{12}$ . The  $H_2$ /LQG method accepts a default value of 1 for  $\mathbf{R}$ .

Observers are required intensely in full state feedback control and real-world control applications (see Section 5.1 for reasons). In the simulations of Section 4.5, the aim was to compare the performances of the controllers. The attention was not on the observer. Therefore, it was assumed that any measurement was not performed, and all states were directly fed back to the controller. In the numerical simulations of Chapter 5 of the thesis, the measured values were performed by adding randomly produced noise values to the calculated values. For the present example, noise was assumed to be zero.

#### 4.5.5. Fuzzy Logic Control

In the present subsection, the damping properties of the MRD are regulated by a fuzzy logic control algorithm. In general, the fuzzy logic algorithms consist of three steps:

1. fuzzification during which numerical input variables are transformed into linguistic variables by means of input membership functions (input membership functions may be triangular, trapezoidal, Gaussian and etcetera),
2. fuzzy inference rule that determines the output by means of inputs and logical IF-THEN statements (Mamdani- and Sugeno-type fuzzy inference systems),
3. defuzzification during which the output is produced by defuzzifying the results of the inference rules.

In the present fuzzy control design, complicated differential equations are not required. The suitable inputs, membership functions and rules are sufficient enough to reflect the nature of the system. Additionally, the semi-active fuzzy controller gives directly the output voltage while the semi-active optimal controller performs its duty in two stages (see Figure 4.8). The fuzzy controller produces the output by means of the fuzzy rule inference. The block diagram is presented in Figure 4.12.

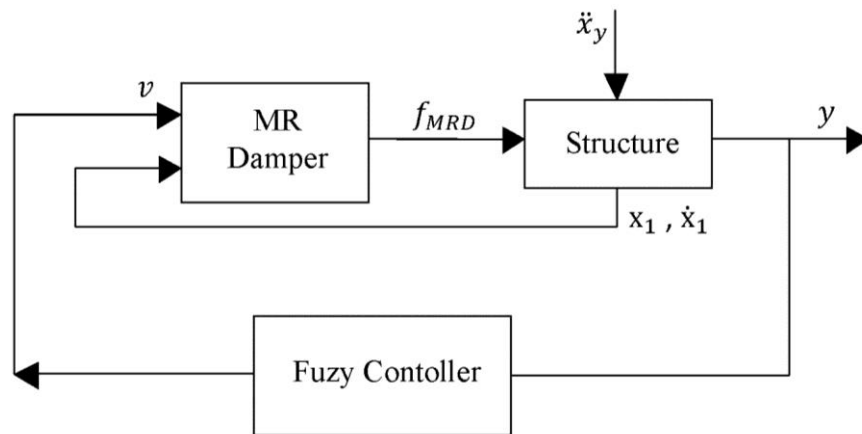


Figure 4.12. Block diagram of semi-active fuzzy control system

The input variables to the fuzzy controller were chosen as the first floor's displacements and velocities relative to the ground since the displacement and velocity difference on the MRD were required. The boundaries of the input variables has to be defined priori to the simulation. In the present simulations, the boundaries of the input variables were selected as the maximum values of the first floor responses of the uncontrolled structure. The boundaries of the input variables were chosen in such a way that the controlled displacements and velocities of the first floor can not be greater than those of the uncontrolled ones. If a case different from this occurs in a real earthquake, then the fuzzy controller becomes useless. Seven identical triangles with 50% overlap were utilized for the input membership functions (Figure 4.13).

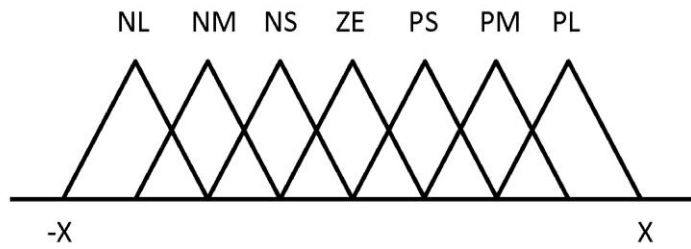


Figure 4.13. Input membership function

For the input fuzzy variables in Figure 4.13, the linguistic abbreviations NL, NM, NS, ZE, PS, PM, and PL refer to negative large, negative medium, negative small, zero, positive small, positive medium, and positive large, respectively.

The output was chosen as the voltage applied to the MRD. Six identical triangles with 50% overlap were chosen for the output, which took values between zero and the maximum voltage (Figure 4.14). The output variables took values between zero and the maximum voltage (2.25 volts).

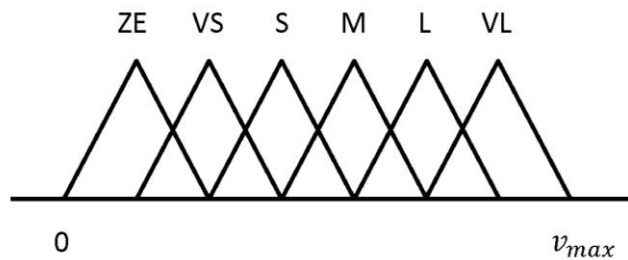


Figure 4.14. Output membership function

For the output fuzzy variables in Figure 4.14, the abbreviations ZE, VS, S, M, L, and VL refer to zero, very small, small, medium, large, and very large, respectively. The fuzzy inference rules are presented in Table 4.3. The calculations were performed by the Mamdani-type fuzzy inference system (FIS) within the fuzzy logic toolbox of MATLAB.

The fuzzy inference rule were determined according to this principle: if the structure is away from its neutral position and is moving further away from its neutral position, then the voltage applied should be increased to provide more damping. However, when the structure is away from its neutral position, and is moving towards it, little or no voltage needs to be applied (Wilson, 2005). The reasoning of the fuzzy inference rules and modified clipped algorithm is similar.

Table 4.3. Fuzzy inference rule

	NL	NM	NS	ZE	PS	PM	PL
NL	VL	L	L	M	S	VS	ZE
NM	L	L	M	S	VS	ZE	VS
NS	L	M	S	VS	ZE	VS	S
ZE	M	S	VS	ZE	VS	S	M
PS	S	VS	ZE	VS	S	M	L
PM	VS	ZE	VS	S	M	L	L
PL	ZE	VS	S	M	L	L	VL

In the present fuzzy logic design, the fuzzy rules were combined by the Boolean *and*. The rule strength was determined by taking the minimum of the two input membership values, which is the most common definition of the Boolean *and* in fuzzy logic. Then, the output membership function was clipped at the rule strength, and the outputs of all fuzzy rules were combined by taking the maximum value of the membership functions to obtain one fuzzy output distribution. Finally, a single crisp output value was obtained from the fuzzy output distribution by defuzzification process. This output value was determined by the center-of-gravity (COG) method, which simply calculated the centroid of the area under the fuzzy output distribution.

## 4.5.6. Simulations

### 4.5.6.1. Interpolation of the Seismic Excitation Data

In the simulations, the system was excited by the data of the Imperial Valley event presented in Figure 2.4. In general, any simulation should run at least 20 times faster than the fastest mode to take into account the contribution of the fastest mode (see Section Signal Construction in APPENDIX I). This case is visualized by Figure I.1. In the current simulations, the fastest mode of the model structure had a frequency of 8.33 Hz. The simulation frequency had to be at least 167 Hz. Therefore, the records were interpolated to the one fifth of the original time increment of the data, resulting in 500 Hz (see Figure 4.15). The energy imparted to the system did not change by interpolation since the magnitude in time-domain and total duration of the data remained constant.

The number of data was increased by interpolation. The magnitudes in frequency-domain remained unchanged (see Figure 4.15(b)).

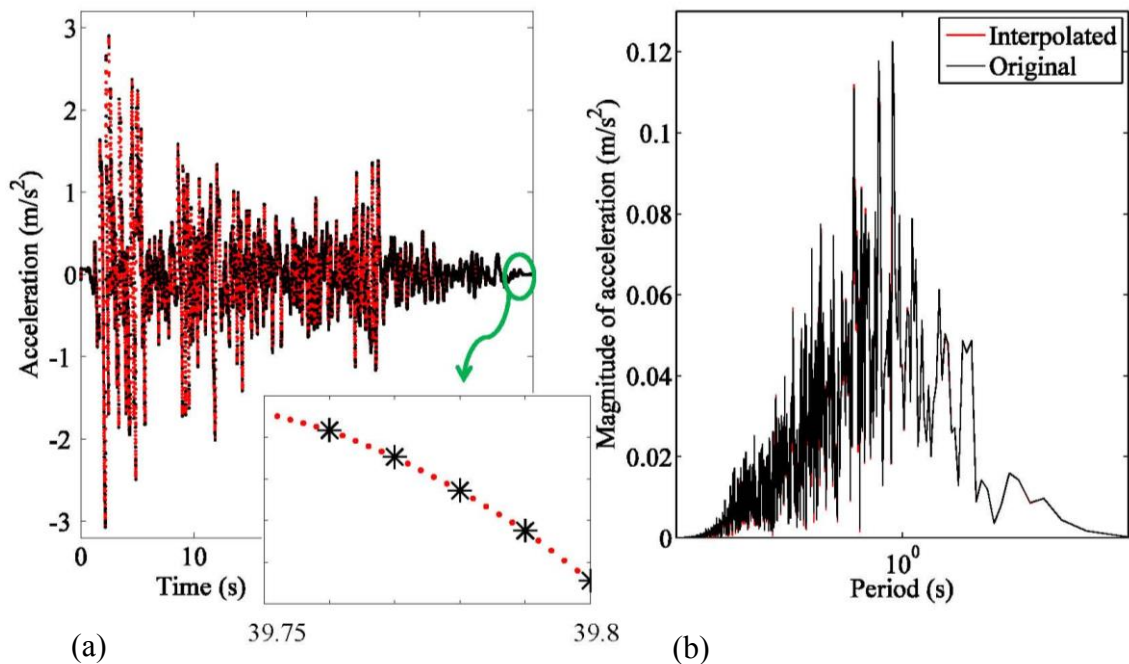


Figure 4.15. Interpolated form of the Imperial Valley earthquake record in (a) time and (b) frequency domains

In Figure 4.15, the magnitudes in time and frequency domains were not the same for the original and interpolated data. The reason of this fact may have been two-folded: Firstly, the energy of the signal leaked into a number of frequencies instead of a concentrating at a single frequency due to spectral leakage (see Figure I.2). Secondly, the peak of  $3 \text{ m/s}^2$  in time-domain was composed of sine waves with different frequencies.

#### 4.5.6.2. Simulations and Comparison of the Results

The seismic response of the three-storey model structure in Figure 3.1 was controlled by an MRD attached between the ground and the first floor (see Figure 4.11). Four controllers were designed, depending on the LQR, SMC,  $H_2$ /LQG, and fuzzy logic. These methods and details about the simulations are explained in Sections 4.5.2-4.5.5.

The LQR, SMC, and  $H_2$ /LQG are optimal control methods. By choosing the optimal control algorithm, control signals that will cause the system to satisfy some

physical constraints, and at the same time, maximize or minimize a chosen performance criteria (cost function) are determined. On the other hand, the fuzzy logic controller is not an optimal controller.

The controllers based on LQR, SMC, and  $H_2$ /LQG consisted of two stages: an optimal controller and a modified clipped algorithm. The required control force  $u$  was calculated by the control methods (see Section 4.5.2-4.5.4). Then, the voltage that had to be applied to supply  $u$  was determined by the modified clipped control algorithm (see Section 4.4.1). The control voltage lay between 0 and  $v_{max}$  (Yoshida & Dyke, 2004; Yuen et al., 2007). On the other hand, the proposed fuzzy logic controller provided the voltage value to be applied in a single step (see the related MATLAB codes in APPENDIX J). In the proposed fuzzy controller, the voltage to be applied was determined by the fuzzy inference rules presented in Table 4.3. Therefore, the modified clipped algorithm was not utilized. The fuzzy inference rules were determined by a logic similar to the one in the modified clipped algorithm (see Section 4.4.1 and Table 4.3).

The responses relative to the ground were controlled. The  $\mathbf{Q} - R$  couple of the LQR design was determined by a trial-and-success procedure similar to the one summarized in Table 5.4. They were selected as

$$\mathbf{Q}_{LQR} = \begin{bmatrix} 1 & 0 & 0 & 0 & 0 & 0 \\ 0 & 1 & 0 & 0 & 0 & 0 \\ 0 & 0 & 1 & 0 & 0 & 0 \\ 0 & 0 & 0 & 0.1 & 0 & 0 \\ 0 & 0 & 0 & 0 & 0.1 & 0 \\ 0 & 0 & 0 & 0 & 0 & 0.1 \end{bmatrix}, R_{LQR} = 1 \cdot 10^{-7} \quad (4.28)$$

By this configuration of the  $\mathbf{Q} - R$  couple, the ratio between the absolute values of maximum control and MRD forces became 1.28 for the data of the Imperial Valley earthquake. The  $\mathbf{Q} - R$  couples of the SMC and  $H_2$ /LQG designs are presented in Equation (4.29) and Equation (4.30), respectively. The  $H_2$ /LQG method accepts a default value of 1 for R.

$$\mathbf{Q}_{SMC} = 1000 \begin{bmatrix} 10 & 0 & 0 & 0 & 0 & 0 \\ 0 & 10 & 0 & 0 & 0 & 0 \\ 0 & 0 & 10 & 0 & 0 & 0 \\ 0 & 0 & 0 & 1 & 0 & 0 \\ 0 & 0 & 0 & 0 & 1 & 0 \\ 0 & 0 & 0 & 0 & 0 & 1 \end{bmatrix}, R_{SMC} = 2 \cdot 10^{-6} \quad (4.29)$$

$$\mathbf{Q}_{H_2/LQG} = 10^5 \begin{bmatrix} 100 & 0 & 0 & 0 & 0 & 0 \\ 0 & 100 & 0 & 0 & 0 & 0 \\ 0 & 0 & 100 & 0 & 0 & 0 \\ 0 & 0 & 0 & 1 & 0 & 0 \\ 0 & 0 & 0 & 0 & 1 & 0 \\ 0 & 0 & 0 & 0 & 0 & 1 \end{bmatrix}, R_{H_2/LQG} = 1 \quad (4.30)$$

The inputs of the fuzzy logic controllers were the displacement and velocity of the first floor. Hence, the first floor responses were controlled directly while the responses of the other floors were controlled indirectly. On the other hand, in optimal controllers, all states were controlled with an equal weight. The control ability of optimal controllers were shared among all states.

In an experiment or in a real-world application, for the LQR method, all states need to be sensed since there is not an observer involved. On the other hand, for the  $H_2/LQG$  method, only some of the states have to be sensed since an observer is designed within the method to estimate all the states. The present example was a priori, and comparison of performances of the controllers was mainly aimed. Therefore, it was assumed that measurement was not performed and all states were directly fed back to the controller.

The interstory drift responses are presented in Figure 4.16 and Figure 4.17 although the responses relative to the ground are controlled. The absolute acceleration responses are presented in Figure 4.18 and Figure 4.19.

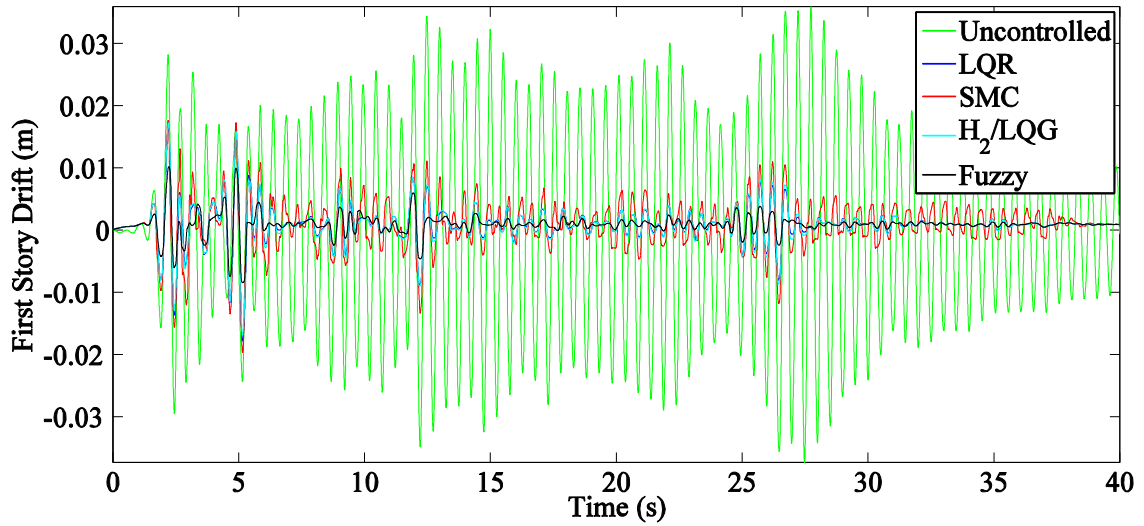


Figure 4.16. The response of the first story displacement with respect to the ground due to the Imperial Valley earthquake for different control strategies

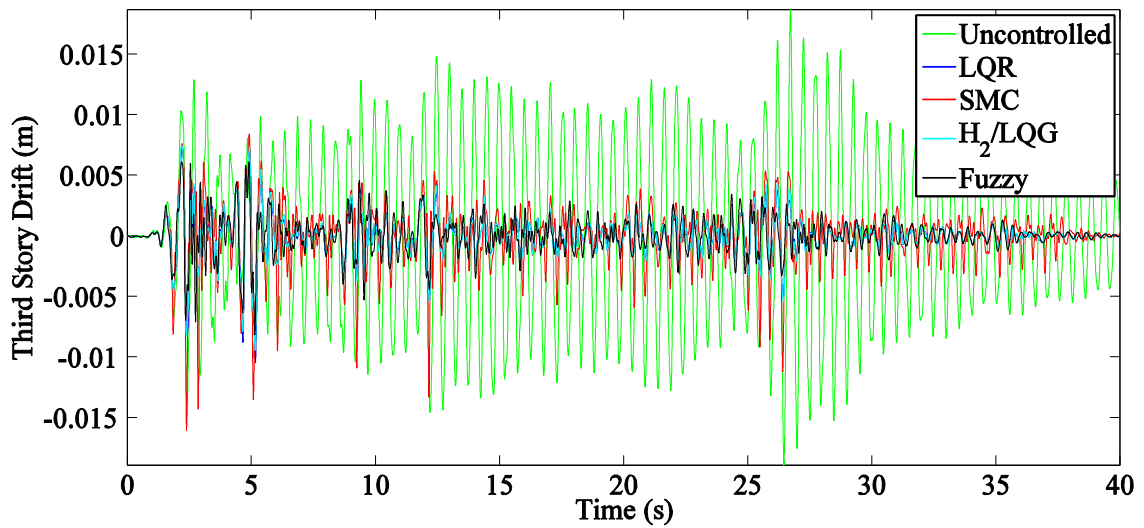


Figure 4.17. Interstory drift of the third floor due to the Imperial Valley earthquake for different control strategies

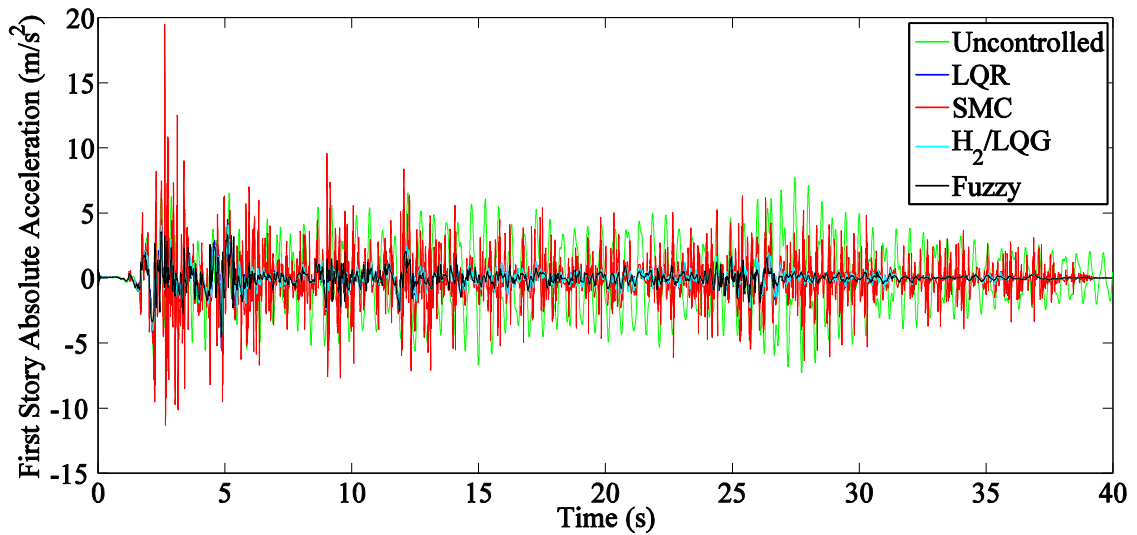


Figure 4.18. Absolute acceleration of the first floor due to the Imperial Valley earthquake for different control strategies

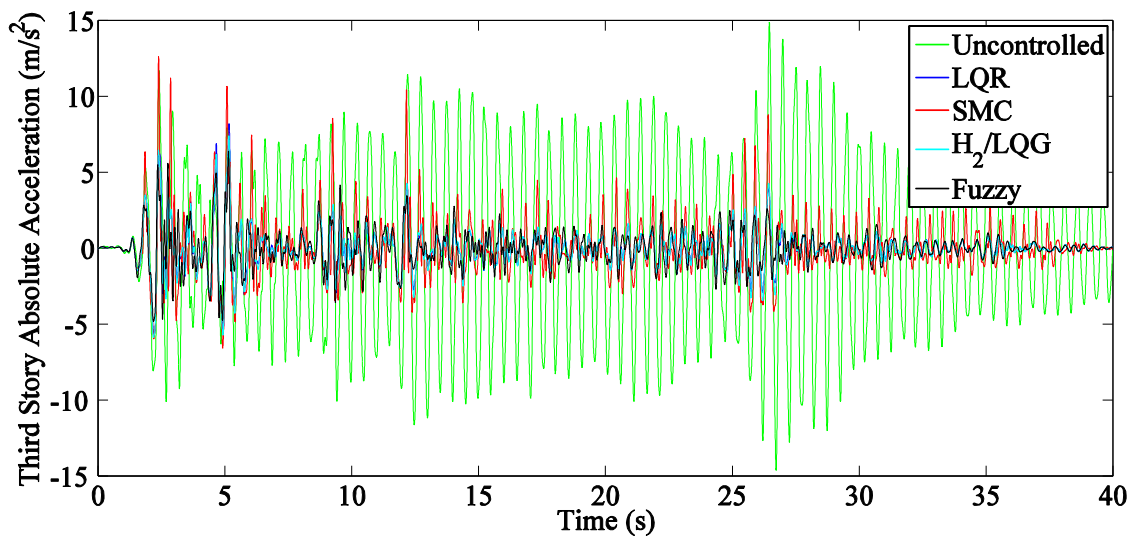


Figure 4.19. Absolute acceleration of the third floor due to the Imperial Valley earthquake for different control strategies

The absolute acceleration response of the first floor contains not only the structure's acceleration value, but also acceleration coming from the damping force of the MRD. Therefore, the absolute accelerations of the second and third floors supply more correct information about the behavior of the structure. Furthermore, the peak values of the responses for different control strategies are presented in Table 4.4.

Table 4.4. Peak responses of the Imperial Valley earthquake for different control strategies

		Uncontrolled	LQR	SMC	$H_2/LQG$	Fuzzy
Drifts (cm)	$q_3$	1.9	1.1	1.6	1.0	0.8
	$q_2$	3.1	1.7	2.0	1.6	1.2
	$q_1$	3.7	1.7	2.0	1.7	1.0
Total accelerations (m/s <sup>2</sup> )	$\ddot{q}_{3t}$	14.9	8.2	12.6	7.4	6.4
	$\ddot{q}_{2t}$	10.8	7.1	10.5	6.9	6.3
	$\ddot{q}_{1t}$	7.7	5.6	19.5	4.5	4.5
Maximum shear force of the 1 <sup>st</sup> floor (N)	$V_{max}$	2918	1750	2070	1668	1238
Damper force (N)	$f_{MRD}$	-	533	1858	591	817

In Table 4.4, the maximum shear force at the first floor of the superstructure was calculated by

$$V_{max} = \max \left| \sum_{i=1}^3 m_{ss_i} \ddot{q}_{i_{total}} \right| \quad (4.31)$$

where  $V_{max}$  is the maximum shear force at the first floor of the superstructure.  $m_{ss_i}$  is the mass of the  $i$ -th story of the superstructure.  $\ddot{q}_{i_{total}}$  is the absolute acceleration of the  $i$ -th floor of the superstructure.

According to Table 4.4, the SMC method is undesirable due to its high absolute acceleration responses compared to the responses of the other control methods. Additionally, the maximum damper force of the SMC is distinctively high compared to that of the other methods.

In Table 4.4, on the other hand, the fuzzy logic controller exhibits the best controlled responses among all applied strategies due to its low drift, absolute acceleration, and total shear force values. It reduces all responses to half of the uncontrolled ones. It performs this task by a damper force of one third of the capacity of the MRD ( $f_{MRD_{max}} = 3000 \text{ N}$ ). Thus, the MRD is not forced to work close to its limits compared to the responses of the SMC method. The proposed fuzzy controller is effective in reducing seismic response of the model structure. In addition to its

affirmative contribution, the fuzzy control design is very simple compared to the other control methods.

The controllers based on the LQR and  $H_2/LQG$  algorithms reduces the interstory drifts more than 45% compared to the uncontrolled case although responses relative to the ground are controlled. Additionally, the reduction in the maximum total shear forces is 40% with respect to the uncontrolled case. On the other hand, the reductions of the interstory drifts in the fuzzy controller are more than 58% compared to the uncontrolled case. Besides, the fuzzy controller performs a reduction of 58% in the maximum total shear force with respect to the uncontrolled case.

#### 4.6. Comparison of the Responses of a Passively Controlled MRD and a Semi-Actively Controlled MRD

In the present subsection, the responses of a passive damper and a semi-active MRD were compared. The aim was to answer the question of controlling a damper was necessary or it was better to place a passive damper instead of a semiactively controlled MRD to limit the structural responses. The responses of the model superstructure in Figure 4.11 were simulated for four different seismic excitations as: Imperial Valley, Düzce, *Synthetic1*, and *Synthetic2* (see Section 5.8.1 for synthetic production of the data *Synthetic1* and *Synthetic2*). The excitation data was interpolated to one fifth of the original time increment of the data, resulting in 500 Hz.

In the simulations the responses of uncontrolled, passive-off, and passive-on systems were calculated. Zero voltage was applied for passive-off case. Different constant voltage values were applied for passive-on case (0.45, 0.90, 1.35, 1.80, 2.25 V). Additionally, in optimal control case the calculations were performed for different R values varying from  $10^{-11}$  to  $10^{-7}$ . The configuration of the  $\mathbf{Q}$  matrix in the LQR design was chosen as:

$$\mathbf{Q} = \begin{bmatrix} 1.0 & 0 & 0 & 0 & 0 & 0 \\ 0 & 1.0 & 0 & 0 & 0 & 0 \\ 0 & 0 & 1.0 & 0 & 0 & 0 \\ 0 & 0 & 0 & 0.01 & 0 & 0 \\ 0 & 0 & 0 & 0 & 0.01 & 0 \\ 0 & 0 & 0 & 0 & 0 & 0.01 \end{bmatrix} \quad (4.32)$$

In the simulations of the present thesis, the states were the displacements and velocities relative to the ground. The order of the velocities was approximately ten times the order of the displacement responses in the simulations. Therefore, the weights of the displacements in the LQR design were chosen ten times higher than those of velocities harmoniously with the numerical situation. The configuration of the  $\mathbf{Q}$  matrix in Equation (4.32) coincided with the magnitudes of the states.

The reduction of the maximum absolute values of displacements and total accelerations were presented in Figure 4.20-Figure 4.23 for the four seismic excitations. The reduction percentage of the responses with respect to the uncontrolled case was defined as:

$$Reduction\ percentage = \frac{\max|x_{uncon}| - \max|x_{cont}|}{\max|x_{uncon}|} \cdot 100 \quad (4.33)$$

The value of the variable *Reduction percentage* had to be smaller than 100% and could be negative indicating that the controlled maximum value was greater than the uncontrolled maximum value. The responses indicated by  $x$  in Equation (4.33) were the floor displacements relative to the ground and total accelerations of the floors. The floor displacements relative to the ground were controlled. The responses of the first and third floors were presented in Figure 4.20-Figure 4.23 for the four seismic excitations. Additionally, on the right vertical axis of (a) and (b) of Figure 4.20-Figure 4.23 the ratio of the maximum damper force and the maximum control force were presented. It was named *Force ratio*, and indicated the amount of the required damping force that the damper could provide. The acceptable region of the responses had to be around the region which *Force ratio* was equal to one, meaning that the required damping force could be provided by the MRD. Therefore, its acceptable values were chosen in the region of

$$75\% \leq Force\ ratio = \frac{\max|f_{MRD}|}{\max|u|} \leq 125\% \quad (4.34)$$

In (a) and (b) of Figure 4.20-Figure 4.23, the distribution of the variable *Force ratio* indicated by a line as distinct from the variables *Reduction percentage*. The aim was to emphasize its linearly increasing trend by increasing  $R$  values. On the

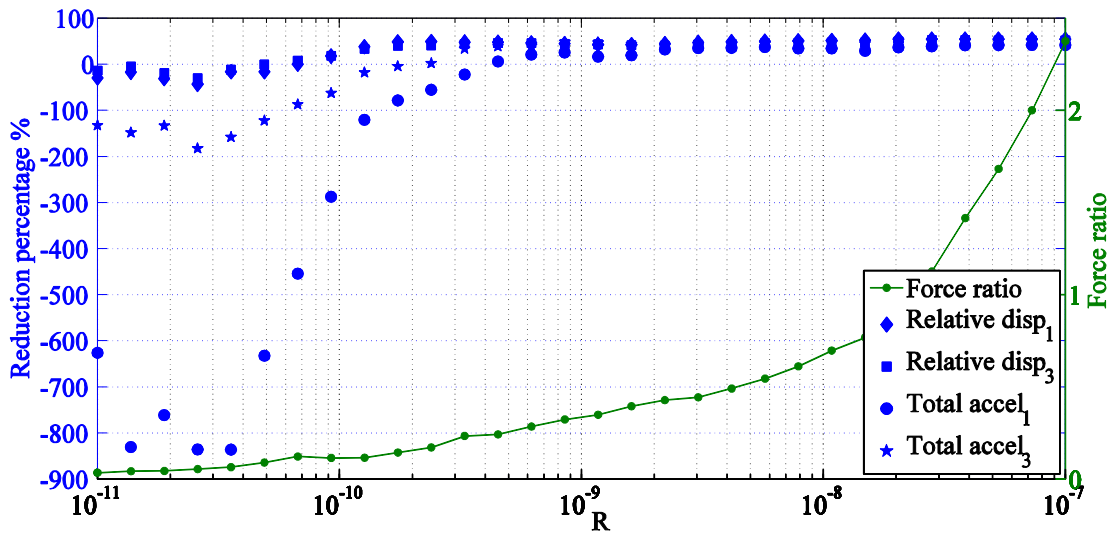
other hand, the variables *Reduction percentage* of the responses did not have a linear trend by changing *R* values. Especially *Reduction percentage* of the total accelerations behaved unpredictably due to the existence of the MRD.

The reduction percentage values are presented for various *R* values of the optimally controlled MRD in (a) of Figure 4.20-Figure 4.23. Then, the graph in (a) was zoomed in the allowable region of force ratio, and the results were presented in (b) of Figure 4.20-Figure 4.23. Finally, the reduction percentage values were presented for various applied voltage values of the passive MRD in (c) of Figure 4.20-Figure 4.23.

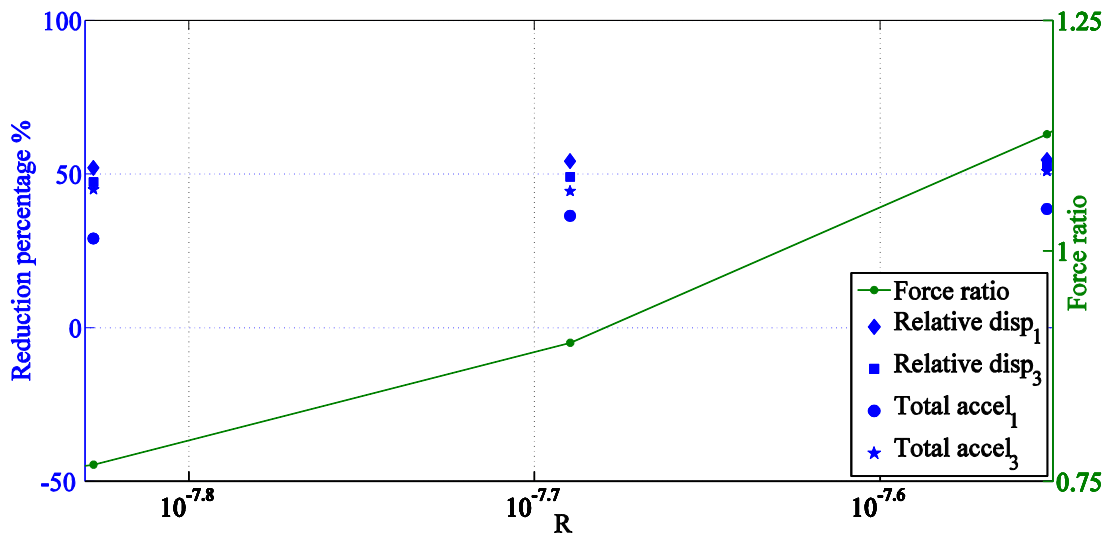
In general, possible expected outcomes due to the existence of the damper were the cases that the highest reductions occurred at the displacement of the first floor and the lowest reductions occurred at the total accelerations of the first floor. Additionally, the absolute acceleration response of the first floor contained not only the structure's acceleration value, but also acceleration coming from the damping force of the damper. Therefore, the absolute accelerations of the other floors supplied more correct information about the behavior of the structure.

According to (a) of Figure 4.20-Figure 4.23, the response of the optimally controlled system was mainly affected by the selection of *R* for the certain configuration of the *Q* matrix in Equation (4.32). Inconvenient selection of the *R* value caused unacceptable reductions in the total accelerations. Decreasing *R* values led to increasing control force values. This fact created improper total acceleration responses specially at the first floor level, at which the MRD was attached.

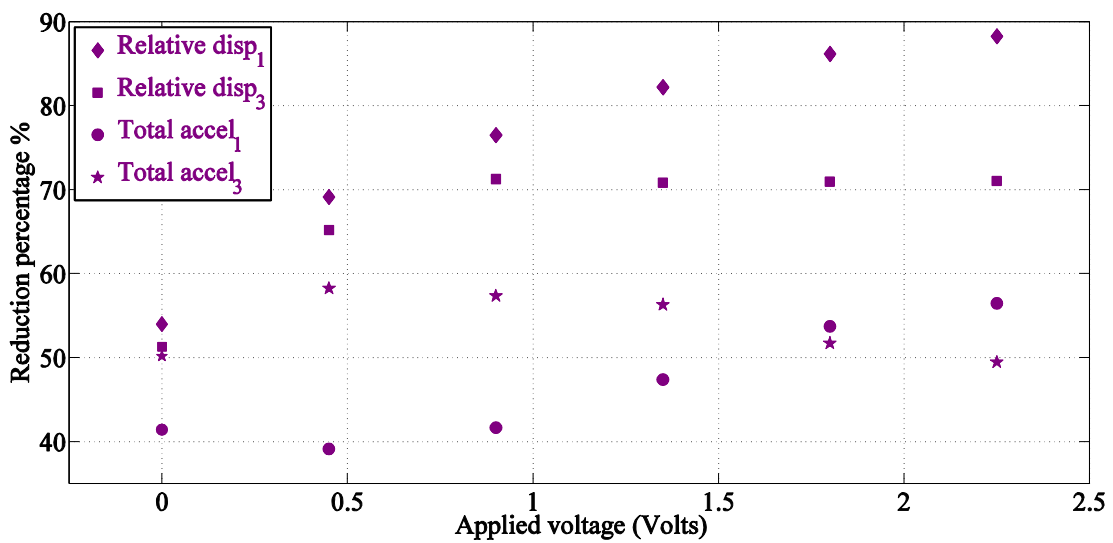
According to the graphs in (b) of Figure 4.20-Figure 4.23, the region of the optimal *R* values was determined as  $10^{-8.3} - 10^{-7.3}$  for the present system due to the allowable region of force ratio. In each excitation case, the reductions were close to each other for different *Force ratio* values in (b) of Figure 4.20-Figure 4.23. For the simulations of the Imperial Valley and Düzce earthquakes, the reductions in the responses were in the region of approximately 25-50 and 15-40 percent, respectively. On the other hand, the reductions in the responses of the *Synthetic1* excitation were higher compared to the others. The reductions in the responses of the *Synthetic2* excitation were the smallest ones. One of the controlled responses of the *Synthetic2* excitation was greater than the uncontrolled response for *Force ratio* close to the boundary of the acceptable region.



(a) Reduction percentage for various  $R$  values of the optimally controlled MRD

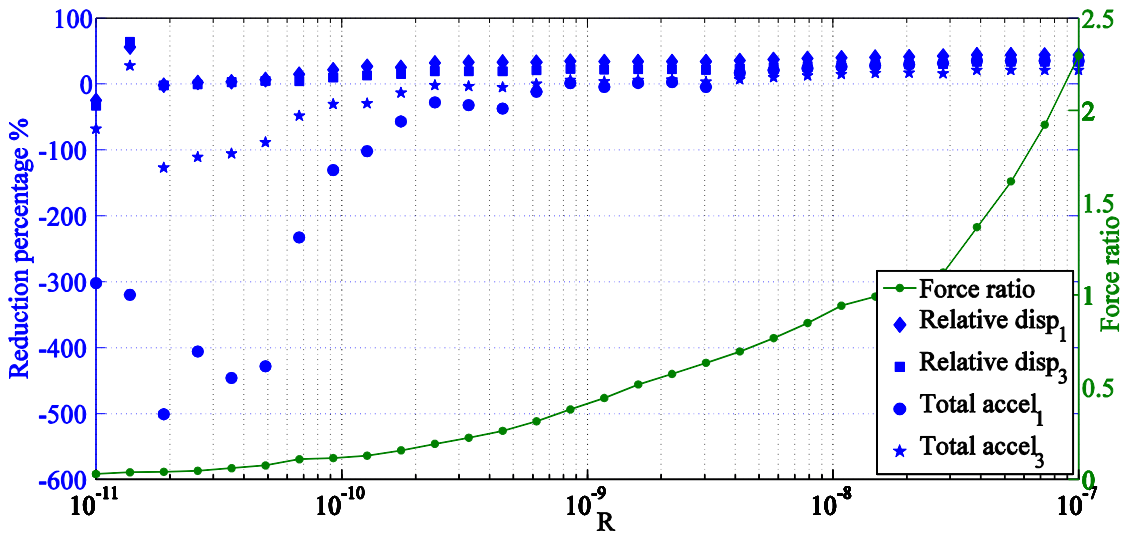


(b) The graph in (a) is zoomed in the allowable region of force ratio (75%-125%)

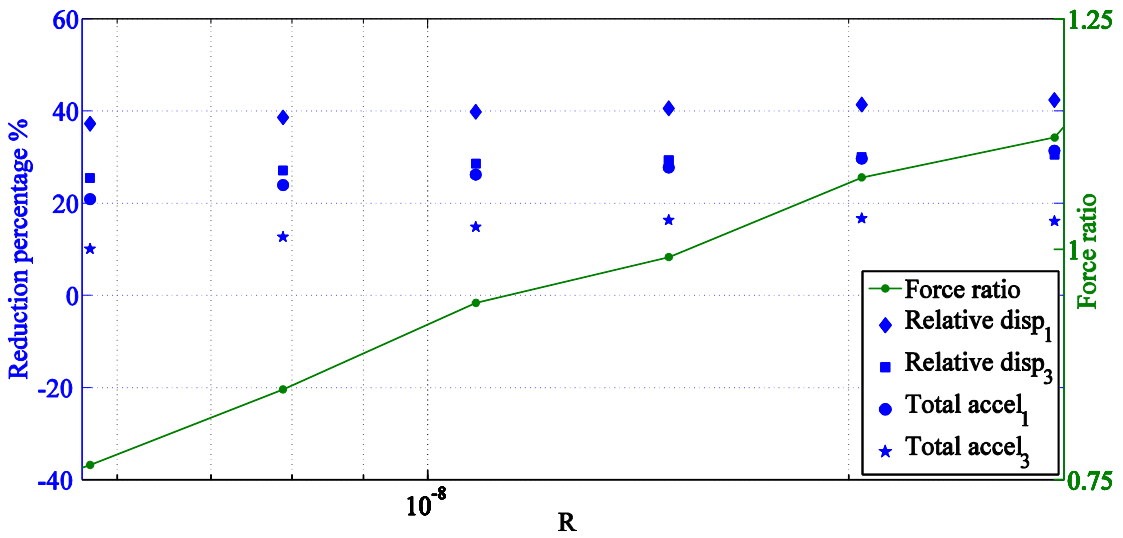


(c) Reduction percentage for various applied voltage values of the passively controlled MRD

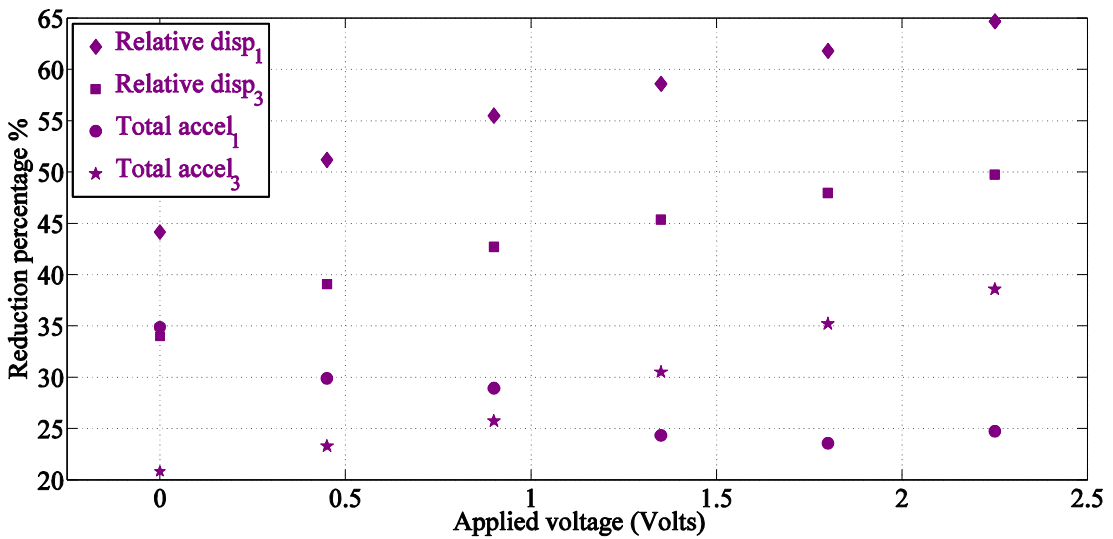
Figure 4.20. Reduction percentage values of the optimally and passively controlled MRD for the Imperial Valley earthquake



(a) Reduction percentage for various R values of the optimally controlled MRD

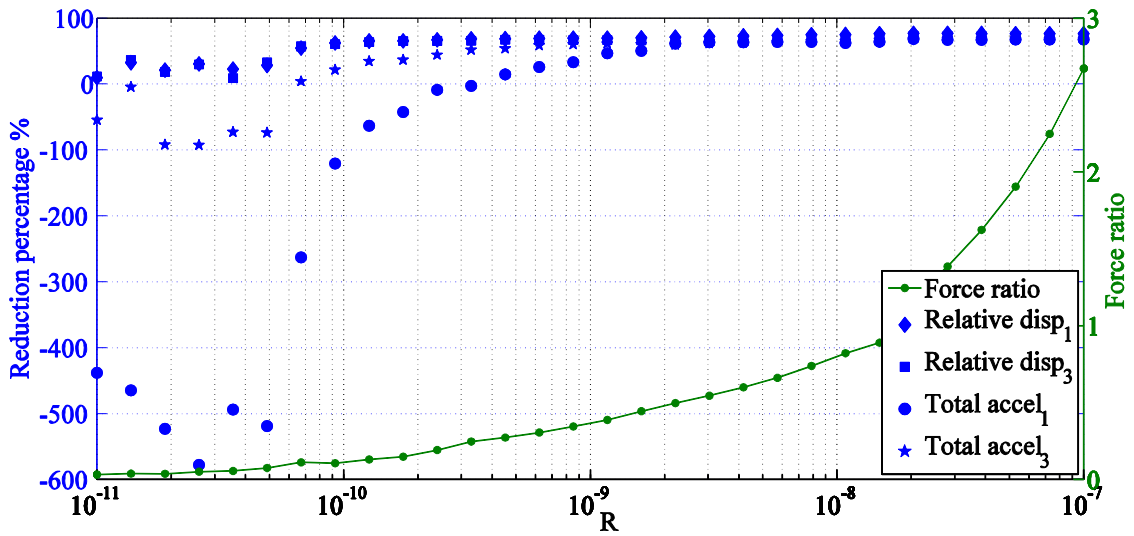


(b) The graph in (a) is zoomed in the allowable region of force ratio (75%-125%)

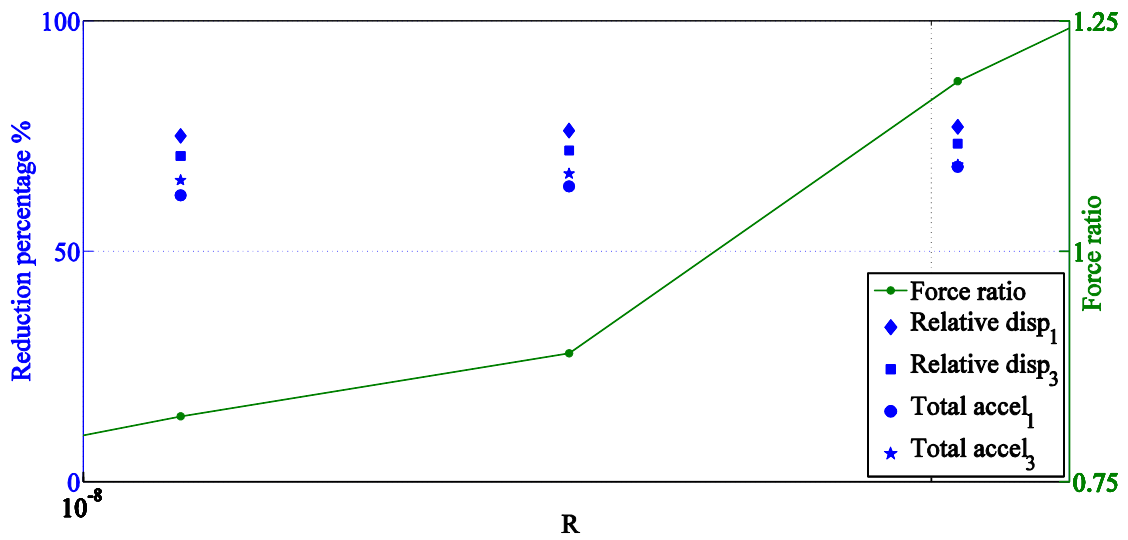


(c) Reduction percentage for various applied voltage values of the passively controlled MRD

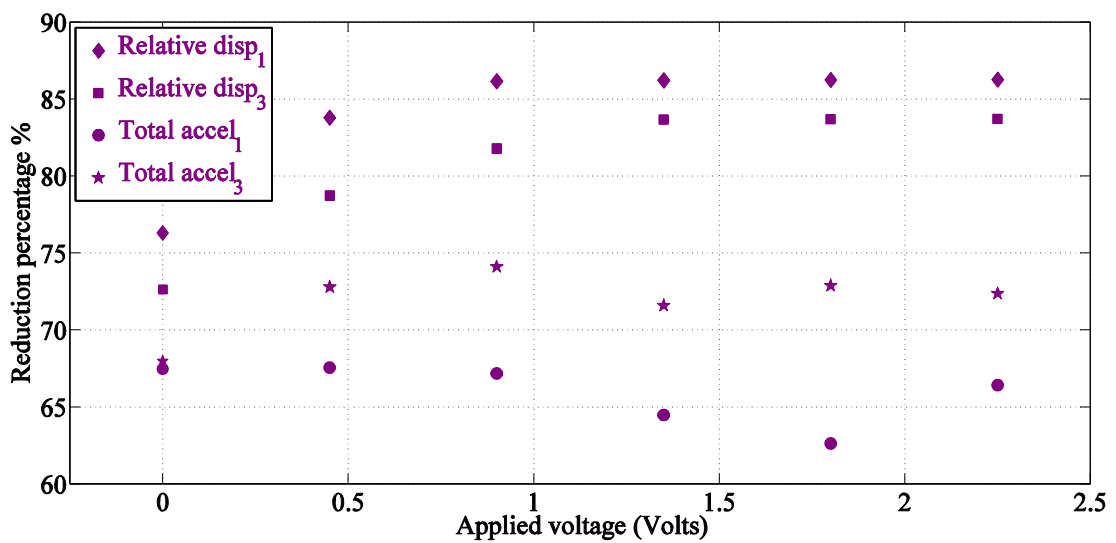
Figure 4.21. Reduction percentage values of the optimally and passively controlled MRD for the Düzce earthquake



(a) Reduction percentage for various  $R$  values of the optimally controlled MRD

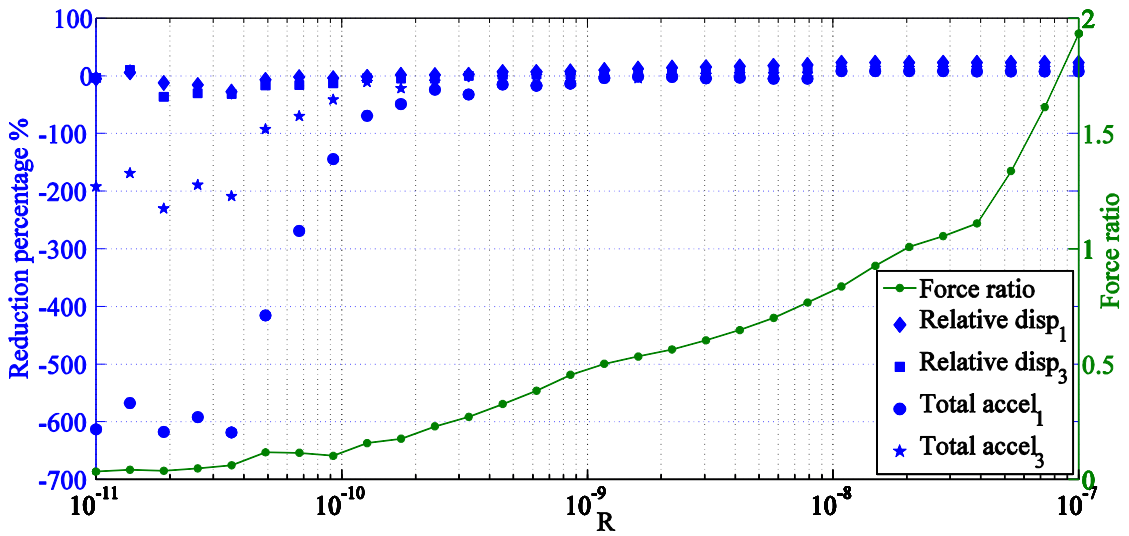


(b) The graph in (a) is zoomed in the allowable region of force ratio (75%-125%)

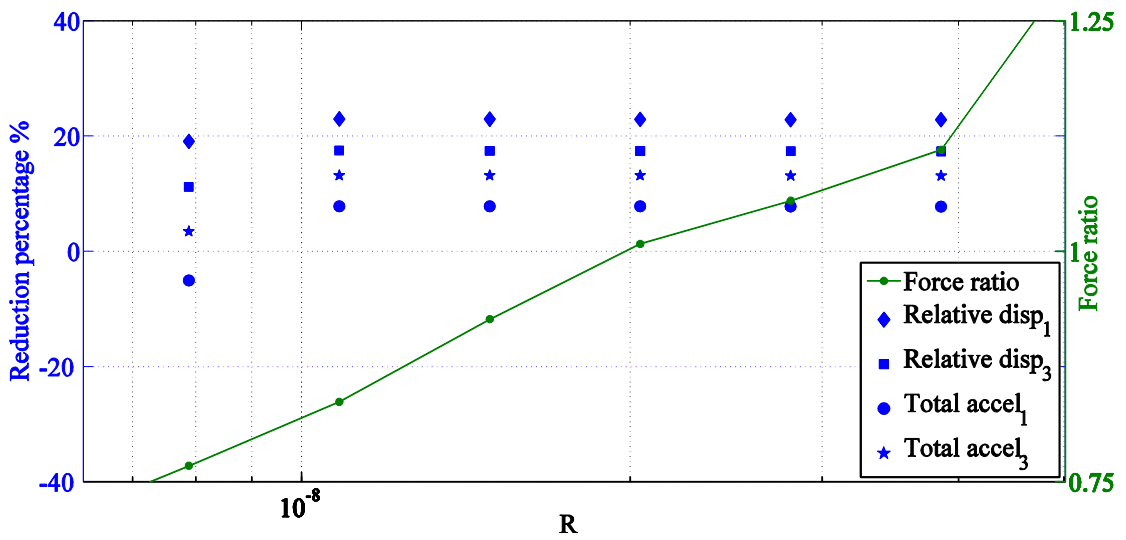


(c) Reduction percentage for various applied voltage values of the passively controlled MRD

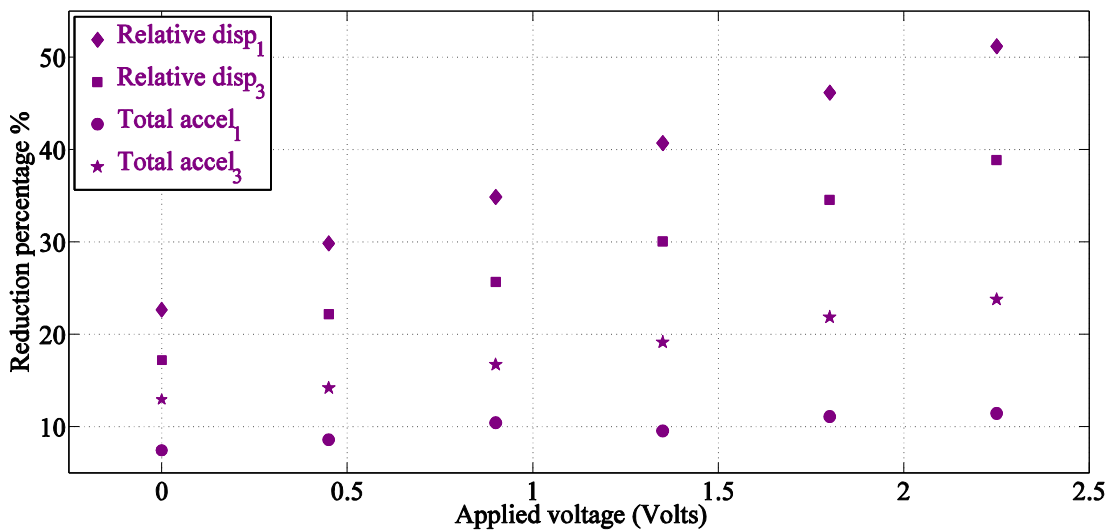
Figure 4.22. Reduction percentage values of the optimally and passively controlled MRD for the Synthetic1 excitation



(a) Reduction percentage for various R values of the optimally controlled MRD



(b) The graph in (a) is zoomed in the allowable region of force ratio (75%-125%)



(c) Reduction percentage for various applied voltage values of the passively controlled MRD

Figure 4.23. Reduction percentage values of the optimally and passively controlled MRD for the *Synthetic2* excitation

The *Reduction percentage* values were plotted versus applied voltage values of passive dampers in (c) of Figure 4.20-Figure 4.23. A better controlled response was an expected outcome as the applied voltage increased. Usually, the reductions in total accelerations were smaller than the reductions in relative displacements. This difference became more apparent as the applied voltage increased. The highest reductions were observed in the responses of the *Synthetic1* excitation. On the other hand, the lowest reductions were in the responses of the *Synthetic2* excitation.

Furthermore, the increase in the applied voltage did not cause a significant change in the total acceleration responses in (c) of Figure 4.20-Figure 4.23. This case indicated that the controlled system was highly overdamped, and the capacity of the utilized MRD was beyond the control requirements of the model structure utilized within the thesis.

Consequently, the comparison of (b) and (c) of Figure 4.20-Figure 4.23 in each case provides valuable comments about the question whether controlling a damper is necessary. The designer may perform the selection due to the control requirements, the distance of the structure to the closest (possible) fault, and convenience of the implementation of the optimal control action.

#### **4.7. Hybrid Control of a Base Isolated Model Structure by MRD**

In the present subsection, a hybrid control, which consists of passive and semi-active controllers, was studied. The aim was to benefit from advantages of both strategies and to compensate for their weak properties. The hybrid seismic response control of the three-storey model superstructure was performed. The model superstructure is presented in Figure 3.1. It was isolated seismically and a semi-active MRD in parallel to the base isolation system was attached between the base and the ground (see Figure 4.24). The benefits of hybrid application of two control systems were revealed. The control method was based on the theory of the LQR.

### 4.7.1. Base Isolation

Passive base isolation systems are currently more adopted in the control technology than semi-active MRDs. There are two types of base isolation, namely, the elastomeric-based systems and sliding-base systems. The elastomeric-based systems can be divided into two subgroups: low-damping rubber bearings and lead-core bearings.

Chandiramani (2004, p.6) explains the main idea of base isolation as: “*Structure mounted on a suitably flexible base such that the high frequency component of ground motion is filtered out and the fundamental vibration period is lengthened. This results in deformation in the isolation system only, thus keeping the structure above almost rigid. However, if the earthquake excitation contains a major component of this fundamental period, there will be large sidesway (albeit almost rigid) motions*”

Additionally, Kelly (1998, para.1) explains how the base isolation performs its duty: “*In this approach, the building or structure is decoupled from the horizontal components of the earthquake ground motion by interposing a layer with low horizontal stiffness between the structure and the foundation*”. In that respect, the researcher points out that it is better to utilize the term *dynamic stiffness* instead of the term *stiffness*. The *dynamic stiffness* is defined as  $k - \omega^2 m + i\omega c$  (Ewins, 2000), where  $\omega$  is the angular frequency of the excitation in rad/s.  $k$ ,  $m$ , and  $c$  are the stiffness, mass, and damping, respectively. In low frequency and small damping cases, the dynamic stiffness is close to the stiffness). Hence, the fundamental period of the isolated structure is lengthened by comparison with that of the fixed-base structure. In the frequency spectrum, it is placed at the higher period range of the ground excitation whose magnitudes are low. Thus, the high frequency component of ground motion is filtered out, and the structure is decoupled from the horizontal components of the seismic excitation. However, if the seismic excitation contains components with large magnitudes at the fundamental period of the isolated structure, then detrimental deformations occurs.

If the base isolator is assumed to have zero stiffness, then the base displacement relative to the ground is almost the reverse of the ground displacement. It performs relative displacements almost the same as ground, but in the opposite direction. The total displacement of the base is low. Conversely, the structure becomes a conventional one in case of a rigid base.

The isolators should be stiff enough in the vertical direction to resist the weight of the structure, while being flexible in the horizontal direction. In the present study, elastomeric-type base isolators were utilized, and the emphasis was not on the properties of the isolators. Therefore, details about the isolators were not provided.

In structural control design, one of the primary criteria is that the interstory drifts are restricted to limit the internal forces of structural elements (displacement control). For that purpose, the story drifts should be at low, or at least, moderate levels. Also, it can be suggested to limit the total accelerations for protecting the goods inside the building (absolute acceleration control). Additional design criteria may be added due to some special design demands (in museums, hospitals etc.).

The base isolation system may control the displacements or accelerations of the superstructure, depending on the frequency content of the ground excitation and the frequency range that the structure is shifted by the seismic isolation. In an isolated structure, the responses are mainly driven by the fundamental mode, and most of the deformation occurs at the base level. A small amount of deformation remains in the superstructure, resembling a rigid-body-motion. Therefore, in the present study, the mass of the whole structure was taken into account while calculating the damping and stiffness of the base. They were determined by the following formulas,

$$\begin{aligned}
 m_b &= 154.5 \text{ kg} \\
 c_b &= 2\zeta_b \left( \sum_{i=1}^3 m_i + m_b \right) \omega_b = 45.43 \frac{Ns}{m} \\
 k_b &= \left( \sum_{i=1}^3 m_i + m_b \right) \omega_b^2 = 706 \frac{N}{m}
 \end{aligned} \tag{4.35}$$

where  $m_b$ ,  $c_b$ , and  $k_b$  are the mass, damping, and stiffness values of the base.  $m_i$  is the mass of the  $i$ th floor.  $\omega_b$  is the circular frequency of the base.  $\zeta_b$  is the damping ratio of the base. In the present study, the base mass is chosen to be 154.5 kg, which is one and a half of the first story mass. The base system was considered to have 4% damping. Such a damping value was assumed for the isolator due to the very low damping level of the superstructure ( $\zeta_1 = 0.0058$ ,  $\zeta_2 = 0.0038$ , and  $\zeta_3 = 0.0041$  from Table 3.2). The elastomeric stiffness was approximately 706 N/m (For comparison purposes, the first floor had a stiffness of 78000 N/m).

The undamped period of the base was chosen as 10 times the fundamental undamped period of the superstructure, resulting in 5.06 s (Naeim & Kelly, 1999). This value was selected in such a way that the structure was pushed to the range of the excitation components with smaller magnitudes.

The isolation system designed in the present subsection was also used in the hybrid application of the VOD in Chapter 5. A linear observer and regulator design was considered for the isolated building in Section 5.5. Therefore, the overall stiffness of the isolators was assumed to be equal to a constant value so that the resulting model structure was linear at the starting point of the control design. The controllers of all subsystems were designed priori to the response calculations (a subsystem in the hybrid application of the VOD was the system with a certain orifice opening). The simulations were also performed with these linear isolators to investigate the effectiveness of the control algorithm towards the system for which it was designed for. The neglected non-linear effect of the isolators would cause an additional damping in the structure. For natural rubbers, the introduced damping was very low when compared to the MRD or VOD effect, whose damping ratios started range from 0.16 to extremely overdamped values. Therefore, the linear isolator assumption that was made in this study was not expected to cause a significant difference in the obtained results.

#### **4.7.2. Hybrid-Controlled Building Model**

In a base isolation system, it is aimed to reflect some portion of the seismic excitation energy by lengthening the period of the structure. Hence, the structure is protected from the detrimental effects of the ground excitation. In a near-source seismic event, the magnitude of the high-period components is larger compared to far-source seismic events. On the other hand, the distance of the structure to the epicenter of a possible future earthquake cannot be known. A place far away from a fault at the moment may become closer to the fault in time. Especially, this case can be considered to be more possible in a country like Turkey, in which most of the social and industrial regions are located near seismic zones. Therefore, this possibility should be taken into consideration while designing seismically isolated structures whose period is high compared to conventional structures. Consequently, it is advised to utilize hybrid control systems in seismic zones in place of bare base isolation systems. Hence, the

isolation system is protected by semi-actively controllable dampers placed in the base level.

The hybrid control system is a system, in which two or more control devices are utilized simultaneously. Passive supplemental damping in a seismically isolated structure provides the necessary energy dissipation to limit the isolation system displacement. However, damper forces can become quite large as the passive damping level is increased. Utilization of an intelligent hybrid application of a semi-active damper, whose damping coefficient can be modulated, is a possible solution to limit the level of damping force while simultaneously controlling the isolation system displacement (Symans & Kelly, 1999). On the other hand, additional damping at the base level reduces the base velocity directly and decreases the base displacement indirectly at the expense of larger drifts and floor accelerations of the superstructure.

Dampers are utilized to absorb energy from the structure. Thus, the larger the damping is, the less the relative structural velocity and displacement will be. The accelerations, however, will increase. If the latter behavior is not detrimental, then the act of controlling a damper appears to be useless. Since the maximum damping yields the best response, placing a controller into the system is not required. For building type structures, the control of dampers seems to be feasible only when buildings are seismically isolated. The function of the dampers in these types of structures is to limit the displacement of the dampers so that they cannot rupture. The presence of a damper in parallel to a base isolation system obviously decreases the effectiveness of the seismic isolation. Nevertheless, it will keep the elastomeric bearings from being driven into large displacements, thus securing the base isolation system.

The hybrid-controlled structure is presented in Figure 4.24. It has one base and three stories. In the present study, elastomeric base isolators were utilized at the base. A semi-active MRD in parallel to the base isolation system was attached between the base and the ground.

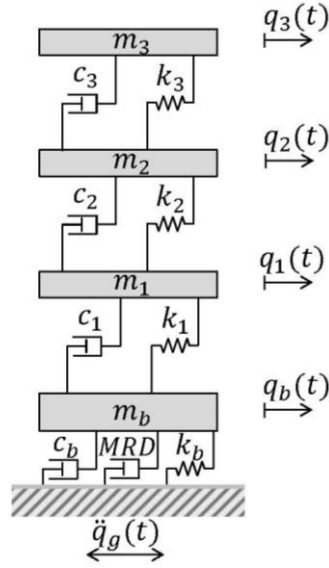


Figure 4.24. Hybrid-controlled building model (including base isolation and MRD)

In Figure 4.24,  $m_b$  and  $m_i$  are the base and floor masses.  $c_b$  and  $c_i$  are the base and floor damping.  $k_b$  is the base stiffness, and  $k_i$  is the floor stiffness for  $i = 1, 2, 3$ . The equation of motion with respect to the ground is as follows

$$\mathbf{M}_s \ddot{\mathbf{q}}_s(t) + [\mathbf{C}_s \dot{\mathbf{q}}_s(t) + \mathbf{h}_2 f_{MRD}(t)] + \mathbf{K}_s \mathbf{q}_s(t) = -\mathbf{M}_s \mathbf{h}_1 \ddot{q}_g(t) \quad (4.36)$$

where  $\mathbf{q}_s(t)$  is the displacement vector of the hybrid controlled structure relative to the ground.  $\mathbf{M}_s$ ,  $\mathbf{C}_s$ , and  $\mathbf{K}_s$  are the mass, damping, and stiffness matrices, respectively. They are presented in Equation (4.38).  $\ddot{q}_g(t)$  is the process noise (disturbance) that is the ground acceleration in the current problem.  $\mathbf{h}_1$  is the location matrix of the external excitation. It specifies how the ground excitation  $\ddot{q}_g$  enters into the system. It is equal to  $(1 \ 1 \ 1 \ 1)^T$ , indicating that the ground excitation acts to all degrees of freedom.  $f_{MRD}$  is the damping force of the controlled damper. The damper force is assumed as an internal damping, but, for simplicity of presentation and simulation, it is taken from the left-hand-side of the equation of motion to the right-hand-side, as follows

$$\mathbf{M}_s \ddot{\mathbf{q}}_s(t) + \mathbf{C}_s \dot{\mathbf{q}}_s(t) + \mathbf{K}_s \mathbf{q}_s(t) = -\mathbf{M}_s \mathbf{h}_1 \ddot{q}_g(t) - \mathbf{h}_2 f_{MRD}(t) \quad (4.37)$$

where  $\mathbf{h}_2$  is the location matrix of the control force and specifies how the control force  $f_{MRD}$  enters into the system. It is presented by  $\mathbf{h}_2 = (1 \ 0 \ 0 \ 0)^T$ , indicating that the damping force is present only at the base level.

Assembly of the global mass, damping, and stiffness matrices of the isolated structure was performed. The superstructure and base were individual subsystems. The superstructure was assumed to be classically damped since its damping ratios were close to each other (see Section 3.1.1). The mass, stiffness, and damping matrices of the superstructure ( $\mathbf{M}_{ss}, \mathbf{K}_{ss}, \mathbf{C}_{ss}$ ) are presented in Equation (3.3) and (3.13), respectively. The coefficient of the Rayleigh damping  $\alpha$  and  $\beta$  were calculated as 0.1231 rad/s and  $1.1667 \cdot 10^{-4}$  s/rad, respectively, in Section 3.1.1. Then, the global mass, stiffness, and damping matrices were constructed directly by assembling the matrices of the two subsystems: superstructure and base. For the base isolated structure, the global mass, stiffness, and damping matrices are as follows

$$\begin{aligned} \mathbf{M}_s &= \begin{bmatrix} 154.5 & 0 & 0 & 0 \\ 0 & 103 & 0 & 0 \\ 0 & 0 & 100 & 0 \\ 0 & 0 & 0 & 99.5 \end{bmatrix} kg \\ \mathbf{K}_s &= \begin{bmatrix} 78706 & -78000 & 0 & 0 \\ -78000 & 156000 & -78000 & 0 \\ 0 & -78000 & 156000 & -78000 \\ 0 & 0 & -78000 & 78000 \end{bmatrix} N/m \\ \mathbf{C}_s &= \begin{bmatrix} 54.53 & -9.1 & 0 & 0 \\ -9.1 & 30.88 & -9.1 & 0 \\ 0 & -9.1 & 30.51 & -9.1 \\ 0 & 0 & -9.1 & 21.35 \end{bmatrix} \frac{Ns}{m} \end{aligned} \quad (4.38)$$

The portions of the matrices in Equation (4.38), which are related with common DOFs at the interface between subsystems, include contributions from both subsystems. Additionally, the state-space representation of the system was required for the LQR design. The equation of motion of the hybrid controlled structure in Equation (4.37) is transformed into a first order state-space representation as follows:

$$\begin{bmatrix} \dot{\mathbf{x}}_s(t) \\ \ddot{\mathbf{q}}_s(t) \end{bmatrix} = \begin{bmatrix} \mathbf{0} & \mathbf{A}_s \\ -\mathbf{M}_s^{-1}\mathbf{K}_s & -\mathbf{M}_s^{-1}\mathbf{C}_s \end{bmatrix} \begin{bmatrix} \mathbf{q}_s(t) \\ \dot{\mathbf{q}}_s(t) \end{bmatrix} + \begin{bmatrix} \mathbf{0} \\ -\mathbf{h}_1 \end{bmatrix} \ddot{\mathbf{q}}_g(t) + \begin{bmatrix} \mathbf{B}_s \\ -\mathbf{M}_s^{-1}\mathbf{h}_2 \end{bmatrix} u_s(t) \quad (4.39)$$

where  $\mathbf{x}_s(t)$  is the state vectors.  $u_s(t)$  is the control input.  $w_s(t)$  is the disturbance.  $\mathbf{A}_s$  is the state matrix.  $\mathbf{G}_s$  is the disturbance vector.  $\mathbf{B}_s$  is the control input vector. The state-space representation of the system was constituted by the equation of motion of the model structure remaining in the linear region. The states were chosen as the floor

displacements and velocities relative to the ground. All the states and the damper force were assumed to be sensed for full state feedback.

The undamped periods and frequencies of the base isolated structure are presented in Table 4.5. The undamped periods of the superstructure are approximately 0.51, 0.18, 0.13 seconds from Table 3.1. By the addition of the base isolator, the undamped periods take the values presented in Table 4.5, softening the first mode of vibration.

Table 4.5. Undamped periods and frequencies of the base isolated structure

	Period (s)	Undamped frequency (Hz)	Undamped circular frequency (rad/s)
First mode	5.07	0.20	1.24
Second mode	0.32	3.10	19.47
Third mode	0.17	5.98	37.57
Fourth mode	0.12	8.08	50.75

A value for isolator period was chosen in such a way that the structure was pushed to the smaller magnitude range on the acceleration spectra of the far-fault excitation record (see Figure 4.25). Hence, the structure and the damper were protected from the detrimental effects of earthquake excitations. In Figure 4.25, the fundamental undamped periods of the fixed-base and isolated structures are marked by the dashed and bold lines, respectively. The magnitude of the corresponding excitation is marked by a grey dot.

The responses of a conventional and an isolated structure are mainly driven by the fundamental damped period since they are under-damped systems (the damping ratio of the base and the first mode of the superstructure are 0.04 and 0.0058, respectively, see Section 4.7.1 and Section 3.1.1). The undamped and damped periods of the bare and isolated structure are close to each other due to the low damping ratio ( $T_d = T_n / \sqrt{1 - \zeta^2}$  where  $\zeta$  is the damping ratio). On the other hand, the damping effect of the MRD on the damped periods does not presented in Figure 4.25. This fact should be taken into consideration while interpreting the response of the hybrid-controlled structure.

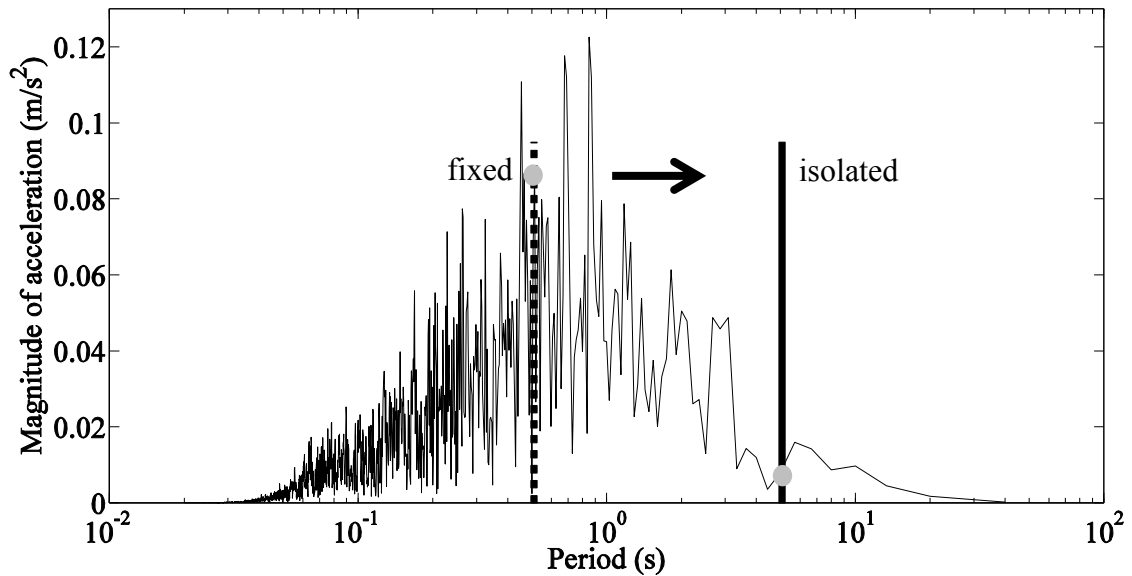


Figure 4.25. Original data of the Imperial Valley event in the frequency domain (The fundamental undamped periods of the fixed-base and isolated structure are marked by the dashed and bold lines)

The isolation effect was created by choosing relatively high periods for isolators to rescue the structure from the range of high frequency excitations. In other words, the isolator acted as a low pass filter (see Figure 4.25).

#### 4.7.3. Current State in the Simulations and Results of the Simulations

The hybrid control system, which consists of a semi-active MRD in parallel to a base isolation system, is presented in Figure 4.24. The simulation was performed by using the data provided from the record of the 1940 Imperial Valley earthquake. The excitation data is displayed in Figure 2.4 in time- and frequency-domains. The excitation data was interpolated to one fifth of the original time increment of the data, resulting in 500 Hz.

The control method was based on the theory of LQR. In the present simulations, the base isolator and the hydraulic damper were always in action during a seismic excitation, sharing the control task. The  $Q - R$  couple of the LQR design was determined by a trial-and-success procedure similar to the one summarized in Table 5.4. They are presented in Equation (4.40).

$$\mathbf{Q} = \begin{bmatrix} 100 & 0 & 0 & 0 & 0 & 0 & 0 & 0 \\ 0 & 1 & 0 & 0 & 0 & 0 & 0 & 0 \\ 0 & 0 & 1 & 0 & 0 & 0 & 0 & 0 \\ 0 & 0 & 0 & 1 & 0 & 0 & 0 & 0 \\ 0 & 0 & 0 & 0 & 1 & 0 & 0 & 0 \\ 0 & 0 & 0 & 0 & 0 & 0.01 & 0 & 0 \\ 0 & 0 & 0 & 0 & 0 & 0 & 0.01 & 0 \\ 0 & 0 & 0 & 0 & 0 & 0 & 0 & 0.01 \end{bmatrix}, R = 1 \cdot 10^{-5} \quad (4.40)$$

In the present work, the states were treated as uncoupled. Therefore, the off-diagonal terms of the  $\mathbf{Q}$  matrix were zero. The weights of the base responses were ten times higher than those of the floor responses assigning more control effort to the response control of the base. The weights of the displacements were ten times higher than those of the velocities coinciding the nature of degrees of freedom in the present problem.  $R$  should be strictly positive definite. It should be noted that the important issue in the LQR is not the individual values of  $\mathbf{Q}$  and  $R$ , but the ratio between them is important.

By this configuration of the  $\mathbf{Q} - R$  couple, the ratio between the absolute values of maximum control force and MRD force became 0.99 for the data of the Imperial Valley earthquake. On the other hand, the maximum MRD force was at the level of one third of the force capacity of the MRD (3000 Newton), indicating that the capacity of the MRD was not benefitted from completely. If  $R$  had been decreased to increase the control force  $u$ , then the ratio between  $u$  and  $f_{MRD}$  would have increased, and the controlled response would have deteriorated. This fact indicated that the capacity of the utilized MRD was beyond the control requirements of the model structure utilized within the thesis.

The displacement time histories of the ground, the seismic isolated base, and the hybrid controlled base are presented in Figure 4.26. The values of the base were relative to the ground. The black dashed line stands for the displacement of the ground. The black solid line belongs to the passive controlled system and green solid one is for the hybrid system. In Figure 4.26, the significance of the hybrid controller was observed after the ground acceleration peaks at 25-28 seconds. The base isolated structure performed large deformation, and the isolators were damaged. On the other hand, the hybrid controller protected the base from large displacement response.

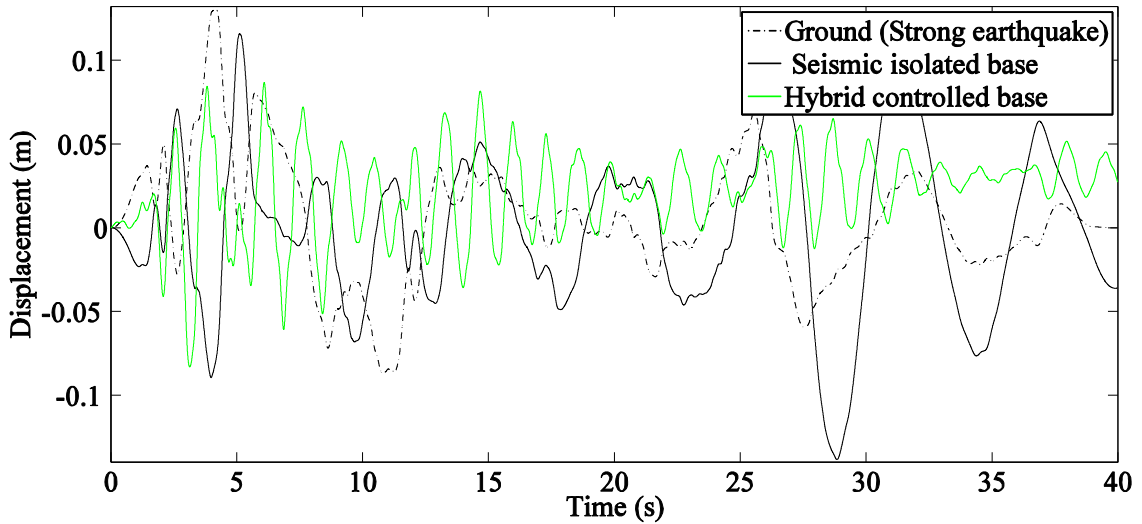


Figure 4.26. Displacement time histories of the ground, the seismic isolated base and the hybrid controlled base due to the Imperial Valley earthquake (The values of the base are relative to the ground)

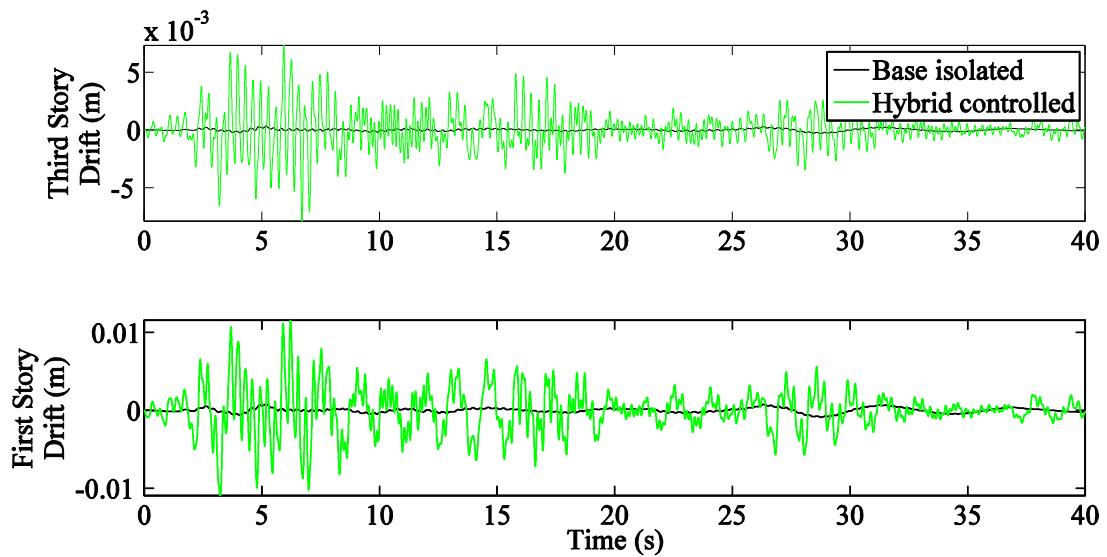


Figure 4.27. Interstory drifts of the superstructure due to the Imperial Valley earthquake

According to Figure 4.26, since the isolators were very soft, their relative displacements with respect to the ground were almost equal to the negative value of the earthquake's displacement, at least for the first two seconds. At time  $t=22$  seconds, the ground moved at a period of approximately 6 seconds, which was close to the fundamental period of the isolated structure, for a total duration of approximately 12 seconds. Hence, the structure got into resonance, causing large structural displacements. The isolated structure had low damping, resulting in large amplitude harmonic motion

with a small decay. On the other hand, the amplitude for the hybrid controlled structure was approximately 50% smaller.

The simulation responses of the interstory drifts of the superstructure are presented in Figure 4.27. Examining the graphs, the floor responses of the hybrid controlled structure were larger compared to the base isolated case. But, they were still in acceptable ranges ( $< 1$  cm). This was an expected result that was taken into account during the engineering design.

At the beginning of the studies of the related hybrid control, the designer intended to activate the MRD after the base drift exceeded 3 centimeters not to utilize the MRD at low levels of excitation. When this condition was applied, the maximum displacement of the base was 11 centimeters while the base of the isolated structure performed a displacement of 14 centimeters (all values were relative to the ground). The contribution of the hybrid control was only a reduction of 21 percent at the base level. On the other hand, if the MRD had been always in action during the seismic excitation, then the base would have performed a maximum displacement of 9 centimeters resulting in a displacement reduction of 36 percent. Therefore, it was preferred to keep the MRD always in action. Otherwise, the passive control system, which was only composed of the base isolation, seemed a better design since it did not increase the total accelerations of the system (see Figure 4.30).

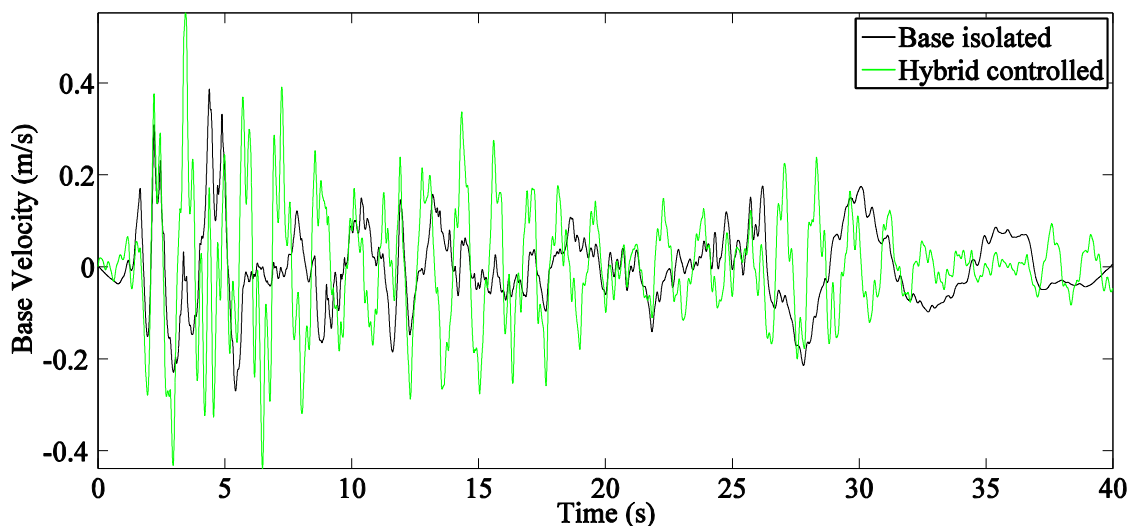


Figure 4.28. Response of the base velocity with respect to the ground due to the Imperial Valley earthquake

The interstory velocity responses of the base and the superstructure are presented in Figure 4.28 and Figure 4.29, respectively. The total acceleration values of the base, first, and third floors are presented in Figure 4.30.

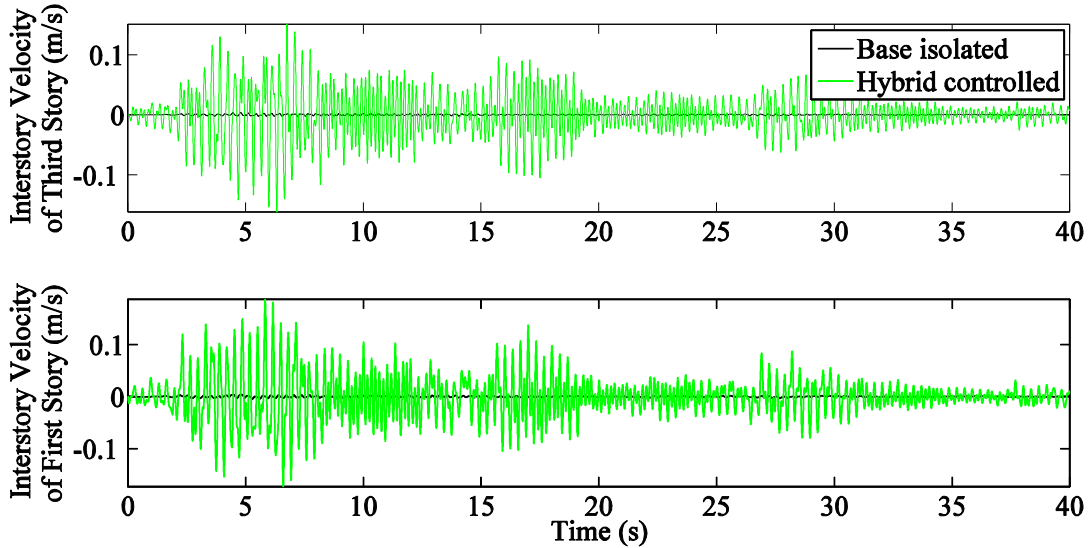


Figure 4.29. Interstory velocities of the superstructure due to the Imperial Valley earthquake

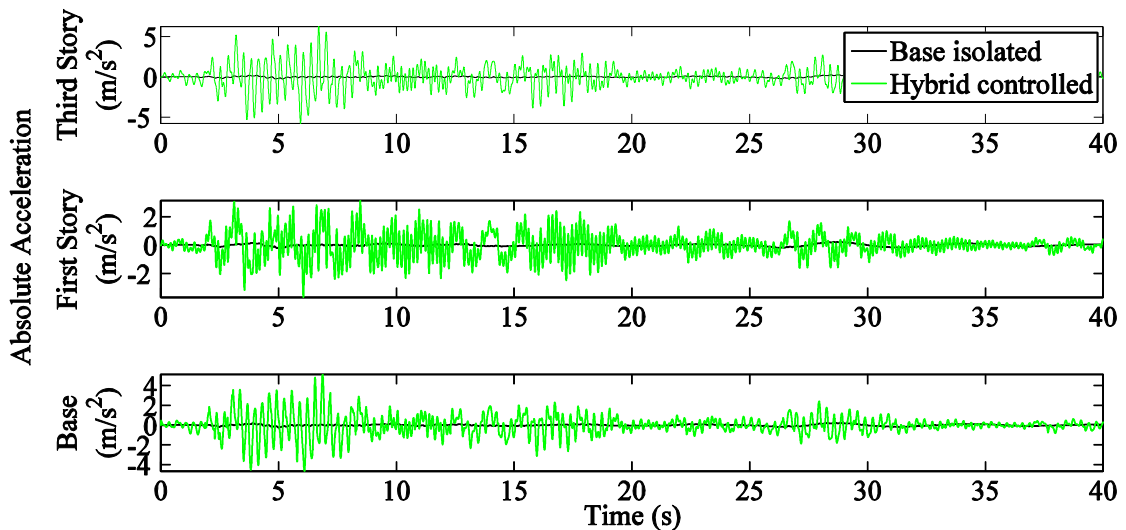


Figure 4.30. Absolute accelerations due to the Imperial Valley earthquake

The hybrid controller protected the base from large displacement and velocity responses after the ground acceleration peaks at 25-28 seconds while the base isolated structure underwent large deformation. The absolute acceleration peak value reached to  $2g$  ( $g$ : gravitational acceleration). It was a considerable value compared to the benefit in

the displacements and velocities. The increases in the accelerations when compared to those of the isolated structure was due to the existence of the damper at the base level.

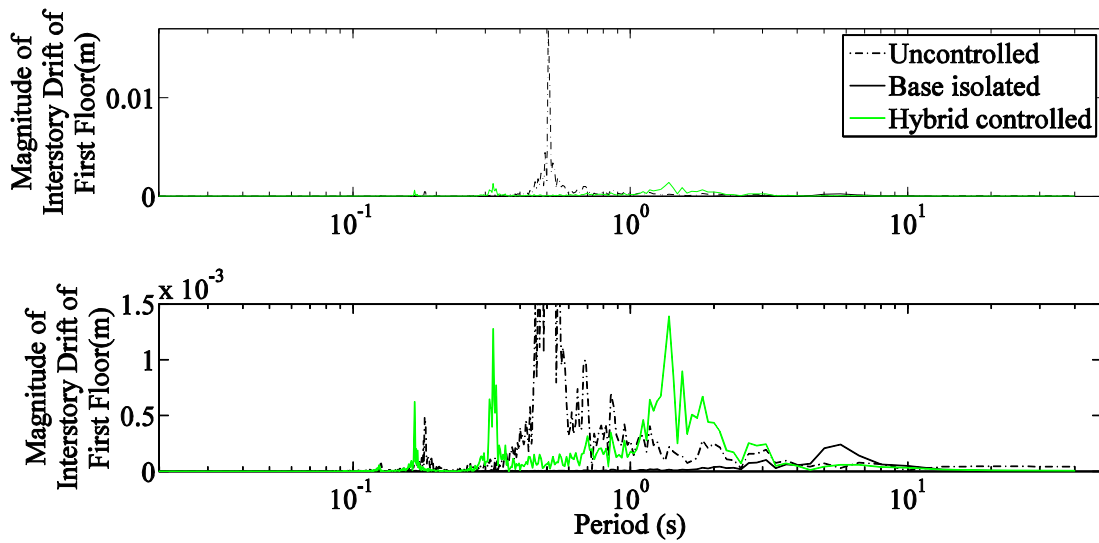


Figure 4.31. Interstory drift of the first floor in frequency domain ((b) is zoomed in vertical axis)

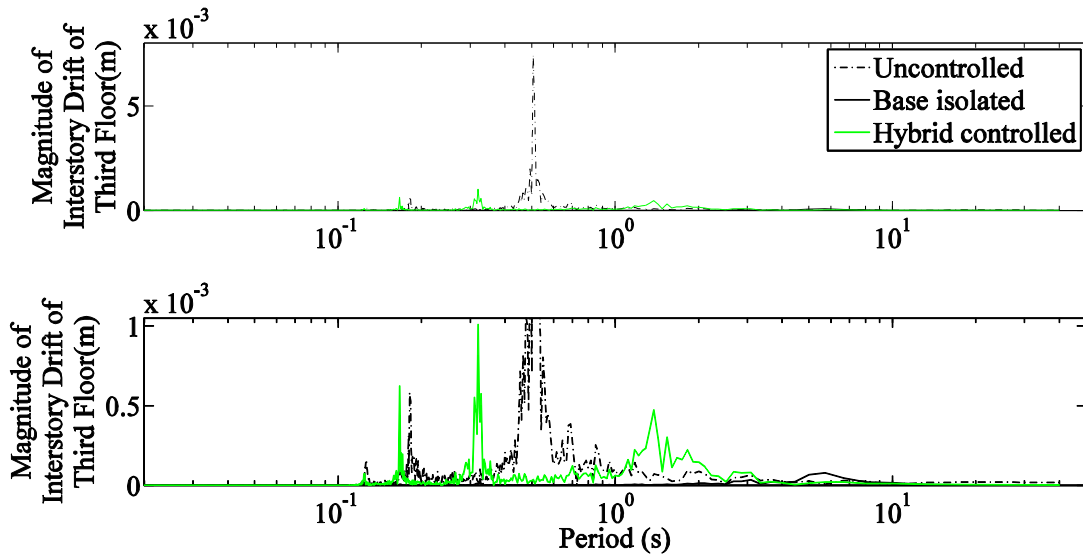


Figure 4.32. Interstory drift of the third floor in frequency domain ((b) is zoomed in vertical axis)

The interstory drifts of the first and third floors in frequency domain are presented in Figure 4.31 and Figure 4.32, respectively. The response of the uncontrolled structure was driven mainly by the first mode. The second mode exhibited a smaller contribution to the response. On the other hand, the base isolated structure's response

was driven by its fundamental mode, and the effect of the other modes on the response could not be observed. When the MRD was added to the structure in addition to the base isolation, the first mode's period was slightly shortened, and the contribution of the second and third modes had a larger effect at this time than the first mode.

The beneficial effect of hybrid system was obviously revealed by the results of the present simulation: In the absence of the MRD, the base displacement was much higher and damped out in a longer period of time. By adding extra damping (MRD) to the structural control system, a reduction of 50% in terms of base displacement was obtained. On the other hand, the floor displacements increased, but they were still in an acceptable range. Consequently, the base isolators were protected from rupture or damage due to large deformations.

## CHAPTER 5

# HYBRID CONTROL OF A BASE ISOLATED MODEL STRUCTURE WITH A VARIABLE ORIFICE DAMPER (VOD)

### 5.1. Overview

The variable orifice dampers are semi-actively controlled hydraulic dampers, whose damping coefficient can be changed by mechanically adjusting a valve. In the context of the present section, a hybrid control system, which consists of the seismic isolator and VOD, is designed. The hybrid system contains advantages of both components and compensates for weak properties of them. The base isolation prevents acting of some portion of the seismic energy into the superstructure. The energy dissipating device limits the displacement of an isolation system to an acceptable level and, hence, protects the isolator. The base isolator is always in action during a seismic excitation. The hydraulic damper, on the other hand, shares the control task only if the displacement demand is large.

The current section of the research focuses on gain scheduling control of a three story frame structure. The hybrid control system consists of a passive controller (elastomeric isolators) and a semi-actively controlled hydraulic damper, namely a VOD, that is connected in parallel to the base isolator. The damping value of the VOD is varied by adjusting the orifice opening size. The system behaves nonlinearly as the orifice opening of the damper changes. Linear subsystems were assigned for a number of different orifice settings, and a controller was designed for each of these linear subsystems.

Generally, in control examples, only the displacements are sensed. On the other hand, the story velocities are not measured although they are required for the full state information. Therefore, the necessity of designing an observer is crucial to predict the unmeasured states. On the other hand, in real-world applications with state feedback control all the states of the system have to be known. But, quite often it is not practical

or possible to measure all the states. This fact enforces the researchers to employ observers in the control of civil engineering structures, in which some of the states have to be estimated from the measurements. Therefore, in the present study, special attention was paid for the subject of observers in the context of the LQG control.

The linear quadratic Gaussian (LQG) based controllers were designed for various orifice openings of the damper in the isolated structure. The whole system consists of sub-systems, their controllers, and their observers. During a simulation, the optimum orifice size was selected among the previously defined orifice opening values at each time step by means of an upper controller, by which large isolator displacements and isolator damages were prevented.

At the beginning of the studies, the observer could not predict the responses successfully. Therefore, Kalman and Kalman-Bucy observers were studied in detail, and some remedies for the observer design were applied: The observer was modified by sending the recorded disturbance. Besides, the base was prewhitened to satisfy the white input prerequisite of the Kalman-Bucy filter. The superstructure was diagonalized to obtain independent subsystems for the observer design. The observer was designed for the prewhitened base and diagonalized superstructure separately. The substructured configuration was utilized only for the observer design. The responses of the hybrid controlled system were calculated for the 4-by-4 structure.

## **5.2. Literature Review**

A hydraulic actuator was implemented with a controllable orifice, which was designed by Sack and Patten (1996) for a full-scale highway bridge (Patten et al., 1999). Some researchers investigated the application of VODs for seismic response reduction of buildings and bridges (Symans & Constantinou, 1997; Symans & Kelly, 1999).

In some experiments performed by Symans & Constantinou (1999), a structure with semi-active dampers exhibited a linear behavior in a certain limit of applied control voltage. The findings revealed that the linear relationship was deteriorated when closer to maximum speed or force levels. The models of the seismic isolators and damper were determined experimentally by Wongprasert and Symans (2005).

An extended review of the gain scheduling literature was provided by Leith & Leithead (2000). The related study explained the fundamental theoretical and design

procedures briefly. Other references related with gain scheduling control are presented in Section 5.6.

Wu et al. controlled the JZ20-2NW offshore platform in Bohai Gulf of China by MRDs (2010). Due to the limited number of measurements, a Kalman filter was designed (see Section 4.2 for details).

$H_2$ /LQG control including Kalman estimator was applied to an active base isolation system in (Chang & Spencer, 2010). Kalman-Bucy filter was designed for output feedback control of a cable-stayed bridge by Schemmann and Smith (1998). LQG control system was employed in a benchmark structural control problem by Spencer et al. (1998). Kalman filter modified by inserting  $\alpha_0$ -degree relative stability to the algorithm was designed by Wang (2003).

A control algorithm that can estimate ground excitation by using a Kalman filter was proposed by Aldemir (2009). The suggested algorithm exhibits results similar to those of a completely optimal control system, except for the maximum values.

Three-dimensional response of a structure by placing semi-active VODs in two directions was controlled by Turan (2010). Gain-scheduling control of a VOD was performed for a three story building subjected to earthquake excitation by Kınay et al (2010).

### **5.3. Variable Orifice Damper (VOD)**

The VOD was manufactured by modifying a piston with a pipe that interconnects its two chambers. A stepper motor controlled valve was placed in series with this pipe (see Figure 5.1). The damping value of the VOD is related to the size of the orifice opening (Turan & Aydın, 2011). The critical damping value  $c_{cr}$  for the isolated structure was determined as 1115 Ns/m. Its calculation was performed by Equation (5.2) and was summarized in Table 5.1.

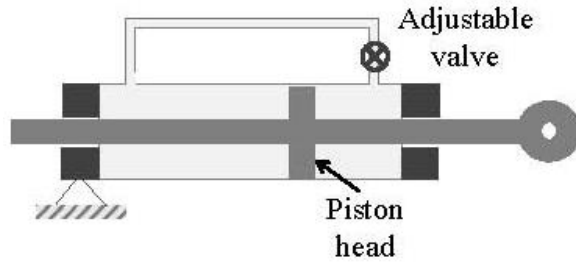


Figure 5.1. Longitudinal section of the utilized semi-active damper

At the early simulations of the present research, the damping values of the VOD were from 100 till 2500 Ns/m by increments of 100 Ns/m. On the other, the maximum damper force was at the level of 1000 N indicating that the capacity of the damper was not utilized (maximum damper force is 5000 N). By this selection of damping values, it was aimed to create an under-damped response that the structure approached to a reference zero by performing oscillations, instead of an over-damped response. This selection (100 till 2500 Ns/m by increments of 100 Ns/m) was left behind due to the low force levels and the damping values were chosen as 100, 200, 300, 400, 500, 600, 700, 800, 900, 1000, 1500, 2000, 2500, 3000, 10000, 15000, 20000, and 25000 Ns/m to increase the damper force levels. The upper limit was selected so that the piston's capacity did not exceed, whereas the lower limit corresponded to approximately 10% of the critical damping. The chosen damping range allowed the controller to put the structure into a harmonic, or a very stiff state. The structure might damp out the seismic energy while performing oscillations, or the structure might converge to a zero state rapidly in an exponential manner leading to a very stiff response (see Appendix F for details).

In an under-damped SDOF system, the damping ratio can be determined via the drop in the amplitude of the response within one cycle of vibration (Meirovitch, 2001). Hence, the critical damping  $c_{cr}$  of the SDOF system can be obtained. This fact can be utilized for a linear MDOF system whose response is a superposition of SDOF responses at different frequencies. The procedure was illustrated in Section 3.1.1. The logarithmic decrement  $\delta$  is

$$\delta = \ln \frac{q(t_1)}{q(t_2)} = 2\pi \frac{\zeta}{\sqrt{1 - \zeta^2}} \quad (5.1)$$

There is only one restriction for Equation (5.1) as the system is to be under-damped ( $\zeta < 1$ ). The damping ratio  $\zeta$  can be determined via

$$\zeta = \frac{\delta}{\sqrt{4\pi^2 + \delta^2}} \quad (5.2)$$

where the damping ratio  $\zeta$  is not linearly proportional to the logarithmic decrement  $\delta$  (see Table 5.1). Equation (5.2) is valid for under-damped cases.

The damping of the structure with a VOD varies as the orifice size of the damper changes. Hence, the response of the system becomes under-damped or over-damped depending on the orifice opening. Therefore, the under-damped and over-damped responses in the context of a SDOF system are presented in Appendix F.

The VOD does not have a critical damping value since it does not have a mass as a mechanical device. It is just a dashpot. A certain critical damping value can be pronounced when the VOD is mounted to a system. In the present study, the critical damping  $c_{cr}$  and the damping ratio  $\zeta$  corresponding to every orifice size were determined by the logarithmic decrement within one period of the system. The system was excited by an initial condition in the shape of the first mode as  $[0.1 \ 0.1 \ 0.1 \ 0.1 \ 0 \ 0 \ 0 \ 0]$ . The initial condition was in the shape of the state vector: the first four ones were for displacements, and the remaining ones stood for the velocities. The values related with velocity were set to zero in order to excite the first mode only. Otherwise, a relation between the displacements and velocities would have been defined.

The damping value  $c_D$  of the VOD was held constant like a passive damper. Then, it could be assumed to be a linear system, and the principle of superposition was valid. When  $c_D$  was set to zero, the damping observed in the response was the damping of the base. For the first mode, a damping value of 45.43 Ns/m was always present as the damping of the base and  $c_D$  was an additional damping. The calculations are presented in Table 5.1.

Table 5.1. Determination of the critical damping value of the fundamental mode of the system

Damping of VOD $c_D$ (Ns/m)	Damping of system $c$ (Ns/m)	Logarithmic decrement $\delta = \ln \frac{q(t_1)}{q(t_2)}$	Damping ratio $\zeta = \frac{\delta}{\sqrt{4\pi^2 + \delta^2}}$
0	45.43	$\ln \frac{0.1}{0.062980} = 0.4624$	0.0734
100	145.43	$\ln \frac{0.1}{0.036033} = 1.0207$	0.1603
200	245.43	$\ln \frac{0.1}{0.020032} = 1.6078$	0.2479
300	345.43	$\ln \frac{0.1}{0.010650} = 2.2396$	0.3358
400	445.43	$\ln \frac{0.1}{0.005317} = 2.9343$	0.4231
500	545.43	$\ln \frac{0.1}{0.002394} = 3.7322$	0.5107
600	645.43	$\ln \frac{0.1}{0.000912} = 4.6973$	0.5988
700	745.43	$\ln \frac{0.1}{0.000263} = 5.9408$	0.6870
800	845.43	$\ln \frac{0.1}{0.000044} = 7.7287$	0.7759
850	895.43	$\ln \frac{0.1}{0.000013} = 8.9327$	0.8179

where  $c_D$  is the damping of the damper.  $\zeta$  is the calculated damping ratio of the excited mode.  $c$  is the damping present in the first story.  $c_{cr}$  is the critical damping of the fundamental mode of the isolated structure.  $q(t_1)$  and  $q(t_2)$  are two successive peaks in the displacement response.

The first peak could be seen in the displacement response. As the damping increased, the second peak could not be obviously seen (for  $\zeta > 0.75$ ). Therefore, a damping value of VOD as 850 Ns/m was applied numerically. Actually this value is not one of the damping value values of the VOD, but it was applied to make the data denser in the region close to the critical damping case.

The damping values  $c$  are presented versus the damping ratios  $\zeta$  in Figure 5.2. These values are in the second and forth columns of Table 5.1. They are dependent

linearly by  $= \frac{c}{c_{cr}}$ , in which  $c_{cr}$  is a constant value. Therefore, fitting a linear curve to the data was a convenient choice. Hence, the critical damping value  $c_{cr}$ , at where  $\zeta = 1$ , was determined as  $c_{cr} \cong 1102.34$  Ns/m. The damping value of the base was always present ( $c_b = 45.43$  Ns/m). The value remaining for the VOD was 1057 Ns/m. The closest damping value of the VOD was 1000 Ns/m. Therefore, the fundamental response of the hybrid-controlled structure is over-damped for the damping values of the VOD higher than 1000 Ns/m.

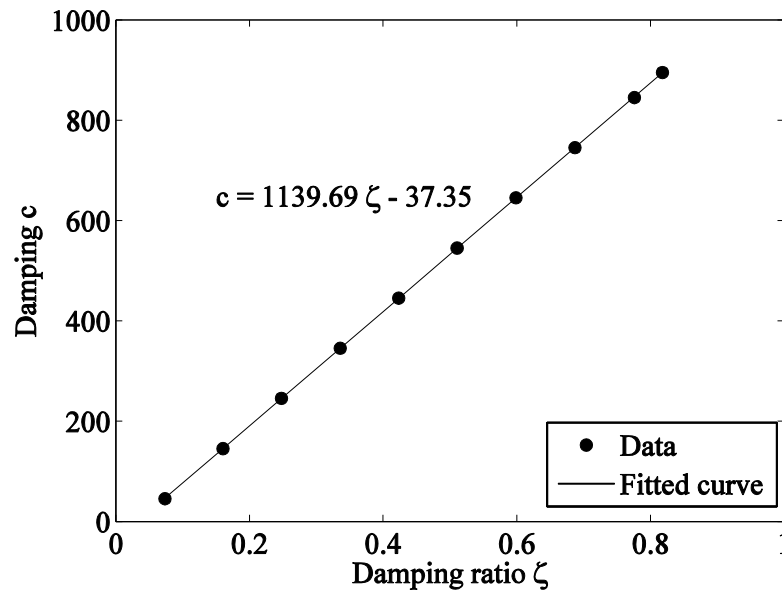


Figure 5.2. Determination of the critical damping value of the fundamental mode of the system

Instead of utilizing the procedure explained above, the critical damping value  $c_{cr}$  can be determined approximately by obtaining the damped period  $T_d$  from the response. Then, the damped circular frequency  $\omega_d$  in rad/s is calculated, and the corresponding damping ratio  $\zeta$  can be obtained by  $\omega_d = \omega_n \sqrt{1 - \zeta^2}$ . Hence, the critical damping value  $c_{cr}$  is calculated by  $c_{cr} = \frac{c}{\zeta}$ . It was preferred to utilize moderate or high damping values to prevent numerical errors while calculating  $\zeta$ .

#### 5.4. Hybrid-Controlled Building Model

In the present research, a hybrid control system, which is constituted from a passive controller (elastomeric bearings) and a semi-actively controlled hydraulic

damper, was designed. The damper was connected in parallel to the base isolator. In a similar research, the MRD was activated only when the base drift exceeded 50 per cent of the isolator displacement capacity (Ribakov & Gluck, 2002). In the present simulations, the displacement limit of the base to start the control scheme was 0.03 m. If the base displacement had been smaller than this value, then a control action would not have been applied. In this case, the damping of the VOD was set to the minimum value. It is physically not possible to completely remove the damper when control action is not applied.

The hybrid-controlled structure is presented in Figure 5.3. It has one base and three stories. Elastomeric base isolators were utilized at the base. A semi-active VOD in parallel to the base isolation system was attached between the base and the ground.

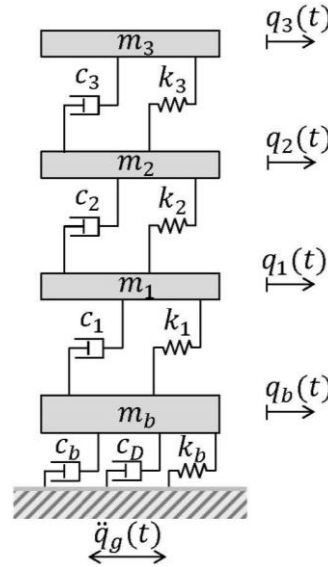


Figure 5.3. Hybrid-controlled building model (including base isolation and VOD)

In Figure 5.3,  $m_b$  and  $m$  are the base and floor masses.  $c_b$  and  $c_i$  are the base and floor damping.  $k_b$  and  $k_i$  are the base and floor stiffness for  $i = 1, 2, 3$ . The equation of motion with respect to the ground is as follows

$$\mathbf{M}_s \ddot{\mathbf{q}}_s(t) + \mathbf{f}[\mathbf{q}_s(t), \dot{\mathbf{q}}_s(t)] \dot{\mathbf{q}}_s(t) + \mathbf{K}_s \mathbf{q}_s(t) = -\mathbf{M}_s \mathbf{h}_1 \ddot{q}_g(t) \quad (5.3)$$

where  $\mathbf{q}_s(t)$  is the displacement vector of the hybrid controlled structure relative to the ground.  $\mathbf{M}_s$  and  $\mathbf{K}_s$  are the mass and stiffness matrices, respectively.  $\ddot{q}_g(t)$  is the process noise (disturbance), which is the ground acceleration in the current problem.  $\mathbf{h}_1$

is the location matrix of the external excitation. It specifies how the ground excitation  $\ddot{q}_g$  enters into the system. It is equal to  $(1 \ 1 \ 1 \ 1)^T$ , indicating that the ground excitation acts to all degrees of freedom.

The term  $\mathbf{f}[\mathbf{q}_s(t), \dot{\mathbf{q}}_s(t)]$  indicates that the damping of the structure depends directly on the displacement and velocity of the base by the upper controller. Additionally, it is based on the displacements and velocities of the superstructure indirectly. Therefore, the system is nonlinear.

The isolated structure and VOD contribute to the damping force in Equation (5.3), which is indicated by  $\mathbf{f}[\mathbf{q}_s(t), \dot{\mathbf{q}}_s(t)] \dot{\mathbf{q}}_s(t)$ . Nonlinearity arises from the VOD, which can be assumed to be a passive damper for every orifice opening size. In the light of this fact, linear system approach can be applied to the structure in smaller constant damping ranges restricted by the damping value of the VOD. Then, the nonlinear system in Equation (5.3) can be regarded as a composition of linear systems at different operating points. The transition among different damping values of the VOD is performed by the gain scheduling technique (see Section 5.6 for details). Thus, the equation of motion in Equation (5.3) is transformed into the following equation.

$$\mathbf{M}_s \ddot{\mathbf{q}}_s(t) + \mathbf{C}_s \dot{\mathbf{q}}_s(t) + \mathbf{K}_s \mathbf{q}_s(t) = -\mathbf{M}_s \mathbf{h}_1 \ddot{q}_g(t) \quad (5.4)$$

In Equation (5.4),  $\mathbf{C}_s$  is the damping matrix of the isolated structure including VOD and is presented in Equation (5.6). Assembly of the global mass, damping, and stiffness matrices of the isolated structure was performed in Section 4.7.2. The mass, stiffness, and damping matrices of the isolated structure are presented in Equation (4.38). They are as follows

$$\begin{aligned}
\mathbf{M}_s &= \begin{bmatrix} 154.5 & 0 & 0 & 0 \\ 0 & 103 & 0 & 0 \\ 0 & 0 & 100 & 0 \\ 0 & 0 & 0 & 99.5 \end{bmatrix} kg \\
\mathbf{K}_s &= \begin{bmatrix} 78706 & -78000 & 0 & 0 \\ -78000 & 156000 & -78000 & 0 \\ 0 & -78000 & 156000 & -78000 \\ 0 & 0 & -78000 & 78000 \end{bmatrix} N/m \\
\mathbf{C}_s &= \begin{bmatrix} 54.53 & -9.1 & 0 & 0 \\ -9.1 & 30.88 & -9.1 & 0 \\ 0 & -9.1 & 30.51 & -9.1 \\ 0 & 0 & -9.1 & 21.35 \end{bmatrix} \frac{Ns}{m}
\end{aligned} \tag{5.5}$$

The portions of the matrices related with common DOFs at the interface between subsystems include contributions from both subsystems. The damping value of the VOD is added to the related DOF of the damping matrix of the isolated structure in Equation (5.5) for the hybrid controlled structure, as follows

$$\mathbf{C}_s = \begin{bmatrix} 54.53 + c_D & -9.1 & 0 & 0 \\ -9.1 & 30.88 & -9.1 & 0 \\ 0 & -9.1 & 30.51 & -9.1 \\ 0 & 0 & -9.1 & 21.35 \end{bmatrix} \frac{Ns}{m} \tag{5.6}$$

The matrix  $\mathbf{C}_s$  includes a varying value  $c_D$ , which is the damping value of the VOD. Its numerical values were assigned as: 100, 200, 300, 400, 500, 600, 700, 800, 900, 1000, 1500, 2000, 2500, 3000, 10000, 15000, 20000, and 25000 Ns/m (see Section 5.3). The equation of motion of the hybrid controlled structure in Equation (5.4) is transformed into a first order state-space representation as follows

$$\begin{bmatrix} \dot{\mathbf{x}}_s(t) \\ \mathbf{q}_s(t) \\ \dot{\mathbf{q}}_s(t) \end{bmatrix} = \underbrace{\begin{bmatrix} \mathbf{0} & \mathbf{I} \\ -\mathbf{M}_s^{-1}\mathbf{K}_s & -\mathbf{M}_s^{-1}\mathbf{C}_s \end{bmatrix}}_{\mathbf{A}_s} \begin{bmatrix} \mathbf{x}_s(t) \\ \mathbf{q}_s(t) \\ \dot{\mathbf{q}}_s(t) \end{bmatrix} + \underbrace{\begin{bmatrix} \mathbf{0} \\ \mathbf{0} \\ -\mathbf{h}_1 \end{bmatrix}}_{\mathbf{G}_s} \overbrace{w_s(t)}^{\dot{q}_g(t)} \tag{5.7}$$

where  $\mathbf{x}_s(t)$  is the state vectors.  $w_s(t)$  is the disturbance.  $\mathbf{A}_s$  is the state matrix.  $\mathbf{G}_s$  is the disturbance vector. The state-space representation of the system was constituted by the equation of motion of the model structure remaining in the linear region. In all formulations, the states were chosen as the floor displacements and velocities relative to the ground. There is not an explicit control input to the system since the control effect is applied by changing the damping value of the VOD. The floor displacements and the

damper force were assumed to be sensed. The measurement equation of the hybrid controlled structure is as follows

$$\overbrace{\begin{bmatrix} q_{1noisy}(t) \\ q_{2noisy}(t) \\ q_{3noisy}(t) \\ q_{4noisy}(t) \\ f_{Dnoisy}(t) \end{bmatrix}}^{\mathbf{y}_s(t)} = \overbrace{\begin{bmatrix} \mathbf{I}_{4 \times 4} & \mathbf{0}_{4 \times 4} \\ \mathbf{0}_{1 \times 4} & -c_D \ 0 \ 0 \ 0 \end{bmatrix}}^{\mathbf{D}_s} \mathbf{x}_s(t) + \mathbf{v}(t) \quad (5.8)$$

where  $\mathbf{y}_s(t)$  and  $\mathbf{D}_s$  are the measurements and its matrix, respectively.  $\mathbf{v}(t)$  is the measurement noise. The measured terms contain some amount of measurement noise  $\mathbf{v}(t)$ . In order to distinguish between the states and the measured terms, the subscript *noisy* was added. On the other hand, the measurement vector  $\mathbf{y}_s(t)$  does not have a subscript *noisy* since it is well-known that it contains noisy terms.

In the simulations, the observer and regulator was designed priori to the calculations of the responses. Therefore, the stiffness of the isolators was assumed to be a constant value and was not determined hysteretically. On the other hand, if the isolator properties had been determined hysteretically, then a constant stiffness would have used for the priori designs and hysteretic values would have been utilized for the response calculations. This remedy corresponded to the special architecture of the code within MATLAB. The responses would not have differed dramatically in constant and hysteretic stiffness cases. Therefore, the choice of constant stiffness would not effect the responses significantly (see Section 4.7.1).

The undamped periods and frequencies of the base isolated structure are presented in Table 4.5. The original data of the Imperial Valley event in the frequency domain is presented in Figure 4.25. As long as the expected seismic excitations obey the frequency trends as shown in Figure 4.25, the isolated structure does not require any further design consideration. If a near-fault earthquake occurs, on the other hand, then the isolated structure is likely to be excited by large amplitudes of motion as can be depicted from Figure 5.17 and Figure 5.18. At this stage, the significance of a VOD becomes apparent. It can be adjusted to have small damping in the case of small amplitude vibrations, or large damping in the case of large magnitude vibrations.

## 5.5. Linear Quadratic Gaussian (LQG) Control of the VOD

At the early stages of the current study, different control methods were applied for the VOD mounted structure. The controller studies started with the LQR method. In case of near-field seismic excitation, there were some unacceptable single peaks in the displacements of LQR. Then, the on-off control was implemented in place of LQR. The absolute floor accelerations were too high in near-source seismic data case. Later,  $H_2$ /LQG control was applied. The problem was similar to the one in the on-off control. Finally, the route was oriented towards the LQG control. Besides, in real-world applications with state feedback control all the states of the system have to be known. Nevertheless, quite often it is not practical or possible to measure all the states. This fact motivates the researchers to employ observers in the control of civil engineering structures, in which some of the states have to be estimated from the measurements. Therefore, in the present study, special attention was paid for the subject of observers in the context of the LQG control.

In stochastic optimal control, inclusion of Gaussian disturbance and measurement noise into the system definition convert the problem from a deterministic LQR design into a LQG control. In some cases, it is not possible to access all the states. Hence, they are not available for feedback. Therefore, they have to be estimated from measurements. The LQG algorithm is a combination of a linear quadratic estimator (LQE) and a LQR. Independent design and computation of two stages are guaranteed by the *separation principle* (Başar et al., 1998). Brezinski (2002) divides the optimal feedback control for a linear stochastic system into two designs: the optimal observer to estimate the states of the system and the optimal deterministic controller which is fed by the observed states.

Additionally, the controller is fed by the observed states assuming that they are the actual ones since the system state is not completely accessible, which is known as the *certainty equivalence principle* (Bosgra & Kwakernaak, 2001). The observer and controller are designed individually. Then, they are combined by the feedback relation  $\mathbf{u}(t) = -\mathbf{K}\hat{\mathbf{x}}(t)$  (for a time-invariant system). For a time-invariant continuous-data linear system

$$\dot{\mathbf{x}}(t) = \mathbf{A}\mathbf{x}(t) + \mathbf{B}\mathbf{u}(t) + \mathbf{G}\mathbf{w}(t) \quad (5.9)$$

whose measurement equation is as follows

$$\mathbf{y}(t) = \mathbf{D}\mathbf{x}(t) + \mathbf{v}(t) \quad (5.10)$$

where  $\mathbf{A}, \mathbf{B}, \mathbf{G}$  and  $\mathbf{D}$  are the state, input, disturbance, and measurement matrices, respectively.  $\mathbf{x}(t), \mathbf{u}(t)$  and  $\mathbf{w}(t)$  are the state, input and disturbance vectors, respectively.  $\mathbf{y}(t)$  and  $\mathbf{v}(t)$  are the measurement vector and its noise, respectively.

A stochastic observer may be assumed to be in the form of the state equation (5.9) since it will reproduce the state by an arbitrary precision (Bosgra & Kwakernaak, 2001). Nevertheless, the disturbances cannot be included to a conventional stochastic observer system since they are not known during the event. The definitions of the variables in Equations (5.9) and (5.10) are presented in Table 5.3.

$$\dot{\hat{\mathbf{x}}}(t) = \mathbf{A}\hat{\mathbf{x}}(t) + \mathbf{B}\mathbf{u}(t) + \mathbf{L}(\mathbf{y}(t) - \hat{\mathbf{y}}(t)) \quad (5.11)$$

with a measurement equation without measurement noise, as follows

$$\hat{\mathbf{y}}(t) = \mathbf{D}\hat{\mathbf{x}}(t) \quad (5.12)$$

where  $\hat{\mathbf{x}}(t)$  is the observer state vector that represents the estimate of  $\mathbf{x}(t)$ . The extra input term in Equation (5.11) is the measurement error term  $\mathbf{y}(t) - \hat{\mathbf{y}}(t)$ . It provides a correction, and the correction is active until the estimation error becomes zero.  $\mathbf{L}$  is the observer gain, which is a weighting matrix that relates the error in the measured values to the state estimates. This correction is the key idea of the observer. Substituting the observer measurement equation into the observer system yields the common form of the observer system as

$$\dot{\hat{\mathbf{x}}}(t) = \overbrace{(\mathbf{A} - \mathbf{L}\mathbf{D})}^{\hat{\mathbf{A}}}\hat{\mathbf{x}}(t) + \mathbf{B}\mathbf{u}(t) + \mathbf{L}\mathbf{y}(t) \quad (5.13)$$

where  $\hat{\mathbf{A}}$  is the state matrix of the observer.

The observer differential equation presented in Equations (5.11) or (5.13) is similar to the system differential equation in Equation (5.9) with an additional weighted

error term of the measured values. The control input is the same in both equations. But, the disturbances are not fed into the observer system equation since they are not known.

In the present work, the observer gain was obtained by the Kalman-Bucy filter, which is a stochastic predictor-corrector type estimator. It is optimal in the sense of minimizing the expected value of the squared state estimation error (Equation (C.13)). It also filters out sensor noise from the measurements.

The independence of the observer and the controller design is shown for the system in Equations (5.9) and (5.10). A full-state feedback is combined with a Kalman-Bucy filter. The states of the resultant closed loop system are composed of the actual states  $\mathbf{x}(t)$  and the estimation error  $\mathbf{e}(t) = \mathbf{x}(t) - \hat{\mathbf{x}}(t)$  (Equation (C.7)). The fundamental aim of any observer is estimating the actual states properly. Therefore, the estimation error is chosen as a convenient tool to exhibit the system behavior. In Kalman filter design, the performance index to be minimized is chosen in terms of the estimation error (Equation (C.13)). Substitution of the feedback law  $\mathbf{u}(t) = -\mathbf{K}\hat{\mathbf{x}}(t)$  and  $\hat{\mathbf{x}}(t) = \mathbf{x}(t) - \mathbf{e}(t)$  into Equation (5.9) yields

$$\dot{\mathbf{x}}(t) = (\mathbf{A} - \mathbf{BK})\mathbf{x}(t) + \mathbf{BK}\mathbf{e}(t) + \mathbf{G}\mathbf{w}(t) \quad (5.14)$$

The error system is performed by subtracting Equation (5.13) from Equation (5.9). Then, the measurement equation in Equation (5.10) is plugged into it, and the error system appears as in the following form,

$$\dot{\mathbf{e}}(t) = (\mathbf{A} - \mathbf{LD})\mathbf{e}(t) + \mathbf{G}\mathbf{w}(t) - \mathbf{L}\mathbf{v}(t) \quad (5.15)$$

Collecting Equations (5.14) and (5.15) in matrix form yields

$$\begin{bmatrix} \dot{\mathbf{x}}(t) \\ \dot{\mathbf{e}}(t) \end{bmatrix} = \overbrace{\begin{bmatrix} \overbrace{\mathbf{A} - \mathbf{BK}}^{A_{cl}} & \mathbf{BK} \\ \mathbf{0} & \underbrace{\mathbf{A} - \mathbf{LD}}_{\hat{\mathbf{A}}} \end{bmatrix}}^{\bar{\mathbf{A}}} \begin{bmatrix} \mathbf{x}(t) \\ \mathbf{e}(t) \end{bmatrix} + \begin{bmatrix} \mathbf{G} \\ \mathbf{G} \end{bmatrix} \mathbf{w}(t) + \begin{bmatrix} \mathbf{0} \\ -\mathbf{L} \end{bmatrix} \mathbf{v}(t) \quad (5.16)$$

Dynamics of the system in Equation (5.16) is governed by the eigenvalues of the coefficient matrix  $\bar{\mathbf{A}}$  of the homogeneous part of the equation. The characteristic equation of the system is the product of the characteristic equations of the regulator and

observer since  $\bar{\mathbf{A}}$  is a triangular matrix. Thus, the controller and the observer are independent of each other (Bosgra & Kwakernaak, 2000; Schemmann, 1997; Brezinski, 2002). Additionally, stability of the LQG controller is validated by the asymptotical stability of two independent subsystems whose eigenvalues should have strictly negative real parts.

### 5.5.1. Kalman Observer

While controlling the seismic response of the civil engineering structures, some of the states have to be estimated from the measurements since quite often it is not practical or possible to measure all the states. At the former simulations of the Kalman-Bucy filter, it was not possible to obtain the desired ratio between the poles of the observer and the system for all the modes of the base-isolated and damped structure (see Equation (5.22)). Some of the modes were not possible to speed up, while others were extremely fast. The slow modes were undesired because they may have been too slow to approach the true modes. The fast modes were unacceptable due to stability constraints. The remedies were investigated, which did not increase the frequencies of the slower modes (see Section 5.5.2). Thus, for the numerical simulations, it was decided to constitute a Kalman-Bucy filter functionality instead of utilizing the Kalman-functionality within MATLAB. For this purpose, the present subsection was formed to increase the understanding on the inner dynamics of the Kalman-Bucy filter. The derivation of the Kalman filter, which was a discrete-time formulation, was presented in Appendix C. In the present research, continuous-time systems are dealt with. Therefore, after deriving the Kalman observer, the Kalman-Bucy filter for continuous-time problems was obtained from a limiting process of the Kalman estimator. The details were presented in Appendix B and D.

An *observer* is an algorithm utilized to estimate the states of the system. If the dimensions of the system and the observer state vectors are of the same size, then it is a *full-order observer*, which is the case for a Kalman filter. Otherwise, it is a *reduced-order observer*.

If a system is *deterministic*, then it does not contain any randomness while evolving the future states of the system. It gives the same output for a certain input starting from a certain set of initial conditions. In reality, the process may be corrupted

by some unwanted input signals, as *disturbance (process noise)*. Additionally, some measurements may be required, and measurements are corrupted by some degree of noise, biases, and device inaccuracies. Then the system turns into a *stochastic* one. An observer may be deterministic as a *Luenberger observer* or may be stochastic leading to the Kalman or Kalman-Bucy filter (Meirovitch, 1989).

In 1960, Rudolf Emil Kalman represented a recursive solution to the discrete-data linear filtering and prediction problems (Kalman, 1960). One year later, Kalman and Bucy extended the formulation for continuous-time linear systems (Kalman & Bucy, 1961). The fundamental problem is to predict the internal states of a linear system by accessing only to the noisy sensor measurements. The Kalman and Kalman-Bucy filters perform stochastic estimates, which are optimal in the sense of minimizing the state estimation error covariance under predefined noise covariances (Meirovitch, 1989; Welch & Bishop, 2001).

The system utilized in Chapter 5 is time-invariant for each orifice opening of the VOD. However, during the derivation of the Kalman filter, a time-variant formulation was preferred to prevent any knowledge loss that might appear due to the assumption of the system being time-invariant. At the final stage, the formulation is adopted for the time-invariant system.

For a linear time-variant system, the process to be estimated is presented as a linear combination of the previous state  $\mathbf{x}_{j-1}$ , control input  $\mathbf{u}_{j-1}$ , and process noise  $\mathbf{w}_{j-1}$  in discrete-time.

$$\mathbf{x}_j = \Phi_{j-1}\mathbf{x}_{j-1} + \Gamma_{j-1}\mathbf{u}_{j-1} + \Lambda_{j-1}\mathbf{w}_{j-1} \quad (5.17)$$

whose measurement model is as follows

$$\mathbf{y}_j = \mathbf{H}_j\mathbf{x}_j + \mathbf{v}_j \quad (5.18)$$

The linear stochastic time-variant plant model is summarized in Table 5.2 for continuous- and discrete-time cases. The definitions of the variables are presented in Table 5.3. The subscript  $j$  indicates the  $j$ th time step.

Table 5.2. Linear time-variant plant and measurement models

Model	Continuous-time	Discrete-time
Process	$\dot{\mathbf{x}}(t) = \mathbf{A}(t)\mathbf{x}(t) + \mathbf{B}(t)\mathbf{u}(t) + \mathbf{G}(t)\mathbf{w}(t)$	$\mathbf{x}_j = \Phi_{j-1}\mathbf{x}_{j-1} + \Gamma_{j-1}\mathbf{u}_{j-1} + \Lambda_{j-1}\mathbf{w}_{j-1}$
Measurement	$\mathbf{y}(t) = \mathbf{D}(t)\mathbf{x}(t) + \mathbf{v}(t)$	$\mathbf{y}_j = \mathbf{H}_j\mathbf{x}_j + \mathbf{v}_j$
Process noise	$E\{\mathbf{w}(t)\} = 0$ $E\{\mathbf{w}(t)\mathbf{w}^T(\tau)\} = \mathbf{Q}(t)\delta(t - \tau)$	$E\{\mathbf{w}_j\} = 0$ $E\{\mathbf{w}_j\mathbf{w}_i^T\} = \mathbf{Q}_j\Delta(j - i)$
Measurement noise	$E\{\mathbf{v}(t)\} = 0$ $E\{\mathbf{v}(t)\mathbf{v}^T(\tau)\} = \mathbf{R}(t)\delta(t - \tau)$	$E\{\mathbf{v}_j\} = 0$ $E\{\mathbf{v}_j\mathbf{v}_i^T\} = \mathbf{R}_j\Delta(j - i)$

Table 5.3. Definitions of terms in Table 5.2

Continuous-time		Discrete-time		Dimension
$\mathbf{x}$	State vector	$\mathbf{x}_j$	State vector at time $t_j$	$n_x \times 1$
$\mathbf{A}$	State matrix	$\Phi_{j-1}$	Matrix transforms the previous state to the current state in the absence of either a forcing function or process noise	$n_x \times n_x$
$\mathbf{B}$	Control input matrix	$\Gamma_{j-1}$	Control input matrix at time $t_{j-1}$	$n_x \times n_u$
$\mathbf{u}$	Control input vector	$\mathbf{u}_{j-1}$	Control input vector at time $t_{j-1}$	$n_u \times 1$
$\mathbf{G}$	Disturbance matrix	$\Lambda_{j-1}$	Disturbance matrix at time $t_{j-1}$	$n_x \times n_w$
$\mathbf{w}$	Disturbance	$\mathbf{w}_{j-1}$	Process noise (disturbance) at time $t_{j-1}$	$n_w \times 1$
$\mathbf{y}$	Measurement	$\mathbf{y}_j$	Measurement at time $t_j$	$n_y \times 1$
$\mathbf{D}$	Measurement matrix	$\mathbf{H}_j$	Matrix describing the noiseless connection between the measurement and the state vector at $t_j$	$n_y \times n_x$
$\mathbf{v}$	Measurement noise	$\mathbf{v}_j$	Measurement noise at time $t_j$	$n_y \times 1$
$\mathbf{Q}$ $\mathbf{R}$	Positive-definite covariance matrices of process and measurement noises	$\mathbf{Q}_j$ $\mathbf{R}_j$	Positive-definite covariance matrices of process and measurement noises	$n_x \times n_x$ $n_u \times n_u$
$\delta$	Dirac delta function	$\Delta$	Kronecker delta function	$1 \times 1$

The main idea of the Kalman observer is similar to the one presented in Equation (5.11). Distinctively, it is not a single-step algorithm, it is a *predictor-corrector* type algorithm. Firstly, a priori predictions  $\hat{\mathbf{x}}_j^-$  and  $\mathbb{P}_j^-$  for the state estimate and estimation error covariance are performed by means of the estimates of the previous step,  $\hat{\mathbf{x}}_{j-1}$  and  $\mathbb{P}_{j-1}$ . Then, these estimates are corrected or improved by performing an actual measurement  $\mathbf{y}_j$  at the current step. The actual measurements correct the predicted state by adding the residual weighted by a gain factor  $\mathbf{L}_j$ . A similar improvement is performed for the estimate error covariance. The steps of the Kalman

estimator are summarized in Figure 5.4 (see Appendix C for a detailed explanation of equations displayed in Figure 5.4).

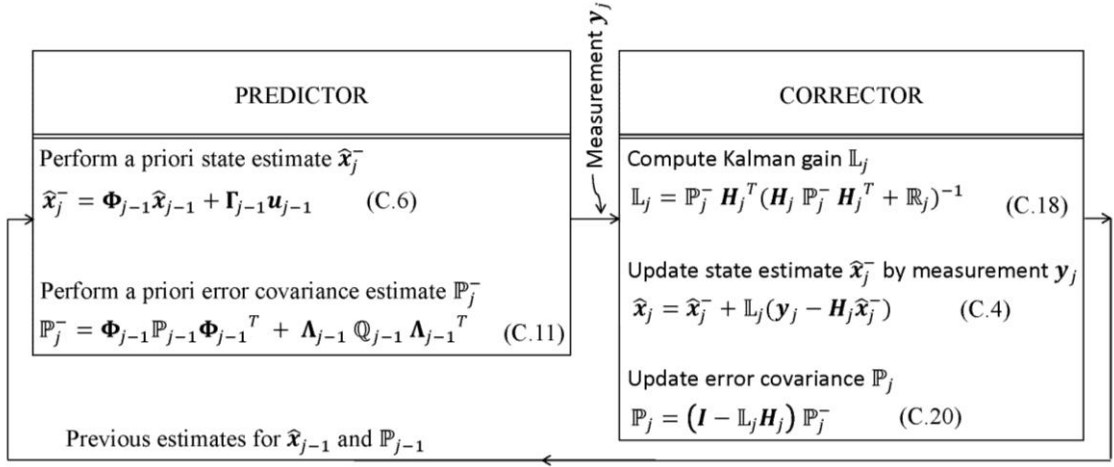


Figure 5.4. Kalman filter (discrete-time) (The equation numbers belong to Appendix C) (Source: Welch & Bishop, 2001)

In the current optimization problem, it is desired to determine optimal state estimates. Therefore, a state error, which is the difference between the real and predicted states, would be the most feasible variable to be utilized in the cost function. Therefore, the heart of the Kalman observer design, the gain  $\mathbb{L}_j$ , is determined by minimizing the expected value of the squared state estimation error. The computational origins of the Kalman filter are presented in Appendix C. The Kalman gain is as,

$$\mathbb{L}_j = \mathbb{P}_j^- \mathbf{H}_j^T (\mathbf{H}_j \mathbb{P}_j^- \mathbf{H}_j^T + \mathbb{R}_j)^{-1} \quad (5.19)$$

where  $\mathbb{P}_j^-$  is the covariance matrix of the error of the a priori state estimate. Furthermore, the statistical assumptions of the Kalman filter can be summarized as follows:

- The initial state has a known mean and covariance.
- The disturbance and measurement noise sequences  $\mathbf{w}_j$  and  $\mathbf{v}_j$  are white (spectrally) and zero-mean (statistically) random signals with known autocorrelation of

$$E\{\mathbf{w}_j \mathbf{w}_i^T\} = \mathbb{Q}_j \Delta(j - i) \quad (5.20)$$

$$E\{\mathbf{v}_j \mathbf{v}_i^T\} = \mathbb{R}_j \Delta(j - i)$$

where  $\mathbb{Q}_j$  and  $\mathbb{R}_j$  are positive-definite covariance matrices.

- The initial state (or the initial state error) and two noise sequences are uncorrelated.

$$\begin{aligned} E\{\mathbf{x}_0 \mathbf{v}_i^T\} &= \mathbf{0} & \forall i \\ E\{\mathbf{x}_0 \mathbf{w}_i^T\} &= \mathbf{0} & \forall i \\ E\{\mathbf{v}_i \mathbf{w}_j^T\} &= \mathbf{0} & \forall i, j \end{aligned} \quad (5.21)$$

The autocorrelation function of a signal  $\mathbf{n}(t)$  is  $E\{\mathbf{n}(t)\mathbf{n}^T(\tau)\} = \mathfrak{I}(t) \delta(t - \tau)$  where  $\mathfrak{I}(t)$  is the positive definite covariance matrix of the signal. If the signal is *stationary*, then spectrum of its autocorrelation function is constant, meaning that the covariance matrix does not vary with time ( $E\{\mathbf{n}(t)\mathbf{n}^T(\tau)\} = \mathfrak{I} \delta(t - \tau)$ ).

*White noise* is a random signal whose autocorrelation function (its correlation with itself over time) is a delta function, meaning that white noise is completely uncorrelated with itself at any time except for the present. The whiteness of a signal is represented by a delta function as a correlation function. In continuous-time case it is a Dirac delta function as  $\delta(t - \tau)$ , and in discrete case it is a Kronecker delta function as  $\Delta(j - i)$ .

The Kalman filter describes a *recursive* solution to the discrete-data linear filtering problem. In a recursive procedure, the key point is the use of the results of the previous step to calculate the desired result of the current step. The recursive nature is one of the attractive features of the Kalman filter in contrast to other approaches, such as the Wiener filter, in which all the past data are required to perform calculations at the current step (Brown & Hwang, 1992).

It is required to give information about the stability of the filter in steady-state case roughly. In most of the problems, within a certain period of time after starting the initiation, the Kalman filter reaches to a steady-state or quasi-steady-state case, and the gain becomes constant (Brown & Hwang, 1992). For the asymptotic stability of the Kalman-Bucy filter, the closed loop system should have eigenvalues whose real-parts are strictly negative (Williams & Lawrence, 2007).

Furthermore, the *duality* of two optimization problems (the Kalman (or Kalman-Bucy) observer and the LQR problem) was mentioned briefly: In both cases, a quadratic cost function is minimized subjected to linear dynamic constraints. The differential equations (Equation (G.13) and Equation (D.24)) and their solutions have the same shapes (Meirovitch, 1989; Williams & Lawrence, 2007; Stengel, 1994; Grewal & Andrews, 2008).

The numerical calculations were performed via the Kalman-Bucy function coded within MATLAB. The solution of the ARE in the optimization problem was performed via the MATLAB command *care* abbreviated for continuous-time ARE.

### 5.5.2. Observer Design

The fundamental design criterion for a convenient observer is the measure of the closeness of the observed responses to the simulated responses. Another design criterion is how fast its modes are compared to the modes of the original system. In the literature, it is suggested that the modes of an observer should be 2-4 times faster than those of the system (Arıkan & Ercan, 2011). Extremely fast observer modes are unacceptable due to the stability constraints. The ratio of the real parts of the poles of the observer to those of the system is defined as,

$$PoleRatio = \frac{real(eigenvalue(\hat{\mathbf{A}}))}{real(eigenvalue(\mathbf{A}))} = \frac{real(eigenvalue(\mathbf{A} - \mathbf{LD}))}{real(eigenvalue(\mathbf{A}))} \quad (5.22)$$

The real component is responsible for determining how fast the response approaches to zero while the imaginary part creates the oscillatory behavior (see Appendix F). Therefore, the ratio of the real parts of the poles is chosen as the decision criterion for the observer design.

For the Kalman-Bucy filter, the noise variances  $\mathbf{Q}$  and  $\mathcal{R}$  were selected in such a way that the variable *PoleRatio* was aimed to be in the range of 2-4. At the former simulations of the current study, it was not possible to obtain this ratio for all the modes of the base-isolated and damped structure. Some modes were not possible to speed up (*PoleRatio*~1), while others were extremely fast (*PoleRatio*~30 to 120). This fast ratio was unacceptable due to stability constraints. On the other hand, slow modes of the observer were undesired (*PoleRatio* < 1). Various  $\mathbf{Q}$  and  $\mathcal{R}$  values were examined,

nevertheless any desirable result was not obtained to increase the frequencies of the slower modes of the observer. This may have been due to the fact that a convenient observer was searched in a range that was limited by the  $\mathbf{Q} - \mathcal{R}$  couples tried.

### 5.5.2.1. Modification of the Kalman-Bucy Observer

In the present study, an observer similar to the one in Equation (5.13) is designed for the hybrid-controlled building model in Equation (5.7). There are not any explicit control inputs to the system since the control effect is applied by changing the damping value of the VOD.

$$\begin{aligned}\dot{\hat{\mathbf{x}}}(t) &= \hat{\mathbf{A}}\hat{\mathbf{x}}(t) + \mathbf{L}\mathbf{y}(t) \\ \hat{\mathbf{y}}(t) &= \mathbf{D}\hat{\mathbf{x}}(t)\end{aligned}\tag{5.23}$$

where  $\hat{\mathbf{x}}(t)$  is the observer state.  $\hat{\mathbf{A}}$  is the state matrix of the observer as  $\hat{\mathbf{A}} = \mathbf{A} - \mathbf{L}\mathbf{D}$  where  $\mathbf{L}$  is the gain matrix of the Kalman-Bucy observer.  $\mathbf{y}(t)$  is the vector of measured values.

In a regular Kalman-Bucy observer, the disturbances are not fed into the observer system equation since they are not known. On the other hand, in structural engineering applications, this is not the case. The ground excitation can be recorded and be sent to the observer in addition to the measurements during the event. While recording, measurement noise is included to the disturbance. The observer system in Equation (5.23) is modified to reflect this special feature as follows

$$\begin{aligned}\dot{\hat{\mathbf{x}}}(t) &= \hat{\mathbf{A}}\hat{\mathbf{x}}(t) + \mathbf{G}w_{noisy}(t) + \mathbf{L}\mathbf{y}(t) \\ \hat{\mathbf{y}}(t) &= \mathbf{D}\hat{\mathbf{x}}(t)\end{aligned}\tag{5.24}$$

The term  $w_{noisy}(t)$  in Equation (5.24) indicated this unusual noisy disturbance case. In the present simulations, the observer was designed for the sub-structured base and superstructure, separately (see Section 5.5.3 and 5.5.5.1 for details).

The floor responses of the superstructure were observed in absence of a controller to validate the enhancement of the modification of the Kalman-Bucy filter. It was aimed to focus only on the distinction which arose by modification of the observer.

Therefore, the superstructure was utilized instead of the isolated structure to design an observer with desired poles (for the diagonalized superstructure).

The responses of the two observers were compared with the simulated responses. The two observers were the original and modified Kalman-Bucy estimators. The displacements and velocities of the first floor are presented in Figure 5.5 and Figure 5.6 for the Imperial Valley and Düzce earthquakes, respectively.

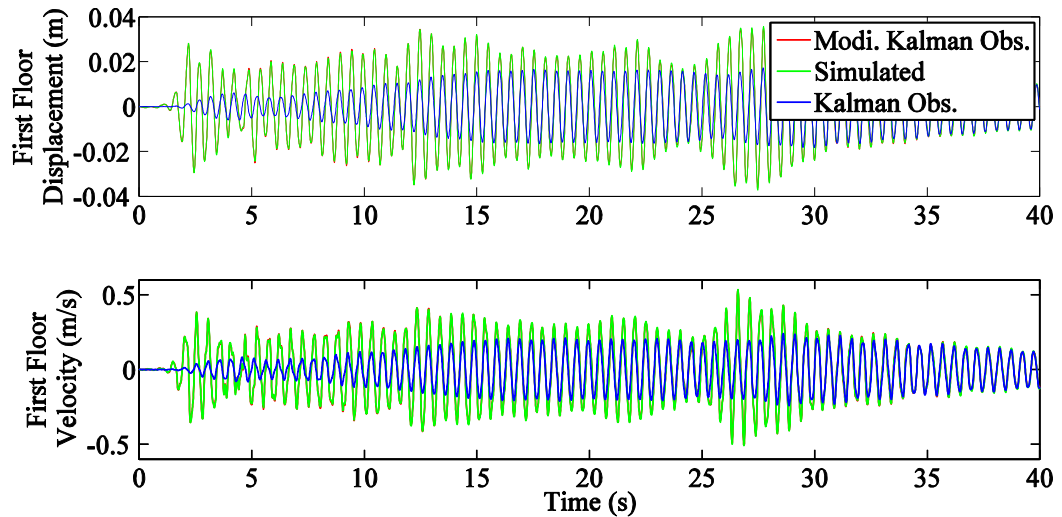


Figure 5.5. The first floor responses due to the Imperial Valley event (only superstructure and no control action)

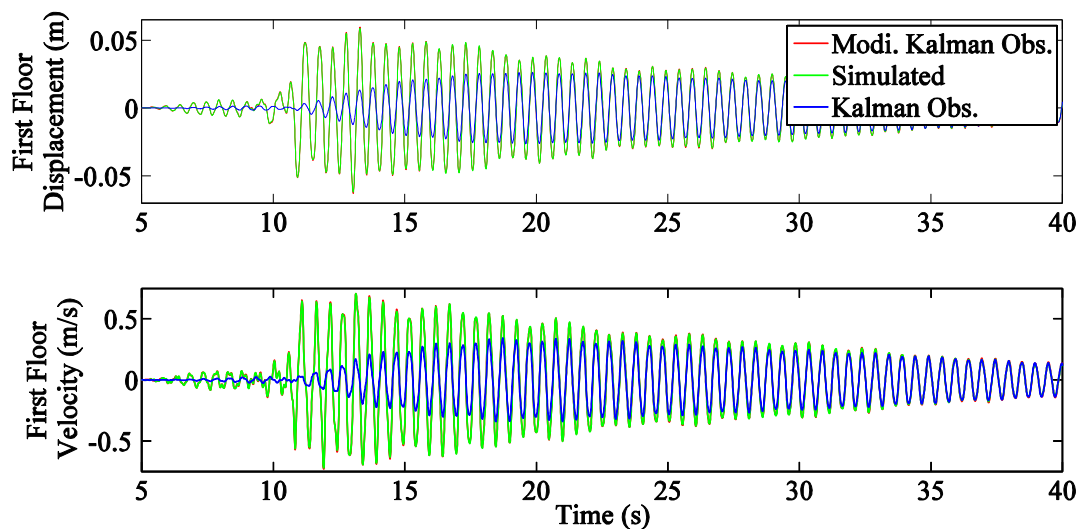


Figure 5.6. The first floor responses due to the Düzce event (only superstructure and no control action)

The same  $Q - \mathcal{R}$  couple and the same observer gain matrix  $L$  were utilized for the conventional and modified observers.  $Q = 1$  for the disturbance and  $\mathcal{R}$  had a shape of identity matrix as  $r_d \begin{bmatrix} 1 & 0 & 0 \\ 0 & 1 & 0 \\ 0 & 0 & 1 \end{bmatrix}$  for the measurement noises.  $r_d = 0.001, 0.001,$  and  $0.1$  for the three independent subsystems. An conditional loop was coded to determine a convenient  $Q - \mathcal{R}$  couple for a better observer design. The *PoleRatios* defined in Equation (5.22) are 1.04, 1.94, and 3.16 for states of the subsystems, respectively.

The responses of the conventional observer for both excitations were unacceptable. Additionally, there was some amount of phase difference in the response of the conventional observer. On the other hand, the structural response with the modified observer overlapped with the simulated response. Consequently, the enhancement of the modification of the Kalman-Bucy filter was observed.

### 5.5.2.2. Selection of $Q$ and $\mathcal{R}$ Values by Genetic Algorithms

The GA studies mentioned in the present subsection were performed only for the superstructure, not for the isolated structure. By doing this, it was aimed to encounter with the numerical difficulties step by step. Thus, in the first instance, the calculations were started by the superstructure whose damping matrix is proportional. At the end of the GA studies, even in case of proportional damping, various numerical challenges occurred in GA. Consequently, the GA studies were not utilized select a convenient  $Q - \mathcal{R}$  couple. The details about the GA studies are presented in the following lines.

In the current study, the poles of the observer could not be placed in desired ranges by convenient selection of  $Q - \mathcal{R}$  couple. Therefore, a genetic algorithms study was performed to obtain the  $Q - \mathcal{R}$  couple in such a way that *PoleRatio* values in the range of 2-4 were obtained.

In genetic algorithms (GA), the design variables which minimize the objective function are searched within the defined bounds and under some constraints. The range of the initial conditions, which the genetic algorithms start calculations, is very important. Usually, the success of a case depends on the fact that whether the selected range of the initial conditions is close to a global extremum.

In the present studies, the objective (fitness) function was chosen as the sum of square of the difference between the simulated and observed states. The design

variables were the elements of the  $\mathbf{Q}$  and  $\mathcal{R}$  matrices. *PoleRatio* was applied as the nonlinear constraint to force the GA tool to find the optimal  $\mathbf{Q}$  and  $\mathcal{R}$  matrices in such a way that the observer poles were in the desired range.

In general, the algorithm works as follows: First, the GA produces design variables within the boundaries by means of the range of the initial conditions. Then, these design variables are sent to the constraint file to check whether the constraints are satisfied. If they are fulfilled, the design variables are sent to the fitness function file. On the other hand, if they are not satisfied, then the GA should produce new design variables that satisfy the constraints.

In the present GA studies, none of the cases explained in the previous paragraph were obtained for the Kalman observer. For most of the design variables, MATLAB quitted the GA calculations due to an error that occurred in the Kalman function of MATLAB instead of trying a new set of design variables. Additional constraints were added to overcome the numerical problems in the Kalman function, and this locked the system. Therefore, some of the constraints, which were directly related with the problem, were not taken into consideration. As a result, not being able to reach any results in GAs was the motivation to derive the formulation in the appendices B, C, and D and to utilize the Kalman-Bucy function which was coded within MATLAB in the context of the present thesis.

Various remedies were conducted such as reducing the number of design variables, changing the boundaries, changing the range of the initial conditions, and changing the constraints. The results were not satisfactory. Later, the problem definition was completely changed, and the objective function was chosen as the *PoleRatio*. The results were similar to the previous ones. At the end, the GA studies were not utilized to select a convenient  $\mathbf{Q} - \mathcal{R}$  couple since global extrema could not be obtained in any of the calculations.

### **5.5.3. Substructured Form of the Building for the Observer Design: Base & Superstructure**

The observer was aimed to be designed for independent subsystems. These independent subsystems were obtained via diagonalization. On the other hand, the base isolated structure could not be diagonalized since its damping matrix was non-

proportional (see Section 3.1 and Section 5.5.5.1 for details). Therefore, the structure was sub-structured into the base and the superstructure for the observer design as in Figure 5.7. The responses were calculated for the 4-by-4 structure presented in Section 5.4.

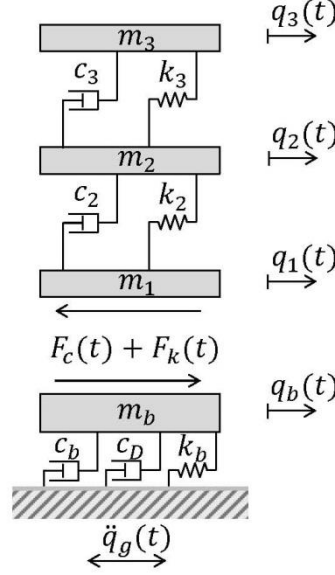


Figure 5.7. Substructured configuration of the structure for the observer design– base and superstructure

In Figure 5.7,  $m_b$  and  $m$  are the base and floor masses.  $c_b$  and  $c_i$  are the base and floor damping.  $k_b$  and  $k_i$  are the base and floor stiffness for  $i = 1, 2, 3$ . The forces emerged due to the sub-structured configuration ( $F_c = c_1(\dot{q}_1(t) - \dot{q}_b(t))$  and  $F_k = k_1(q_1(t) - q_b(t))$ ). The state-space representation of the base that is shown in Figure 5.7 is as follows

$$\dot{\mathbf{x}}_b(t) = \mathbf{A}_b \mathbf{x}_b(t) + \mathbf{G}_b \mathbf{w}_b(t)$$

$$\begin{bmatrix} \dot{q}_b(t) \\ \ddot{q}_b(t) \end{bmatrix} = \begin{bmatrix} 0 & 1 \\ \frac{-(k_b+k_1)}{m_b} & \frac{-(c_D + c_b + c_1)}{m_b} \end{bmatrix} \begin{bmatrix} q_b(t) \\ \dot{q}_b(t) \end{bmatrix} + \begin{bmatrix} 0 & 0 & 0 \\ -1 & \frac{k_1}{m_b} & \frac{c_1}{m_b} \end{bmatrix} \begin{bmatrix} \ddot{q}_g(t) \\ q_1(t) \\ \dot{q}_1(t) \end{bmatrix} \quad (5.25)$$

where  $\mathbf{x}_b(t)$ ,  $\mathbf{A}_b$ , and  $\mathbf{G}_b$  are the state vector, state matrix, and disturbance matrix of the base, respectively. The last two terms in the disturbance vector  $\mathbf{w}_b(t)$  come from the superstructure.  $k_1$  is the stiffness of the first floor.  $c_1$  is the stiffness-proportional part of

the damping of the first floor and is approximately assumed to be  $\beta k_1$ . The measurement equation is

$$\mathbf{y}_b(t) = \mathbf{D}_b \mathbf{x}_b(t) + \mathbf{v}(t)$$

$$\overbrace{\begin{bmatrix} q_{b\text{noisy}}(t) \\ f_{D\text{noisy}}(t) \end{bmatrix}}^{\mathbf{y}_b(t)} = \overbrace{\begin{bmatrix} 1 & 0 \\ 0 & -c_D \end{bmatrix}}^{\mathbf{D}_b} \mathbf{x}_b(t) + \mathbf{v}(t) \quad (5.26)$$

where  $\mathbf{y}_b(t)$  and  $\mathbf{D}_b$  are the measurements of the base and its corresponding matrix, respectively.  $\mathbf{v}(t)$  is the measurement noise. The state-space representation of the superstructure is as follows

$$\dot{\mathbf{x}}_{ss}(t) = \mathbf{A}_{ss} \mathbf{x}_{ss}(t) + \tilde{\mathbf{G}}_{ss} \tilde{\mathbf{w}}_{ss}(t)$$

$$\dot{\mathbf{x}}_{ss}(t) = \overbrace{\begin{bmatrix} \mathbf{0}_{3 \times 3} & \mathbf{I}_{3 \times 3} \\ -\mathbf{M}_{ss}^{-1} \mathbf{K}_{ss} & -\mathbf{M}_{ss}^{-1} \mathbf{C}_{ss} \end{bmatrix}}^{\mathbf{A}_{ss}} \mathbf{x}_{ss}(t) + \overbrace{\begin{bmatrix} \mathbf{0}_{3 \times 3} & \mathbf{0} \\ -1 & \mathbf{M}_{ss}^{-1} \begin{bmatrix} k_1 \\ 0 \\ 0 \end{bmatrix} \\ -1 & \mathbf{M}_{ss}^{-1} \begin{bmatrix} c_1 \\ 0 \\ 0 \end{bmatrix} \\ -1 & \mathbf{0} \end{bmatrix}}^{\tilde{\mathbf{G}}_{ss}} \overbrace{\begin{bmatrix} \ddot{q}_g(t) \\ q_b(t) \\ \dot{q}_b(t) \end{bmatrix}}^{\tilde{\mathbf{w}}_{ss}(t)} \quad (5.27)$$

where  $\mathbf{x}_{ss}(t) = [q_1(t) \quad q_2(t) \quad q_3(t) \quad \dot{q}_1(t) \quad \dot{q}_2(t) \quad \dot{q}_3(t)]^T$  is the state vector.  $\mathbf{A}_{ss}$  and  $\tilde{\mathbf{G}}_{ss}$  are the state and disturbance matrices of the superstructure, respectively. The last two terms in the disturbance vector  $\tilde{\mathbf{w}}_{ss}(t)$  comes from the formulation of the base. The *tilde* indicates that  $\tilde{\mathbf{G}}_{ss}$  and  $\tilde{\mathbf{w}}_{ss}$  in the superstructure part of the sub-structured formulation is different from  $\mathbf{G}_{ss}$  and  $\mathbf{w}_{ss}$  in the state equation of the bare superstructure (Equation (4.13)). The measurement equation is as follows

$$\tilde{\mathbf{y}}_{ss}(t) = \tilde{\mathbf{D}}_{ss} \mathbf{x}_{ss}(t) + \mathbf{v}(t)$$

$$\overbrace{\begin{bmatrix} q_{1\text{noisy}}(t) \\ q_{2\text{noisy}}(t) \\ q_{3\text{noisy}}(t) \end{bmatrix}}^{\tilde{\mathbf{y}}_{ss}(t)} = \overbrace{\begin{bmatrix} \tilde{\mathbf{D}}_{ss} \\ \mathbf{I} & \mathbf{0} \end{bmatrix}}^{\tilde{\mathbf{D}}_{ss}} \mathbf{x}_{ss}(t) + \mathbf{v}(t) \quad (5.28)$$

where  $\tilde{\mathbf{y}}_{ss}(t)$ ,  $\tilde{\mathbf{D}}_{ss}$  are the measurements and its matrix of the superstructure in the sub-structured formulation, respectively.  $\mathbf{v}(t)$  is the measurement noise. The floor displacements of the superstructure are assumed to be sensed.

### 5.5.4. Prewhitening

In practice, colored noise sources are more realistic than white noise assumption. Especially in structural engineering applications with low-frequency ground excitations, the Kalman-Bucy filter is not appropriate since it is based on white noise disturbance input.

In various examples of Kalman observer in civil structures, prewhitening was applied (Schemmann, 1997; Meirovitch, 1989). Besides, prewhitening was recommended for different applications of the Kalman observer in the literature in case of colored noises instead of white ones (Bar-Shalom et al., 2001; Grewal & Andrews, 2008).

It is not necessary for the observer to focus on the high frequencies that are not present in any ground excitation record. If it is concentrated on the earthquake-related frequencies, then its performance will be better. In this light, the plant is prewhitened by augmenting the system by a shaping filter. It is important to note that, for a prewhitened system, the observer performs better within the defined frequency range while performing worse outside of this range when compared to the original (raw) controller. The resulting system is a linear system driven by white signal (see Figure 5.8). The observer is designed for the augmented system.

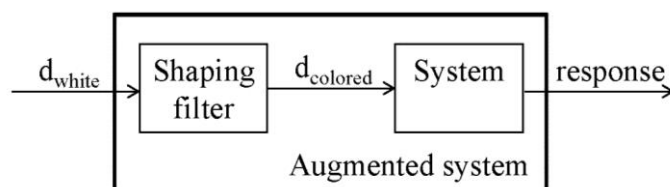


Figure 5.8. System augmented by a shaping filter for prewhitening

In the current research, all the responses were calculated with respect to the ground. Hence, the earthquake acceleration signal was applied as an input to all degrees of freedoms. At the beginning, only the base was prewhitened. The responses of the system were satisfactory. Therefore, the superstructure was not prewhitened although its input was ground excitation, which was a colored signal.

If the responses of the system had been unacceptable, then the superstructure would have been prewhitened, and the augmented superstructure would have been diagonalized to design observers for the three independent subsystems. On the other

hand, if the whole system had been prewhitened together including the base, then it would have been convenient to apply the same shaping filter to the base and to the superstructure since their input signal was the same.

The shaping filter was designed as a second-order low-pass transfer function as follows

$$\frac{\omega_c^2}{s^2 + 2\zeta\omega_c s + \omega_c^2} \quad (5.29)$$

where  $\omega_c$  is the cut-off frequency in rad/s.

In order to determine the value of  $\omega_c$ , the two different earthquake records, which were used in the present study, were sent to the filter. The smallest  $\omega_c$  value that resulted in the same output as the input was found by trial-and-success. Finally, the cut-off frequency  $\omega_c$  was specified as  $2\pi \cdot 100$  rad/s.

A filter response was desired in such a way that it converged to a resultant value as fast as possible without performing any oscillations. Therefore, an over-damped case was chosen ( $\zeta > 1.0$ ). On the other hand, if the damping ratio had been chosen to be 1.5, then the poles of the filter would have become -1645 and -240. Extremely fast modes were unacceptable due to the stability constraints. Therefore, the damping ratio was chosen 1.01 which was at the boundary of the region of the over-damped response. The damping ratio 1.01 led to poles of -724 and -546. Hence, the fastest pole got closer to the origin while the magnitude of the other pole increased. The absolute values of the poles were also high, and this case was due to the high value of the cutoff frequency. In order to investigate the response, if  $\zeta$  had been chosen as 0.5, then the poles would have been  $-314 \pm 544i$ , leading to an oscillatory behavior which was undesired in the present case (see Appendix F for the response of second-order systems). Hence, the damping ratio  $\zeta$  was chosen 1.01. The system of the applied shaping filter is as:

$$\dot{\mathbf{x}}_{SF}(t) = \overbrace{\begin{bmatrix} -1269 & -394780 \\ 1 & 0 \end{bmatrix}}^{A_{SF}} \mathbf{x}_{SF}(t) + \overbrace{\begin{bmatrix} 1 \\ 0 \end{bmatrix}}^{G_{SF}} \ddot{q}_g(t) \quad (5.30)$$

$$\underbrace{\ddot{q}_{g_{filtered}}(t)}_{y_{SF}(t)} = \underbrace{\begin{bmatrix} 0 & 394780 \end{bmatrix}}_{D_{SF}} \mathbf{x}_{SF}(t) \quad (5.31)$$

The output of the shaping filter is the filtered ground acceleration. Different shaping filters can be designed due to the needs of the random process (Grewal & Andrews, 2008). In the present example, the base in Equation (5.25) is augmented by the shaping filter defined in Equation (5.30) and Equation (5.31) for prewhitening. The ground excitation  $\ddot{q}_g(t)$  in the disturbance vector  $\mathbf{w}_b(t)$  of the base is a colored signal in Equation (5.25). Therefore, Equation (5.25) turns into the following form as,

$$\dot{\mathbf{x}}_b(t) = \mathbf{A}_b \mathbf{x}_b(t) + \overbrace{\begin{bmatrix} 0 & 0 & 0 \\ -1 & \frac{k_1}{m_b} & \frac{c_1}{m_b} \end{bmatrix}}^{\mathbf{G}_b} \overbrace{\begin{bmatrix} \mathbf{D}_{SF} \mathbf{x}_{SF}(t) \\ q_1(t) \\ \dot{q}_1(t) \end{bmatrix}}^{\mathbf{w}_b(t)} \quad (5.32)$$

Taking the term  $\mathbf{D}_{SF} \mathbf{x}_{SF}(t)$  out of the vector  $\mathbf{w}_b(t)$  yields,

$$\dot{\mathbf{x}}_b(t) = \mathbf{A}_b \mathbf{x}_b(t) + \overbrace{\begin{bmatrix} 0 \\ -1 \end{bmatrix}}^{\tilde{\mathbf{G}}_b} \mathbf{D}_{SF} \mathbf{x}_{SF}(t) + \mathbf{G}_b \begin{bmatrix} 0 \\ q_1(t) \\ \dot{q}_1(t) \end{bmatrix} \quad (5.33)$$

By collecting the systems in Equation (5.33) and Equation (5.30) in matrix form, the system of the augmented base is obtained as follows

$$\overbrace{\begin{bmatrix} \dot{\mathbf{x}}_{ab}(t) \\ \dot{\mathbf{x}}_{SF}(t) \end{bmatrix}}^{\dot{\mathbf{x}}_{ab}(t)} = \overbrace{\begin{bmatrix} \mathbf{A}_b & \tilde{\mathbf{G}}_b \mathbf{D}_{SF} \\ \mathbf{0}_{2 \times 2} & \mathbf{A}_{SF} \end{bmatrix}}^{\mathbf{A}_{ab}} \overbrace{\begin{bmatrix} \mathbf{x}_b(t) \\ \mathbf{x}_{SF}(t) \end{bmatrix}}^{\mathbf{x}_{ab}(t)} + \overbrace{\begin{bmatrix} \mathbf{G}_b & \mathbf{0}_{2 \times 1} \\ \mathbf{0}_{2 \times 3} & \mathbf{G}_{SF} \end{bmatrix}}^{\mathbf{G}_{ab}} \overbrace{\begin{bmatrix} 0 \\ q_1(t) \\ \dot{q}_1(t) \\ \ddot{q}_g(t) \end{bmatrix}}^{\mathbf{w}_{ab}(t)} \quad (5.34)$$

where  $\mathbf{A}_{ab}$  and  $\mathbf{G}_{ab}$  are the state and disturbance matrices of the base that is augmented by the shaping filter, respectively.  $\mathbf{x}_{ab}(t)$  and  $\mathbf{w}_{ab}(t)$  are the state and disturbance vector of the augmented base, respectively.  $\mathbf{x}_b(t)$ ,  $\mathbf{A}_b$ , and  $\mathbf{G}_b$  are the state vector, state matrix, and disturbance matrix of the base, respectively.  $\tilde{\mathbf{G}}_b$  is the first column of the disturbance matrix of the base.  $\mathbf{x}_{SF}(t)$ ,  $\mathbf{A}_{SF}$ , and  $\mathbf{D}_{SF}$  are the state vector, state matrix, and measurement matrix of the shaping filter, respectively.  $q_1(t)$  and  $\dot{q}_1(t)$  are displacement and velocity of the first floor of the superstructure.  $\ddot{q}_g(t)$  is the ground acceleration. The measurement equation of the augmented base system is as

$$\mathbf{y}_{ab}(t) = \mathbf{D}_{ab}\mathbf{x}_{ab}(t) + \mathbf{v}(t)$$

$$\overbrace{\begin{bmatrix} q_{b\text{noisy}}(t) \\ f_{D\text{noisy}}(t) \end{bmatrix}}^{\mathbf{y}_{ab}(t)} = \overbrace{\begin{bmatrix} \mathbf{D}_b & & & \\ 1 & 0 & 0 & 0 \\ 0 & -c_D & 0 & 0 \end{bmatrix}}^{\mathbf{D}_{ab}} \mathbf{x}_{ab}(t) + \mathbf{v}(t) \quad (5.35)$$

where  $\mathbf{y}_{ab}(t)$  and  $\mathbf{v}(t)$  are the measurement vector and its noise, respectively. The observer of the augmented base is modified as in Equation (5.24) for the ground excitation case since the earthquake shaking can be sent to the observer in a recorded form. It is presented as follows

$$\dot{\hat{\mathbf{x}}}_{ab}(t) = \overbrace{(\mathbf{A}_{ab} - \mathbf{L}_{ab}\mathbf{D}_{ab})}^{\hat{\mathbf{A}}_{ab}} \hat{\mathbf{x}}_{ab}(t) + \mathbf{G}_{ab} \overbrace{\begin{bmatrix} 0 \\ q_1(t) \\ \dot{q}_1(t) \\ \ddot{q}_{g\text{noisy}}(t) \end{bmatrix}}^{\mathbf{w}_{ab\text{noisy}}(t)} + \mathbf{L}_{ab} \overbrace{\begin{bmatrix} q_{b\text{noisy}}(t) \\ f_{D\text{noisy}}(t) \end{bmatrix}}^{\mathbf{y}_{ab}(t)} \quad (5.36)$$

$$\hat{\mathbf{y}}_{ab}(t) = \mathbf{D}_{ab}\hat{\mathbf{x}}_{ab}(t)$$

where  $\hat{\mathbf{x}}_{ab}(t)$  is the observer state vector that represents the estimate of  $\mathbf{x}_{ab}(t)$ .  $\mathbf{L}_{ab}$  is the observer gain matrix of the augmented base.  $\hat{\mathbf{y}}_{ab}(t)$  is the observer measurement vector.  $\mathbf{w}_{ab\text{noisy}}(t)$  is the disturbance vector of the observer of the augmented base.  $q_1(t)$  and  $\dot{q}_1(t)$ , on the other hand, are the inputs from the superstructure. Therefore, they do not contain any noise. The situation is similar in the superstructure formulation.

It has been emphasized earlier that the recorded earthquake acceleration were sent to the observer during simulations (see Section 5.5.2.1). Noise was added to the disturbance signal numerically due to the recording process. The subscript *noisy* in  $\mathbf{w}_{ab\text{noisy}}(t)$  indicates the unusual noisy character of the disturbance vector of the observer.

The augmented observer is focused on a smaller frequency range so that it may have a better performance within the related frequency range and may have a worse performance out of the related frequency range compared to the non-augmented system. The original and augmented systems are not identical anymore. Therefore, their simulated responses are not similar.

The responses of two observers without and with a prewhitened base were calculated to validate the enhancement of the prewhitening. The base responses are presented without and with prewhitening in Figure 5.9 and Figure 5.10 for the Imperial Valley and the Düzce earthquakes, respectively.

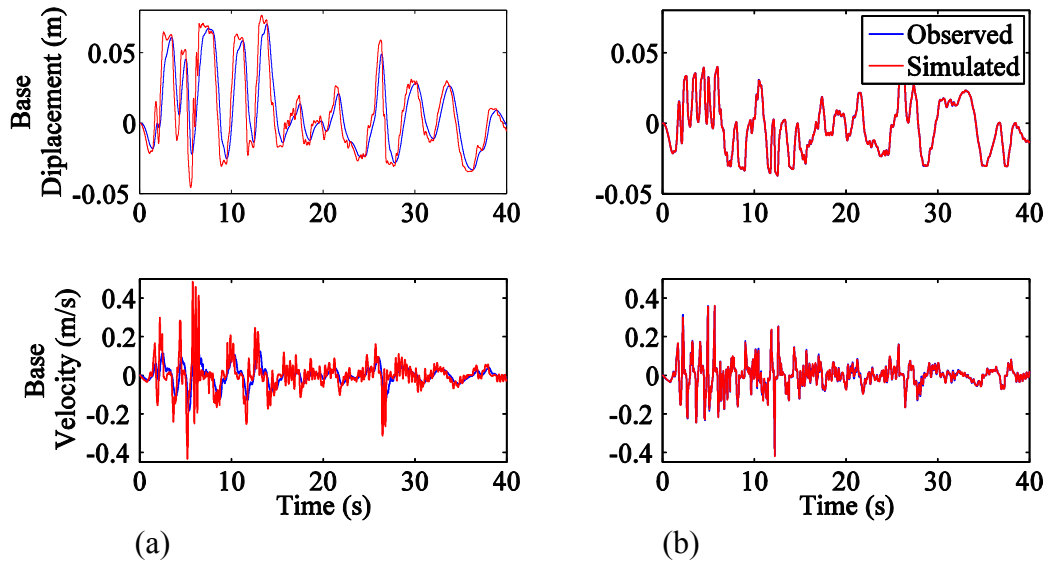


Figure 5.9. Base responses (a) prewhitening was not applied to the base and (b) prewhitening was applied to the base (the Imperial Valley earthquake)

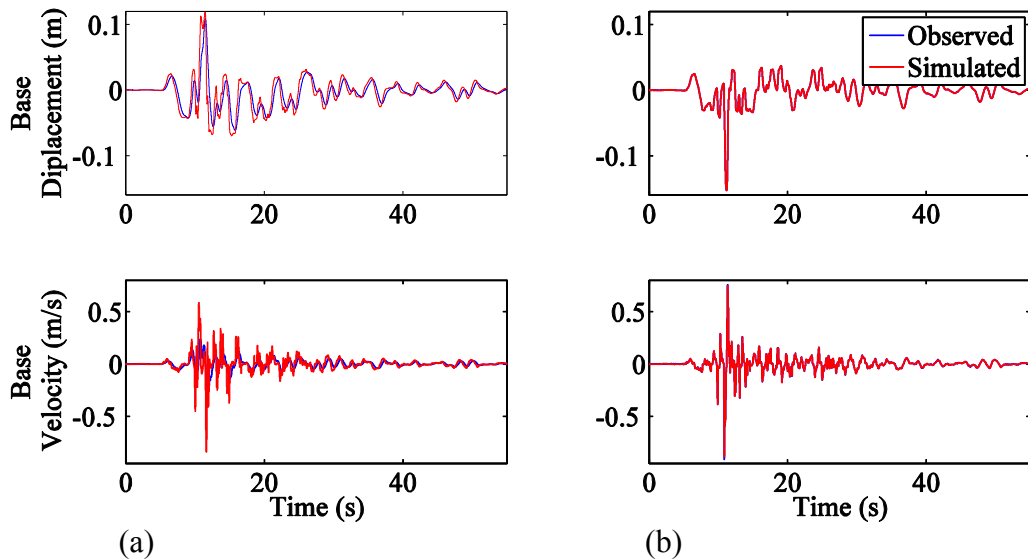


Figure 5.10. Base responses (a) prewhitening was not applied to the base and (b) prewhitening was applied to the base (the Düzce earthquake)

Despite violating the white noise assumption of the Kalman-Bucy filter, the conventionally designed observer estimated responses of the superstructure well. But, it was not successful to predict the base responses (see Figure 5.9(a) and Figure 5.10(a)). Therefore, the system was prewhitened to improve the performance of the observer by satisfying the white input prerequisite of the Kalman-Bucy filter.

The enhancement of the prewhitening in the base responses were observed in Figure 5.9 and Figure 5.10 for the Imperial Valley and Düzce earthquakes, respectively. The nonaugmented observer performed well in the simulations except for the base responses. The nonaugmented observer was not able to predict the base velocity correctly while estimating the base displacement successfully with a phase difference between the simulated and observed responses. On the other hand, the observer could estimate the base responses successfully when prewhitening was applied even only to the base. The responses of the prewhitened system are presented on the right-hand-side of the figures.

### **5.5.5. Observer of the Superstructure**

The base system was prewhitened only. This improved the responses of the observer of the base, which was the only remaining problem in the simulation results. Therefore, the superstructure was not augmented for prewhitening although the colored signal (earthquake acceleration) was sent to it.

In the observer design, transforming any system into generalized coordinates and designing Kalman-Bucy observers with convenient poles for these independent subsystems may be a convenient engineering solution. On the other hand, the augmented base cannot be diagonalized since the damping ratios of the base and the shaping filter have extremely different magnitudes ( $\zeta_b = 0.04$  and  $\zeta_{SF} = 1.01$ ) (see Section 3.1 for details).

In Section 5.5.5.1, the superstructure was transformed into generalized coordinates to obtain independent subsystems. Then, three Kalman-Bucy observers with convenient poles were designed for three independent subsystems of the superstructure. Afterwards, the observers of the subsystems were superposed. Finally, the resultant observer of the superstructure was obtained by transforming the superposed observers back into physical coordinates.

The superstructure system is presented in Equations (5.27) and (5.28). Its observer is designed as follows

$$\hat{\mathbf{x}}_{ss}(t) = \overbrace{(\mathbf{A}_{ss} - \mathbf{L}_{ss}\tilde{\mathbf{D}}_{ss})}^{\tilde{\mathbf{A}}_{ss}} \hat{\mathbf{x}}_{ss}(t) + \tilde{\mathbf{G}}_{ss} \begin{bmatrix} \overbrace{\dot{q}_{g\ noisy}(t)}^{\tilde{\mathbf{w}}_{ss\ noisy}(t)} \\ q_b(t) \\ \dot{q}_b(t) \end{bmatrix} + \mathbf{L}_{ss} \begin{bmatrix} \overbrace{q_{1\ noisy}(t)}^{\tilde{\mathbf{y}}_{ss}(t)} \\ q_{2\ noisy}(t) \\ q_{3\ noisy}(t) \end{bmatrix} \quad (5.37)$$

$$\hat{\mathbf{y}}_{ss}(t) = \tilde{\mathbf{D}}_{ss} \hat{\mathbf{x}}_{ss}(t)$$

where  $\mathbf{L}_{ss}$  is the observer gain matrix of the superstructure.  $\tilde{\mathbf{w}}_{ss\ noisy}$  is the disturbance vector of the observer of the superstructure in the sub-structured formulation. It has the subscript *noisy* due to the existence of the noise in the recorded earthquake acceleration which is sent to the observer during simulations.  $q_b(t)$  and  $\dot{q}_b(t)$  are the inputs from the augmented base and they do not contain any noise. The *tilde* indicates that the superstructure system in the sub-structured formulation (Equations (5.27) and (5.28)) is different from the state equation of the bare superstructure in Equation (4.13).

### 5.5.5.1. Diagonalization of the System Equations of the Superstructure

In the context of the current research, the superstructure (Equation (5.27))

$$\dot{\mathbf{x}}_{ss}(t) = \mathbf{A}_{ss}\mathbf{x}_{ss}(t) + \tilde{\mathbf{G}}_{ss}\tilde{\mathbf{w}}_{ss}(t) \quad (5.38)$$

was diagonalized via the following transformation

$$\mathbf{x}_{ss}(t) = \mathbf{\Psi}\mathbf{r}_{ss}(t) \quad (5.39)$$

where  $\mathbf{x}_{ss}(t)$  is the state vector of the superstructure.  $\mathbf{\Psi}$  is the eigenvector matrix of  $\mathbf{A}_{ss}$  since dynamics of a system is governed by the coefficient matrix of the homogeneous part of the equation.  $\mathbf{r}_{ss}(t)$  is the state vector of the superstructure in generalized coordinates.

The time derivative of the transformation in Equation (5.39) was substituted into Equation (5.38). Then, the expression was premultiplied by  $\mathbf{\Psi}^{-1}$  results in the system equation for the superstructure as follows

$$\dot{\mathbf{r}}_{ss}(t) = \bar{\mathbf{A}}_{ss} \mathbf{r}_{ss}(t) + \bar{\mathbf{G}}_{ss} \tilde{\mathbf{w}}_{ss}(t) \quad (5.40)$$

in which the diagonal state matrix is  $\bar{\mathbf{A}}_{ss} = \mathbf{\Psi}^{-1} \mathbf{A}_{ss} \mathbf{\Psi}$  and  $\bar{\mathbf{G}}_{ss} = \mathbf{\Psi}^{-1} \tilde{\mathbf{G}}_{ss}$  (see Appendix H for details). The superstructure was diagonalized only to design the observer. The diagonalized formulation of the superstructure was not utilized to calculate the responses. Therefore, only the state equation was diagonalized, and the output equation was not diagonalized. For the observer system (Equation (5.37-a)),

$$\dot{\hat{\mathbf{x}}}_{ss}(t) = \overbrace{(\mathbf{A}_{ss} - \mathbf{L}_{ss} \tilde{\mathbf{D}}_{ss})}^{\tilde{\mathbf{A}}_{ss}} \hat{\mathbf{x}}_{ss}(t) + \tilde{\mathbf{G}}_{ss} \tilde{\mathbf{w}}_{ssnoisy}(t) + \mathbf{L}_{ss} \tilde{\mathbf{y}}_{ss}(t) \quad (5.41)$$

The observer states were transformed via

$$\hat{\mathbf{x}}_{ss}(t) = \mathbf{\Psi} \hat{\mathbf{r}}_{ss}(t) \quad (5.42)$$

Equation (5.42) and its time derivative were plugged into Equation (5.41). Then, the expression was premultiplied by  $\mathbf{\Psi}^{-1}$ . Finally, the observer system equation for the superstructure was obtained as follows

$$\dot{\hat{\mathbf{r}}}_{ss}(t) = (\bar{\mathbf{A}}_{ss} - \bar{\mathbf{L}}_{ss} \bar{\mathbf{D}}_{ss}) \hat{\mathbf{r}}_{ss}(t) + \bar{\mathbf{G}}_{ss} \tilde{\mathbf{w}}_{ss}(t) + \bar{\mathbf{L}}_{ss} \tilde{\mathbf{y}}_{ss}(t) \quad (5.43)$$

where

$$\begin{aligned} \bar{\mathbf{L}}_{ss} &= \mathbf{\Psi}^{-1} \mathbf{L}_{ss} \\ \bar{\mathbf{D}}_{ss} &= \tilde{\mathbf{D}}_{ss} \mathbf{\Psi} \end{aligned} \quad (5.44)$$

The *tilde* indicates that the superstructure system in the sub-structured formulation (Equations (5.27) and (5.28)) is different from the state equation of the bare superstructure in Equation (4.13).

### 5.5.5.2. Physical Interpretation of Complex Eigen Quantities

The eigenvalues of the matrix  $\mathbf{M}_{SS}^{-1}\mathbf{K}_{SS}$  which is a real symmetric matrix are real (Meirovitch, 2001). Its distinct eigenvectors are orthogonal with respect to the mass or stiffness matrices. This case is an orthogonality with respect to a weighting matrix and is different from the ordinary orthogonality. On the other hand, the eigenquantities of a nonsymmetric matrix  $\mathbf{A}_{SS}$  in Equation (4.13) are not guaranteed to be real. Additionally, the eigenvectors of a nonsymmetric matrix are not orthogonal with respect to a weighting matrix. They have the biorthogonality property which means that the distinct right eigenvectors are orthogonal to the left eigenvectors with respect to the nonsymmetric matrix  $\mathbf{A}_{SS}$ .

A real mode is the shape of deformation, in which all points of the structure are either in-phase or out-of-phase by  $\pi$  radians with any other points of the structure. Therefore, all points of the structure reach their own maxima and minima simultaneously within one vibration cycle. Additionally, all points of the structure pass through their zero deflection position at the same time within one period.

On the other hand, relative phase differences between responses of adjacent parts of the structure indicate a complex mode. The facts mentioned for real modes are no longer valid for structures with complex mode shapes. A real mode looks like a standing wave, while a complex mode exhibits a travelling deflection shape (Ewins, 2000; He & Fu, 2001).

Ewins (2000) summarizes the origins of complex modes as: nonproportionally distributed damping mechanism in structures with close modes, gyroscopic effects of rotation, and identical natural frequencies even in the absence of nonclassical damping or gyroscopic effects (see Section 3.1 about the nonclassical damping).

The calculated eigenvalues and eigenvectors may be interpreted as follows: While the real part of a complex eigenvalue is equal to  $\zeta\omega_n$ , the imaginary part of it is equal to  $\omega_n\sqrt{\zeta^2 - 1}$ . The real and imaginary parts of a complex eigenvalue represents the decay and oscillatory components of the natural frequency in the response (Ewins, 2000). The magnitude of a complex eigenvalue gives the natural circular frequency  $\omega_n$  (Gavin, 2001). A complex mode shape can be defined by both amplitude and phase, or by its real and imaginary components (Zad, 1997).

In the state-space representation, the size of the system is twice of the number of the DOFs, and generally the states contain the displacements and velocities. Therefore, the eigenvectors have components for displacements and velocities. The first half of the eigenvector belongs to the displacements, depending on the definition of the state vector. Besides, every eigenmode appears by its conjugate pair. Consequently, a  $2n \times 2n$  complex eigenvector matrix is reduced to a  $n \times n$  vector for displacement modes, where  $n$  is the number of the DOFs. If the damping is proportional, then the phase differences between the displacements of the related DOFs are 0 or  $\pi$  radians. On the other hand, there is a certain amount of phase difference between the displacements and velocities of the related DOFs. If the phase difference between DOFs is different from 0 or  $\pi$  radians, this case indicates a complex mode.

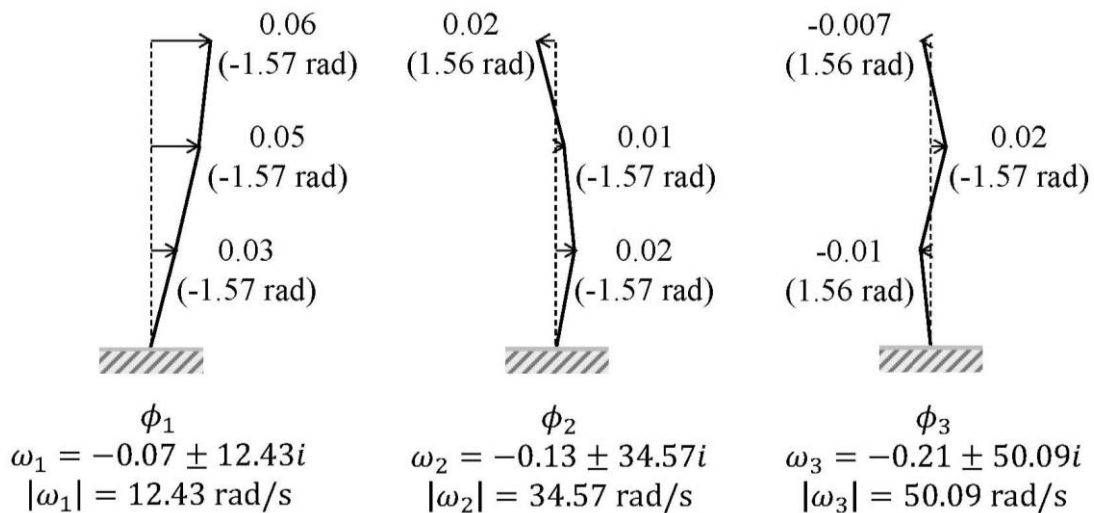


Figure 5.11. Damped mode shapes of the superstructure (displacement phase angles of the DOFs and damped circular frequencies of the modes are presented)

The damped mode shapes of the superstructure are presented in Figure 5.11. Additionally, the damped mode shapes of the base isolated structure are presented in Figure 5.12. The phase angles of the displacements of the DOFs and the damped circular frequencies of the modes are displayed. According to Figure 5.11, all DOFs of the classically damped structure are either in-phase or out-of-phase by approximately  $\pi$  radians with any other DOFs of the structure. This case is also valid for the non-proportionally damped structure in Figure 5.12.

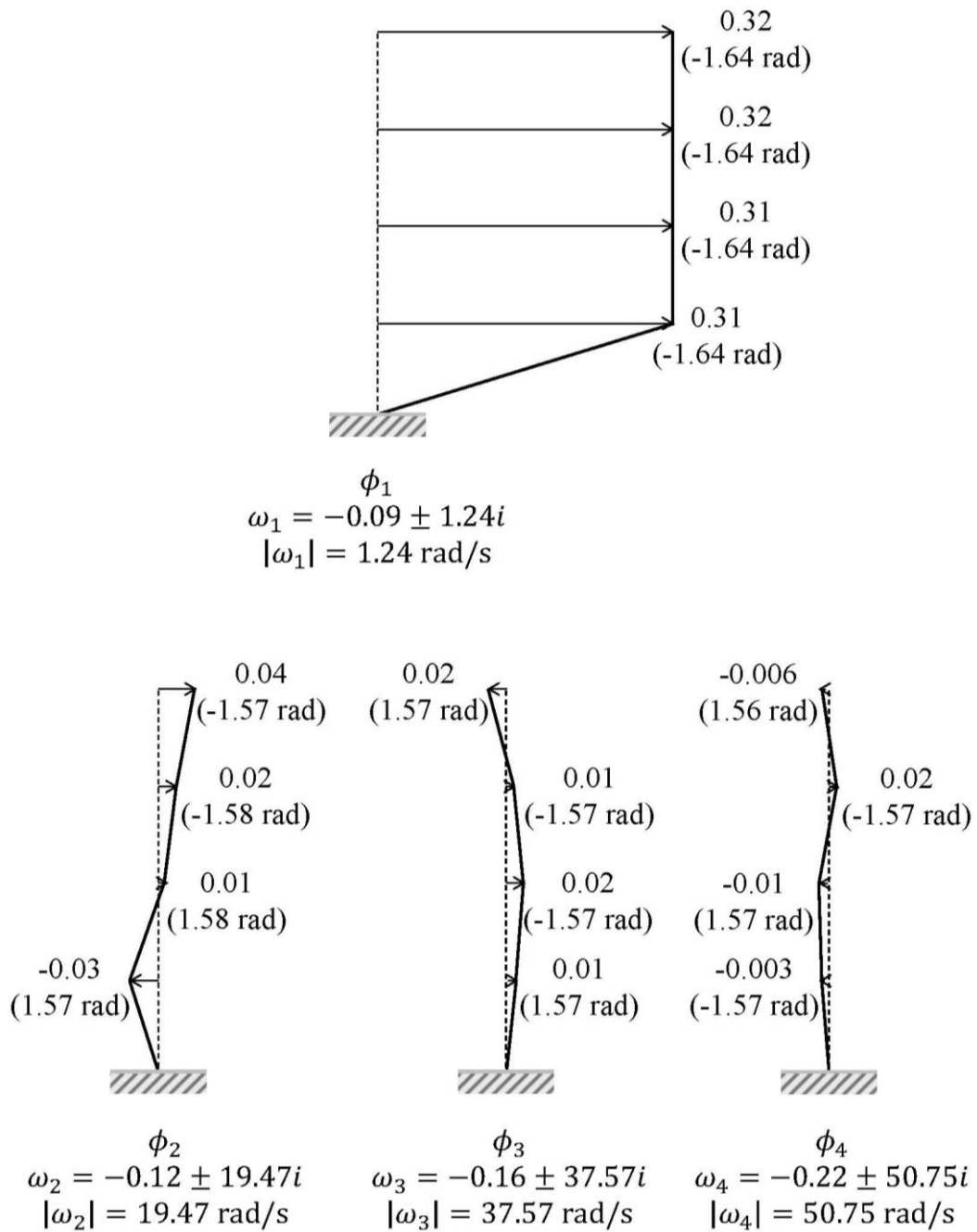


Figure 5.12. Damped mode shapes of the base isolated structure (the phase angles of the DOFs and the damped circular frequencies of the modes are presented)

According to the definition of the complex modes, the non-proportionally damped structure in Figure 5.12 has real modes. It is important to note that the non-proportionality is a necessary condition for complex modes to exist, but it is not sufficient (Ewins, 2000). The other necessary condition is that two or more modes should be close to each other (see (Ewins, 2000) for the discussion about the measure of the closeness of the modes).

Furthermore, in the literature there are different approximations for realization of complex modes (Rad, 1997). For a second-order nonproportionally damped system, a relationship between the real and imaginary parts of complex modes is presented in case of real and symmetric mass, stiffness, and damping matrices (Garvey et al., 1998).

### 5.5.5.3. Complex Analysis

The observer of the superstructure was designed for the three independent subsystems of the superstructure. The convenient  $\mathcal{Q} - \mathcal{R}$  couples were determined in a loop to obtain a *PoleRatio* in the range of 2-4 (see Equation (5.22) for the definition of the variable *PoleRatio*).

Then, the observer gain matrix  $\bar{\mathbf{L}}_{SS}$  of the diagonalized superstructure was obtained by stacking the observer gain matrices of the three independent subsystems in matrix form. Finally,  $\bar{\mathbf{L}}_{SS}$  in generalized coordinates was transformed back to the physical coordinates by  $\mathbf{L}_{SS} = \mathbf{\Psi} \bar{\mathbf{L}}_{SS}$  (Equation (5.44)). Some of the elements of the eigenvector matrix  $\mathbf{\Psi}$  presented in Equation (H.2-b) were complex eigenvectors. Therefore, imaginary components appeared in the observer gain matrix  $\mathbf{L}_{SS}$ , even  $\bar{\mathbf{L}}_{SS}$  did not contain a complex value. The imaginary components in  $\mathbf{L}_{SS}$  appeared due to the back transformation performed via the eigenvector matrix  $\mathbf{\Psi}$ . Hence, the observer state matrix  $\hat{\mathbf{A}}_{SS} = \mathbf{A}_{SS} - \mathbf{L}_{SS} \tilde{\mathbf{D}}_{SS}$  involved complex components that required dealing with complex arithmetic throughout the analysis. The system matrices  $\mathbf{A}_{SS}$ ,  $\tilde{\mathbf{G}}_{SS}$ , and  $\tilde{\mathbf{D}}_{SS}$  were real matrices since they were defined for an ordinary second order mechanical system presented in Figure 5.7.

In order to determine the responses of the system, the state equation of the continuous system had to be solved. The MATLAB function *lsim* simulates the time response of linear time invariant models to arbitrary inputs. The solution process within *lsim* cannot deal with systems whose differential equations have complex coefficients.

Instead, a function was coded within MATLAB to calculate the response of the observer of the superstructure via Equation (5.46). The general solution to the dynamic response of a linear system defined by Equation (5.41) is presented by Equation (A.6). It is as follows

$$\hat{\mathbf{x}}_{ss}(t_i) = \boldsymbol{\Phi}(t_i, t_{i-1}) \hat{\mathbf{x}}_{ss}(t_{i-1}) + \int_{t_{i-1}}^{t_i} \boldsymbol{\Phi}(t_i, \tau) \mathbf{G}(\tau) \boldsymbol{w}(\tau) d\tau \quad (5.45)$$

where  $\hat{\mathbf{x}}_{ss}(t_i)$  is the observer response of the superstructure at time  $t_i$ .  $\boldsymbol{\Phi}(t_j, t_{j-1})$  is the state transition matrix.  $\mathbf{G}(\tau)$  is the input matrix, and  $\boldsymbol{w}(\tau)$  is the corresponding input.

In the simulations, the responses were calculated in a time loop. Therefore, the time-variant system could be assumed to be time-invariant within each time step. Hence, the state transition matrix  $\boldsymbol{\Phi}(t_j, t_{j-1})$  turned into  $e^{\hat{\mathbf{A}}_{ss} dt}$  (see Equation (A.9)) in which  $\hat{\mathbf{A}}_{ss} = \mathbf{A}_{ss} - \mathbf{L}_{ss} \tilde{\mathbf{D}}_{ss}$  was the state matrix of the observer of the superstructure. Consequently, the response of the observer of the superstructure in Equation (5.41) is calculated by

$$\hat{\mathbf{x}}_{ss}(t_i) = e^{\hat{\mathbf{A}}_{ss} dt} \hat{\mathbf{x}}_{ss}(t_{i-1}) + \int_{t_{i-1}}^{t_i} e^{\hat{\mathbf{A}}_{ss}(t_i - \tau)} \overbrace{[\tilde{\mathbf{G}}_{ss} \quad \mathbf{L}_{ss}]}^{\mathbf{G}(\tau)} \overbrace{\begin{bmatrix} \tilde{\mathbf{w}}_{ssnoisy}(\tau) \\ \tilde{\mathbf{y}}_{ss}(\tau) \end{bmatrix}}^{\boldsymbol{w}(\tau)} d\tau \quad (5.46)$$

where  $\mathbf{G}(\tau) = [\tilde{\mathbf{G}}_{ss} \quad \mathbf{L}_{ss}]$  is the input matrix.  $\boldsymbol{w}(\tau) = [\tilde{\mathbf{w}}_{ssnoisy}(\tau) \quad \tilde{\mathbf{y}}_{ss}(\tau)]^T$  is the corresponding input vector.  $dt$  is the time increment. The first term in Equation (5.46) is the homogenous solution, and the second part is the particular solution. The particular solution in Equation (5.46) is a convolution integral.

In the function *complexanalysis*, the homogenous solution was computed via the MATLAB command *expm*. The input  $\boldsymbol{w}(\tau)$  could not be taken out of the integral since it was a function of  $\tau$ . It was known numerically, but not functionally. Therefore, the integral was calculated numerically via the Simpson's 1/3 rule. The results of the function *complexanalysis* were confirmed via the MATLAB function *lsim* in case of an arbitrary system whose (ordinary) differential equation had real coefficients. *lsim* simulated the time response of linear time invariant models to arbitrary inputs. While confirming the results of the function *complexanalysis* via *lsim*, the inputs were formed as step, triangle, half-period sine wave, and impulse loadings. The outputs for the first three loading case completely overlapped. Nevertheless, the impulse responses had different magnitudes since *lsim* performed interpolation within the time step, and the

utilized time increment was not small enough to create an impulsive loading which is similar to a white signal.

Additionally, a function was coded within MATLAB to calculate the matrix exponential  $e^{\hat{A}_{ss}dt}$  in Equation (5.46) symbolically via the Cayle-Hamilton theorem. Due to the calculation time being long, it was preferred to employ the MATLAB command *expm* instead of utilizing this coded function.

After the simulations, the responses were obtained numerically. The imaginary parts of the displacements and velocities of the superstructure had the order of  $10^{-17}$ . The complex components were neglected while plotting the responses due to their very small magnitudes. The displacements and velocities of the base did not have any imaginary parts since the base was not diagonalized for the observer design (see Sections 5.8.4 and 5.8.5 for details).

### 5.5.6. LQR Part of the LQG Control of the VOD

After designing a convenient observer, the required control force had to be determined. The LQR design was performed for the 4-by-4 full structure, which is presented by Equation (5.7). There was not an explicit control input to the system since the control effect was applied by changing the damping value of the VOD. On the other hand, the LQR design required a control matrix (see Equation (4.15)). Therefore, it was defined as follows

$$\mathbf{B}_s = \begin{bmatrix} \mathbf{0}_{4 \times 1} \\ 1 \\ \mathbf{M}_s^{-1} \mathbf{0} \\ 0 \\ 0 \end{bmatrix} \quad (5.47)$$

In the usual formulation of the present research, the matrix  $\mathbf{B}_s$  had a negative sign. On the other hand, in the VOD design, the damping force was defined by  $f_{VOD} = -c_D \dot{q}_b$  in the MATLAB code, including the negative sign. Therefore, the matrix  $\mathbf{B}_s$  of the VOD design did not contain the negative sign (see Equation (5.47)).

The floor displacements and velocities, relative to the ground, were aimed to be controlled. As a customary way, the weighting matrices  $\mathbf{Q}$  and  $R$  of the LQR were chosen in such a way that the calculated control force  $u$  and the damping force  $f_{VOD}$

were to be as close as possible. Initially, the  $\mathbf{Q}$  matrix in Equation (5.48) was determined.

$$\mathbf{Q} = \begin{bmatrix} 100 & 0 & 0 & 0 & 0 & 0 & 0 & 0 \\ 0 & 1 & 0 & 0 & 0 & 0 & 0 & 0 \\ 0 & 0 & 1 & 0 & 0 & 0 & 0 & 0 \\ 0 & 0 & 0 & 1 & 0 & 0 & 0 & 0 \\ 0 & 0 & 0 & 0 & 1 & 0 & 0 & 0 \\ 0 & 0 & 0 & 0 & 0 & 0.01 & 0 & 0 \\ 0 & 0 & 0 & 0 & 0 & 0 & 0.01 & 0 \\ 0 & 0 & 0 & 0 & 0 & 0 & 0 & 0.01 \end{bmatrix} \quad (5.48)$$

The  $\mathbf{Q}$  matrix was chosen in such a way that its configuration coincided with the magnitudes of the states since the states were the displacements and velocities, respectively. The weights of the displacements were chosen ten times higher than those of velocities harmoniously with the numerical situation (order of the velocities was approximately ten times the order of the displacement responses in the simulations).

Additionally, the base responses were controlled ten times more heavily than those of the superstructure since controlling the base responses would control the floor responses indirectly. The controller allocated more control effort to the control of the base response by increasing the damper force. This remedy decreased the translation of the isolation.

After selection of the  $\mathbf{Q}$  matrix, the weight of the control input, which should be strictly positive definite, was determined as follows: Holding the value given for the  $\mathbf{Q}$  matrix in Equation (5.48) constant,  $R$  values were varied, and the results were displayed in Table 5.4. The ratio of the maximum values of  $u$  and  $f_{VOD}$  was presented for different  $\mathbf{Q}$  and  $R$  values. The maximum values of the base responses were listed in Table 5.4, and they did not completely reflect the behaviour of the states within the whole time range. The LQR was designed for the records of the 1940 Imperial Valley and 1999 Düzce events.

Table 5.4. Determination of the weighting matrices  $\mathbf{Q}$  and  $R$  for the LQR design

	$R$	$\frac{\max u }{\max f_{VOD} }$	$\max q_b $ (m)	$\max \dot{q}_b $ (m/s)
Imperial Valley event	$5 \cdot 10^{-3}$	0.02	0.0901	0.30
	$5 \cdot 10^{-7}$	0.38	0.0407	0.35
	$5 \cdot 10^{-8}$	0.79	0.0400	0.39
	$3 \cdot 10^{-8}$	1.04	0.0399	0.42
	$1.44 \cdot 10^{-8}$	1.28	0.0402	0.38
Düzce event	$5 \cdot 10^{-3}$	0.02	0.2545	0.64
	$5 \cdot 10^{-7}$	0.79	0.1511	1.00
	$5 \cdot 10^{-8}$	1.73	0.1482	0.92
	$3 \cdot 10^{-8}$	2.29	0.1532	0.89
	$1.44 \cdot 10^{-8}$	3.30	0.1539	0.86

where  $q_b$  and  $\dot{q}_b$  are the displacement and velocity of the base relative to the ground, respectively. In Table 5.4, four digits were presented for displacements in order to show and comment the numerical changes. The responses relative to the ground were controlled. Therefore, the responses of the superstructure were similar to those of the base and were not presented in Table 5.4. The positive semi-/definiteness of the chosen  $\mathbf{Q} - R$  values were confirmed by their eigenvalues in the MATLAB code.

The important issue in the LQR design is not the individual values of  $\mathbf{Q}$  and  $R$ , but the ratio between them is important. The judgement about  $\mathbf{Q}$  and  $R$  was made by means of Table G.1 due to the desired performance specifications. As  $R$  decreased,  $u$  increased, hence the ratio  $\max|u|/\max|f_{VOD}|$  increased. Decreasing  $R$  was equivalent to increasing  $\mathbf{Q}$  and led to smaller values of the states, and vice versa. This case was obvious when distinctive numerical changes were applied while selecting  $R$  values. For instance this case was observed when a numerical value decreased from  $5 \cdot 10^{-3}$  to  $5 \cdot 10^{-7}$ . On the other, if the numerical changes in  $R$  values were not huge, this case could not be obviously observed.

In Table 5.4, the maximum displacement values for the Düzce earthquake were higher compared to those of the Imperial Valley event (This fact was due to the single high peak shock with a value of  $0.8g$  in the seismic record in Figure 2.4).

According to Table 5.4, the  $R$  value was chosen in such a way that the damper force was close to the calculated control force  $u$ . This situation indicated that the damper could supply the required control effort. Control force values, which were greater than the damper force, pointed out the case of capacity exceeding in terms of the damping value or the velocity difference on the VOD (At an instant of the simulations, the controller may have selected the maximum damping value of the VOD. Nevertheless, if the velocity difference on the VOD had not been sufficient enough, then the VOD could not have provided the required damping force.). On the other hand, control force values smaller than the damper force indicated that the damper provided a redundant amount of damping force. Consequently, keeping a balance between the demands of the system (the calculated control force  $u$ ) and the control effort that the system could supply (the damping force of the VOD,  $f_{VOD}$ ), the  $R$  value was chosen as follows:

$$R = 3 \cdot 10^{-8} \quad (5.49)$$

A special algorithm was not coded to determine a better  $Q - R$  couple. Only a trial-and-success procedure summarized in Table 5.4 was applied. In the context of the present research, the studies were focused on enhancing the performance of the observer. As a future work, some investigations by GA may be performed for  $Q - R$  couple of the LQR to obtain such controlled responses better than the present ones.

## 5.6. Gain Scheduling Control

A nonlinear system can be subdivided into linear sub-systems at different operating points, and its control law may consist of a bundle of alternative controllers. The corresponding operating region of the system is determined by monitoring its system variables. Then, the corresponding linear controller for the current operating region is applied. This switching technique is the gain scheduling scheme, which is an adaptive control technique for nonlinear systems. A similar supervisory control architecture is presented in Figure 5.13, where  $c_{Di}$  ( $i=1,2,\dots,n$ ) are the damping coefficients of the damper, which belongs to different orifice openings (Spong & Tsao, 1998).

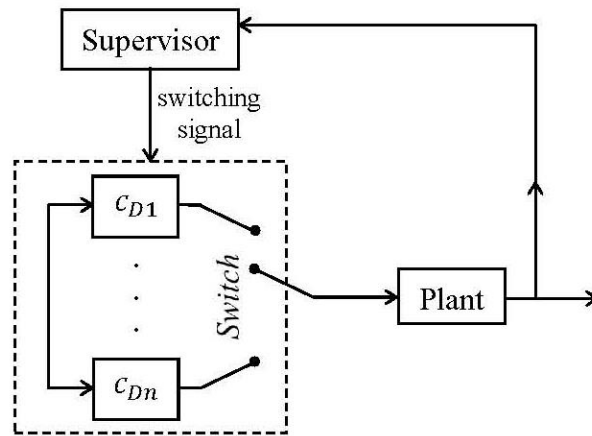


Figure 5.13. Supervisory control  
(Source: Spong & Tsao, 1998)

The analysis and design of gain scheduled control systems were investigated in detail by Shamma (1988). In the literature, there is a wide variety of applications of gain scheduling control (Lin & Yu, 1993; Choi & Lim, 2005). It was applied for control of web transport systems (Claveau et al., 2008), for control of air/fuel ratio in diesel engines (Alfieri et al., 2009), and for robust global stabilization of linear systems (Zhou et al., 2010). Gain scheduling scheme of a proportional integral control was designed for a synchronous generator (Sedaghati, 2006). Leith and Leithead (2000) presented an extended review of the gain scheduling literature and linearization techniques that can be applied to the nonlinear control systems.

The stability of a system with frozen parameters does not guarantee the stability of the system for a certain parameter trajectory. The variations in the scheduling parameter should be sufficiently slow to guarantee the closed-loop stability of the overall system. In the literature, various researchers investigated the stability of gain-scheduled control systems. Shamma and Athans emphasized the necessity of developing a theory for the stability of LPV systems without any limitations (1992). Stability of nonlinear systems with slowly varying inputs was studied (Lawrence & Rugh, 1990). The results of the work can be implemented in the context of gain-scheduled control systems. The stability of switched systems with average dwell-time was studied by Hespanha and Morse (1999). Morse investigated the estimator-based supervisory control (1996). The stability analysis of switching  $H^\infty$  controllers for a class of linear parameter varying (LPV) systems with slow parameter variations were presented by

Yan and Özbay (2007). The asymptotic stability of switched linear systems with time delays was investigated (Yan & Özbay, 2008).

In the current example, the system was a LPV system, which depended on the damping coefficients  $c_{Di}$  ( $i=1,2,\dots,18$ ) of the VOD. Thus, the system was linearized indirectly without applying a certain linearization procedure. Linear feedback controllers were designed for all linear sub-systems to achieve the desired performance, and they were linear sub-controllers. The controller consisted of these linear sub-controllers, and its parameters were determined by monitoring the scheduling variables. The switching logic was carried out by the supervisor. In the current problem, this task was performed by the upper controller (see Section 5.7).

In the present example, the varying parameter was the damping coefficient of the VOD. Damping of a mechanical system cannot be negative, therefore, cannot add energy to the system. The damper always absorbed energy from the system, annihilating the possibility of instability. Thus, the overall stability of the switching system was guaranteed.

## 5.7. Upper Controller

In the current simulations, any explicit control force was not input to the system. The optimal control force was calculated by the LQR and was applied to the system by simply changing the orifice setting of the damper. The system behaved nonlinearly as the orifice size of the damper changed. A different linear system occurred for every different orifice size. Every lower controller and observer belonged to these linear sub-systems. The whole system consisted of sub-systems, their controllers, and their observers. The optimum orifice size was selected among many lower control systems by means of an upper controller due to the system requirements. The upper controller was designed to switch between different feedback control gains during earthquake simulations. The system matrices  $A$  and  $C$  of the state-space representation were calculated for different  $c_D$  values which belonged to different orifice positions. The optimum feedback gain and the observer gain were evaluated for each differently damped building models. In Equation (5.50), the optimum  $c_D$  value was directly determined by dividing the additionally required damper force in the next time step by the velocity  $q_D$  of the damper.

$$c_{D_i} = \frac{c_{D_{i-1}} q_{D_i} - u_{c_i}}{q_{D_i}} \quad (5.50)$$

A passive device may only absorb energy from the system, which is the case for dampers. That is why the damping force can only act in the opposite direction of its velocity. In the present example, if the calculated optimum damping constant had had a negative sign, then it would have been impossible to produce the required force. In this case, the damping constant would have taken its minimum value. If the calculated  $c_D$  value had been out of the limits of the variable orifice damper, it would have chosen to be the limit value. If the calculated  $c_D$  value had been within the limits, it would have rounded to the nearest possible damping value. Then, the simulation of the  $i$ th step took place, and the optimum damping value for the next step was obtained. The damper force was calculated for the new optimum  $c_D$  value by

$$c_{D_i} = \begin{cases} c_{min}, & c_{D_i} < c_{min} \\ c_{D_i}, & c_{min} < c_{D_i} < c_{max} \\ c_{max}, & c_{max} < c_{D_i} \end{cases} \quad (5.51)$$

where  $c_{D_i}$  is the damping constant of the semi-active damper in the  $i$ th time step.  $c_{min}$  and  $c_{max}$  are the limit damping constants of the damper.

A numerical precaution was taken to prevent a “divide by zero” error during the calculation of the optimum damper constant. Therefore, the smallest absolute damper velocity was limited to 1 mm/s. This case would not have a detrimental effect to the structural response since the worst case caused a small magnitude of force ( $c_{max} \cdot 0.001 \frac{m}{s} = 25000 \frac{Ns}{m} \cdot 0.001 \frac{m}{s} = 25 N$ ).

The upper controller also decides when the optimum control forces should be applied. In Figure 5.14, the decision mechanism is presented. The sections when the controller is in action are marked by the bold lines in a representational example in Figure 5.15. Initially, the controller is at rest, during which the damper is at its minimum resistance. Whenever the displacement of the damper gets into danger, the controller applies the optimum damping constant to the damper. The term “danger” in this study is defined as an isolator displacement of 3 cm or more. Once an isolator

exceeds this value, the controller is in action until an extremum that is less than 3 cm is reached.

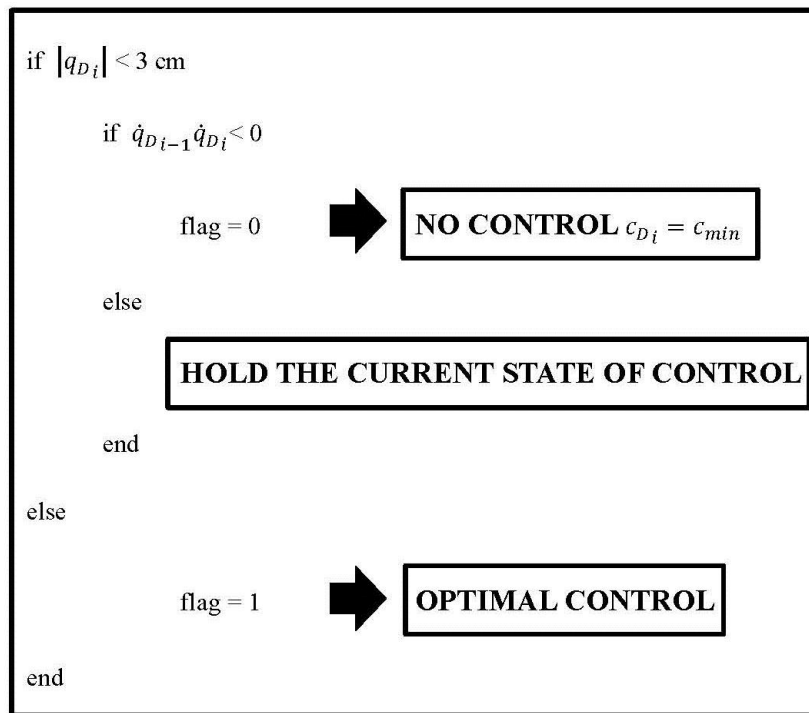


Figure 5.14. Decision of the upper controller

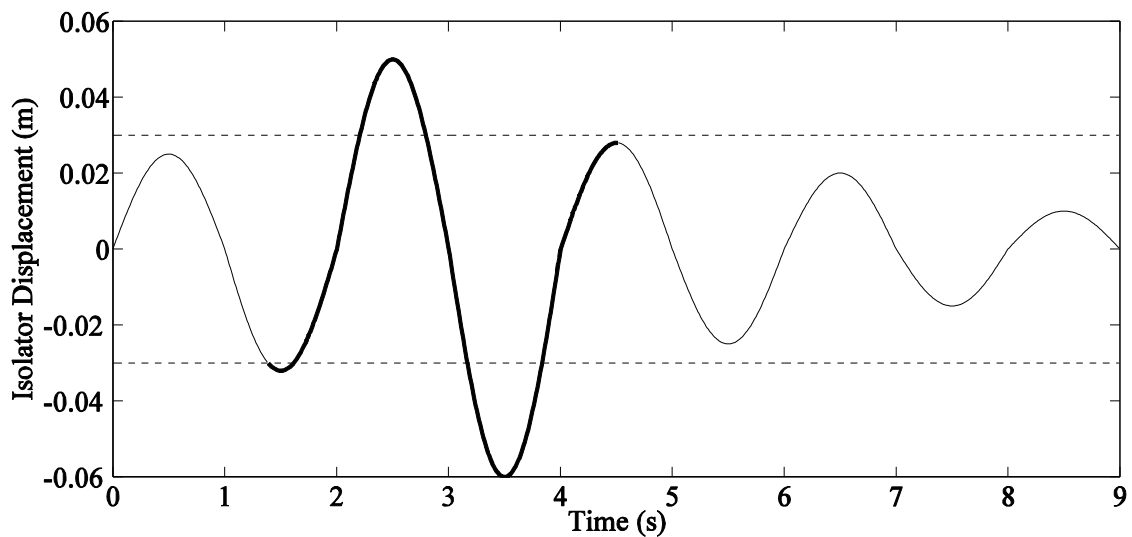


Figure 5.15. Illustration of the upper controller on a representational displacement graph (the controller is in action along the sections marked by the bold line)

## 5.8. Numerical Simulations

### 5.8.1. Interpolation & Synthetic Production of the Seismic Excitation Data

In the current numerical simulations, the required control force was applied to the system by changing the orifice opening of the VOD. The ground excitation record was read and interpolated to the one fifth of the original time increment of the data due to the computational requirements. Utilization of a smaller time increment within the simulations made the transition among different VOD damping values smoother. Otherwise, the rapid changes in the damper force may have caused a bang-bang type behavior, and the responses would completely change undesiredly.

A base isolated structure is protected by lengthening the fundamental period of the system. In a near-fault seismic event, the magnitude of the high-period components is high. Therefore, isolating a structure that is located close to a seismic fault may cause detrimental consequences. In the context of the present work, the seismic data were produced synthetically by interpolating the Imperial Valley and Düzce earthquakes to investigate the controller performance for near-fault earthquakes. Thus, a situation of a frequency overlap of excitation and system was performed. The procedure of seismic data production is illustrated in Figure 5.16.

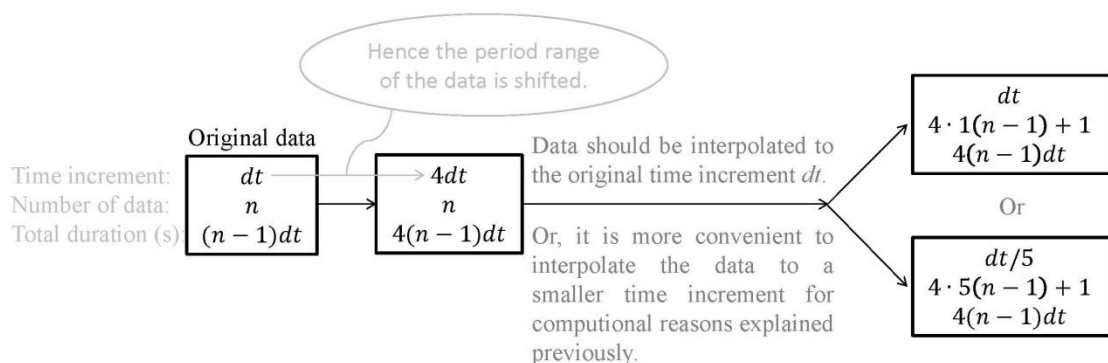


Figure 5.16. Schematic representation of how the synthetic near-fault data are produced and interpolated

The original time increment  $dt$  was increased four times, hence the data was shifted to the high-period range in frequency spectrum. At this point, the number of data remained constant, while the total duration of the data was lengthened. The data became

sparse, and it had to be interpolated to a smaller time increment due to the computational reasons explained earlier.

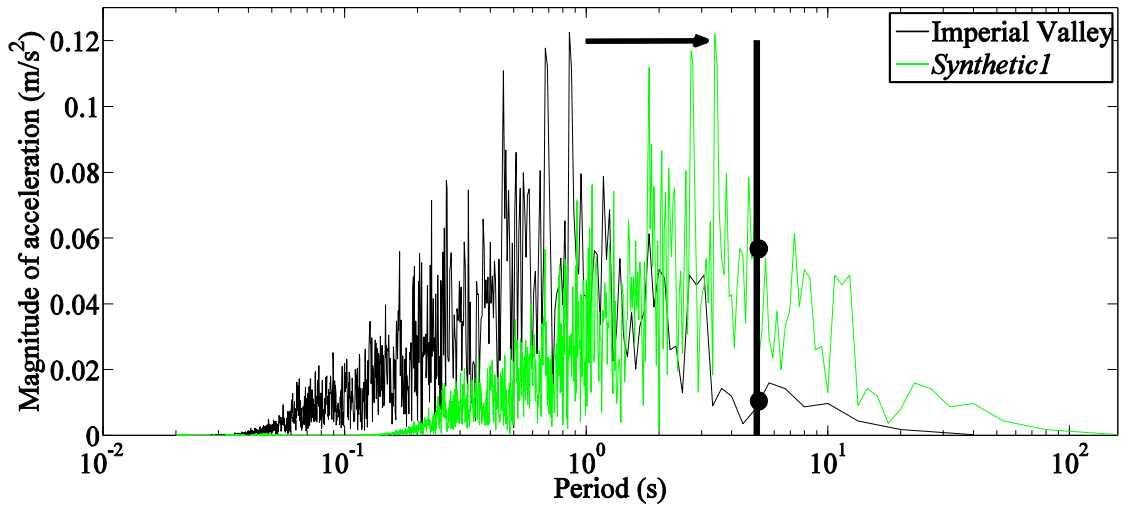


Figure 5.17. Imperial Valley earthquake and *Synthetic1* data in frequency domain (The fundamental undamped period of the isolated structure is marked by a thick line)

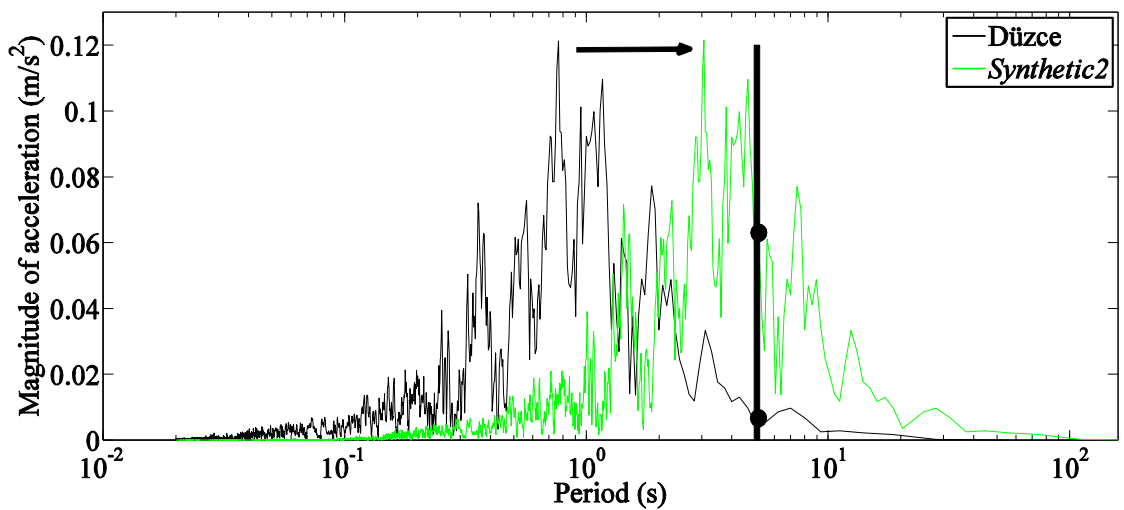


Figure 5.18. Düzce earthquake and *Synthetic2* data in frequency domain (The fundamental undamped period of the isolated structure is marked by a thick line)

The synthetically produced data were named *Synthetic1* and *Synthetic2*. *Synthetic1* was obtained by modifying the data of the Imperial Valley event. *Synthetic2* was formed from the data of the Düzce earthquake. In Figure 5.17 and Figure 5.18, they were presented together with the data which were utilized to produce them. Actually, the original and synthetic data were completely different. They were presented together

just to exhibit how the structure would be effected if an excitation closer to the structure had acted.

The synthetic data in Figure 5.17 and Figure 5.18 were interpolated to their original time increment  $dt$  due to the last step of the procedure illustrated in Figure 5.16 due to the computational reasons. The original data are represented by black line and the grey line stands for the synthetic near-fault excitation. The fundamental undamped period of the seismic isolated structure is marked by a thick line ( $T_{n_{fund}} = 5.07$  seconds). In Figure 5.17 and Figure 5.18, the seismic data are offset to the higher period range in the frequency spectrum. As a result, the fundamental mode of the isolated structure will be maximally affected in case of a near-fault ground excitation.

The (under-damped) response of the seismic isolated structure is mainly driven by the fundamental damped period. The base is assumed to have 4% damping (see Section 4.7.1). The fundamental damped period of the isolated structure is approximately equal to the undamped one due to the low damping ratio ( $T_{d_{fund}} = T_{n_{fund}}/\sqrt{1 - \zeta^2} \cong 5.07$  seconds where  $\zeta$  is the damping ratio).

On the other hand, the fundamental damped period of the hybrid-controlled structure varies leading to an under-damped or over-damped response depending on the orifice opening of the VOD. A periodic behavior cannot be observed for an over-damped system. The exponential response is driven by the damping ratio  $\zeta$  and the natural circular frequency  $\omega_n$  in Equation (F.6) and the definition of damped period (or damped frequency) is not valid for over-damped response. Therefore, in order to form an opinion about the response of the hybrid-controlled structure, the damped period at the upper limit of the under-damped region was calculated: the limit damping value of the VOD is 850 Ns/m corresponding to a damping of 81.79% (see Section 5.3). This value leads to a fundamental damped period of approximately twice of the undamped one ( $T_{d_{fund}} = 8.81$  s). This fact should be taken into consideration while interpreting the time behavior of the hybrid-controlled structure in Figure 5.17 and Figure 5.18.

## 5.8.2. Current State in the Numerical Simulations

The current state of the system and calculations is summarized in the present subsection. The gain scheduling control of a substructured system with a VOD was performed. The controller is presented in Section 5.7. The block diagram of the system is presented in Figure 5.19.

The floor displacements and floor velocities relative to the ground were controlled. The measured story displacements and unmeasured story velocities were observed. The controller was fed by the observed states since they were less noisy than the measured ones by means of the filtering character of the Kalman-Bucy observer. In a real-world application, which is not the case for the present research, the calculated responses cannot be obtained, only the estimated and measured values are achieved. Therefore, the controller is fed by the observed values which are less noisy than the measured ones.

The ground excitation input to the observer was prewhitened due to the white noise prerequisite of the Kalman filter. This was performed by augmenting the observer system of the base by a shaping filter (see Section 5.5.3 for details). Augmenting the base only by this method, improved the responses of the observer of the base, which was the only remaining problem in the simulation results (Figure 5.9 and Figure 5.10). Therefore, the superstructure was not augmented for prewhitening although the colored signal (earthquake acceleration) was sent to the superstructure.

The superstructure was diagonalized into three subsystems to design an observer whose poles were placed in a desired range. Three Kalman-Bucy observers with convenient poles were designed for three independent subsystems of the superstructure. Then, the final observer of the superstructure was obtained by superposing and transforming them back into physical coordinates. On the other hand, the augmented base could not be diagonalized since its damping ratios had extremely different magnitudes. (see Section 5.5.5 for details).

The system equations of the structure and the observer, which were utilized at the final simulations, are presented in Table 5.5. Additionally, the block diagram of the system and the text file in MATLAB are presented in Figure 5.19 and Appendix E, respectively. The definitions of the variables in the equations are presented in the related sections of the thesis.

Table 5.5. System equations utilized in the simulations

Building			
$\mathbf{M}_s \ddot{\mathbf{q}}_s(t) + \mathbf{C}_s \dot{\mathbf{q}}_s(t) + \mathbf{K}_s \mathbf{q}_s(t) = -\mathbf{M}_s \mathbf{h}_1 \ddot{q}_g(t), \quad \mathbf{C}_s = \begin{bmatrix} 54.53 + c_D & -9.1 & 0 & 0 \\ -9.1 & 30.88 & -9.1 & 0 \\ 0 & -9.1 & 30.51 & -9.1 \\ 0 & 0 & -9.1 & 21.35 \end{bmatrix} \frac{Ns}{m}$			Equation (5.4) Equation (5.6)
$\begin{matrix} \mathbf{y}_s(t) \\ \begin{bmatrix} q_{1noisy}(t) \\ q_{2noisy}(t) \\ q_{3noisy}(t) \\ q_{4noisy}(t) \\ f_{Dnoisy}(t) \end{bmatrix} \end{matrix} = \begin{matrix} \mathbf{D}_s \\ \begin{bmatrix} \mathbf{I}_{4 \times 4} & \mathbf{0}_{4 \times 4} \\ \mathbf{0}_{1 \times 4} & -c_D \mathbf{0} \mathbf{0} \mathbf{0} \end{bmatrix} \end{matrix} \mathbf{x}_s(t) + \mathbf{v}(t)$			Equation (5.8)
The responses of the structure were calculated via the Newmark's linear numerical integration method by the equation of motion.			
Substructured observer			
Augmented base		Superstructure	
$\dot{\hat{\mathbf{x}}}_{ab}(t) = \overbrace{(\mathbf{A}_{ab} - \mathbf{L}_{ab} \mathbf{D}_{ab})}^{\tilde{\mathbf{A}}_{ab}} \hat{\mathbf{x}}_{ab}(t) + \mathbf{G}_{ab} \begin{matrix} \mathbf{w}_{abnoisy}(t) \\ \mathbf{0} \\ q_1(t) \\ \dot{q}_1(t) \\ \ddot{q}_{gnoisy}(t) \end{matrix} + \mathbf{L}_{ab} \begin{matrix} \mathbf{y}_{ab}(t) = \mathbf{y}_b(t) \\ q_{bnoisy}(t) \\ f_{Dnoisy}(t) \end{matrix}$		$\dot{\hat{\mathbf{x}}}_{ss}(t) = \overbrace{(\mathbf{A}_{ss} - \mathbf{L}_{ss} \mathbf{D}_{ss})}^{\tilde{\mathbf{A}}_{ss}} \hat{\mathbf{x}}_{ss}(t) + \tilde{\mathbf{G}}_{ss} \begin{matrix} \tilde{\mathbf{w}}_{ssnoisy}(t) \\ \ddot{q}_{gnoisy}(t) \\ q_b(t) \\ \dot{q}_b(t) \end{matrix} + \mathbf{L}_{ss} \begin{matrix} \tilde{\mathbf{y}}_{ss}(t) \\ q_{1noisy}(t) \\ q_{2noisy}(t) \\ q_{3noisy}(t) \end{matrix}$	
Equation (5.36)		Equation (5.37)	
$\hat{\mathbf{y}}_{ab}(t) = \mathbf{D}_{ab} \hat{\mathbf{x}}_{ab}(t)$		$\hat{\mathbf{y}}_{ss}(t) = \tilde{\mathbf{D}}_{ss} \hat{\mathbf{x}}_{ss}(t)$	
Equation (5.36)		Equation (5.37)	
The solutions to the state equations of the observers were obtained via the state transition matrix in an sequential way (see Equation (5.46)).			

Table 5.5 was divided into two sections for the structure and the observer. Besides, the original equation numbers are presented in Table 5.5. The *noisy* subscript in the performed measurements indicates that the related variable contain some amount of noise. The disturbance, i.e. the ground excitation, was sent to the observer after a recording procedure. Therefore, it was noisy.

The responses of the structure were calculated via the Newmark's numerical integration method for multi degree-of-freedom linear systems (Chopra, 1995). The average acceleration method was utilized in the calculations. It is unconditionally stable for every time increment value. On the other hand, the time interval should be small enough for the accuracy of the results. The time increment  $dt$  was chosen as 0.002 seconds for the present research. The solution to the state equations of the observers was obtained via the state transition matrix in Equation (5.46) sequentially.

In the simulations, the relative story displacements and the damper force were assumed to be sensed. The noise was generated by the *randn*-functionality within MATLAB. Noises of all responses were formed individually. Otherwise, they would be correlated, which could create problems in the observer design violating the uncorrelatedness assumption of the noise sequences in the Kalman filter (see Section 5.5.1)

In order to utilize high numerical values for noise generation, the responses of the passive damper with minimum damping value were utilized for the displacements. The responses of the passive damper with maximum damping value were utilized for the damper force. In real world applications, the acceleration measurements are more noisy than the displacement measurements (Turan & Aydın, 2011). Therefore, white noise with a magnitude of 5% of their standard deviation was added to the simulated displacement responses as sensor noise. This value was 15% of its standard deviation for the damper force and the ground acceleration.

In the simulations by near-fault excitation, the displacements of the passive damper with minimum damping increased approximately ten times. Therefore, the noise magnitude in the displacement measurements was taken as 0.5% of the displacements' standard deviation. The noise ratios in damper force and accelerations remained unchanged since their maxima and standard deviations were in the same range as the response that was based on the far-field type ground excitations.

In the present simulations, the stability of the closed loop regulator was checked although there was not an explicit control input to the system (the control effect was

applied by changing the damping value of the VOD). Stability of the augmented base's observer and observer stability of the superstructure were confirmed. Additionally, stability of the shaping filter utilized to prewhiten the base observer was checked.

Observability of the augmented base and the superstructure's observability were confirmed. Positive-definiteness of the chosen  $\mathbf{Q} - \mathbf{R} - \mathbf{P}$  values was confirmed by their eigenvalues in the Kalman-Bucy estimator designs of the augmented base and the superstructure.

### **5.8.3. Block Diagram of the System**

The block diagram of the system is presented in Figure 5.19. The fundamental file of the computer program is present in Appendix E. The sub-files (or subroutines) were executed in the MATLAB file by simply calling their filenames.

The system is mainly composed of the structure, the observer, and the controller. The structure was splitted into two for the observer design as: the base and the superstructure. The base was augmented by a low-pass shaping filter for prewhitening. The superstructure was diagonalized to obtain independent subsystems for the observer design. The observers of the base and the superstructure were designed for the augmented base and the diagonalized superstructure. The observed responses were calculated separately. The dashed line indicates the modification of the Kalman-Bucy observer by sending the disturbances to it.

At the beginning of the simulation, the properties of the base and the superstructure were defined. The ground excitation record was read and interpolated to the one fifth of the original time increment of the data due to the computational requirements. Additionally, this remedy made the transition among different VOD damping values smoother (see Chapter 2 for details).

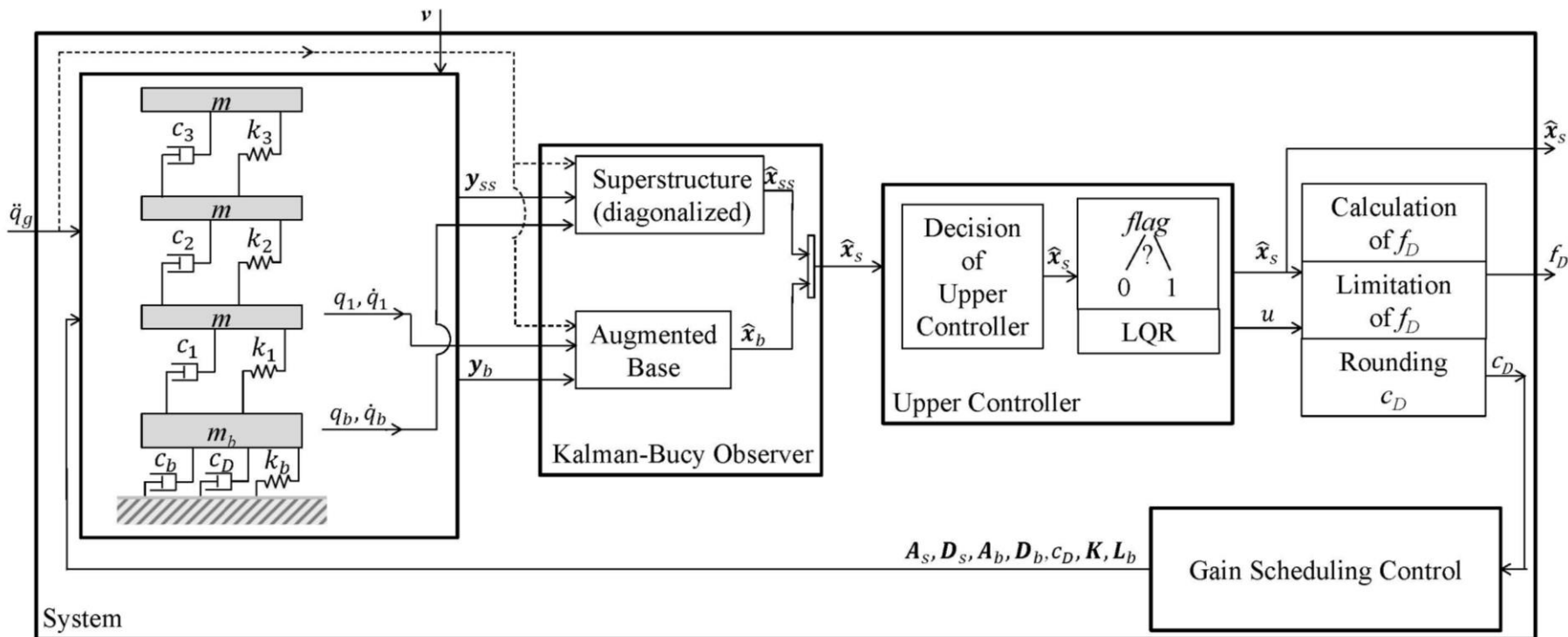


Figure 5.19. Block diagram of the system

Then, the responses of the systems with two passive dampers whose damping values were the minimum and maximum of the damping values defined in Section 5.3 were calculated. By means of these passive responses, the noises were generated for the variables that were assumed to be sensed. The displacements of the base and the floors, which were relative to the ground, were assumed to be measured. Furthermore, the damping force of the VOD was assumed to be measured. White noise with a magnitude of 5% of the standard deviation of the simulated displacements was added to the simulated responses as sensor noise. Additionally, for the damper force measurement, white noise with a magnitude of 15% of the standard deviation of the simulated damper force was added to the simulated responses as sensor noise.

After the memory allocation was performed for the variables that would be used in the time loop, the inner controller was designed. It calculated and stored the damping matrix, state matrix, measurement matrix, LQR gain matrix, and observer gain matrix for all orifice opening positions ( $c_D = 100, 200, 300, 400, 500, 600, 700, 800, 900, 1000, 1500, 2000, 2500, 3000, 10000, 15000, 20000, \text{ and } 25000$  Ns/m, where  $c_D$  is the damping value of the VOD). When the required damping value was determined in the simulation loop, the corresponding matrices were retrieved among the previously calculated matrices by means of a gain scheduling controller. This coding remedy was preferred for reducing the calculation time. The LQR and the Kalman-Bucy observer were designed for all damping values of the VOD (see Section 5.7 for details). The LQR was designed for the 4-by-4 system including the base. On the other hand, the Kalman-Bucy observer was designed for the substructured system.

Afterwards, the response calculation started in a time loop. Initially, the controller was at rest, during which the damper was at its minimum resistance. The plant response was calculated by the matrices of the previous time step. Then, the measured responses were performed. The observed states were obtained individually for the augmented observer and superstructure. The smallest damper velocity was limited to 1 mm/s since a value smaller than 1 mm/s could not be measured correctly. Hence, this numerical precaution also prevented a “divide by zero” error in the calculation of the optimum damper constant.

Any explicit control force was not applied to the system. The optimal control force was calculated by the LQR, and it was supplied to the system by simply changing the orifice setting of the damper. The upper controller was designed to switch between different feedback control gains during earthquake simulations. The upper controller

also decided when the optimum control forces had to be applied. The decision mechanism is presented in Figure 5.14. The observer states were less noisy than the measured ones. Therefore, the upper controller was fed by them. In a simulation, the observer had to calculate the same responses as the actual system in absence of noise since they become identical.

After the required control force  $u$  was determined, the  $c_D$  value was calculated and rounded to an applicable damper force. Additionally, if the calculated  $c_D$  value had been out of the limits of the capacity of the VOD, then it would have been taken into the limits. Finally, the damper force was calculated, and the responses were presented by the graphics.

#### 5.8.4. Simulations of the 1940 Imperial Valley Earthquake

The excitation record utilized in the present subsection belongs to the 1940 Imperial Valley earthquake. It is presented in time- and frequency-domains in Figure 2.4. The simulation responses of the superstructure's drifts are presented in Figure 5.20 and Figure 5.21. While plotting the responses, complex components were neglected due to their very small magnitudes ( $10^{-17}$ ). The displacements and velocities of the base did not have any imaginary part since the base was not diagonalized for the observer design. The accelerations did not have complex components since they were not observed nor diagonalized.

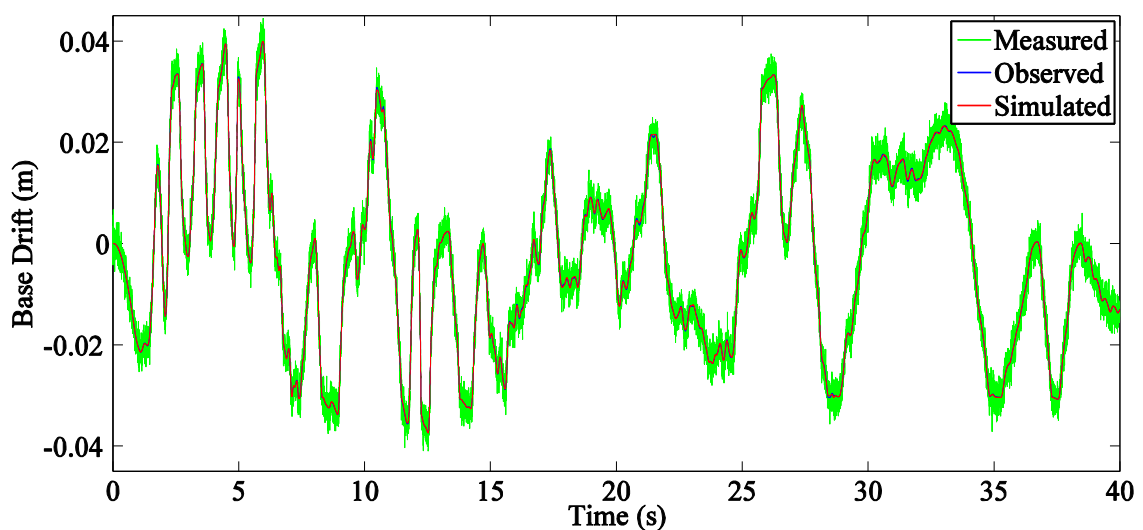


Figure 5.20. Response of the base displacement with respect to the ground due to the Imperial Valley earthquake

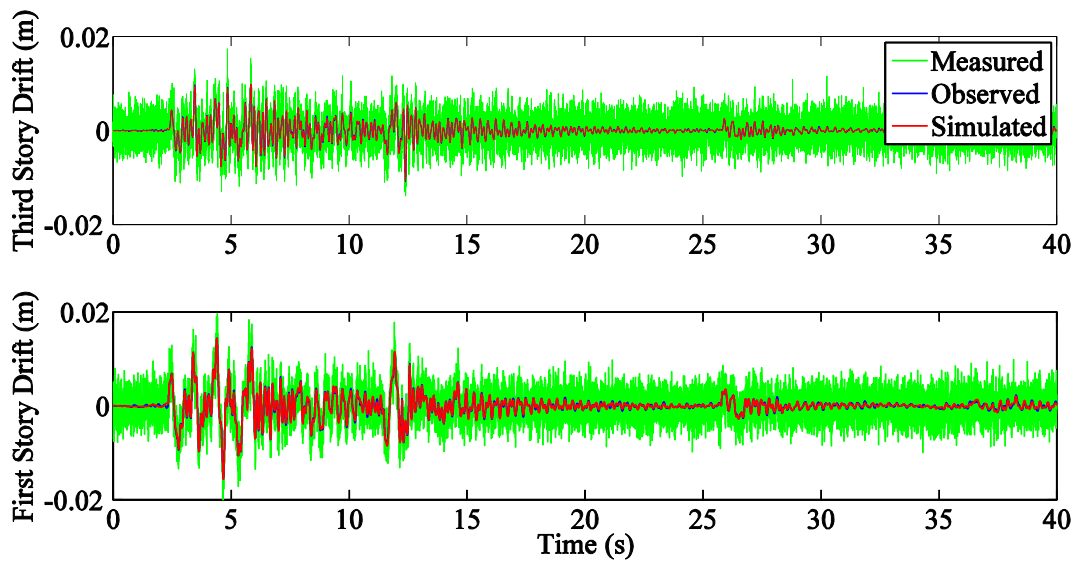


Figure 5.21. Interstory drifts of the superstructure due to the Imperial Valley earthquake

The states of the system were the displacements and the velocities of the floors relative to the ground. The floor displacements relative to the ground and the damper force were assumed to be sensed. In the simulations, the measured values were obtained by adding certain amount of the standard deviation of the related quantity to the simulated responses. Therefore, the magnitudes of the noise of the interstory drifts were high. Eventually, the observer was successful to estimate the simulated responses from the measured ones and to filter out the noisy parts of the response. The interstory velocities of the base and the superstructure are presented in Figure 5.22 and Figure 5.23, respectively.

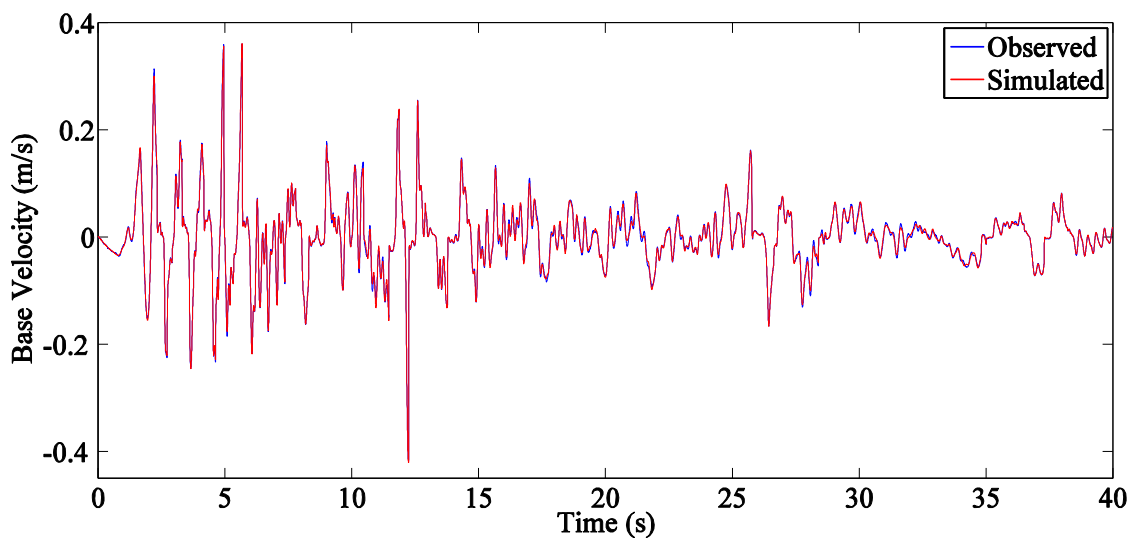


Figure 5.22. Base velocity response due to the Imperial Valley earthquake

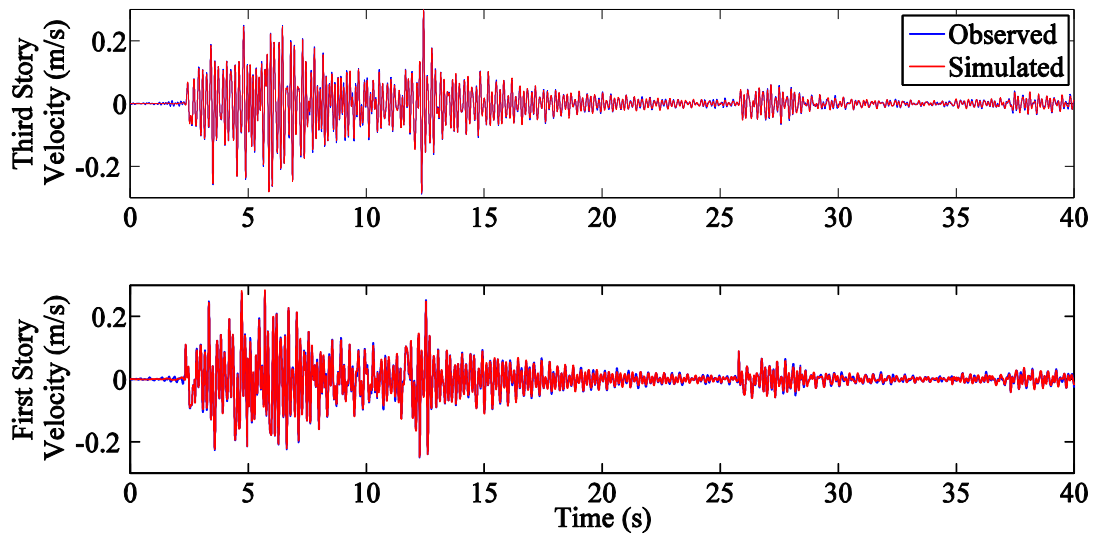


Figure 5.23. Interstory velocities due to the Imperial Valley earthquake

The total acceleration values of the base, first, and third stories are presented in Figure 5.24. According to the responses in Figure 5.20-Figure 5.24, the designed observer satisfactorily filtered out the noise. The absolute acceleration responses of all devices were satisfactory, except for some aggressive peaks which were present in the controlled response of the system at the base level.

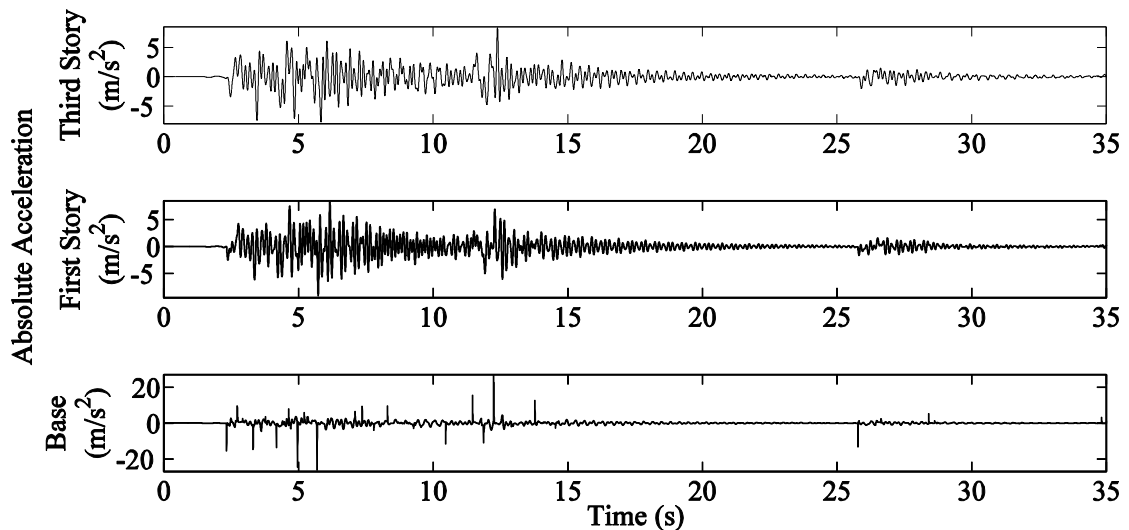


Figure 5.24. Absolute accelerations due to the Imperial Valley earthquake

### 5.8.5. Simulations of the 1999 Düzce Earthquake

The excitation record utilized in the present subsection belongs to the 1999 Düzce earthquake. It is presented in time- and frequency-domains in Figure 2.4. The simulation responses of the superstructure's drifts are presented in Figure 5.25 and Figure 5.26.

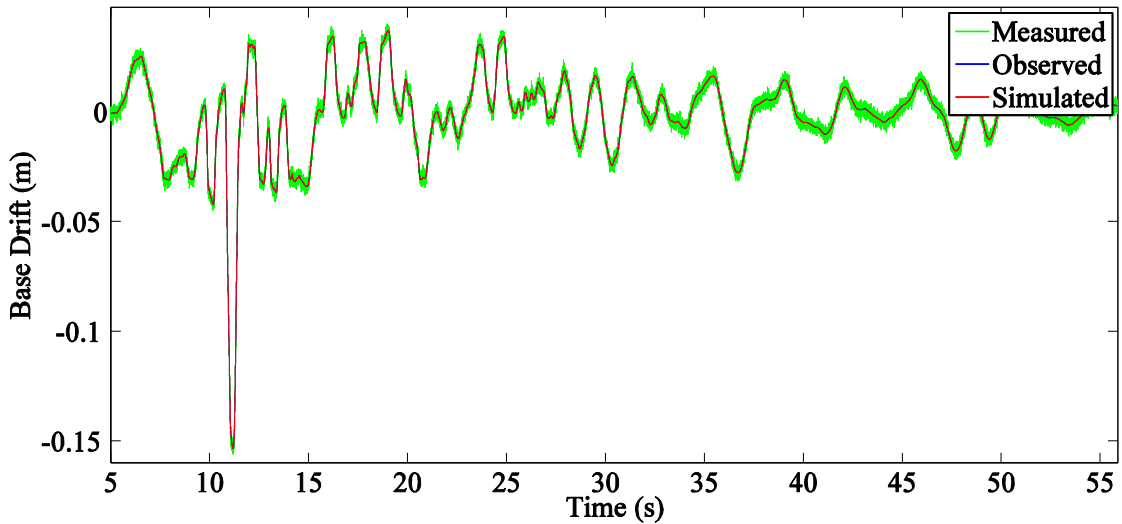


Figure 5.25. Response of the base displacement with respect to the ground due to the Düzce earthquake

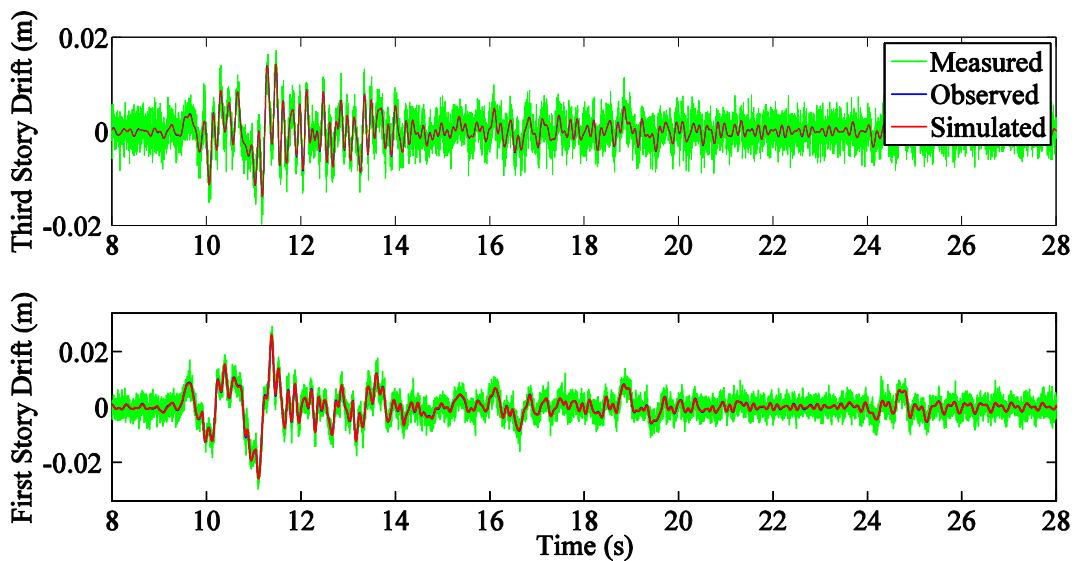


Figure 5.26. Interstory drifts of the superstructure due to the Düzce earthquake

The imaginary parts of the displacements and velocities of the superstructure were neglected due to their very small magnitudes. The interstory velocities of the base and the superstructure are presented in Figure 5.27 and Figure 5.28, respectively. Finally, the absolute accelerations of the base, first, and third floors are presented in Figure 5.29.

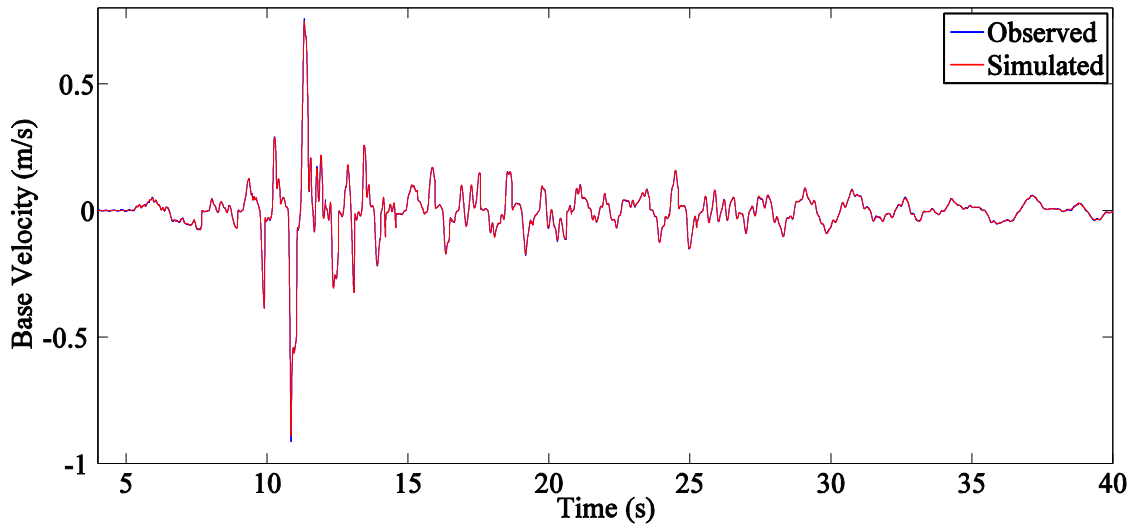


Figure 5.27. Base velocity response due to the Düzce earthquake

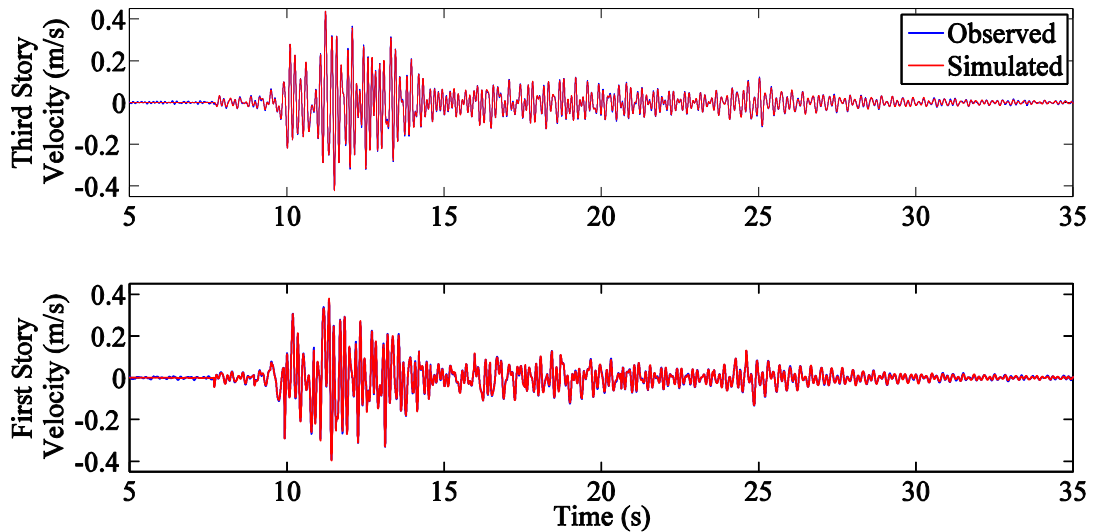


Figure 5.28. Interstory velocities due to the Düzce earthquake

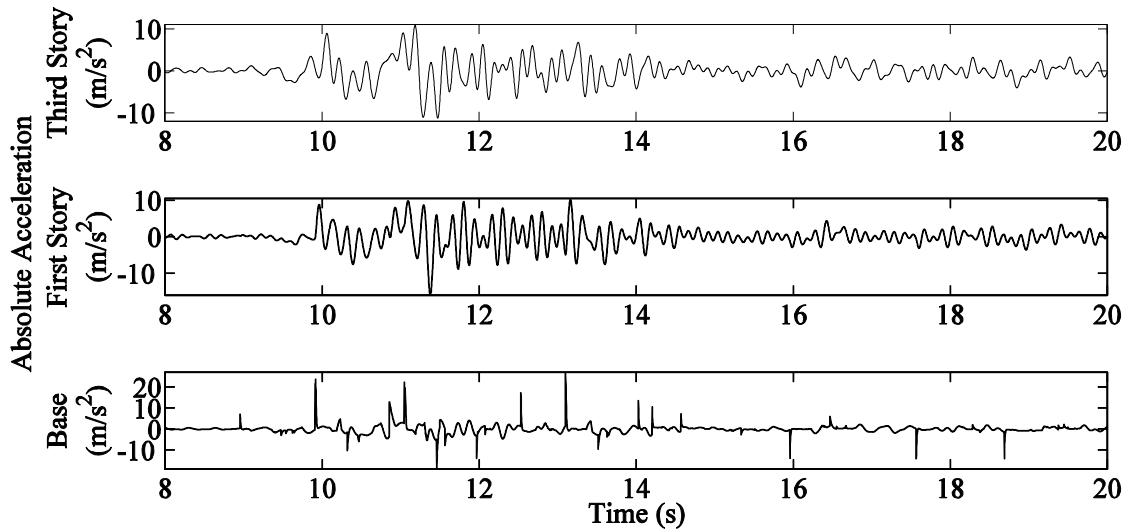


Figure 5.29. Absolute accelerations due to the Düzce earthquake

### 5.8.6. Simulations of the Ground Excitation Data *Synthetic1*

The seismic data in Figure 2.4 was offset to the higher period range in the frequency spectrum to investigate the controller performance for near-fault earthquakes. It was named *Synthetic1*. It is presented in Figure 5.17 in frequency domain. The fundamental mode of the isolated structure were affected maximally due to the frequency spectrum of the excitation *Synthetic1*. The observer and controller designs remained unchanged to test the performance of them under a situation of a frequency overlap of excitation and system. There was only one change in the MATLAB code for synthetic excitations compared to the simulations of the Imperial Valley and Düzce earthquakes: The displacements of the passive damper with minimum damping increased approximately ten times. Therefore, the noise magnitude in the displacement measurements was taken as 0.5% of the standard deviation of the displacements. The noise ratios in damper force and accelerations remained unchanged since their maxima and standard deviations were in the same range as the responses to the Imperial Valley and Düzce earthquakes.

The simulation responses of the superstructure's drifts are presented in Figure 5.30 and Figure 5.31. High displacements and velocities were the expected outcomes of near-fault earthquakes, which were observed in Figure 5.30-Figure 5.32 and Figure 5.34-Figure 5.36.

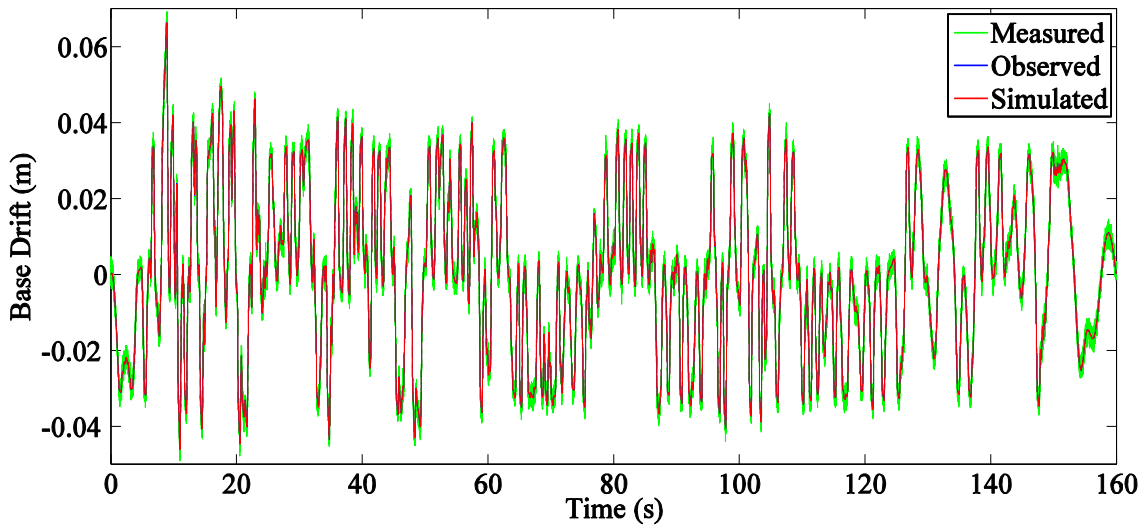


Figure 5.30. Response of the base displacement with respect to the ground due to the data *Synthetic1*

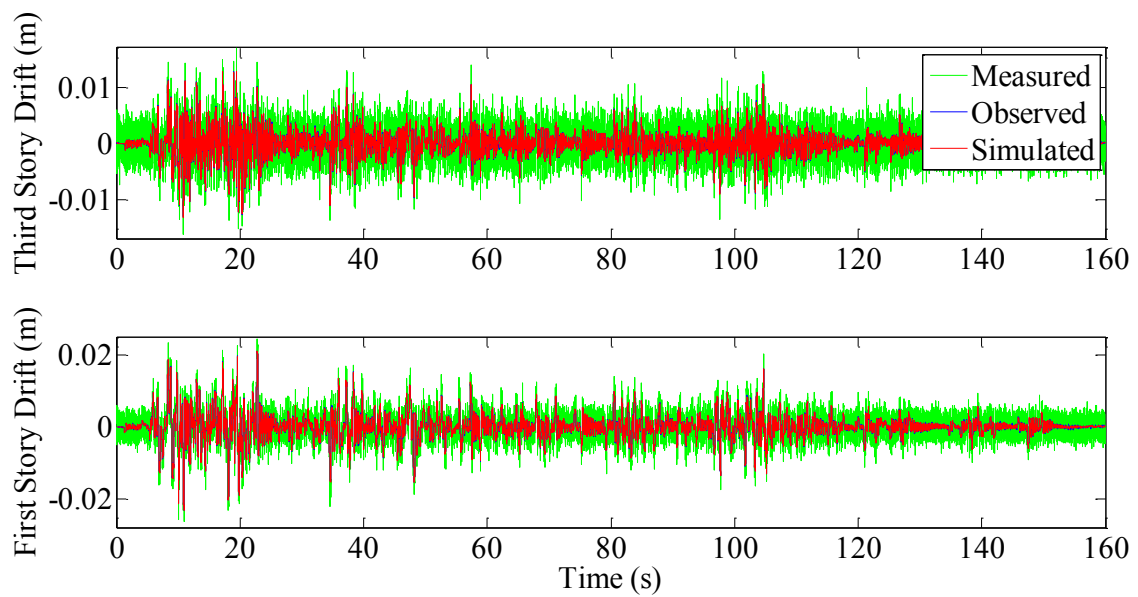
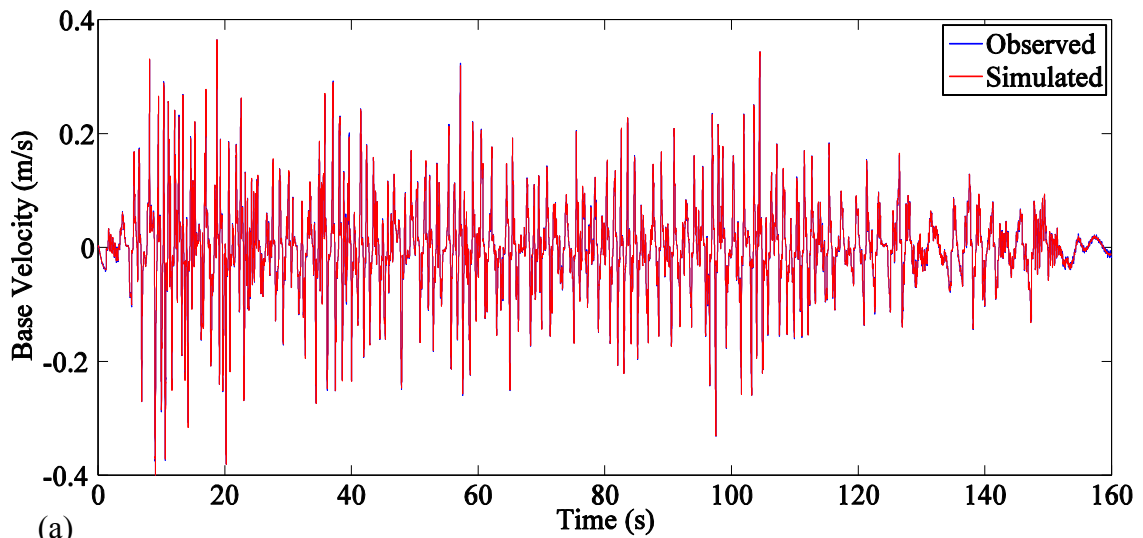
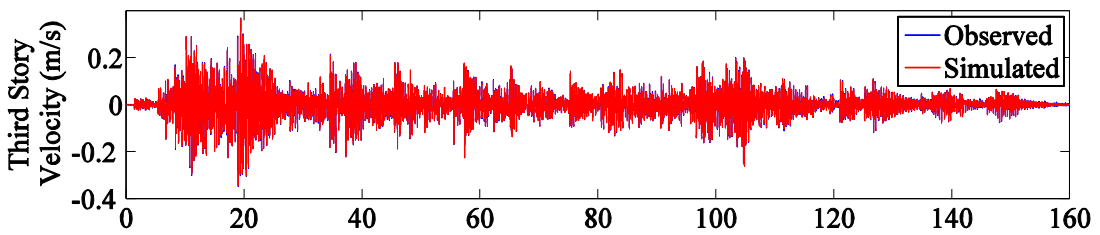


Figure 5.31. Interstory drifts of the superstructure due to the data *Synthetic1*

In Figure 5.30 and Figure 5.31, it was observed that the observer could predict the simulated response successfully, while filtering the measured values successfully. The interstory velocities of the base and the superstructure are presented in Figure 5.32. The total accelerations values of the base, the first, and the third stories are presented in Figure 5.33.



(a)



(b)

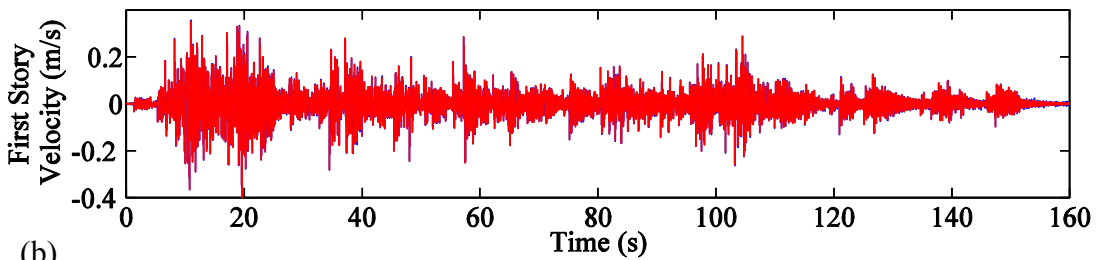


Figure 5.32. (a) Base velocity and (b) interstory velocities due to the data *Synthetic 1*

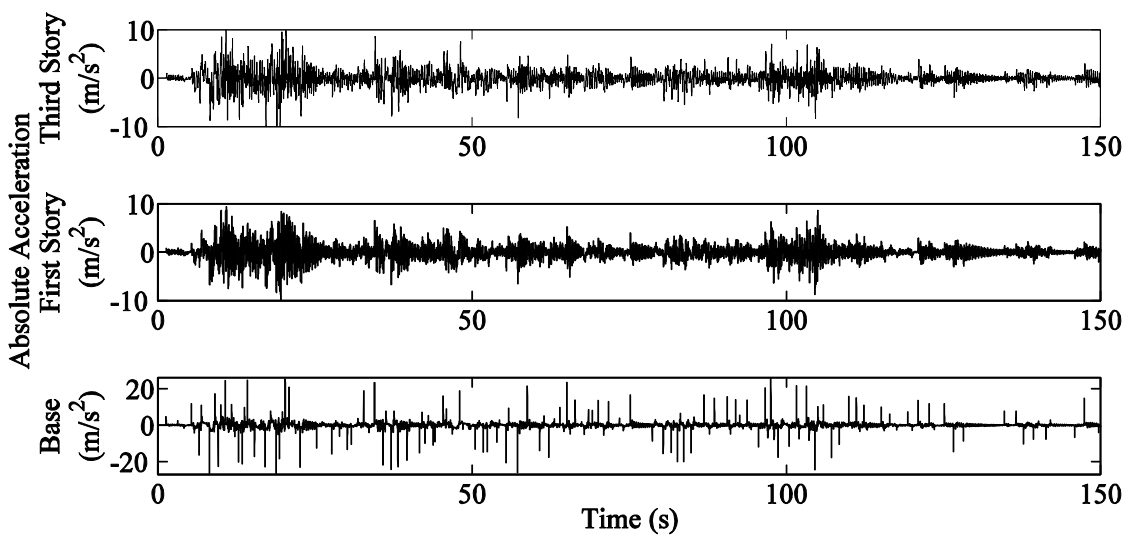


Figure 5.33. Absolute accelerations due to the data *Synthetic 1*

### 5.8.7. Simulations of the Ground Excitation Data *Synthetic2*

The simulation responses of the superstructure's drifts are presented in Figure 5.34 and Figure 5.35 for the near-field *Synthetic2* excitation. The interstory velocities of the base and the superstructure are presented in Figure 5.36. The absolute accelerations of the base and the superstructure are presented in Figure 5.37.

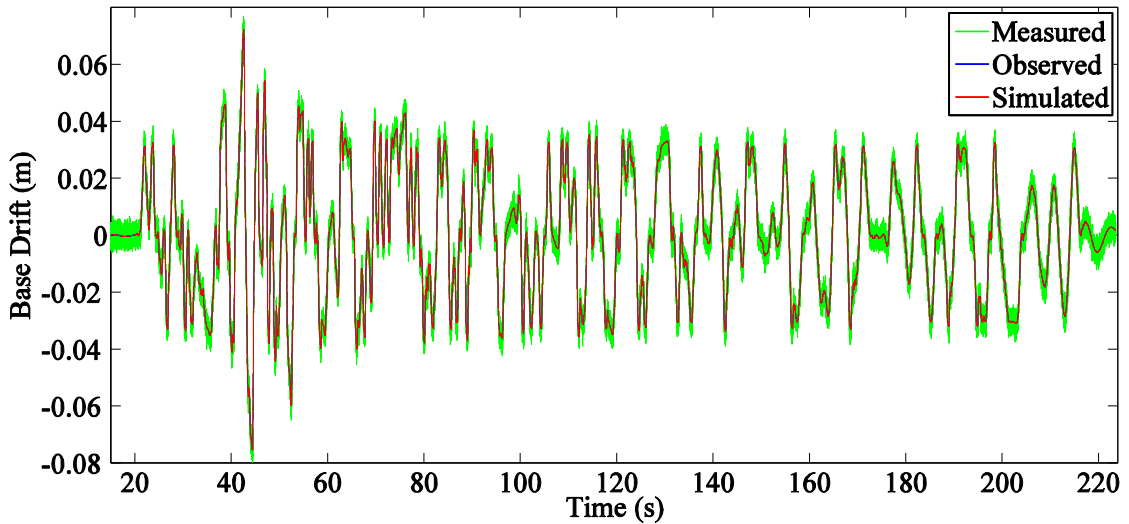


Figure 5.34. Response of the base displacement with respect to the ground due to the data *Synthetic2*

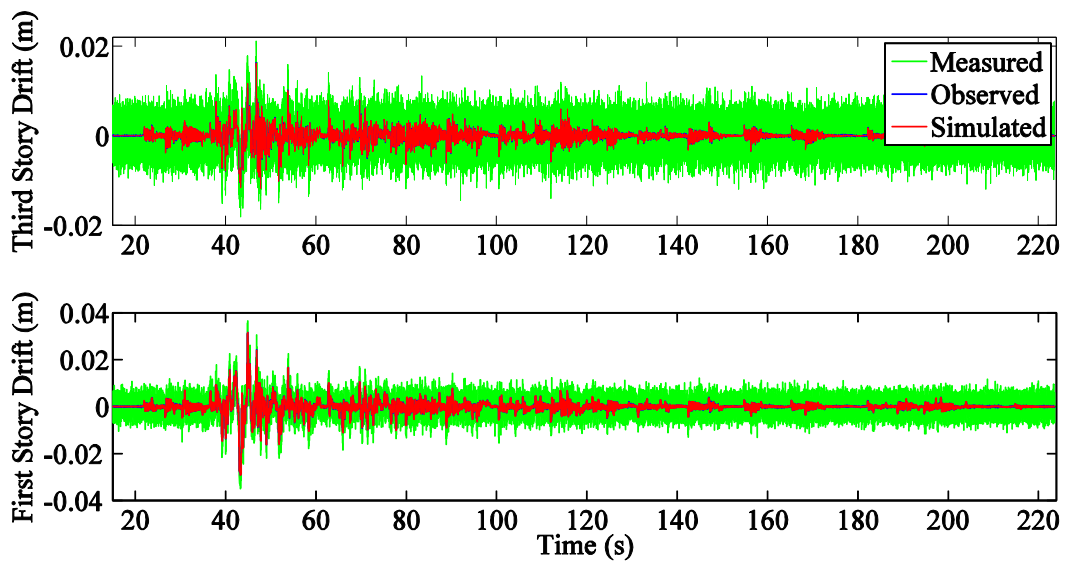


Figure 5.35. Interstory drifts of the superstructure due to the data *Synthetic2*

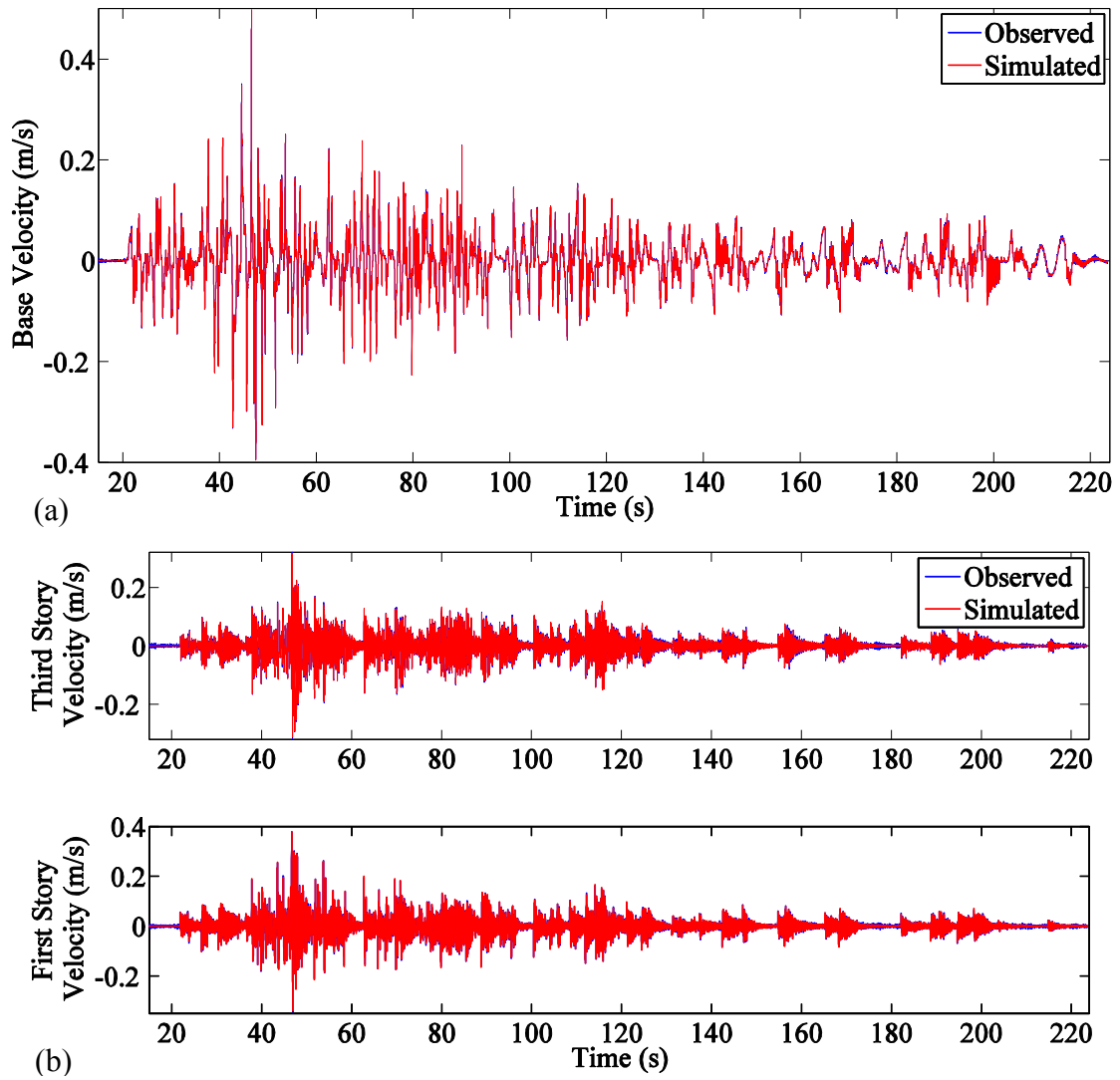


Figure 5.36. (a) Base velocity and (b) interstory velocities due to the data *Synthetic2*

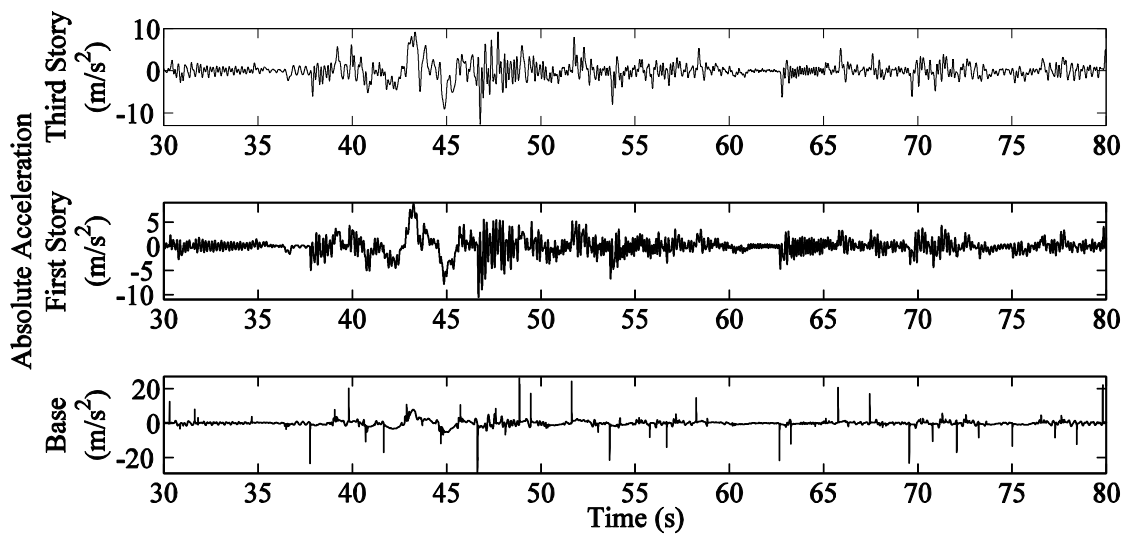


Figure 5.37. Absolute accelerations due to the data *Synthetic2*

### 5.8.8. The Variable *PoleRatio* in the Observer Design

The variable *PoleRatio* defined by Equation (5.22) is one of criteria in the observer design. In the literature, it has been suggested that the modes of an observer should be 2-4 times faster than those of the system (Arıkan & Erçan, 2011). This suggestion could be fulfilled for the observer of the superstructure. Although remarkable effort was paid for the observer design of the augmented base, unfortunately the recommended values for *PoleRatio* could not be achieved (see Table 5.6). Although the elements of the variable *PoleRatio* are one, the observer could estimate the response at the base level successfully. At least, the observer was not slower than the hybrid controlled structure.

The initial values of the  $\mathbf{Q} - \mathbf{R}$  couple for the augmented base and the diagonalized superstructure were chosen as the covariances of the numerical simulation outputs and the noise assumed.  $\mathbf{Q}$  was held constant, and  $\mathbf{R}$  was multiplied by a factor that was depicted from a logarithmically changing vector. An observer was designed for every  $\mathbf{Q} - \mathbf{R}$  couple in an inner loop. When the variable *PoleRatio* was in the desired interval, then the loop was stopped, and the convenient observer system was calculated. The initial values of the  $\mathbf{Q} - \mathbf{R}$  couple for the augmented base and the diagonalized superstructure are listed as follows

$$\mathbf{Q}_{ab} = \begin{bmatrix} 10^{-8} & 0 & 0 & 0 \\ 0 & 3.2 \cdot 10^{-4} & 1.3 \cdot 10^{-6} & -1 \cdot 10^{-4} \\ 0 & 1.3 \cdot 10^{-6} & 4.44 \cdot 10^{-3} & 4 \cdot 10^{-4} \\ 0 & -1 \cdot 10^{-4} & 4 \cdot 10^{-4} & 1.0041 \end{bmatrix} \quad (5.52)$$

$$\mathbf{R}_{ab} = \begin{bmatrix} 3.05 \cdot 10^{-4} & -0.8919 \\ -0.8919 & 61602 \end{bmatrix} \quad (5.53)$$

$$\mathbf{Q}_{ss} = \begin{bmatrix} 0.2715 & 0.0043 & -0.0174 \\ 0.0043 & 0.0005 & 3 \cdot 10^{-8} \\ -0.0174 & 3 \cdot 10^{-8} & 0.0065 \end{bmatrix} \quad (5.54)$$

$$\mathbf{R}_{ss} = 10^{-4} \begin{bmatrix} 0.3255 & 0.0063 & 0.0031 \\ 0.0063 & 0.3339 & -0.0034 \\ 0.0031 & -0.0034 & 0.3541 \end{bmatrix} \quad (5.55)$$

The subscript  $ab$  stands for the augmented base and  $ss$  is for superstructure. The symmetry of the matrices coincides with the physical case of the states. The logarithmically spaced vector started from  $10^{-8}$  till  $10^{12}$  with 1000 elements. Here, the ratios between  $\mathbf{Q}$  and  $\mathbf{R}$  are important, but not their numerical values.

The gains of the controller and observers are presented in Table 5.6 for three of the damping values of the VOD. The superstructure remained the same as the damping value of the VOD changed. Therefore, there was only one  $\mathbf{L}_{ss}$  matrix.

Table 5.6. Gains of the controllers and the observers and  $PoleRatio$  of the observers corresponding to the damping values of the VOD

	Controller	Observer of base		Observer of superstructure	
Damping of VOD $c_D$ (Ns/m)	LQR gain $\mathbf{K}$ $\begin{pmatrix} [kg/s] \\ [kg] \end{pmatrix}$	LQE gain of base $\mathbf{L}_b$ $\begin{pmatrix} 1/s & 1/kg \\ 1/s^2 & 1/(kg \cdot s) \end{pmatrix}$		LQE gain of superstructure $\mathbf{L}_{ss}$ $\begin{pmatrix} 1/s \\ 1/s^2 \end{pmatrix}$	$PoleRatio_{ss}$
100	$\begin{bmatrix} 51284 \\ 3928 \\ -169 \\ 2849 \\ 6862 \\ 793 \\ 660 \\ 676 \end{bmatrix}^T$	$10^{-11} \begin{bmatrix} 29.1 & 0.0004 \\ -21.5 & -0.01 \end{bmatrix}$		$\begin{bmatrix} -0.02 + i10^{-18} \\ -0.24 - i10^{-18} \\ 0.61 - i10^{-18} \\ 0.02 - i10^{-13} \\ -0.19 - i10^{-13} \\ 0.22 + i10^{-13} \end{bmatrix}$	$\begin{bmatrix} 1.00 \\ 1.00 \end{bmatrix}$
200	§	§		$\begin{bmatrix} -0.27 + i10^{-18} \\ 0.90 - i10^{-18} \\ -0.26 \\ -0.23 + i10^{-13} \\ 0.47 - i10^{-14} \\ -0.20 - i10^{-13} \end{bmatrix}$	$\begin{bmatrix} 1.00 \\ 1.00 \end{bmatrix}$
300	§	§		$\begin{bmatrix} 0.90 + i10^{-18} \\ -0.27 - i10^{-18} \\ -0.01 + i10^{-18} \\ 0.43 + i10^{-13} \\ -0.24 + i10^{-13} \\ 0.03 - i10^{-13} \end{bmatrix}$	$\begin{bmatrix} 1.00 \\ 1.00 \end{bmatrix}$
400	§	§			$\begin{bmatrix} 1.00 \\ 1.00 \end{bmatrix}$
500	§	§			$\begin{bmatrix} 1.00 \\ 1.00 \end{bmatrix}$
600	§	§			$\begin{bmatrix} 1.00 \\ 1.00 \end{bmatrix}$
700	§	§			$\begin{bmatrix} 1.00 \\ 1.00 \end{bmatrix}$
800	§	§			$\begin{bmatrix} 1.00 \\ 1.00 \end{bmatrix}$
900	§	§			$\begin{bmatrix} 1.00 \\ 1.00 \end{bmatrix}$
1000	§	§			$\begin{bmatrix} 1.00 \\ 1.00 \end{bmatrix}$

§ The related matrices were not supplied. The matrices of three cases ( $c_D=100, 1500, 25000$  Ns/m) were only presented to give an opinion to the reader.

(cont. on next page)

**Table 5.6. (cont.)**

1500	$\begin{bmatrix} 52410 \\ 2059 \\ 1014 \\ 2410 \\ 5654 \\ 757 \\ 669 \\ 664 \end{bmatrix}^T$	$10^{-11} \begin{bmatrix} 2.9 & 0.00004 \\ -32 & -0.01 \end{bmatrix}$	$\begin{bmatrix} 1.00 \\ 1.00 \end{bmatrix}$		
2000	§	§	$\begin{bmatrix} 1.00 \\ 1.00 \end{bmatrix}$		
2500	§	§	$\begin{bmatrix} 1.00 \\ 1.00 \end{bmatrix}$		
3000	§	§	$\begin{bmatrix} 1.00 \\ 1.00 \end{bmatrix}$		
10000	§	§	$\begin{bmatrix} 1.00 \\ 1.00 \end{bmatrix}$		
15000	§	§	$\begin{bmatrix} 1.00 \\ 1.00 \end{bmatrix}$		
20000	§	§	$\begin{bmatrix} 1.00 \\ 1.00 \end{bmatrix}$		
25000	$\begin{bmatrix} 61173 \\ -4086 \\ 1113 \\ -307 \\ 1022 \\ 231 \\ 240 \\ 234 \end{bmatrix}^T$	$10^{-13} \begin{bmatrix} 18 & 0.0003 \\ -3300 & -1 \end{bmatrix}$	$\begin{bmatrix} 1.00 \\ 1.00 \end{bmatrix}$		

In Table 5.6, the variable *PoleRatio* of the base was displayed. *PoleRatio* of the shaping filter was not presented since it was out of interest. Although the variable *PoleRatio* of the base could not be increased ( $PoleRatio = \begin{bmatrix} 1.00 \\ 1.00 \end{bmatrix}$ ), the responses of the base observer were successful. Therefore, the current observer design was accepted.

### 5.8.9. Damping Demand of the System

The optimum damping values of the VOD and the resulting damper forces are presented in Figure 5.38 and Figure 5.39 for the simulations of the Imperial Valley and *Synthetic1* earthquakes, respectively. Some undesirable peaks occurred in the simulated damper force. Since these peaks were made up of a single point, the damper was not able to perform these aggressive peaks.

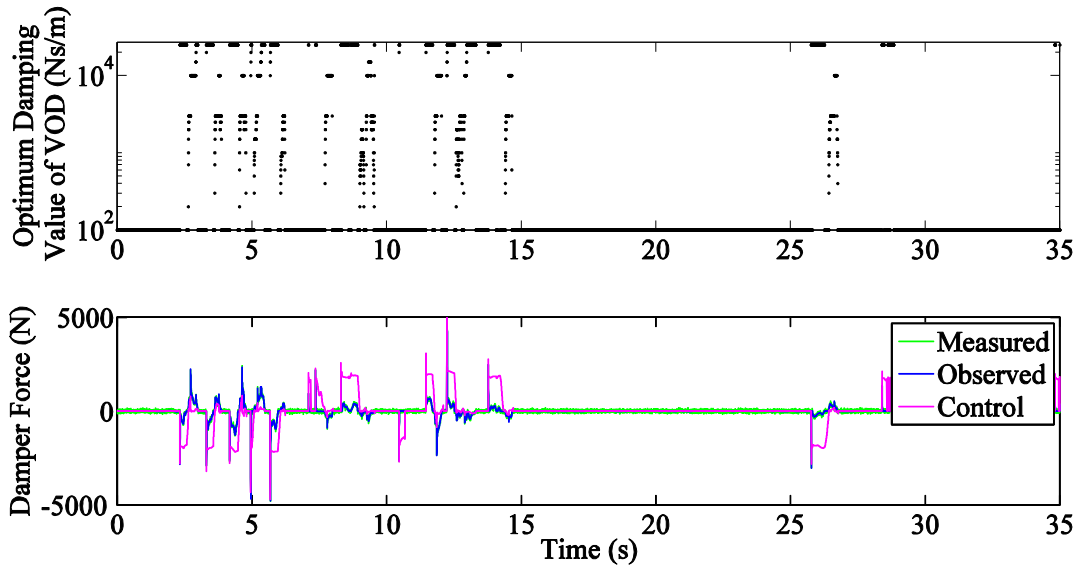


Figure 5.38. Optimum damping values of the VOD and the corresponding damper forces for the Imperial Valley event

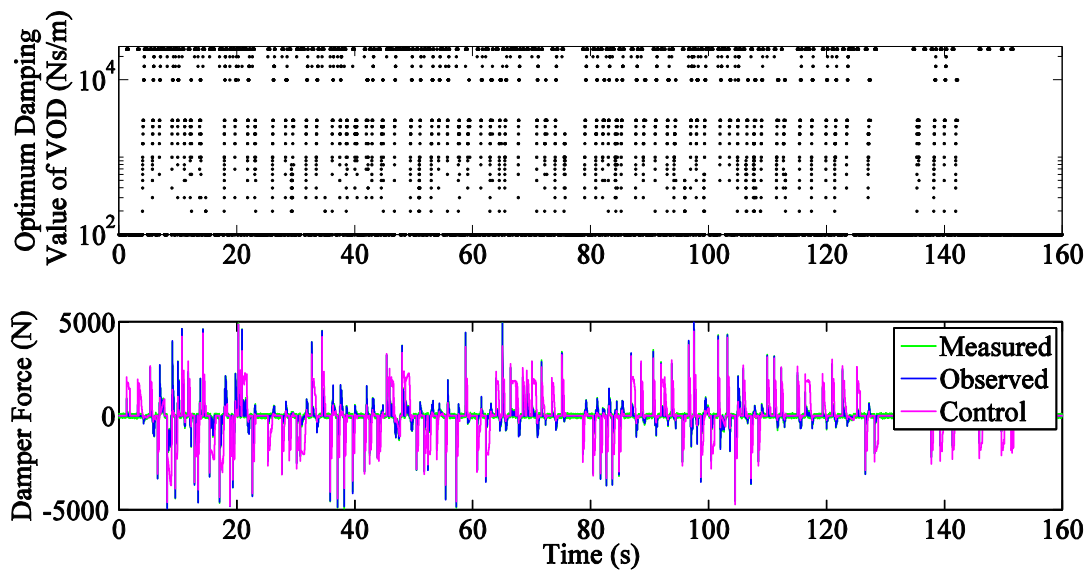


Figure 5.39. Optimum damping values of the VOD and the corresponding damper forces for the *Synthetic1* excitation

For the near-field excitation case (*Synthetic1* earthquake), the control force demand was much higher than that of the Imperial Valley event, as it was expected. The number of the undesirable peaks increased. In order to satisfy such high control demands, the upper controller chose damping values higher than those of the Imperial Valley earthquake, dispersed in the overdamped region.

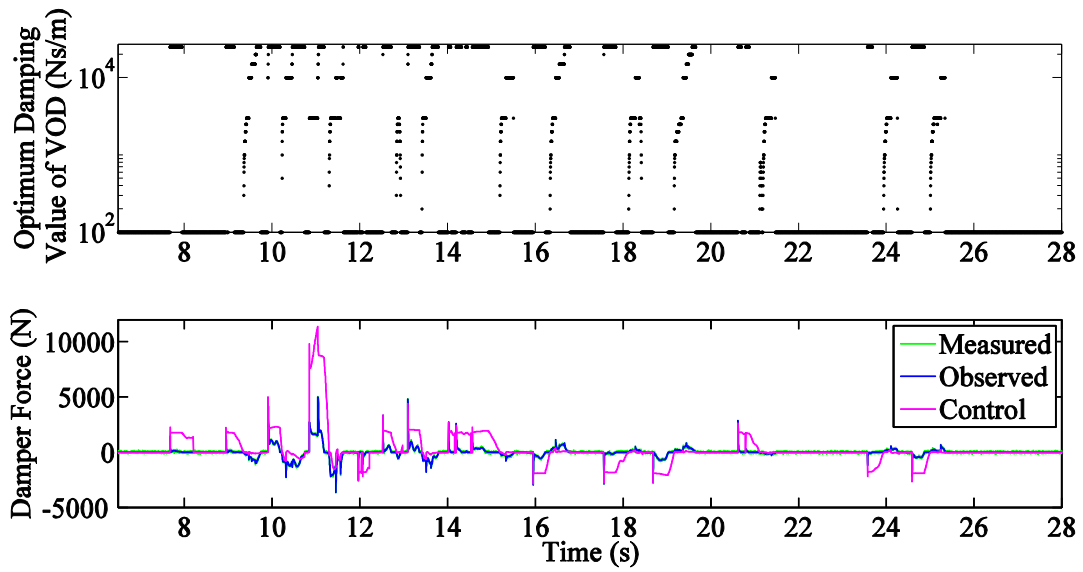


Figure 5.40. Optimum damping values of the VOD and the corresponding damper forces for the Düzce earthquake

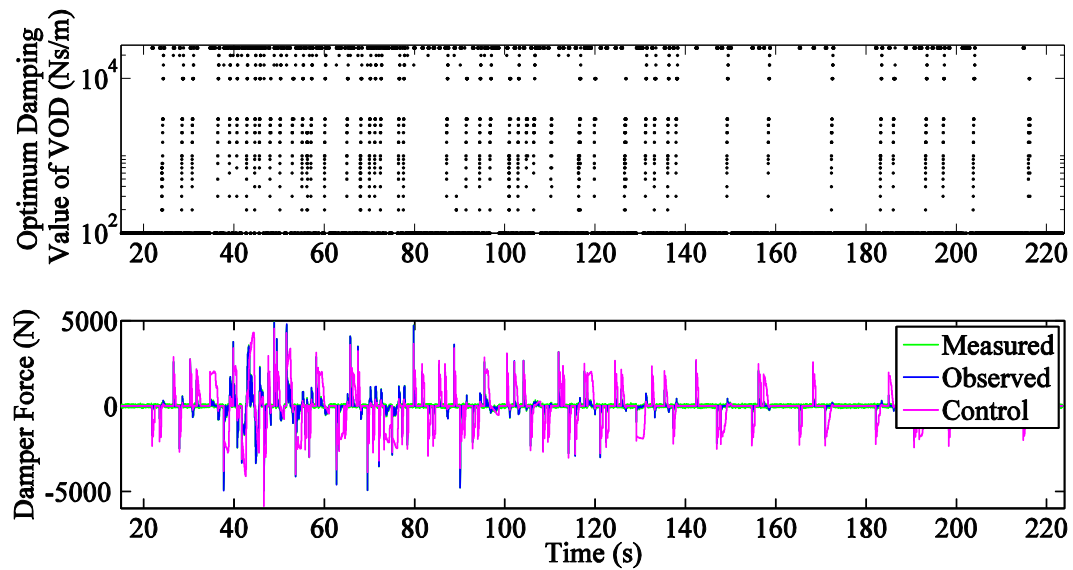


Figure 5.41. Optimum damping values of the VOD and the corresponding damper forces for the *Synthetic2* excitation

The optimum damping values of the VOD and the corresponding damper forces are presented in Figure 5.40 and Figure 5.41 for the simulations of the Düzce and *Synthetic2* earthquakes, respectively. The VOD could not provide the calculated high-frequency damping forces. Either the base velocity was not high enough or the application time of the high-valued control force was too short.

A slow and smooth transition from  $c_{min}$  to  $c_{max}$  could be performed by the damper successfully. If the controller had enforced the damper for an aggressive transition, then the damper would not have been able to achieve this task. In the numerical simulations, the damper force was obtained by the negation of the multiplication of the damping constant (evaluated at the previous time step) and the damper's velocity (or base velocity). At the current time step, the velocity most likely would be different from the velocity, for which the damping constant was evaluated. Thus, a difference in the optimum control force and the obtained damping forces was expected. Certainly, this situation was related to the selection of the  $Q - R$  values of the controller, which were the best ones among the tested values.

The significance of VOD was exhibited even in case of a near-fault excitation. The required damper force was zero within some regions, and the controller chose the minimum damping value (see Figure 5.38-Figure 5.41). The moderate and high level force demands were provided by changing the orifice opening size. If a passive damper with minimum damping had been placed, then the damper would not have satisfied the control requirements of the system. On the other hand, if a passive damper with maximum damping had been placed, then the structure would have exhibited an extremely over-damped behavior without performing oscillations. Therefore, placing a semi-active damper would have been a convenient design.

The fundamental response of the hybrid-controlled structure was over-damped for the damping values of the VOD higher than 1000 Ns/m (see Section 5.3). The number of times that the optimal damping value selected a value greater than 1000 Ns/m is presented in Table 5.7 for four ground excitations. The percentages are with respect to the total number in every excitation.

The critical damping case corresponded to the damping value of the VOD as 1057 Ns/m (see Section 5.3). Therefore, the response could not be critically damped due to the distribution of the damping values of the VOD. The number of under- or over-damped responses was almost same for the Imperial Valley and Düzce events. On the other hand, in case of a near-fault excitation, the response became over-damped more heavily. The toughest ground excitation in terms of number of over-damped response was *Synthetic1* earthquake.

Table 5.7. Number of under- and over-damped responses

Earthquake	Number of under-damped cases & their percentage	Number of over-damped cases & their percentage	Total number
Imperial Valley	16077 80.4%	3919 19.6%	19996 100%
Düzce	24176 86.5%	3770 13.5%	27946 100%
<i>Synthetic1</i>	50278 62.9%	29703 37.1%	79981 100%
<i>Synthetic2</i>	83661 74.8%	28120 25.2%	111781 100%

According to Table 5.7, the hybrid controlled structure can satisfy the system requirements within a large range of under- and over-damped responses for various excitations. This case is not possible for the isolated structure including a passive damper.

### 5.8.10. Maximum Total Shear Forces

The maximum total shear forces at the first floor of the superstructure were calculated according to Equation (4.31). The results are presented in Table 5.8. The aim was to investigate how much the columns of the superstructure were forced. The maximum values of the interstory drifts decreased as the floor number increased. This fact can be observed in Figure 5.21, Figure 5.26, Figure 5.31, and Figure 5.35 for four simulations. Therefore, the maximum shear force only at the first floor of the superstructure was presented.

All excitations were tough for the uncontrolled structure, especially the Düzce and *Synthetic1* data sets in terms of the maximum shear forces (due to the frequency distribution in Figure 5.17 and Figure 5.18). On the other hand, the *Synthetic2* excitation was the toughest one for the isolated structure including passive damper with  $c_{min}$ . The maximum total shear forces of the hybrid controlled structure were approximately 63%-75% of the isolated structure including passive damper with  $c_{max}$ , except for the *Synthetic1* excitation.

Table 5.8. Maximum total shear forces at the first floor of the superstructure

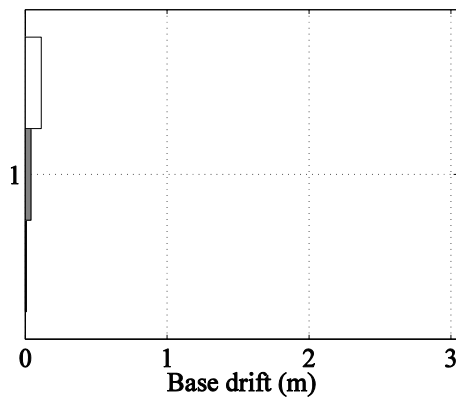
	Maximum shear force at the first floor (Newton)			
	Uncontrolled	Isolated structure + passive damper with $c_{min}$	Hybrid-controlled (isolated structure + VOD)	Isolated structure + passive damper with $c_{max}$
Imperial Valley	2918	94	1230	1905
Düzce	4820	174	2063	3183
<i>Synthetic1</i>	5371	531	1797	1832
<i>Synthetic2</i>	3641	1518	2458	3250

The maximum total shear force of the isolated structure including a passive damper system with minimum damping value was the best among the responses of the others. On the other hand, its base drifts in Figure 5.42 were unacceptable. The reductions of the maximum total shear forces of the hybrid controlled structure were satisfactory compared to those of uncontrolled structure even in case of a frequency overlap of excitation and system. The base drifts of the isolated structure including a passive damper system with maximum damping value were low in Figure 5.42. On the other hand, its maximum total shear forces were high. Therefore, the hybrid controlled structure exhibited a balancing performance between the responses of isolated structures including passive dampers.

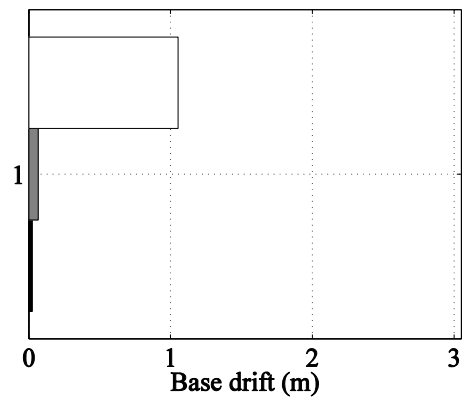
### 5.8.11. Comparison of the Responses of the Hybrid Controlled Structures with Passive Dampers and VOD

In the present subsection, the responses of the hybrid controlled structure with three different dampers were exhibited. The dampers were the optimally controlled VOD and two passive dampers whose damping coefficients were 100 and 25000 Ns/m (the damping constant range of the VOD was inbetween 100 and 25000 Ns/m). The structures with passive dampers were isolated seismically. The control actions applied to the VOD were not performed for the passive dampers. In the present study, the aim was to investigate whether applying a control scheme was profitable or it was better to place passive dampers instead of optimally controlled ones.

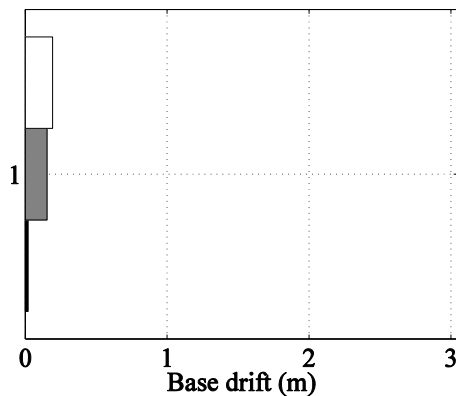
The main objective of controlling the response of the system was to decrease the interstory displacements and total accelerations of the superstructure. For this purpose, the structure was isolated seismically. On the other hand, in a seismic zone, there is always the possibility of a near-fault ground excitation. The isolation systems respond unsuccessfully in such regions due to the frequency distribution of the excitation. Therefore, in the current research, the isolation system was protected by the VOD. On the other hand, more damping at the base level prevented higher deformations of the base. As a result, the isolators were protected, but the story responses were larger when compared to the minimally damped case.



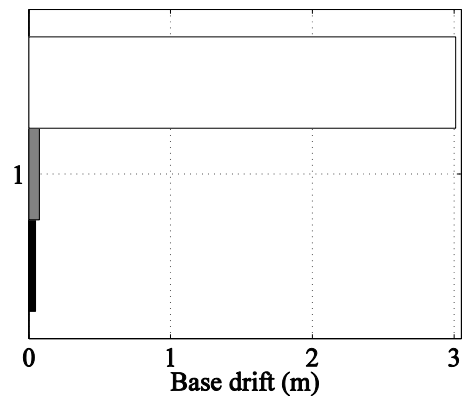
(a) Imperial Valley earthquake



(b) *Synthetic1* excitation



(c) Düzce earthquake



(d) *Synthetic2* excitation

□ Isolation + damper with min damping	■ Isolation + controlled damper	■ Isolation + damper with max damping
---------------------------------------	---------------------------------	---------------------------------------

Figure 5.42. Maximum absolute values of the simulated base drifts of the hybrid controlled structure

The maximum absolute values of the base drifts are presented for the Imperial Valley, Düzce, *Synthetic1*, and *Synthetic2* earthquakes in Figure 5.42. The minimally damped case exhibited poor drift responses in the base level as it was expected. According to Figure 5.42(a), the maximum drift was approximately three times greater than that of the controlled response.

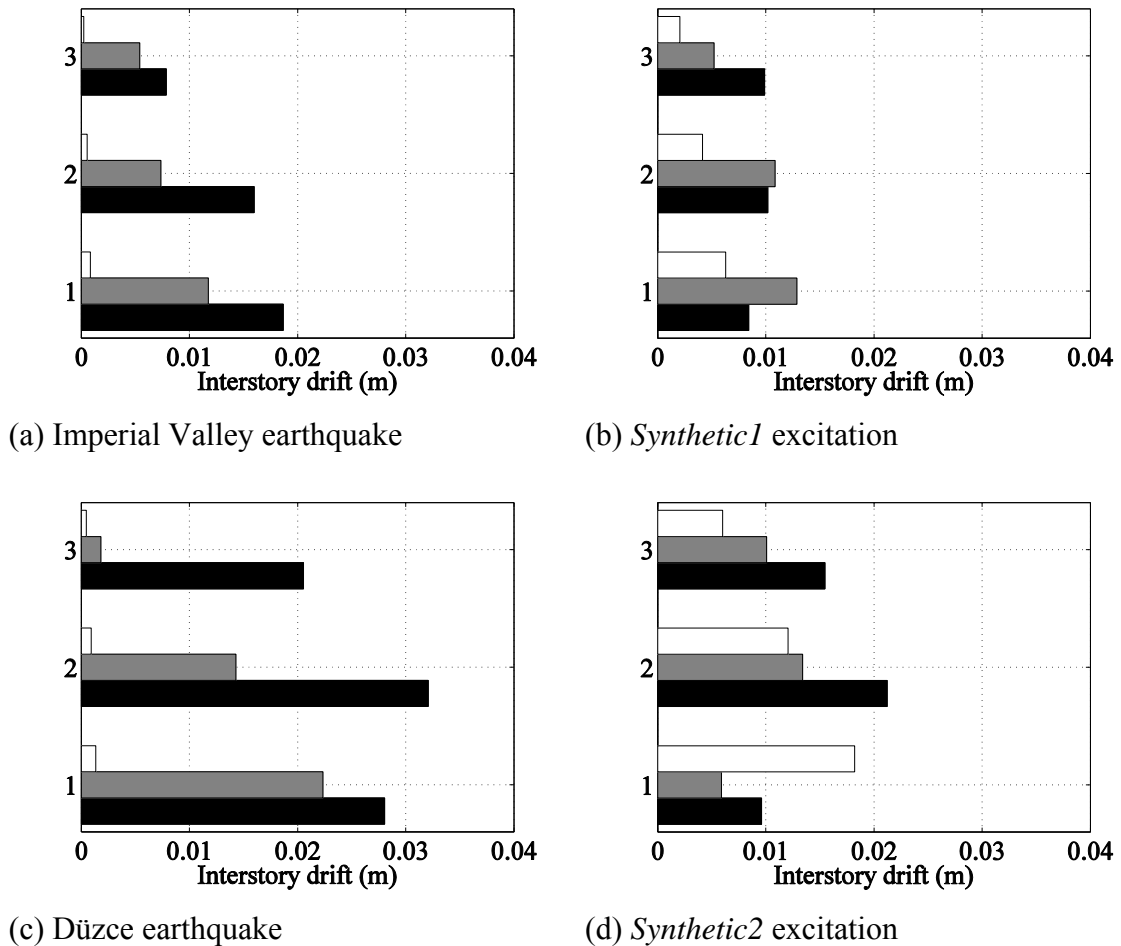


Figure 5.43. Maximum absolute values of the simulated interstory drifts of the hybrid controlled structure (Numbers on the vertical axis indicates the floor numbers)

In Figure 5.43, the base responses of the Düzce event was different from those of the other far-fault excitation due to its single high peak shock with a value of  $0.8g$ . The response of the minimally damped device was 16 and 38 times greater than that of the controlled device, similar to that of a base isolated structure in case of a near-fault

ground excitation since the damping value was very small ( $c_D = 100$  Ns/m). The base drifts of the system including a passive damper with minimum damping value were unacceptable in case of near-fault excitations.

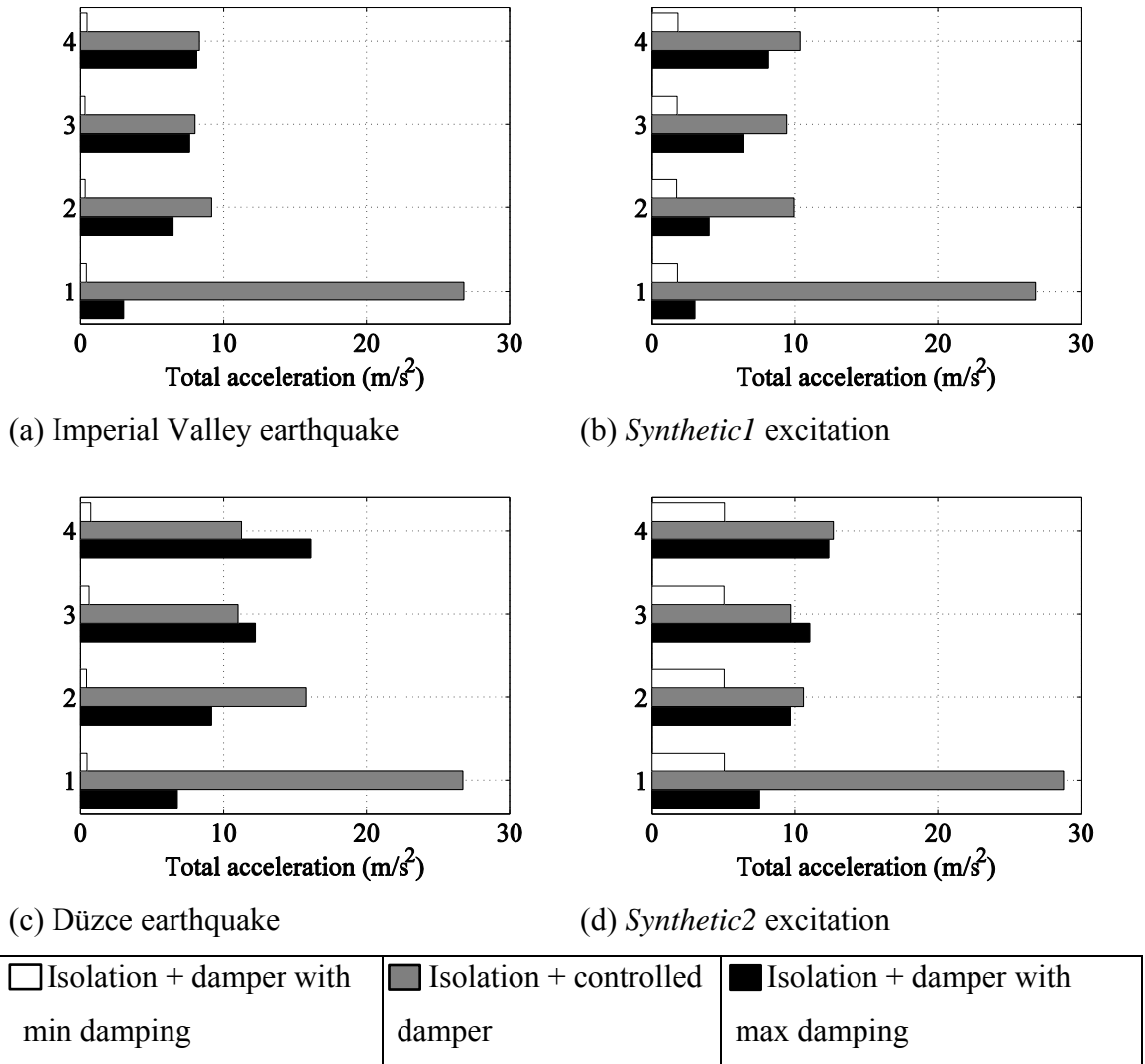


Figure 5.44. Maximum absolute values of the simulated total accelerations of the hybrid controlled structure (Numbers on the vertical axis indicates the floor numbers)

The maximum absolute values of the interstory drifts of the superstructure are presented for the Imperial Valley, Düzce, *Synthetic1*, and *Synthetic2* earthquakes in Figure 5.43. Except for the *Synthetic1* excitation, the interstory drifts of the hybrid controlled system were better than those of the system including a passive damper with maximum damping value. By adding a controllable damping (VOD) to the structural control system a reduction of more than 25% in terms of base displacement was

obtained compared to the case of passive damper with minimum damping value, while the floor displacements, which were still in acceptable range, increased.

The maximum absolute values of the total accelerations of the hybrid controlled structure are presented for the Imperial Valley, Düzce, *Synthetic1*, and *Synthetic2* earthquakes in Figure 5.44. At the first sight, the total accelerations at the base level were unacceptable for the hybrid control system. Nevertheless, its absolute accelerations at the floors were still in an acceptable range except for the response of Düzce earthquake. The absolute accelerations of floors for the VOD and passive damper with a maximum damping value were close for the *Synthetic2* excitation. Considering the advantages of the hybrid control system in terms of drifts, the high total accelerations at the base level may have been accepted by the designer.

The interstory drift of the third floor in frequency domain for the Imperial Valley and Düzce earthquakes are presented in Figure 5.45(a) and Figure 5.45(b), respectively. The simulated responses are presented. The systems are the ones in Figure 5.42-Figure 5.44. The graphics, which are zoomed only in vertical axis, are presented to compare the performance of the passive and hybrid controllers (see Figure 5.45(c) and Figure 5.45(d)). The interstory drift of the third floor in frequency domain for the synthetic earthquakes are presented in Figure 5.46.

According to Figure 5.45 and Figure 5.46, the uncontrolled response of the structure was driven mainly by the first mode at a damped period of approximately 0.51 seconds (indicated by black line). The second mode exhibited a smaller contribution to the response. When the VOD was added to the structure in addition to the base isolation, the period of the first mode was slightly shortened, and the contribution of the second and third modes had a larger effect on the response. The response of the structure with the minimally damped device was similar to the response of the base isolated structure since the damping of the device was small. The response of the structure with the minimally damped device had smaller magnitudes when compared to the responses of the other systems. Its response was driven by its fundamental mode, and the effect of its other modes on the response could not be observed.

According to Figure 5.45, the third floor drift of the structure with the minimally damped device had very small components within the period range for far-fault excitation cases. On the other hand, it responded more heavily in higher period ranges for near-fault excitation cases (see Figure 5.46).

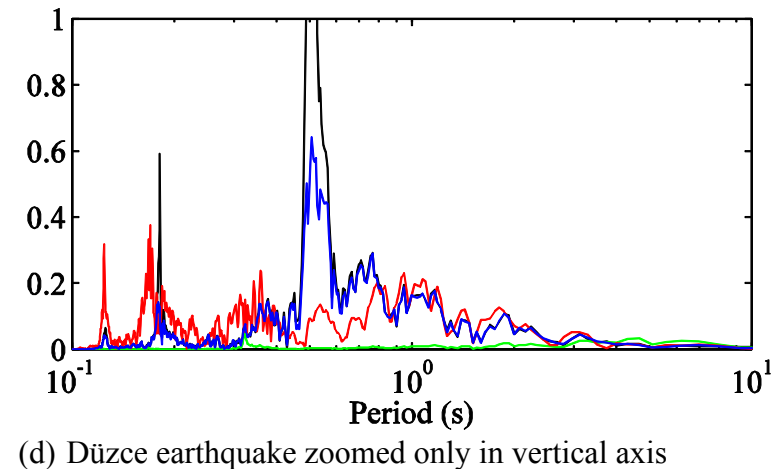
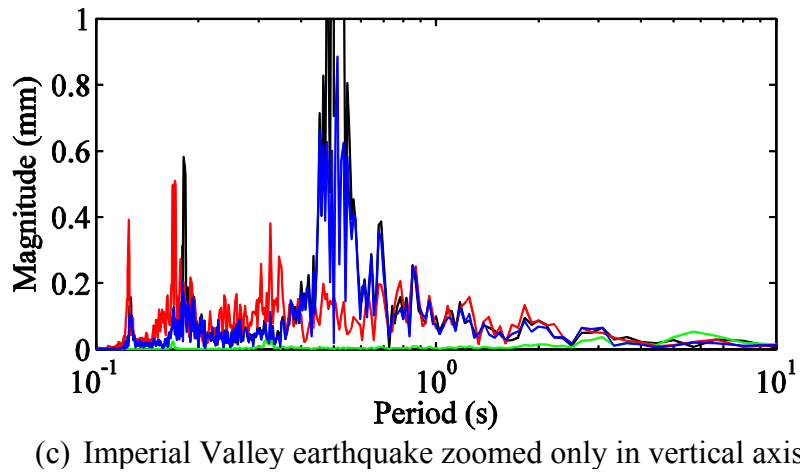
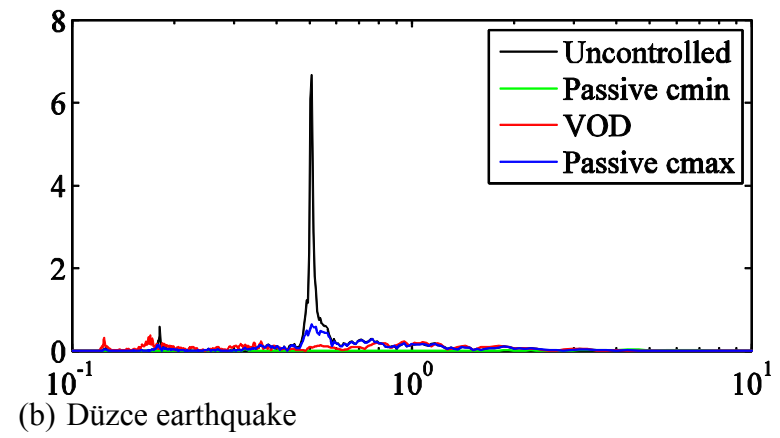
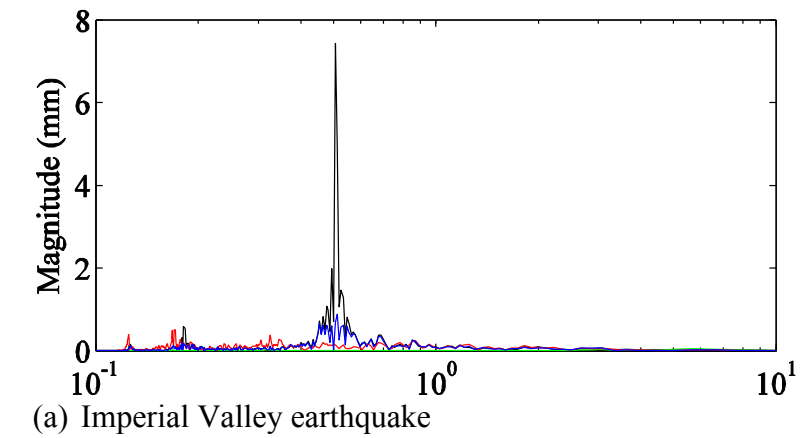
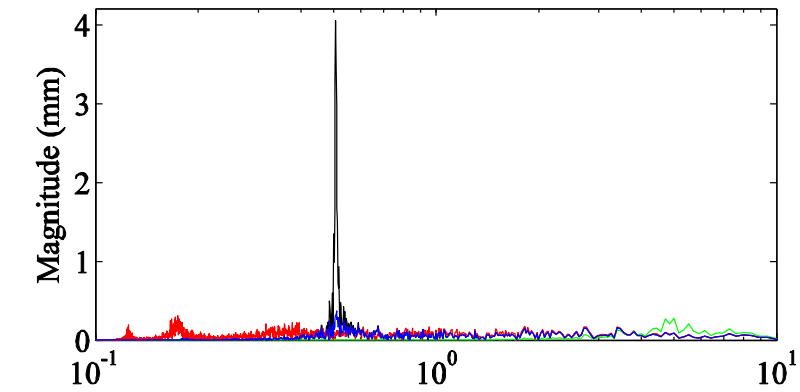
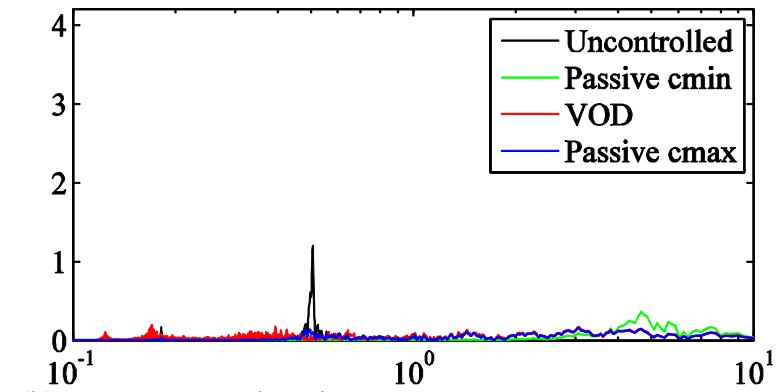


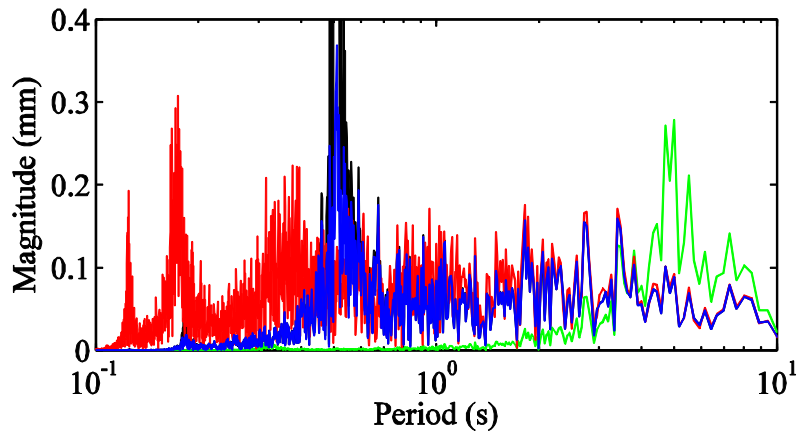
Figure 5.45. Interstory drift of the third floor in frequency domain for the (a) Imperial Valley earthquake, (b) Düzce earthquake, (c) Imperial Valley earthquake zoomed only in vertical axis, and (d) Düzce earthquake zoomed only in vertical axis



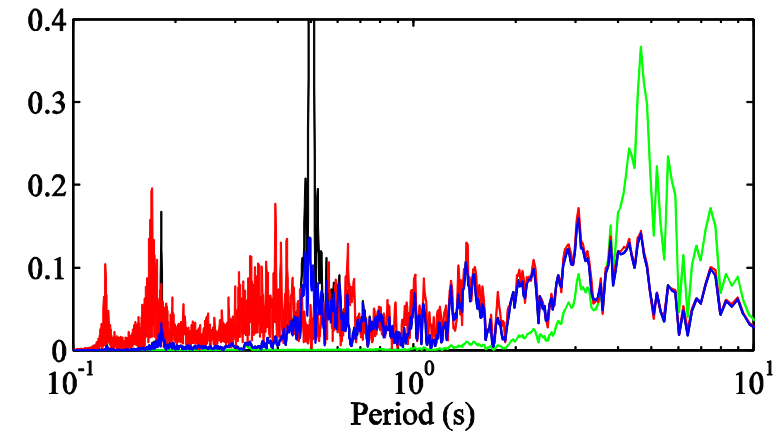
(a) *Synthetic1* earthquake



(b) *Synthetic2* earthquake



(c) *Synthetic1* earthquake zoomed only in vertical axis



(d) *Synthetic2* earthquake zoomed only in vertical axis

Figure 5.46. Interstory drift of the third floor in frequency domain for the (a) *Synthetic1* earthquake, (b) *Synthetic2* earthquake, (c) *Synthetic1* earthquake zoomed only in vertical axis, and (d) *Synthetic2* earthquake zoomed only in vertical axis

Consequently, inclusion of controlled damping in the base level reduces base displacements, protecting the base isolators from rupture or damage due to large deformations. On the other hand, it increases the building floor responses above the isolators.

### **5.8.12. System Sensitivity with Respect to the Stiffness and Mass of the Structure**

Plant models are inherently inaccurate. Controllers (regulators) described by such models must be able to provide satisfactory performance in the presence of system uncertainties and disturbances. The control scheme designed in the present section consists of a controller (including the upper controller, gain scheduling of VOD, and LQR) and an observer. In the sensitivity analysis of the present system, when the performance of the controller is *good*, this indicates that the controlled response is acceptable, and the observer can predict the simulated response successfully. The performance of an observer is associated with the case if the observer can estimate the simulated response successfully even under harsh conditions. For instance, the assumed mass, damping, and stiffness matrices of the system may be different from those of the real system. In other words, the performance of an observer relate to the correctness of its estimation of the system states, basing on an approximate transfer function of the system.

In the present study, the controller contained the LQR and the Kalman-Bucy observer. The controller gain  $\mathbf{K}$  and the observer gain  $\mathbf{L}$  were determined for various VOD damping values prior to response calculation in the simulations. For sensitivity analysis, holding the controller and observer designs constant, the mass and stiffness matrices were varied individually by  $\pm 10$  percent. The upper controller can perform its selection of optimal orifice opening of the VOD independently during the simulations due to the measurements.

The results were very close when the mass was decreased by 10 percent, and the stiffness was increased by 10 percent, and vice versa. Therefore, only the results of the system in which the stiffness matrix  $\mathbf{K}_s$  was varied were presented. All the results were with respect to the ground as in the manner which the equation of motion was written.

The performance of the controller was investigated as the stiffness matrix  $\mathbf{K}_s$  was varied. The damping matrix was determined by the Rayleigh damping. Therefore, the damping matrix changed as  $\mathbf{K}_s$  varied within a consistency with the real case. In such a way that: If the stiffness had been calculated higher than the actual one in a real-world application, then the actual damping which originates from the energy dissipation at the joints would have been smaller.

In Table 5.9, the change in the simulated responses is presented as the stiffness matrix was varied. The ratios of the maximum absolute values of the simulated responses of the varied case with respect to the simulated responses of the unvaried case are listed in Table 5.9, and the ratios had to be commented together with the correlation coefficients in Table 5.10.

Table 5.9. Ratios of the maximum absolute values of the simulated responses with respect to the responses of the unvaried case as the stiffness matrix  $\mathbf{K}_s$  was varied

	Imperial Valley earthquake		Düzce earthquake	
	$0.9 \cdot \mathbf{K}_s$	$1.1 \cdot \mathbf{K}_s$	$0.9 \cdot \mathbf{K}_s$	$1.1 \cdot \mathbf{K}_s$
$q_3(t)$	1.0496	0.9559	1.0005	0.9175
$q_2(t)$	1.0268	0.9689	0.9966	0.9123
$q_1(t)$	0.9911	0.9260	0.9826	0.8485
$q_b(t)$	0.9895	0.9782	0.9468	0.7980
$\dot{q}_3(t)$	0.9700	0.8129	1.1144	1.0545
$\dot{q}_2(t)$	0.9272	1.0010	1.1001	0.8820
$\dot{q}_1(t)$	1.0255	1.0753	1.0176	0.8392
$\dot{q}_b(t)$	1.0212	0.9260	0.8866	0.8136

The correlation coefficients between the observed and simulated responses are presented in Table 5.10 as  $\mathbf{K}_s$  of the hybrid controlled structure is varied. Additionally, the displacement and velocity responses of the two cases in Table 5.10 are presented in Figure 5.47 and Figure 5.48. Before commenting the performance of the observer in case of misdetermination of the system matrices, brief information about the correlation coefficient is provided: The correlation coefficients between the observed and simulated responses were presented. They provide a measure of how close the observed responses to the simulated ones. The correlation coefficient  $r$  is a measure of the linear

dependence between two variables giving a value in the range of -1 and +1. A value of zero correlation coefficient indicates that there is not a correlation between two variables. It takes values close to boundaries -1 and 1 as the relation between two variables gets stronger. If it is positive, then one of the variables increases as the other increases. If it is negative, then one of the variables increases as the other one decreases. In the present simulations, the *corrcoef*-functionality within MATLAB, which is abbreviated for correlation coefficients, is utilized.

The correlation analysis provides numerical information about the relation between two sets of variables. There may be a nonzero correlation coefficient between the variables which can never be directly related to each other (virtual or spurious correlation). Therefore, the analyzer should be aware of this fact while commenting the results of a correlation analysis.

Table 5.10. Correlation coefficients between the estimated and simulated responses as the stiffness matrix  $\mathbf{K}_s$  of the hybrid controlled structure was varied

	Imperial Valley earthquake			Düzce earthquake		
	$0.9 \cdot \mathbf{K}_s$	$\mathbf{K}_s$	$1.1 \cdot \mathbf{K}_s$	$0.9 \cdot \mathbf{K}_s$	$\mathbf{K}_s$	$1.1 \cdot \mathbf{K}_s$
$q_3(t)$	0.9876	0.9998	0.9922	0.9913	0.9999	0.9953
$q_2(t)$	0.9924	0.9999	0.9947	0.9947	0.9999	0.9968
$q_1(t)$	0.9935	1.0000	0.9977	0.9940	1.0000	0.9978
$q_b(t)$	0.9997	1.0000	0.9996	0.9996	1.0000	0.9997
$\dot{q}_3(t)$	0.8342	0.9983	0.9242	0.8683	0.9991	0.9548
$\dot{q}_2(t)$	0.8902	0.9984	0.9300	0.9097	0.9991	0.9554
$\dot{q}_1(t)$	0.7494	0.9990	0.9255	0.7887	0.9995	0.9180
$\dot{q}_b(t)$	0.9926	0.9983	0.9887	0.9937	0.9996	0.9938

The correlation coefficients of the observed and simulated responses were presented within each simulation for all of the system states. The columns in the middle stands to exhibit the observer performance of the unvaried case for both earthquakes. The observer at the base level performed well for all cases since the base was prewhitened for the observer design. The observer could estimate the displacement responses successfully even the stiffness matrix was varied. The correlation coefficient decreased for velocities. The worst case in the sensitivity analysis was obtained for the

velocity of the first floor when  $K_s$  was decreased in the simulation of the Imperial Valley earthquake ( $r=0.7494$ ).

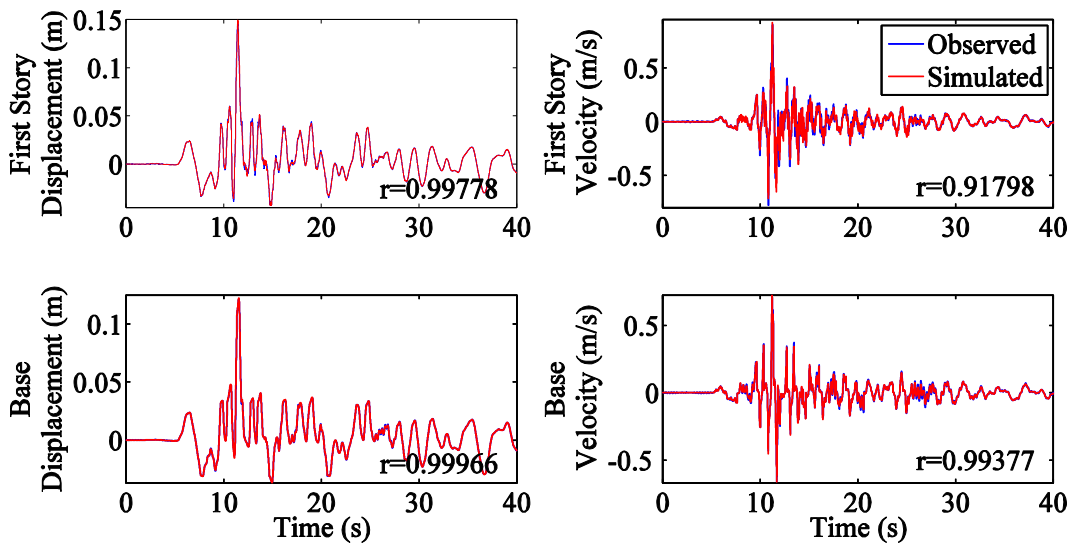


Figure 5.47. Responses for the Düzce event with respect to the ground (The stiffness matrix  $K_s$  was increased by 10%) – Best response in the sensitivity analysis

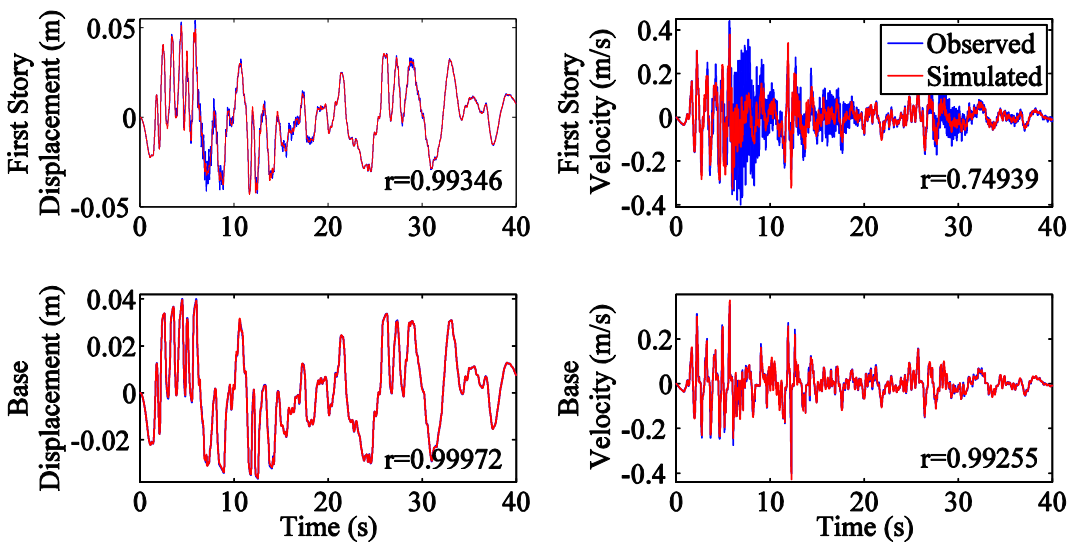


Figure 5.48. Responses for the Imperial Valley event with respect to the ground (The stiffness matrix  $K_s$  is decreased by 10%) – Worst response in the sensitivity analysis

The best performances in the sensitivity analysis were observed when the stiffness matrix  $K_s$  was increased 10 percent in the Düzce event. The related responses

are presented in Figure 5.47. On the other hand, the worst results in the sensitivity analysis were obtained at the velocity of the first floor when the stiffness was decreased by 10% for the Imperial Valley event. The related results of the Imperial Valley event are presented in Figure 5.48.

In all simulations of the sensitivity analysis, the controller performed better at the base level compared to the responses of the superstructure. This may have been due to the fact that the observer of the base was designed for the prewhitened base since the observer of the base was focused on the effective frequency range of earthquake excitation. This was not the case for the observer design of the superstructure. Consequently, it may be better to prewhiten the superstructure, so that the controller can handle possible changes of system properties better in real-world applications.

### **5.8.13. Performance of the Observer Under Arbitrary Initial Conditions**

The performance of an observer is mainly determined by the time duration that lasts for the observer to estimate the system response successfully. Therefore, arbitrary initial conditions were applied in the simulations of the Imperial Valley and Düzce earthquakes. In the earthquake simulations, the time duration passed to estimate the response successfully was investigated in case of a misdetermination of initial conditions.

The initial conditions were chosen as a combination of different mode shapes or only in shape of a certain mode. The first initial condition set was in the shape of  $[0.01 \ 0.015 \ -0.01 \ 0.02 \ 0.1 \ 0.15 \ -0.1 \ -0.2]$ . The first four values stood for the floor displacements, and they corresponded to the form of the third mode shape in meters. The second four values were for the floor velocities, and they coincided with the form of the second mode shape in meter/second. Handling such an initial condition set was a tough task for an observer since high numerical values were applied to all degrees-of-freedom at the same time and in different modes. The displacements and velocities of the base and the first floor are presented in Figure 5.49 for Düzce event under the first initial condition set.

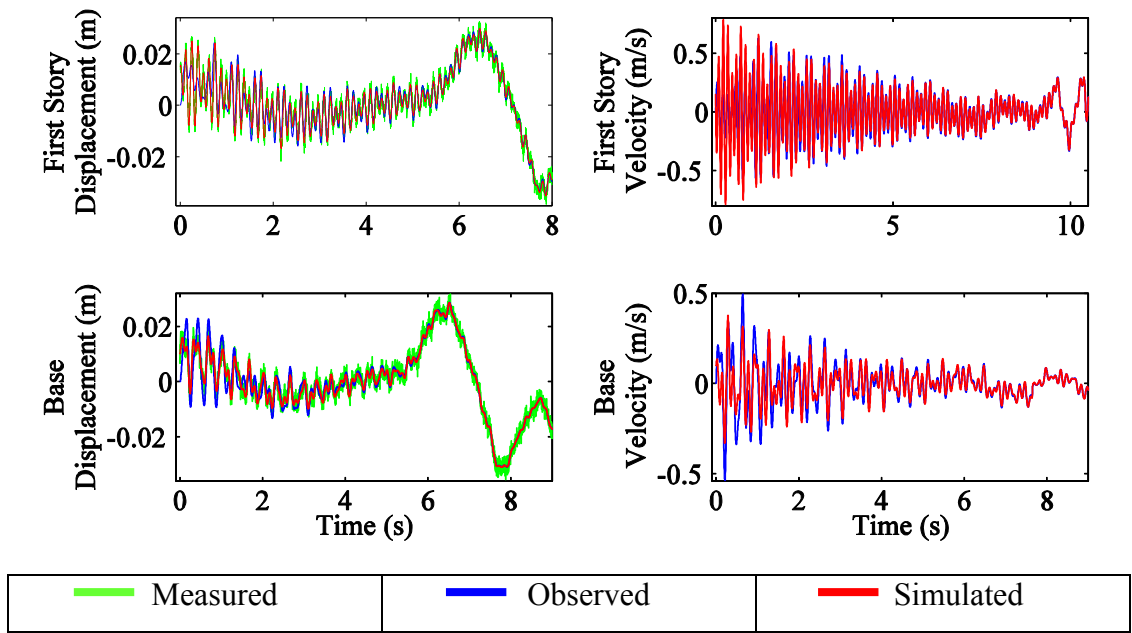


Figure 5.49. Floor responses for the Düzce event under the first initial condition set

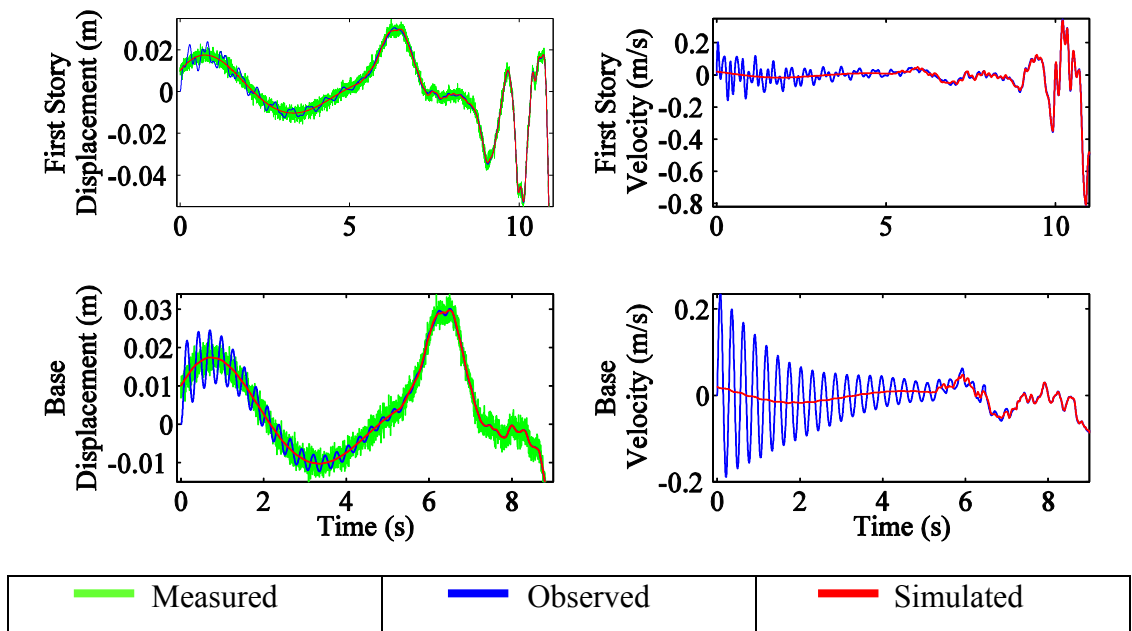


Figure 5.50. Floor responses for the Düzce event under the second initial condition set

In Figure 5.49 and Figure 5.50, the results were presented starting from -0.1 seconds to show the applied initial conditions in the simulated responses. For the first set, the observer estimated the simulated displacement and velocity responses successfully in 8 seconds.

The second initial condition set was in the shape of the first mode as 0.01 meter for displacements and 0.2 meter/second for velocities. The responses of the base and the first floor are presented in Figure 5.50 for the Düzce earthquake under the second initial condition set. The observer predicted the simulated displacement responses effectively in 6 seconds. On the other hand, the time passed to estimate the simulated velocities correctly was approximately 7-8 seconds. Surprisingly, the observer was slower than the former one to estimate the response successfully.

Notably, the performance of the observer was better in the simulations of the Imperial Valley earthquake for both of two initial condition sets compared to its performance for the Düzce event. The time duration passed to estimate the response successfully was reduced by half in the simulations of the Imperial Valley earthquake. The observer predicts the base response in a shorter time duration compared to those of the superstructure. Most probably, this was due to the fact that the observer of the base was focused on the effective frequency range of earthquake excitations by prewhitening.

#### **5.8.14. Filtering Property of the Kalman-Bucy Observer**

The performance of the observer as a filter is exhibited in the present section. The magnitudes of the base drift in the frequency spectrum for the Düzce and *Synthetic2* earthquakes are presented in Figure 5.51 and Figure 5.52, respectively. The responses belonged to the measured and observed values.

The Kalman-Bucy observer received the measured values and output less noisy responses as seen in the zoomed parts of Figure 5.51 and Figure 5.52, acting as a filter. The magnitudes of the responses in the region of interest (periods greater than 0.1 seconds) were close to each other for the measured and observed values, indicating that there was not any data loss that could affect the responses. The remaining components, whose periods were not related with the hybrid controlled system, were assumed to be noise, and they were filtered by the Kalman-Bucy observer.

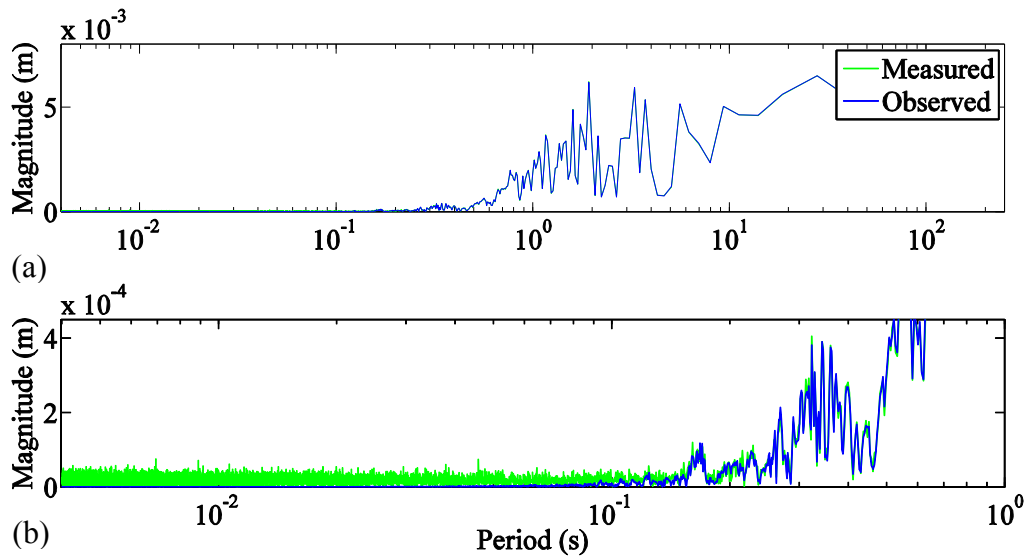


Figure 5.51. Magnitudes of the base displacement (with respect to the ground) in the frequency domain for the (a) Düzce earthquake and (b) the Düzce earthquake zoomed in vertical axis between periods of 0.004-1 s and scaled in the horizontal axis

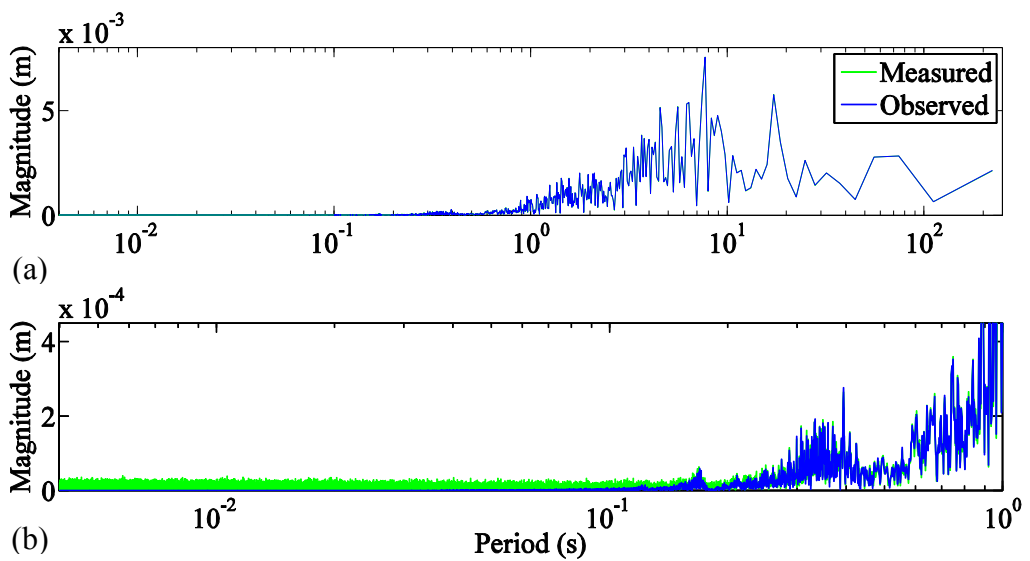


Figure 5.52. Magnitudes of the base displacement (with respect to the ground) in the frequency domain for the (a) *Synthetic2* excitation and (b) the *Synthetic2* excitation zoomed in vertical axis between periods of 0.004-1 s and scaled in the horizontal axis

### **5.8.15. Results of the Simulations**

The data of the Imperial Valley earthquake has a wider frequency range than those of the Düzce event (see Figure 2.4), and its low-frequency components double those of the Düzce event. Therefore, the Imperial Valley data affect the structures with low periods more intensely, which is not the case for a seismic isolated structure. On the other hand, the Düzce earthquake consists of low-valued cycling motion together with single high peak shocks of 50 and 80 percent of the ground acceleration. The results of the simulations have shown that the Düzce earthquake is a more demanding excitation record than the Imperial Valley event for structures whose frequencies and damping values are similar to the system in the present research.

The system response was simulated for near- and far-source earthquake records numerically. The results were compared with respect to two passive damper systems with minimum and maximum damping value. The isolators were protected at the instant of high magnitude responses by means of the controller. The interstory drift and velocity at the base level decreased more than 25% for both excitation types compared to those of the minimally damped passive device.

In the sensitivity analysis, the performance of the observer at the base level was very good for all cases since the base was prewhitened for the observer design. Therefore, the superstructure may be prewhitened in the future studies.

Additional damping at the base level reduces the base velocity directly and decreases the base displacement indirectly at the expense of larger drifts and floor accelerations of the superstructure. One of the important findings of the study is that large damping in the base level is not beneficial for base isolated buildings. On the other hand, regarding the isolation system, the highest damping case would be beneficial, making sure that failure in the isolation system does not occur.

## CHAPTER 6

# NUMERICAL STUDIES ON RESPONSE CONTROL OF A TRUCK SEAT

The primary purpose of the present section is to control the response of a truck seat by a MRD. This chapter describes the setup of the seat suspension. The damper mounted on the seat was replaced by a RD-1005-3 MRD that was manufactured by Lord Corporation. Only the numerical simulations were performed, and the seat response was controlled by the LQR.

### 6.1. Literature Review

Truck drivers spend most of their working hours at tough driving periods. This case may cause attention reduction, which is a risk for the driver, passengers, bystanders, and the goods. Also, during the vertical seat vibrations, the driver may lose the control of the truck and may injure some parts of his body. Therefore, the seat suspensions of trucks and heavy vehicles attract attention of different research groups. Some of the related studies are presented in the following lines.

The Lord Corporation designed the LORD Motion Master™. It has been the only solution that automatically adapts to both the driver's body weight and changing levels of shock and road vibration (Lord, 2007). The system was based on the RD-1005-3 damper. The system has been already mounted more than 30000 systems on the roads and has been logged more than  $10^9$  kilometers in truck, bus, and agricultural operations. The numbers were according to the data of 2007. It satisfied or exceeded the conditions of some standards as SAE J1386, ISO 7096, ISO 5007 (Carlson, 2007).

Reichert studied MRDs and skyhook control in his master thesis by Lord Corporation's support (1997). He modified an Isringhausen seat suspension to replace a passive damper with a controllable MRD. Additionally, the source of the unexpected peak in the acceleration spectrum of the seat was searched.

Engin et al. designed, manufactured, and tested a MRD for a tractor seat application (2008). They performed a fluid dynamics-based analysis of flow inside the

damper, and the flow field inside the MRD was investigated using computational fluids dynamics. Taguchi method was utilized as an optimization tool to optimize the damper geometry. A seat simulator was designed and manufactured to conduct real-time PC-based control tests of the MRD. Various control algorithms (sky-hook, ground-hook, and hybrid) were comparatively designed. The results showed that the displacement, velocity, and acceleration could be suppressed in an effective manner by using the proposed control strategy.

Göksel performed the optimal sliding mode control of a semi-active seat suspension system (2007). He applied different control strategies to control the semi-active MRD. The results showed that the utilized suspension system reduced most of the seat vibrations.

Sapinski and Rosol investigated the shock isolation performance of a driver seat with a MRD suspension system (2007). The aim of the experimental studies was to recognize the MRD performance against shock effects. Rounded pulses and square waves were applied. The controller failed to reduce the accelerations. The reason of the unwanted results was attributable to the properties and operating principles of the electromagnetic circuit of the RD-1005-3 MRD.

Song et al. focused on an experimental implementation of a semi-active seat suspension using MRDs (2007). An adaptive control algorithm was proposed to eliminate the superharmonics from the MRD seat suspension response. The effectiveness and feasibility of the proposed adaptive algorithm were shown by comparing the test results.

Yazıcı et al. tested a semi-active seat suspension system in a real time computer-based application (2008). The results showed that the suspension system reduced the sinusoidal excitation by 70% for certain excitation frequencies.

Six seat suspension systems were tested and analyzed at the National Institute for Occupational Safety and Health<sup>1</sup> – Pittsburgh Research Laboratory (NIOSH – PRL) (Mayton et al.). The investigations were performed for only vertical vibrations and by using a modified version of the ISO 5007 Standard. The seat suspension systems were four passive and two semi-active seat suspension designs, which were typical of seat suspensions commonly found on large off-road heavy surface mining, construction, and agricultural vehicles. The results suggested that the application of rheonetic technology had to provide improved isolation from the vibration transmitted from the seat.

Hiemenz et al. (2009) worked on the seat suspension system of the Expeditionary Fighting Vehicle (EFV). It was an amphibious vehicle designed to operate through harsh conditions and at much higher speeds than its predecessors. The unique capabilities and broadly varying operational conditions required a complicated suspension system different from a conventional passive seat suspension system. Different operating conditions over water and land at high speeds threatened the health of the passengers. Therefore, a semi-active magnetorheological (MR) seat suspension was developed. It could adapt to broadly varying operational conditions and passenger weight. The results showed that the MR seat suspension system reduced the shock and vibration transmitted to the passenger by up to 33% and 65%, respectively, when compared to the existing passive suspension.

Gao et al. studied the problem of robust multi-objective control for a class of uncertain semi-active seat suspension systems with actuator time delay by proposing a state-feedback controller (2010). The essential dynamics of a seated human body vibration was modeled by a three DOF model. The effectiveness and advantages of the proposed controller design was demonstrated by a design example.

Metered et al. introduced a semi-active control strategy for an MRD used in a seat suspension (2009). The proposed control system comprised a system controller that computed the desired damping force using a sliding mode control algorithm, and a neural-based damper controller. Direct estimation of the command voltage was provided to track the desired damping force. The proposed semi-active seat suspension was compared with a passive seat suspension for prescribed base displacements. The simulated results revealed that the semi-active seat suspension provided a significant improvement in ride comfort.

Modeling the human body is an important issue while designing seat suspensions. Various researchers have been studied on modeling the human body under certain conditions. Smith formulated a five DOF model to predict the effects of selected seat cushion (2000). It was based on the measured driving-point impedance and transmissibilities of major anatomical structures contributing to the observed resonance behaviors. The ability of the model to predict the effects of selected seat cushions was examined. The model was effective in simulating both the lower impedance peak observed in the primary resonance region (4-8 Hz) and the prevalent impedance peak observed in the second resonance region (7-10 Hz) in the smaller subjects. However, the model was not effective in predicting the dampening observed in the second resonance

peak with the use of cushions. Improvements were possible by redistributing the model coefficients.

Rodean investigated the biodynamic response of human body subjected to vertical vibrations in an auto vehicle (2008). The different situations were regarded: the driver was sitting on a rigid and vehicle seat with/without seat cushion.

Stein et al. formed a linear model of the seated human body and cushioned seat in the fore-and-aft direction (2007). The fore-and-aft vibrations play an important role in industrial environment. Their model based on the laboratory measurements performed by thirteen male subjects with body masses between 62.2 and 103.6 kg that sat on a cushioned driver seat with hands on a support and backrest contact in the lumbar region. A random signal in the frequency range between 0.3 and 30 Hz were applied.

## **6.2. Truck Seat**

The truck seat was manufactured by Grammer. It was a Grammer MSG 90.3 P and obtained from a BMC cooperation. The seat itself is 22 kilograms and presented in Figure 6.1. The front view of the setup is presented in Figure 6.2. The shaker was mounted on a rigid wall in order to create vertical excitations. The seat and its base was placed on the support unit that was manufactured in the IYTE Central Mechanical Workshop. The required pressure was provided by a compressor. The pressure level was approximately 6.5 bar. The seat suspension system isolated the driver from some part of the excitation, which originated from the road profile. The seat suspension system is presented in Figure 6.3.

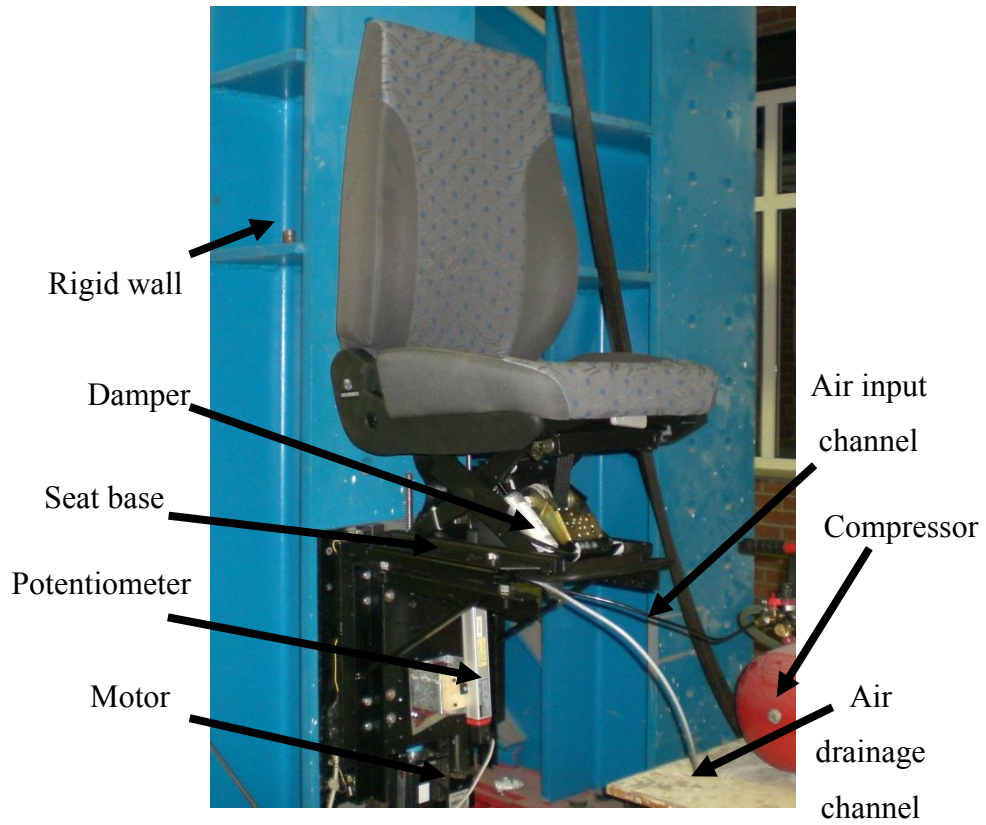


Figure 6.1. Setup

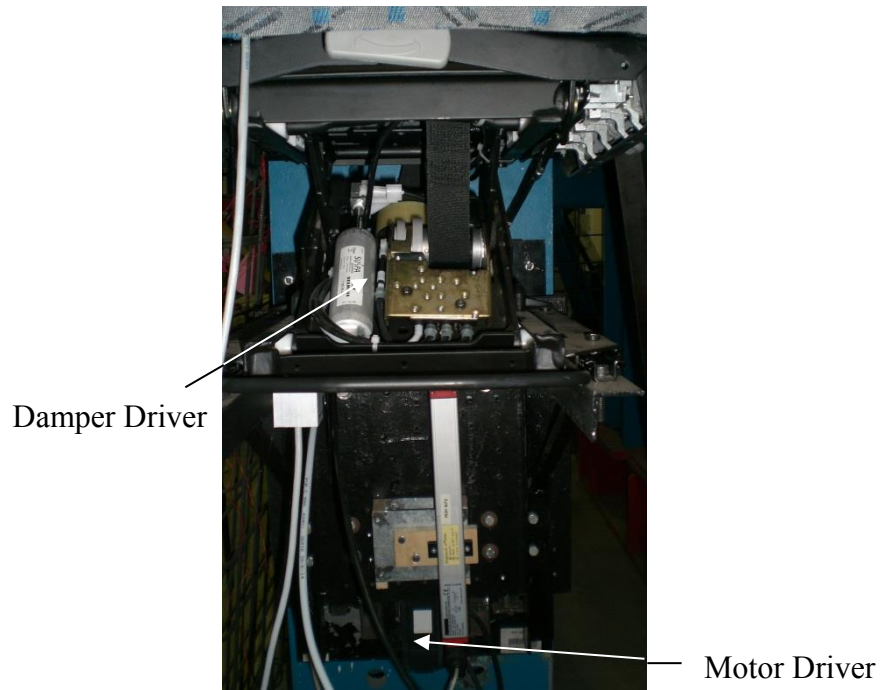


Figure 6.2. Front view of the setup

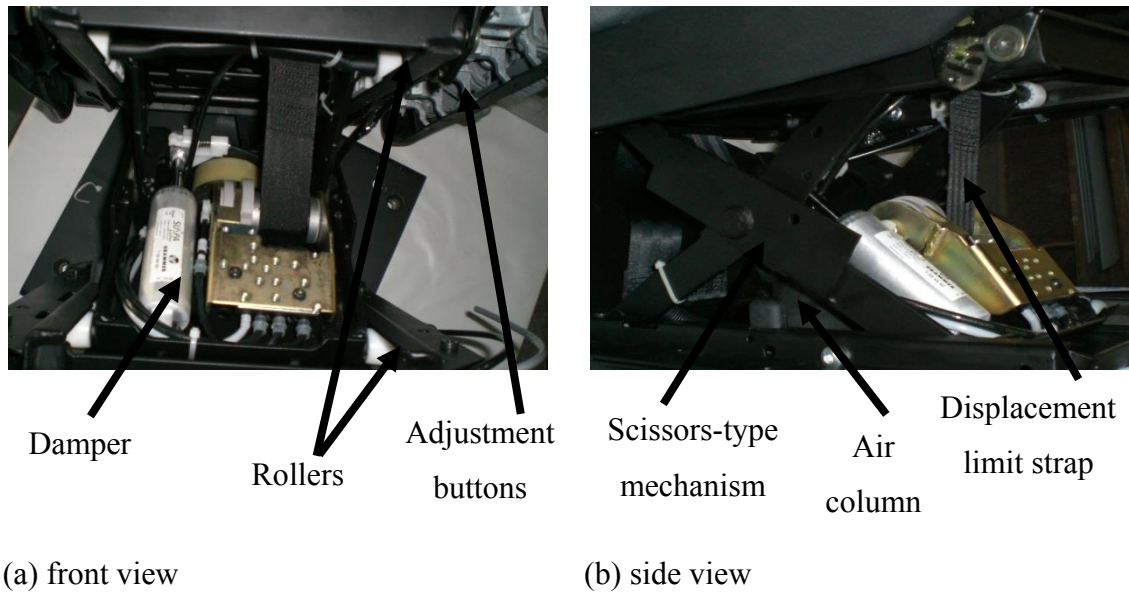


Figure 6.3. Seat suspension

The adjustment buttons of the seat are presented in Figure 6.4. They are for seat angle, shock absorber, and height adjustment from left to right (Grammer, 2010). The last one stands for quick deflation. The shock absorber utilized in the original seat (prior to the placement of the MRD) can be adjusted in 4 levels from soft up to hard. By pulling the handle upwards, the driver seat becomes softer, and vice versa. The seat can be adjusted in range of 100 mm upwards or downwards. The seat has a quick deflation adjustment, which makes it easier to get on and off the seat. By pulling the handle before getting off, the seat moves to its lowest position by discharging air. At actuating the handle before movement, the driver seat moves to its driving position automatically.



Figure 6.4. Seat adjustment buttons

### 6.3. Mechanical Model of the Truck Seat

The truck seat and its seat suspension system in Figure 6.1 was modeled mechanically (see Figure 6.5). The equation of motion of the system is

$$m_{ts}\ddot{q}_{ts} + c_{ts}\dot{q}_{ts} + k_{ts}q_{ts} = c_{ts}\dot{q}_{tsb} + k_{ts}q_{tsb} - f_{MRD} \quad (6.1)$$

where  $m_{ts}$  is the effective part of the total mass of the driver and the seat.  $c_{ts}$  is the damping coefficient due to friction of the mechanism.  $k_{ts}$  is the spring coefficient. The subscript  $ts$  stands for the truck seat and the subscript  $tsb$  stands for the base of the truck seat.  $q_{ts}$  is the seat displacement relative to the ground.  $q_{tsb}$  is the displacement of the base of the truck seat relative to the ground. Dot stands for the first time derivative, and double dot is for the second time derivative.  $f_{MRD}$  is the damping force of the MRD.

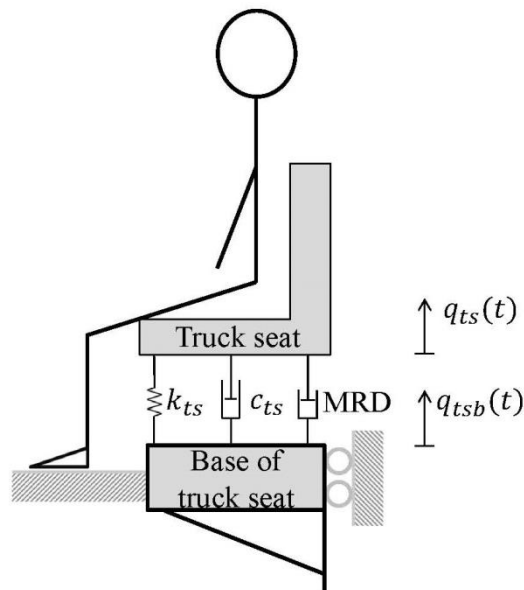


Figure 6.5. Mechanical model of the truck seat

In the state-space representation of the system, the states are the displacement and velocity of the seat relative to the ground. The state-space representation of the equation of motion in Equation (6.1) is as follows

$$\dot{\mathbf{x}}_{ts}(t) = \mathbf{A}_{ts}\mathbf{x}_{ts}(t) + \mathbf{B}_{ts}\mathbf{u}_{ts}(t) + \mathbf{G}_{ts}\mathbf{w}_{ts}(t)$$

$$\begin{bmatrix} \dot{q}_{ts}(t) \\ \ddot{q}_{ts}(t) \end{bmatrix} = \begin{bmatrix} 0 & 1 \\ -\frac{k_{ts}}{m_{ts}} & -\frac{c_{ts}}{m_{ts}} \end{bmatrix} \begin{bmatrix} q_{ts}(t) \\ \dot{q}_{ts}(t) \end{bmatrix} + \begin{bmatrix} 0 \\ -\frac{1}{m_{ts}} \end{bmatrix} f_{MRD}(t) + \begin{bmatrix} 0 & 0 \\ \frac{k_{ts}}{m_{ts}} & \frac{c_{ts}}{m_{ts}} \end{bmatrix} \begin{bmatrix} q_{tsb}(t) \\ \dot{q}_{tsb}(t) \end{bmatrix} \quad (6.2)$$

where  $\mathbf{A}_{ts}$  is the system matrix.  $\mathbf{B}_{ts}$  is the control input matrix.  $\mathbf{G}_{ts}$  and  $\mathbf{w}_{ts}(t)$  are the disturbance matrix and vector, respectively. The output in the simulations is the acceleration of the seat relative to the ground. The output equation is as follows

$$\ddot{q}_{ts}(t) = \begin{bmatrix} -\frac{k_{ts}}{m_{ts}} & -\frac{c_{ts}}{m_{ts}} \end{bmatrix} \mathbf{x}_{ts}(t) + -\frac{1}{m_{ts}} f_{MRD}(t) + \begin{bmatrix} \frac{k_{ts}}{m_{ts}} & \frac{c_{ts}}{m_{ts}} \end{bmatrix} \mathbf{w}_{ts}(t) \quad (6.3)$$

The mass and stiffness of the truck seat were determined by means of the seat obtained from a BMC cooperation. It was assumed that only 70-77% of the human weight acts to the seat (Engin et al., 2008). This reduction was due to the contact of the legs to the ground. The ISO standard for the driver mass is 75 kg and is 65 kg for the passenger. ISO standard considers the reduction due to the contact of the legs to the ground while determining the driver and passenger weights. The Grammer seat weighted 22 kg. The total effective mass for the seat including the driver and the seat was assumed to be 80 kg in the present simulations since only 70-77% of the human weight acts to the seat ( $m_{ts}=80$  kg).

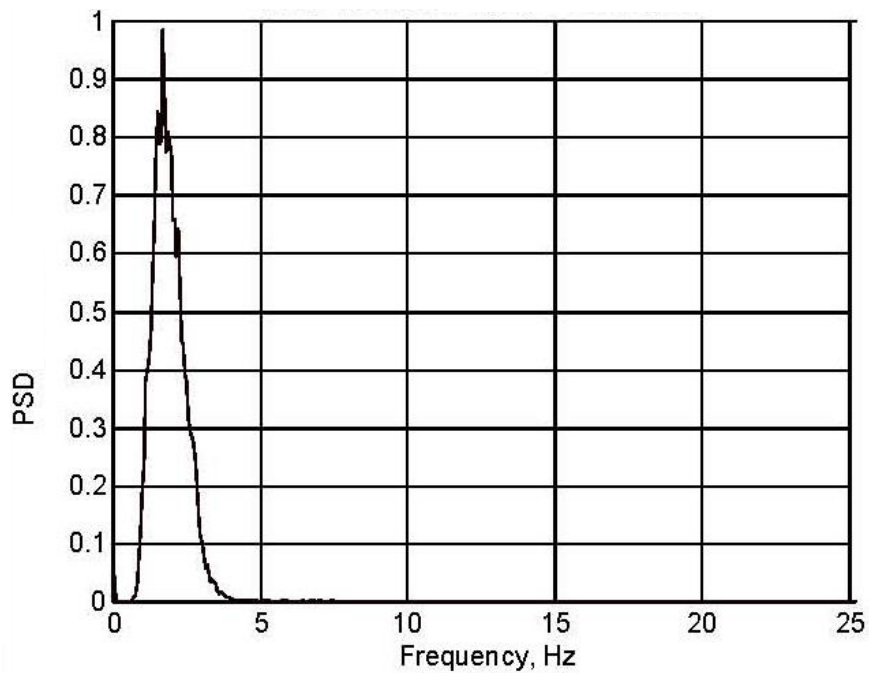
It was observed that sitting of a man of 80 kgf caused a settlement of almost 7 centimeters in the seat after the damper was removed (see Figure 6.1). If only 70-77% of the human weight acted to the seat, then approximately 60 kgf ( $\cong 590$  Newton) acted to the seat. This yielded an average seat stiffness of 8400 N/m ( $k_{ts}=8400$  N/m).

Due to the connections of the seat suspension system, a small amount of damping may have been present. Therefore, the damping ratio of the seat suspension mechanism was assumed to be 0.03. Then, its damping coefficient got the value of 49 Ns/m ( $c_{ts} = 2\zeta\omega_n m_{ts} = 49$  Ns/m).

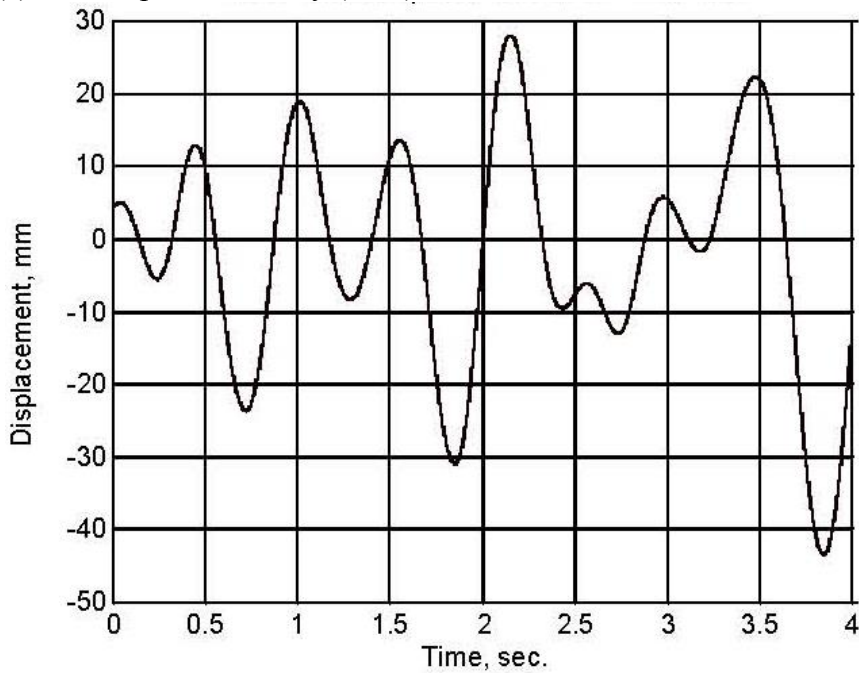
#### 6.4. Frequency Sweep Data

The experiments performed by various researchers shows that truck drivers are exposed to low frequency vibration. This case may cause temporary or even permanent

injuries. The resonance frequency range of a human body is the range of the 2-4 Hz (Engin et al., 2008; Reichert, 1997). The RMS value of the accelerations and the transmission ratio are also limited by the standards. For instance, the RMS value of the accelerations should be smaller than  $1.25 \text{ m/s}^2$ , and the upper limit of the transmission ratio is 2 for tractor seats in Turkey (AT 78/764).



(a) Power spectral density (PSD) of the excitation



(b) Base displacement sample

Figure 6.6. ISO 7096/2000 Class 2 (a) excitation and (b) base displacement sample (Source: Reichert, 1997)

The ISO 7096/2000 is a standard for earth-moving machinery in laboratory evaluation of operator seat vibration. The ISO2 excitation is a relatively broad-band excitation, with frequency content from approximately 1 to 4 Hz. It is preferred since it is commonly used by the Original Equipment Manufacturers (OEM) and seat manufacturers for evaluating seat suspension (Reichert, 1997). The power spectral density (PSD) and a sample time trace are presented in Figure 6.6.

The ISO 5007/1990 is a standard for agricultural wheeled tractors in laboratory measurement of transmitted vibration. The test protocol in ISO 5007 Section 10.1 requires a sinusoidal vibration of amplitude  $\pm 15$  mm (0.59 in) and a frequency range from 0.5 to 2 Hz at 0.05 Hz intervals (Mayton et al.). Test weights or masses of 40 and 80 kg (88 and 176 lbs) are specified by ISO 5007 to simulate the upper and lower ends (5<sup>th</sup> percentile female and 95<sup>th</sup> percentile male) for the range of seated vehicle operators.

Mayton et al. applied a modified version of ISO 5007. The test protocol in ISO 5007 Section 10.1 requires a sinusoidal vibration of amplitude  $\pm 15$  mm (0.59 in) and a frequency range from 0.5 to 2 Hz at 0.05 Hz intervals. Test weights or masses of 40 and 80 kg (88 and 176 lbs) are specified by ISO 5007 to simulate the upper and lower ends (5<sup>th</sup> percentile female and 95<sup>th</sup> percentile male) for the range of seated vehicle operators. They added a range of 2 to 8 Hz at 0.25 Hz intervals to measure the transmissibility characteristics for each seat suspension system in the range most sensitive to the human body overall. They recorded each interval for 15 s.

In the present example, the frequency sweep data was composed of signals with decreasing amplitude and linearly varying period. The period values started from 2 seconds and decreased to 0.1 seconds by intervals of 0.001 seconds. It had a white-like spectrum in the related frequency region and provided a full spectral coverage (see Figure 6.20). It generally used to test the frequency response of systems and to determine the system properties in the system identification problems. In the present research, it was utilized to test the system response whose properties were predefined within a certain frequency range. The results of the experiments performed by various researchers show that truck drivers are exposed to low frequency vibration. The human body is sensitive at the frequencies between 2 and 4 Hz (Engin et al., 2008; Reichert, 1997). Therefore, a sinusoidal wave was utilized in the numerical simulations of the present research. The velocity wave was produced as follows

$$\dot{q}_{tsb}(t) = \zeta (2 - t) \sin\left(2\pi \frac{t}{T(t)}\right), \quad t = 0, 0.001, \dots, 1.9 \quad (6.4)$$

Then, the displacement excitation data was obtained by integrating the velocity data numerically. The coefficient  $(2 - t)$  in Equation (6.4) was added to decrease the magnitude of the signal for increasing time or period values. The coefficient  $\zeta$  in Equation (6.4) was determined according to the fact that the maximum displacement would be 5 centimeters. The excitation data are presented in time domain in Figure 6.7 and in frequency domain in Figure 6.20. The displacement had an initial maximum amplitude of 5 centimeters, then it disturbed the system in the vicinity of a reference zero point of approximately 3.8 centimeters sinusoidally. The amplitude of the displacement was determined corresponding to that of velocity. The displacement and velocity of the base of the seat were applied to the system as disturbances (see Equation (6.2)). The sudden drop in the displacement disturbance may have caused a kind of impulsive loading. In the future studies, the related fact will be dealt with.

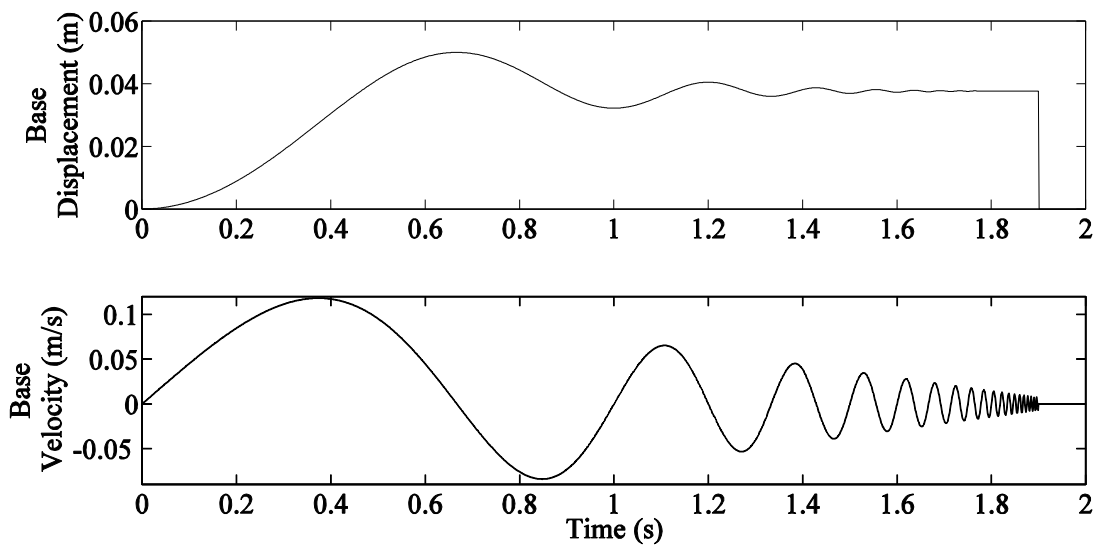


Figure 6.7. Frequency sweep data applied to the base of the truck seat (for the first two seconds of the simulation)

## 6.5. Numerical Simulations

The truck seat was obtained from a BMC cooperation. Its suspension system was modified by three passive dampers and a MRD in the numerical model. The numerical simulations were performed for four individual systems. The system was excited by the frequency sweep data presented in Figure 6.7.

In passive damper cases, three different passive dampers were applied to the system in Figure 6.5 instead of the MRD. The passive dampers were underdamped ( $\zeta_{damper} = 0.8$ ), critically damped ( $\zeta_{damper} = 1$ ), and extremely overdamped ( $\zeta_{damper} = 10$ ). Firstly, the responses of the system, which underdamped passive damper was applied, were displayed. The related displacement, velocity, and acceleration responses relative to the ground are presented in Figure 6.8, Figure 6.9, and Figure 6.10, respectively. The dashed line stands for the responses of the uncontrolled system, while the black line indicates those of the controlled system.

Damping of the uncontrolled system was originated only from the mechanism of the seat suspension system ( $\zeta = 0.03$ ). Therefore, the uncontrolled system exhibited underdamped responses in the forced and unforced regions of the simulation. On the other hand, the controlled system's response was underdamped, critically damped or overdamped depending on the damper which was applied to the suspension system.

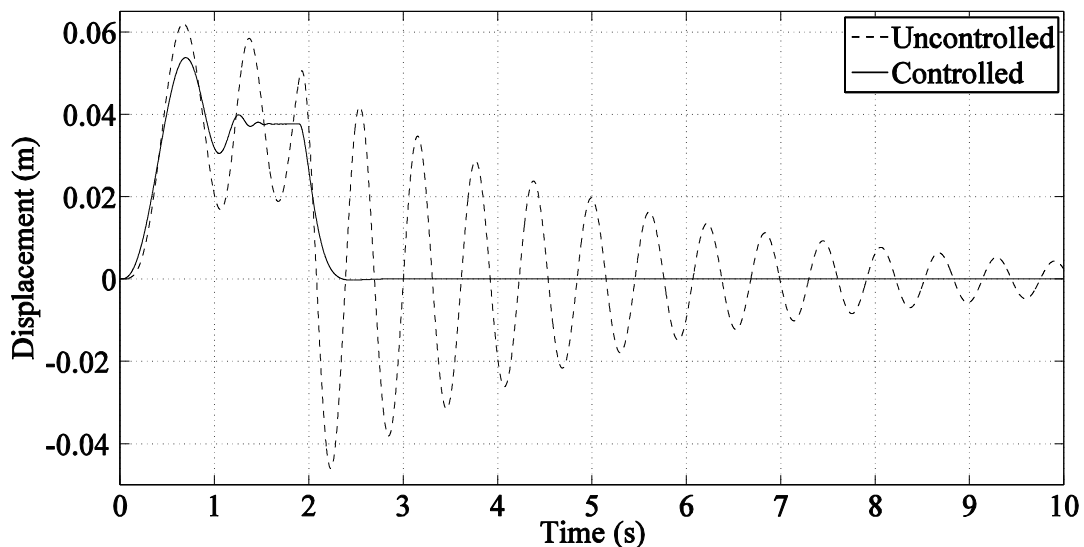


Figure 6.8. Displacement response of the truck seat relative to the ground in the passive damper application (damping ratio of the damper is 0.8, underdamped case)

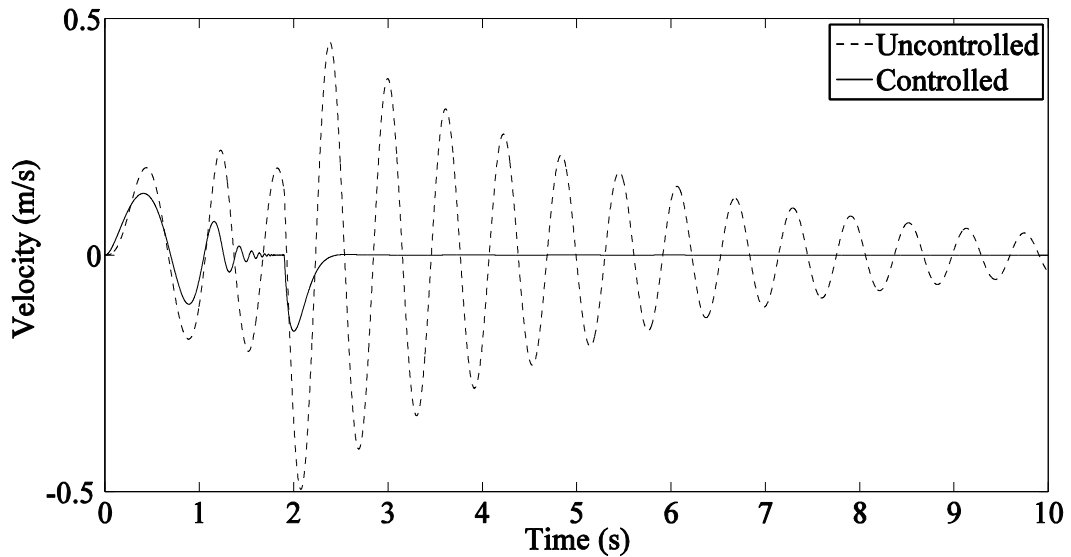


Figure 6.9. Velocity response of the truck seat relative to the ground in the passive damper application (damping ratio of the damper is 0.8, underdamped case)

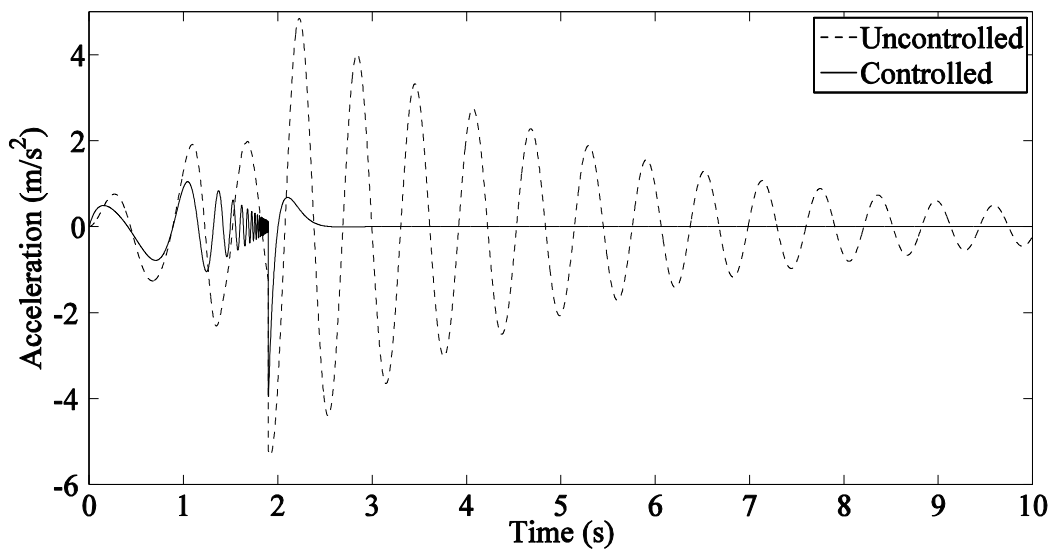


Figure 6.10. Acceleration response of the truck seat relative to the ground in the passive damper application (damping ratio of the damper is 0.8, underdamped case)

Secondly, the responses of the system, which critically damped passive damper was applied, were displayed. The related displacement, velocity, and acceleration responses relative to the ground are presented in Figure 6.11, Figure 6.12, and Figure 6.13, respectively. The dashed line stands for the responses of the uncontrolled system, while the black line indicates those of the controlled system.

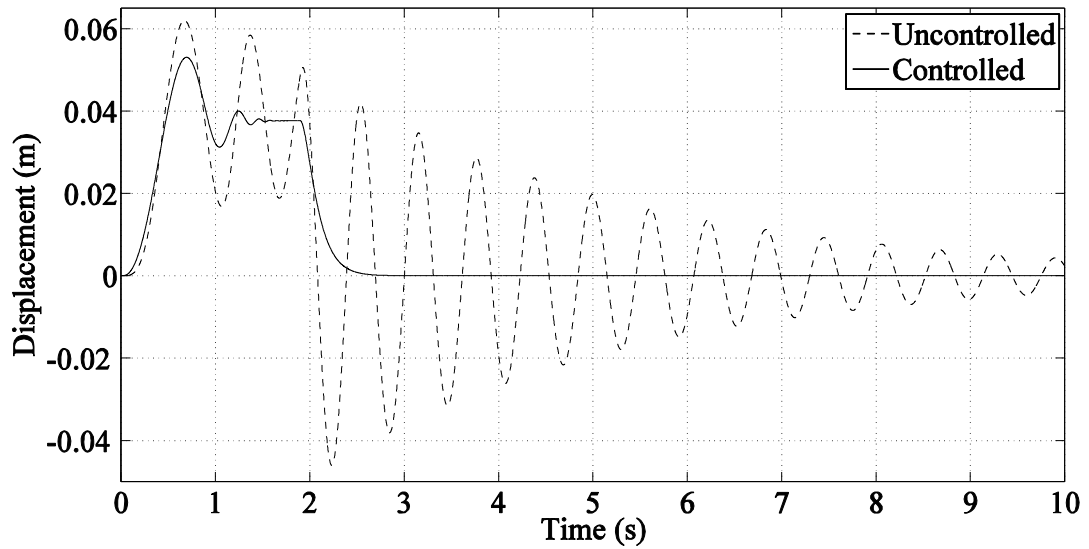


Figure 6.11. Displacement response of the truck seat relative to the ground in the passive damper application (damping ratio of the damper is 1, critically damped case)

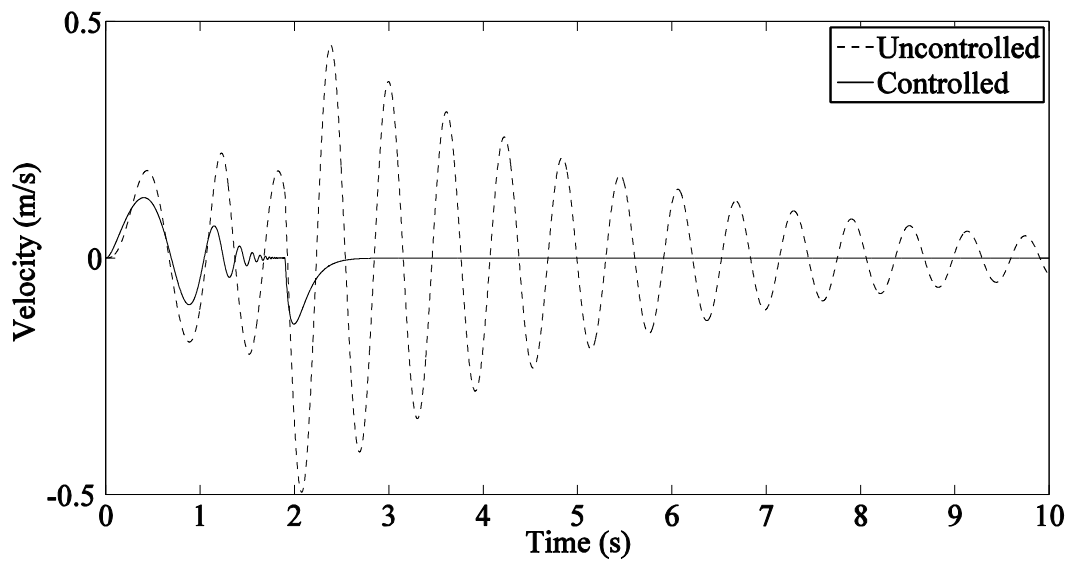


Figure 6.12. Velocity response of the truck seat relative to the ground in the passive damper application (damping ratio of the damper is 1, critically damped case)

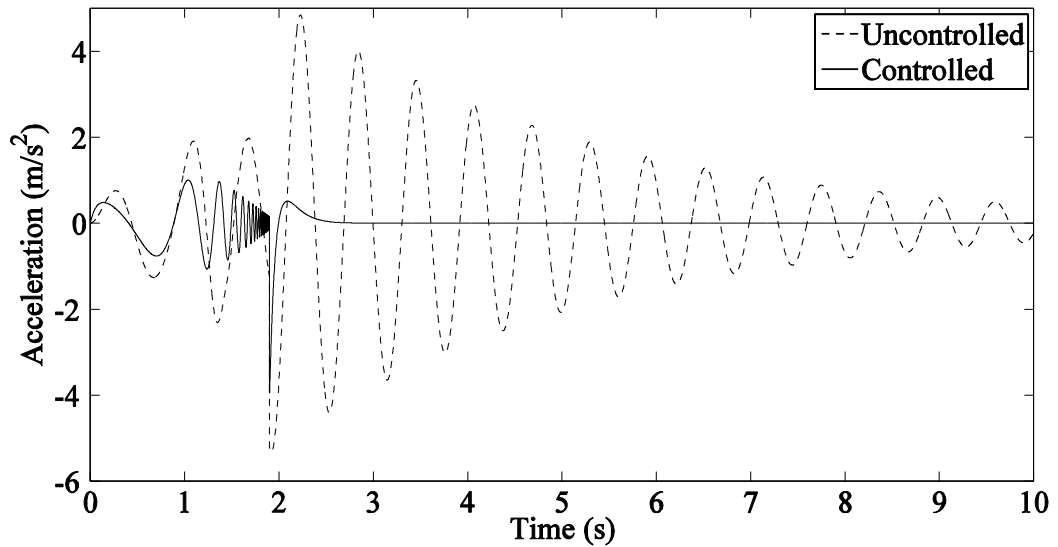


Figure 6.13. Acceleration response of the truck seat relative to the ground in the passive damper application (damping ratio of the damper is 1, critically damped case)

Lastly, the responses of the system, which overdamped passive damper was applied, were displayed. The related displacement, velocity, and acceleration responses relative to the ground are presented in Figure 6.14, Figure 6.15, and Figure 6.16, respectively. The dashed line stands for the responses of the uncontrolled system, while the black line indicates those of the controlled system.

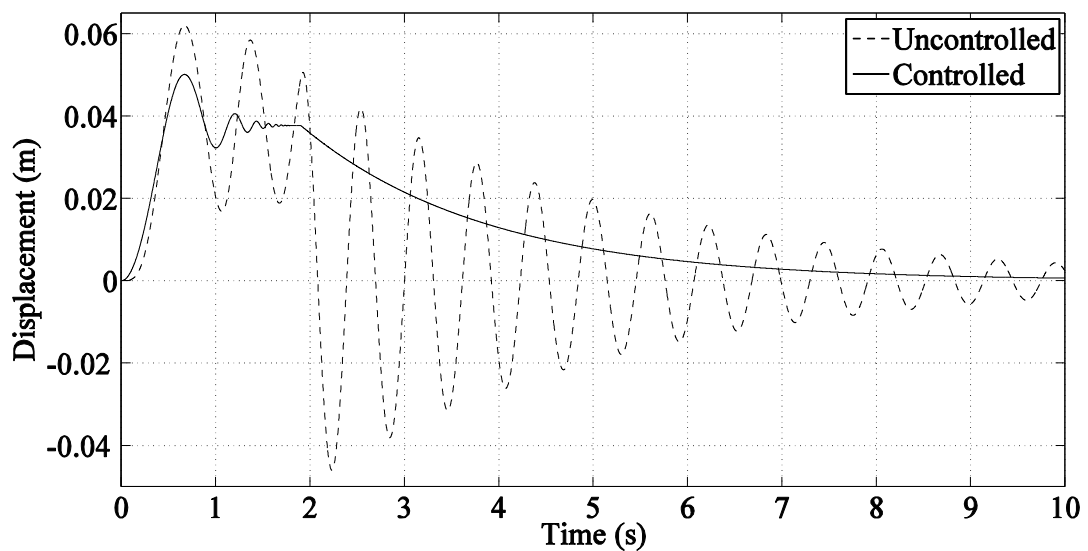


Figure 6.14. Displacement response of the truck seat relative to the ground in the passive damper application (damping ratio of the damper is 10, overdamped case)

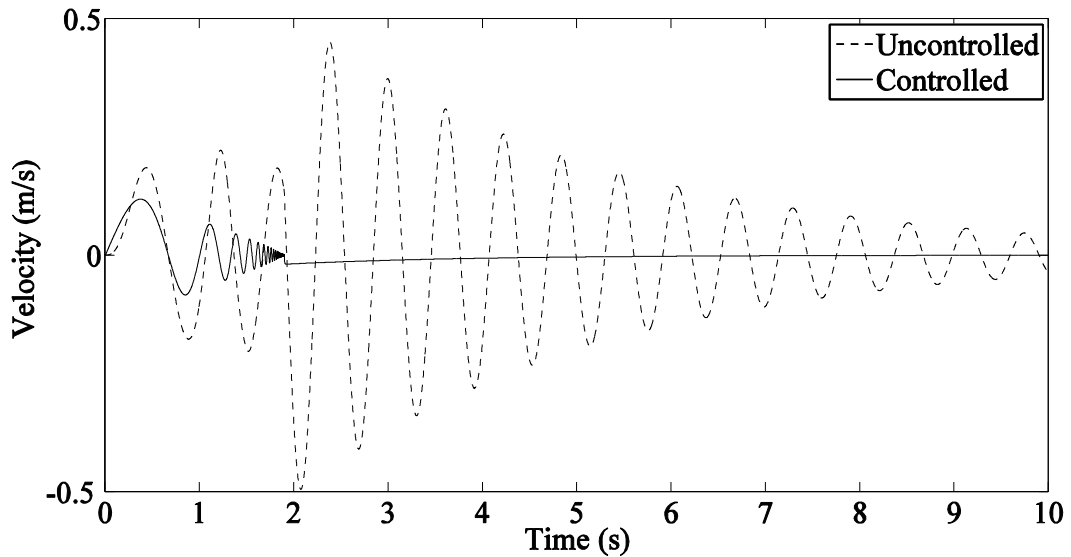


Figure 6.15. Velocity response of the truck seat relative to the ground in the passive damper application (damping ratio of the damper is 10, overdamped case)

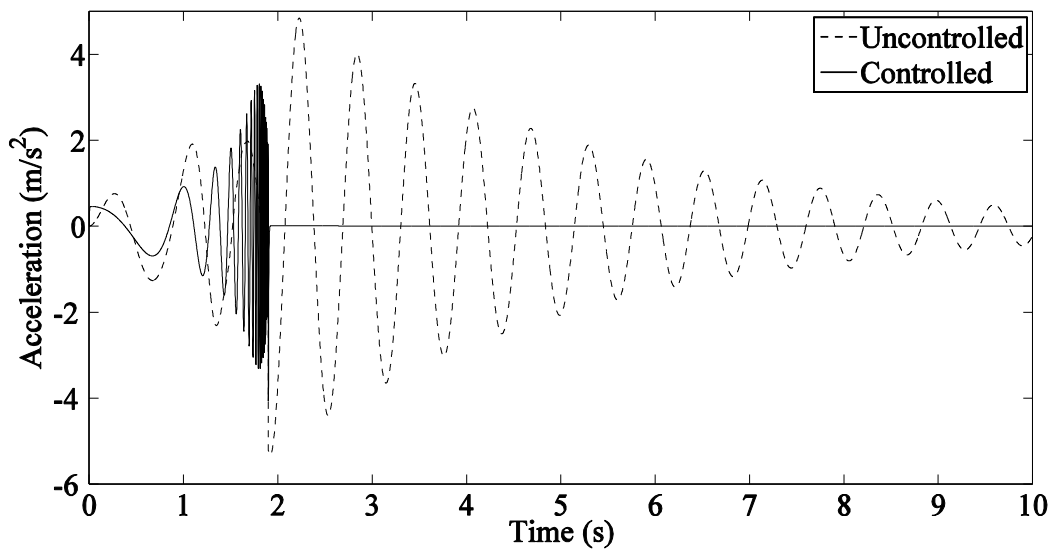


Figure 6.16. Acceleration response of the truck seat relative to the ground in the passive damper application (damping ratio of the damper is 10, overdamped case)

In the MRD simulations, the system in Equation (6.2) was utilized in the numerical simulations. The maximum MRD force was limited by 3000 N. The maximum voltage that could be applied to the electromagnet was limited by 2.25 Volts. The modified clipped algorithm was utilized to calculate the required voltage value. The MRD calculations were run at a rate hundred times faster than the response calculations of the seat. The values presented in Equation (6.5) were utilized for  $Q - R$  values of the

LQR. They were chosen by keeping the required control force  $u$  and damping force  $f_{MRD}$  as close as possible.

$$\mathbf{Q} = \begin{bmatrix} 0.1050 & 0.0 \\ 0.0 & 0.0262 \end{bmatrix}, R = 10^{-8} \quad (6.5)$$

The displacement, velocity, and acceleration responses of the truck seat are presented in Figure 6.17, Figure 6.18, and Figure 6.19, respectively. The dashed line stands for the responses of the uncontrolled system, while the black line indicates those of the controlled system.

In all cases, the uncontrolled system oscillated around the point of displacement of 0.38 meters by its damped period. After removal of the disturbance ( $t > 1.9$  s), the uncontrolled system went on to oscillate around the zero displacement point by the same damped period.

For the first 1.9 seconds of Figure 6.8-Figure 6.19, the forced responses were examined. After removal of the disturbance, the responses became unforced (see the disturbance in Figure 6.7). The underdamped, critically damped, and overdamped responses of an unforced second-order system are presented in Appendix F.

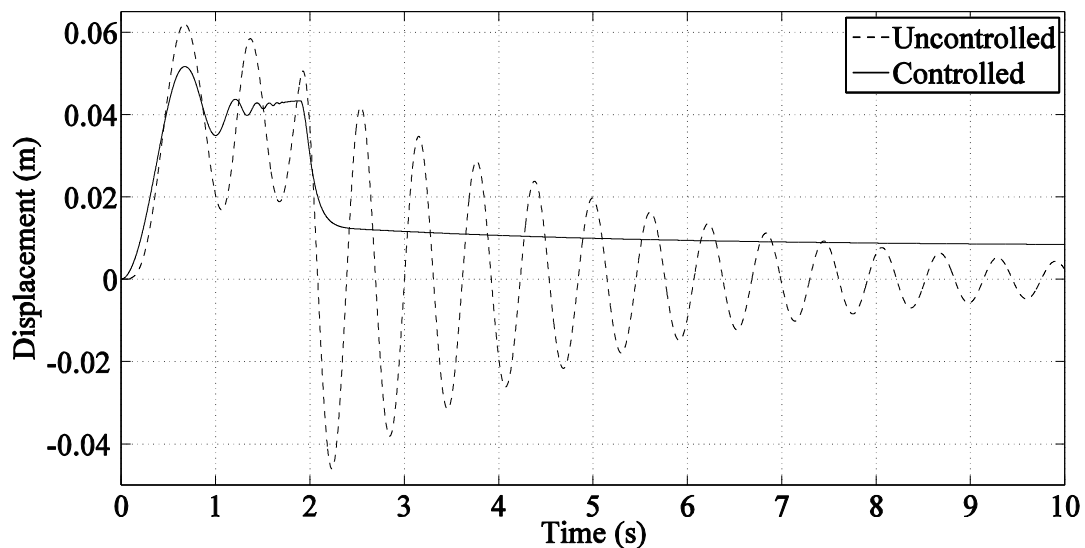


Figure 6.17. Displacement response of the truck seat relative to the ground in the MRD application

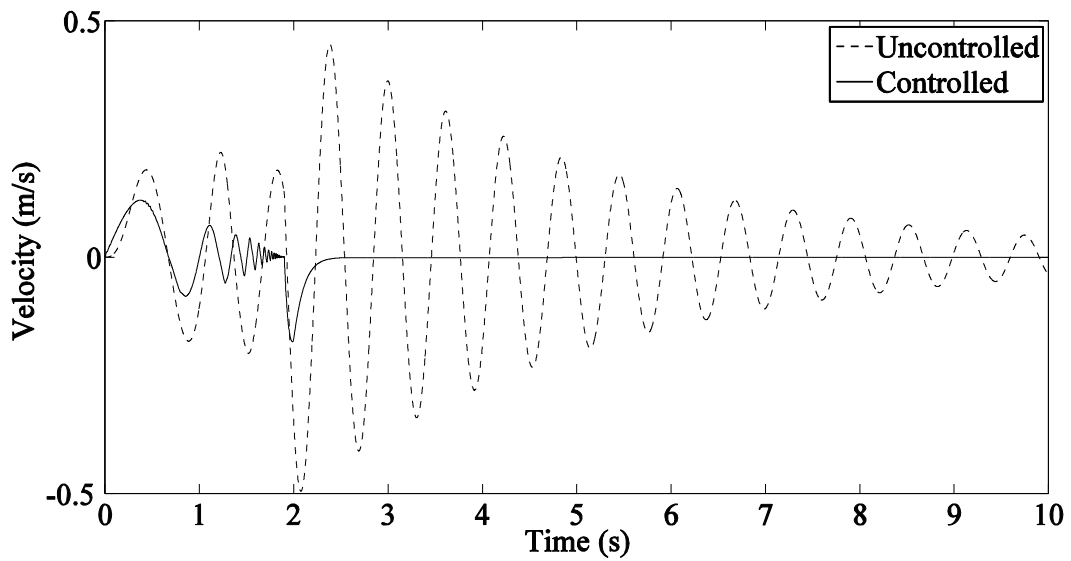


Figure 6.18. Velocity response of the truck seat relative to the ground in the MRD application

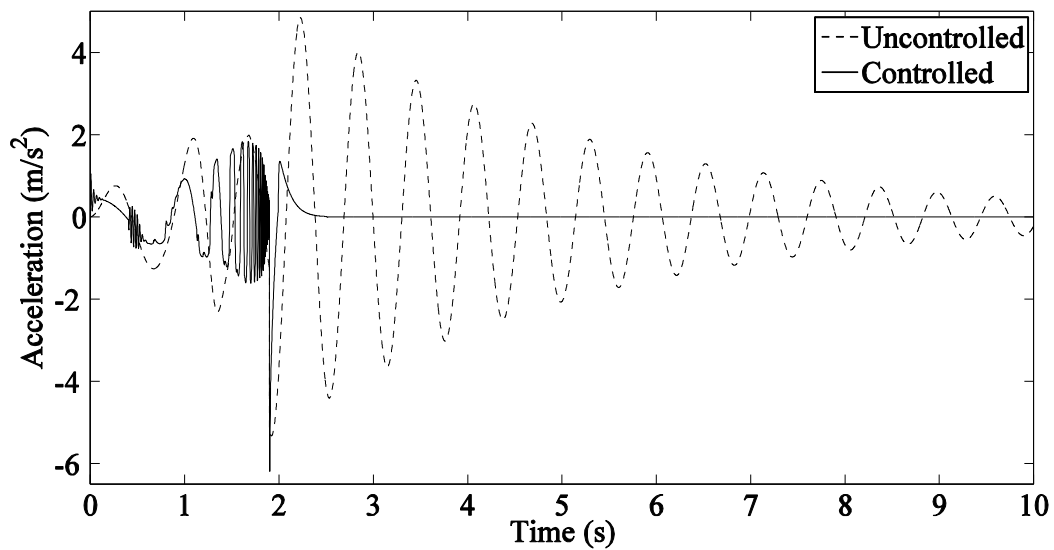


Figure 6.19. Acceleration response of the truck seat relative to the ground in the MRD application

In the unforced region of Figure 6.8, the controlled system did not exhibit visible oscillations since the damping ratio of the damper was 0.8. The waves could be observed obviously for a maximum damping ratio of 0.5-0.6. As the damping ratio got closer to the critical damping ratio, the waves deteriorated. A similar situation was encountered with while determining the critical damping ratio of the VOD in Table 5.1. The overdamped system converged to the zero displacement point slower than the critically damped system in the unforced regions of Figure 6.11 and Figure 6.14, as it

was expected (compare Equation (F.6) and Equation (F.7) in Appendix F for the unforced solutions of overdamped and critically damped second-order systems).

The magnitudes of the seat displacement (relative to the ground) in the frequency domain are displayed in Figure 6.20. In every time step, the excitation period changed, therefore there may have been some amount of spectral leakage in the spectrum (see Figure I.2 for details). Some remedies will be applied in the future studies.

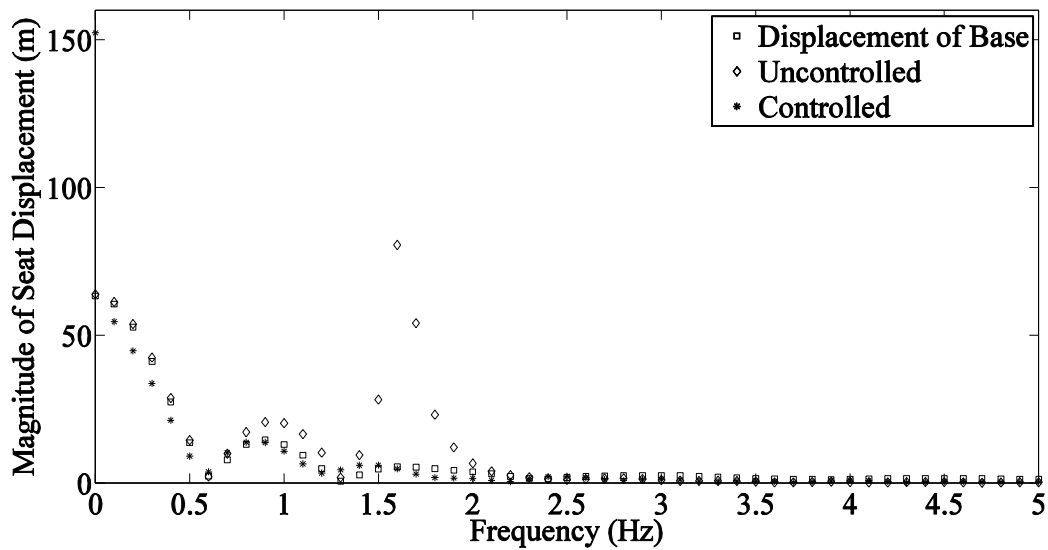


Figure 6.20. Magnitudes of the seat displacement (with respect to the ground) in the frequency domain in the MRD application (the response is displayed in the frequency range of 0-5 Hz)

The displacement response of the control system, which contained a semiactively controlled MRD, was not acceptable in Figure 6.17. Additionally, the maximum damper force  $f_{MRD}$  was approximately 350 Newtons. MRD was not activated. The capacity of the RD-1005-3 MRD was excessive for the truck seat in Figure 6.5.

The systems with passive dampers could effectively reduce the oscillations of the truck seat. On the otherhand, the suspension system with the MRD could not performed its duty in terms of seat displacements relative to the ground. Consequently, the capacity of the RD-1005-3 MRD was excessive for the current system.

# CHAPTER 7

## CONCLUSIONS

### 7.1. Conclusions

The result of subsequent subsections are presented at the end of each subsection. In the present section, the results are mentioned briefly.

Seismic response reductions by the MRD and by its hybrid application were performed in Chapter 4. At the beginning, the individual MRD was excited by sinusoidal displacements. The results have shown that the choice of time step increment is very important for the MRD as usual for nonlinear cases. Therefore, the MRD response was calculated by a loop inside the main loop in which the response was calculated. Hence, the calculations were performed faster instead of carrying out the calculations within a single loop.

In Section 4.5, the seismic response of the three-storey model structure was controlled by a MRD depending on four different control algorithms. The proposed fuzzy controller was the best in reducing seismic response of the structure effectively. In addition to its affirmative contribution, another advantage of fuzzy controllers was that its control algorithm was much simpler than those of the other three control algorithms. On the other hand, the boundaries of the input variables had to be defined priori to the simulation.

The responses of a passive damper and a semi-active MRD were compared in Section 4.6. the results indicated that the choice of  $Q - R$  mainly influenced the responses of the MRD. Furthermore, the results showed that the capacity of the utilized MRD was beyond the control requirements of the model structure utilized within the thesis (see also Section 4.7.3).

In Section 4.7, the hybrid control of the three-storey model structure including the base isolation and the MRD was performed. The structural responses were satisfactory. Moreover, the isolator was protected from detrimental effects of the ground excitation. The interstory drift reduction at the base level was approximately 50% when compared to the response of the base isolated structure. As a result, the base

displacements and velocities were reduced by additional damping in the base level. Thus, the base isolators were protected. On the other hand, the superstructure's responses increased reasonably due to the presence of large damping in the base level. The study has shown that the hybrid control system including the MRD can prevent or significantly reduce structural damage during a seismic event.

In Chapter 5, the hybrid control of the model structure including a VOD was performed. The control scheme was based on the LQG. The optimal control saved the isolator system from too large displacements, while the responses of the superstructure slightly increased when compared to the minimal damping case. Regarding the superstructure, the case with minimum damping, or even further, no damping at all, would be the most feasible situation. On the other hand, regarding the isolation system, the highest damping case would be beneficial, making sure that failure in the isolation system did not occur. The study has shown that the hybrid control system including the VOD can significantly reduce the displacements and velocities of the floors even in case of a frequency overlap of excitation and system. On the other hand, the absolute acceleration of the base increased. In conclusion, simulation results of Chapter 5 demonstrates that the controller keeps a balance among the requirements of the sub- and super-structures even in case of a frequency overlap of excitation and system. According to the results of Section 4.7 and Chapter 5, one of the important findings of the study is that large damping in the base level is not beneficial for base isolated buildings.

The hybrid control system including the MRD did not increase the absolute accelerations of the base (see Figure 4.30). On the other hand, the hybrid application of the VOD increased the absolute accelerations of the base unacceptably.

Finally, the vibration response of the truck seat was controlled by three different passive dampers and the MRD in Chapter 6. The passive dampers could effectively reduce the oscillations of the truck seat. On the other hand, the capacity of the RD-1005-3 MRD was excessive for the current system.

## 7.2. Future Work

There exist different possible future directions of the present research. They are summarized in the following lines: A study which focuses on producing near-fault seismic data synthetically could be useful in monitoring the effects of fling step and forward directivity on seismic response of controlled structures, especially their effects on flexible structures. Additionally, deeper studies in phenomenological model of MRD are suggested to propose a new model including fractional derivatives for the relationship between the inertial force and acceleration at high velocities.

The hybrid application of the optimally controlled VOD was capable of effectively reducing displacements and velocities, but not successful in decreasing the absolute accelerations. Therefore, a further study is suggested to prevent the increase in the absolute acceleration of the base of the hybrid system including the VOD. Furthermore, GA studies are recommended to investigate  $Q - R$  couples to obtain controlled responses better than the present ones in the LQR and LQG control designs.

The results of an experimental study on the control of the model structure may provide more information about the behaviour of the system being controlled. The experimental results obtained in the future studies may be compared with the results of Chapter 4 and Chapter 5. Finally, one of the possible future directions of the present research may be the experimental studies with the setup of the truck seat to validate the responses of the simulations of the thesis.

## REFERENCES

- Aagaard, B.T., Hall J.F., & Heaton T.H. (2000). Sensitivity study of near-source ground motion, *Proceedings of 12WCEE*, 0722. 1-8.
- Alfieri, E., Amstutz, A., & Guzzella, L. (2009). Gain-scheduled model-based feedback control of the air/fuel ratio in diesel engines. *Control Engineering Practice*, 17, 1417-1425.
- Ali, H., & Calayir, Y. (2002). Yapıların sismik izolasyonunda kayan modlu aktif kontrol yöntemi, *DEÜ Mühendislik Fakültesi Fen ve Mühendislik Dergisi*, Cilt: 4(3), s: 45-56,
- Anderson, B.D.O. & Moore, J.B. (1989). *Optimal Control-Linear Quadratic Methods*. USA: Prentice-Hall.
- Anderson, B.D.O. & Moore J.B. (2005). *Optimal Filtering*. USA: Dover Publications.
- Arıkan, O. & Ercan, Y. (2011). Elektrikli ısıtma fırınlarının optimal ve minimum mertebe gözlemleyicili optimal kontrolü, *TOK 2011 Bildiriler Kitabı*, 493-500.
- Artem S. (2008). *Analytical Methods in Engineering Lecture Notes*, İYTE Mechanical Engineering Department.
- AT 78/764, (2000, 30 Kasım), Tekerlekli tarım veya orman traktörlerinin sürücü koltuğu ile ilgili tip onayı yönetmeliği, *Resmi Gazete*, 24246, pp. 161-195.
- Bar-Shalom, Y., Li, X. R., & Kirubarajan, T. (2001). *Estimation with Applications to Tracking and Navigation*: John Wiley & Sons.
- Barroso, L.R., Scott, E.B., & Smith, H.A. (1998). Evaluating the effectiveness of structural control within the context of performance-based engineering, *NCEE 98*, Stanford Univ. Stanford, CA.
- Barroso, L.R., Scott, E.B., & Smith, H.A. (2000). Comparison of story drift demands of various control strategies for the seismic resistance of steel moment frames, *12th WCEE*.
- Başar, T., Meyn, S.P., & Perkins, W.R. (1998). *Control System Theory and Design, Lecture Notes*, University of Illinois at Urbana-Champaign.
- Bilgiç, B. (2007). *Taşıt Süspansiyon Sistemlerinin MR Sönümleyici Kullanarak Kontrolü*, Yüksek Lisans Tezi, İstanbul Üniversitesi, İstanbul.
- Brezinski, C. (2002). *Computational Aspects of Linear Control*. Netherlands: Kluwer Academic Publishers.

- Brown, R. G., & Hwang, P. Y. C. (1992). *Introduction to Random Signals and Applied Kalman Filtering (Second ed.)*: John Wiley & Sons.
- Bryson, A.E. & Ho, Y.-C., (1975). *Applied Optimal Control*. USA: Taylor & Francis,
- Bolt Bruce A., (2008). *Depremler*. TÜBİTAK Popüler Bilim Kitapları, 1. basım. Ankara.
- Bores, (1998). <http://www.bores.com/>, Retrived 10.12.2012.
- Bosgra, O.H. & Kwakernaak, H. (Winter 2000-2001). *Design Methods for Control Systems, Lecture Notes*, Dutch Institute of Systems and Control.
- Carlson, J.D., (2007). *Magnetorheological Fluid Technology, Presentation*, Lord Corporation, Cary, North Carolina, USA.
- Carlson, J., Catanzarite, D.M. & Clair, K.A.St. (1996) Commercial magneto-rheological fluid devices, *International Journal of Modern Physics B*, 10(2857).
- Chandiramani, N.K. (2004) *Civil Engineering Applications of Vibration Control (Structural Control)*, *Lecture notes CE 152*, Department of Civil Engineering, Indian Institute of Technology, Bombay.
- Chang, S.P. & Makris, N. (2000). Effect of various energy dissipation mechanisms in supressing structural response, *12th WCEE*.
- Choi, H.L. & Lim, J.-T. (2005). Gain scheduling control of nonlinear singularly perturbed time-varying systems with derivative information. *International Journal of Systems Science*, 36(6), 357-364.
- Choi, K.M., Cho, S.W., Jung, H.J., & Lee, I.W. (2004). Semi-active fuzzy control for seismic response reduction using magnetorheological dampers. *Earthquake Engineering and Structural Dynamics*, 33, 723-736.
- Chopra, A.K. & Chintanapakdee, C. (2001). Compared response of SDF systems to near-fault and far-fault earthquake motions in the context of spectral regions, *Earthquake Engineering and Structural Dynamics*, 30, 1769–1789.
- Chopra, A. K. (1995). *Dynamics of Structures (Second ed.)*: Prentice-Hall, Inc.
- Claveau, F., Chevrel, P. & Knittel, K. (2008). A 2DOF gain-scheduled controller design methodology for a multi-motor web transport system. *Control Engineering Practice*, 16, 609-622.
- DeRusso, P.M., Roy, R.J., Close, C.M., & Desrochers, A.A. (1998). *State Variables for Engineers*: John Wiley & Sons, Second ed.
- Dobson, S., Noori, M., Hou, Z., Dimentberg, M. & Baber, T. (1997). Modeling and random vibration analysis of SDOF systems with asymmetric hysteresis, *International Journal of Non-Linear Mechanics*, 32(4), 669-680.

- Doyle, J.C., Glover, K., Khargonekar, P.P., & Francis, B.A. (1989). State-space solution to standard  $H_2$  and  $H_\infty$  control problems, *IEEE Transactions on Automatic Control*, 34(8), 831-847.
- Dyke, S.J. (1996). *Acceleration feedback control strategies for active and semi-active control systems: modeling, algorithm development and experimental verification*. PhD Dissertation, University of Notre Dame, Indiana USA.
- Dyke, S.J., Spencer Jr, B.F., Sain, M.K. & Carlson, J.D. (1996). Modeling and control of magnetorheological dampers for seismic response reduction. *Smart Materials and Structures*, 5(5), 565-576.
- Dyke, S.J. & Spencer Jr, B.F. (1997). A comparison of semi-active control strategies for the MRD. *Proceedings of the IASTED International Conference, Intelligent Information Systems*. December 8-10, The Bahamas.
- Engin, T., Öz, H.R., Morgül, Ö.K., Soydan, Y., Şahin, İ., Fırat, M., & Yazıcı, İ. (2008). Yeni nesil yarı-aktif bir süspansiyon sisteminin tasarımı, imalatı ve optimizasyonu, *TÜBİTAK Proje Raporu, Proje No:104M157*, Sakarya, Turkey.
- Ewins, D.J. (2000). *Modal Testing: Theory, Practice and Application*. Research Studies Press Ltd., England, Second ed.
- Fenves, G.L., Huang, W.H., Whittaker, A.S., Clark, P.W. & Mahin, S.A. (1998). Modeling and characterization of seismic isolation bearings. *Workshop on Seismic Protective Systems for Bridges*. U.S. Italy.
- Franklin, G. F., Powell, J. D., & Emami-Naeini, A. (2009). *Feedback Control of Dynamic Systems (Fifth ed.)*: Pearson Prentice Hall.
- Garvey, S. D., Penny, J. E. T. & Friswell, M. I. (1998). The relationship between the real and imaginary parts of complex modes, *Journal of Sound and Vibration*, 212(1), 75-83.
- Gao, H., Zhao, Y., and Sun, W. (2010) Input-delayed control of uncertain seat suspension systems with human-body model, *IEEE Transactions on Control Systems Technology*, 18(3), 591-1601, May.
- Gavin, H. (2001). *Non-classical damping and complex modes*, CE 283 Lecture Notes, Duke University.
- Grammer Operating Instructions* (2010). MSG 90.3 P,
- Göksel, M. (2007). *Yarı Aktif Sönümleyicinin Optimal Kayan Yüzey Kontrolü*, Yüksek Lisans Tezi, Sakarya Üniversitesi, Sakarya.
- Grewal, M. S., & Andrews, A. P. (2008). *Kalman Filtering: theory and practice using MATLAB (Third ed.)*: John Wiley & Sons.

- Hall, J.F. (1999). Discussion: The role of damping in seismic isolation. *Earthquake Engineering and Structural Dynamics*, 28, 1717-1720.
- Hall, J.F., Heaton, T.H., Halling, M.W., & Wald, D.J. (1995 November). Near-source ground motion and its effects on flexible buildings, *Earthquake Spectra*, 11, No: 4,
- He, J. & Fu, Z.-F. (2001). *Modal Analysis (Second ed.)*: Oxford.
- Hespanha, J. P. & Morse, A. S. (1999). Stability of switched systems with average dwell-time. *Proceedings of the 38<sup>th</sup> Conference on Decision & Control*, 2655-2660, Phoenix, Arizona USA.
- Hiemenz, G.J., Hu, W., & Wereley, N.M. (2009). Adaptive magnetorheological seat suspension for the expeditionary fighting vehicle, *11th Conference on Electrorheological Fluids and Magnetorheological Suspensions, Journal of Physics: Conference Series, Vol: 149*.
- Huang, Z.-S., Wu, C., & Hsu, D.-S. (2009). Semi-active fuzzy control of MRD on structures by genetic algorithm. *Journal of Mechanics*. 25(1), N1-N6.
- Inman, D. J. (2007). *Engineering Vibration*, Pearson Education, Inc., Third ed.
- Kalkan, E., Adalier, K., & Pamuk, A. (2004). Near source effects and engineering implications of recent earthquakes in Turkey. *Proceedings of the Fifth International Conference on Case Histories in Geotechnical Engineering*, Paper No. 3.30, New York.
- Kalkan, E. & Chopra, A.K. (2010). Practical guidelines to select and scale earthquake records for nonlinear response history analysis of structures. *U.S. Geological Survey Open-File Report 2010*, 113 p.
- Kalkan E. & Kunnath, S.K. (2006). Effects of fling step and forward directivity on seismic response of buildings. *Earthquake Spectra*, 22, (2), 367–390.
- Kalman, R. E. (1960). A new approach to linear filtering and prediction problems. *Journal of Basic Engineering*, 82 (Series D), 35-45.
- Kalman, R. E. & Bucy, R. S. (1961). New results in linear filtering and prediction theory. *Journal of Basic Engineering*, 95-108.
- Karakan E. (2008). *Estimation of Frequency Response Function for Experimental Modal Analysis*, Master of Science Thesis, İzmir Institute of Technology, İzmir.
- Katsanos E.I., Sextos, A. G. & Manolis, G.D. (2010). Selection of earthquake ground motion records: A state-of-the-art review from a structural engineering perspective. *Soil Dynamics and Earthquake Engineering* 30, 157-169.
- Kawana, M., & Shimogo, T. (1998). Active suspension of truck seat. *Shock and Vibration*, 5, 35-41,

- Kelly, J.M. (1999). The role of damping in seismic isolation. *Earthquake Engineering and Structural Dynamics*, 28, 3-20.
- Kelly, J.M. (1998). <http://nisee.berkeley.edu/lessons/kelly.html>, Retrived 10.11.2012
- Kelly, J.M. (1997). *Earthquake-Resistant Design with Rubber*, Springer-Verlag.
- Kınay, G. & Turan, G. (2009). Yapıların sismik titreşimlerinin kayan mod kontrollü magnetoreolojik sönümleyiciler ile azaltılması, *Otomatik Kontrol Türk Milli Komitesi Otomatik Kontrol Ulusal Toplantısı 2009 Bildiri Özetleri*, 43, YTÜ, İstanbul.
- Kınay, G., & Turan, G., (2009). Comparison of different phenomenological models for magneto-rheological dampers. *Proceedings of 5th Ankara International Aerospace Conference*, 41, METU, Ankara.
- Kınay, G., & Turan, G. (2009). A hybrid control of seismic response by passive and semi-active control strategies, *Proceedings of International Symposium on Engineering and Architectural Sciences of Balkan, Caucasus and Turkic Republics, SDU*, Isparta.
- Kınay, G. & Turan, G. (2010). Gain scheduling control of a variable orifice damper applied to a three story building subjected to earthquake excitation, *5<sup>th</sup> World Conference on Structural control and Monitoring*, 10139, Tokyo, Japan.
- Kınay, G. & Turan, G. (2010).  $H_2/LQG$  control of seismic vibrations of civil structures by magnetorheological dampers, *9<sup>th</sup> International Congress on Advances in Civil engineering*, Trabzon, Turkey.
- Kınay, G. & Turan, G. (2012). A hybrid control of seismic response by passive and semi-active control strategies, *Journal of Engineering Science and Design*, 2(1), 27-36.
- Küçükdemiral, İ.B., Engin, Ş.N., Ömürlü V.E. & Cansever, G. (2005). A robust single input adaptive sliding mode fuzzy logic controller for automotive-active suspension system. *Proceeding of Fuzzy systems and Knowledge Discovery, Second International Conference. Part I*.
- Jabbari, F. & J.E. Bobrow (2002). State of the art of structural control, *Journal of Engineering Mechanics*, 916-924.
- Jansen, L.M., & Dyke, S.J. (1997). Semi-active control strategies for MRDs: A comparative study, *Intelligent Information Systems*, 8(10), 580-584.
- Jin, G., Sain, M.K. & Spencer Jr, B.F., (2005). Nonlinear blackbox modeling of MR-dampers for civil structural control, *IEEE Transactions on Control Systems Technology*, 13(3), 345-355.

- Jolly, M.R., Bender, J.W. & Carlson, J.D. *Properties and Applications of Commercial Magnetorheological Fluids*, Thomas Lord Research Center, Lord Corporation.
- Juang J.N. (1994). *Applied System Identification*, Prentice Hall PTR.
- Jung, H.J., Lee, I.W., & Spencer Jr, B.F. (2002). State-of-the-art of MRD-based control systems in civil engineering applications, *Proceedings of US-Korea Workshop on Smart Infra-Structural Systems*, Korea.
- Lathi, B.P. (2010). *Linear Systems and Signals (Second international ed.)*, Oxford University Press, Newyork.
- Lawrence, D. A. & Rugh, W. J. (1990). On a stability theorem for nonlinear systems with slowly varying inputs. *IEEE Transactions on Automatic Control*, 35(7), 860-864.
- Lee, S.K., Lee, S.H., Min, K.W, Moon, B.W., Youn, K.J. & Hwang, J.S. (2007). Performance evaluation of an MRD in building structures considering soil-structure interaction effects, *The Structural Design of Tall and Special Buildings*, DOI:10.1002,
- Leith, D. J. & Leithead, W. E. (2000). Survey of gain-scheduling analysis and design. *International Journal of Control*, 73(11), 1001-1025.
- Lewis, F.L., & Syrmos, V.L., (1995). *Optimal Control*, John Wiley & Sons Inc.
- Liang, Z. & Lee, G. C. (1991). Damping of structures – Part 1: Theory of complex damping, Technical Report NCEER-91-0004.
- Lin, J.-Y. & Yu, C.-C. (1993). Automatic tuning and gain scheduling for pH control. *Chemical Engineering Science*, 48(18), 3159-3171.
- Lord Corporation (2008), <http://www.lord.com>, Retrieved 05/06/2013.
- Lord Rheonetic™ Rd-1005-3 Product Bulletin, 2007.
- Ljung., L. (2008). *Perspectives on System Identification*, Linköpings Universitet, Linköping, Sweden.
- Ljung., L., (1999). *System Identification: Theory for the User*, Prentice Hall PTR, Second ed.
- Lu, L. (2001). *Extended LQG Methodology for Active Structural Controller Design*, PhD Dissertation, National Central University, China.
- Luca, S.G. & C. Patia (2009), Case Study of Variable Orifice Damper for Seismic Protection of Structures, *Buletinul Institutului Politehnic Din Iași, LV (LIX)*, f. 1.
- Maia, N.M.M., Silva, J.M.M. & Ribeiro, A.M.R. (1998). On a general model for damping, *Journal of Sound and Vibration*, 218(5), 749-767.

- Makris N. (1997). Rigidity plasticity viscosity: Can electrorheological dampers protect base-isolated structures from near-source ground motions?, *Earthquake Engineering and Structural Dynamics*, 26, 571-591.
- MATLAB R2010a, 2010.
- MathWorks, www.mathworks.com. April, 2012.
- Mayton, A.G., Du Carme, J.P., Jobes, C.C., & Matty, T.J., *Laboratory Investigation of Seat Suspension Performance During Vibration Testing*, National Institute for Occupational Safety and Health, Pittsburg Research Laboratory, Pittsburg-Pennsylvania.
- Meirovitch, L. (1989). *Dynamics and Control of Structures*: John Wiley & Sons.
- Meirovitch, L. (2001). *Fundamentals of Vibrations*: Mc Graw Hill.
- Metered, H., Bonello, P., & Oyadiji, S.O. (2009). Vibration Control of a Seat Suspension System Using Magnetorheological Damper, *Proceedings of the ASME 2009 International Design Engineering Technical Conferences & Computers and Information in Engineering Conference*, San Diego, California, USA.
- Morse, A. S. (1996). Supervisory control of families of linear set-point controllers – Part 1: Exact matching. *IEEE Transactions on Automatic Control*, 41(10). 1413-1431.
- Naeim, F., Kelly, J.M., (1999). *Design of Seismic Isolated Structures*: John Wiley & Sons Inc.
- Naidu, D.S. (2003). *Optimal Control Systems*, USA: CRC Press,
- Rad, S. Z. (1997). *Methods for Updating Numerical Models in Structural Dynamics*. PhD Dissertation, Imperial College of Science, Technology and Medicine, University of London, London.
- Paice, A. & Gallestey, E. (2010). *Nonlinear Systems and Control: Gain Scheduling*, Lecture Notes, ETH Zurich Automatic Control Laboratory.
- Patten, W.N., J. Sun, G. Li, J. Kuehn, & G. Song (1999), Field test of an intelligent stiffener for bridges at the I-35 walnut creek bridge, *Earthquake Engineering and Structural Dynamics*, 28, 109-126.
- Patten, W.N., Sack, R.L., & He, Q. (1996). Controlled semi-active hydraulic vibration absorber for bridges, *Journal of Structural Engineering*, 122(2), 187-192.
- PEER Strong Motion Database (2000), <http://peer.berkeley.edu/smcat/>, Retrieved 28/11/2012.
- Proakis, J.G., Manolakis, D.G. (1996). *Digital Signal Processing: Principles, Algorithms, and Applications (Third ed.)*: Prentice Hall

- Ramallo, J.C., Johnson, E.A., & Spencer, Jr, B.F. (2002). "Smart" base isolation systems. *Journal of Engineering Mechanics*, 128(10), 1088-1099.
- Raven, F. H. (1995). *Automatic Control Engineering (Fifth ed.)*: McGraw-Hill.
- Reichert, B.A. (1997). *Application of Magnetorheological Dampers for Vehicle Seat Suspensions*, Master of Science Thesis, Virginia Polytechnic Institute and State University, Blacksburg, Virginia.
- Ribakov, Y. & Gluck, J. (2002). Selective controlled base isolation system with magnetorheological dampers, *Earthquake Engineering and Structural Dynamics*, 31, 1301-1324.
- Rodean, S., (2008). Study about damping ratio of the human body-seat system, *Annals of The Oradea University – Fascicle of Management and Technological Engineering*, VII (XVII), 567-575.
- Safonov, M., Laub, A.J, & Hartmann, G.L. (1981). Feedback properties of multivariable systems: The role and use of the return difference matrix, *IEEE Transactions on Automatic Control*, AC-26(1), 47-65.
- Sain, P.M., Sain, M.K. & Spencer, B.F. (1997). Models for hysteresis and application to structural control, *American Control Conference, Proceedings of the 1997*, (4-6), 16-20.
- Sakai, C., Ohmori, H. & Sano, A. (2003). Modeling of MRD with hysteresis for adaptive vibration control, *Proceedings of the 42nd IEEE Conference on Decision and Control*.
- Sapinski, B., & Rosol, M. (2007). MRD performance for shock isolation, *Journal of Theoretical and Applied Mechanics*, 45(1), 133-145, Warsaw.
- Savaresi, S.M., Bittanti, S. & Montiglio, M. (2005). Identification of semi-physical and black-box nonlinear models: The case of MR-dampers for vehicles control, *Automatica*, 41, 113-127.
- Schemmann, A. G. (1997). *Modeling and Active Control of Cable-Stayed Bridges Subject to Multiple-Support Excitation* (Doctor of Philosophy), Stanford, California.
- Schemmann, A. G., & Smith, H. A. (1998a). Vibration control of cable-stayed bridges - Part 1: Modeling issues. *Earthquake Engineering & Structural Dynamics*, 27(8), 811-824.
- Schemmann, A. G., & Smith, H. A. (1998b). Vibration control of cable-stayed bridges - Part 2: Control analyses. *Earthquake Engineering & Structural Dynamics*, 27(8), 825-843.

- Schurter, K.C. & Roschke, P.N. (2001). Neuro-Fuzzy control of structures using magnetorheological dampers, *Proceedings of the American Control Conference Arlington, VA*, 1097-1102.
- Sedaghati, A. (2006). A PI controller based on gain-scheduling for synchronous generator. *Turkish Journal of Electrical Engineering*, 14(2), 241-251.
- Semblat, J. F. (1997). Rheological interpretation of Rayleigh damping. *Journal of Sound and Vibration*, 206(5), 741–744.
- Shamma, J.S. & Athans, M. (1992). Gain scheduling: Potential hazards and possible remedies, *IEEE Control Systems*, 101-107.
- Shamma, J.S. (1988). *Analysis and Design of Gain Scheduled Control Systems*. PhD Dissertation, Massachusetts Institute of Technology, Cambridge.
- Shamma, J. S. & Athans, M. (1992). Gain scheduling: Potential hazards and possible remedies. *IEEE Control Systems*, 101-107.
- Sharma S., (2012). *Notes of Matrices*, <http://www.scribd.com/doc/95031797/Notes-of-Matrices> , Retrived 20.10.2012.
- Silva W. (2013, March). *Personal communication by Dr. Walter Silva from Pacific Engineering and Analysis*, University of California, Berkeley, CA,
- Simon, D. (2006). *Optimal State Estimation: Kalman, H Infinity, and Nonlinear Approaches*: Wiley -Interscience.
- Smith, S.D. (2000). Technical Note: Modeling differences in the vibration response characteristics of the human body, *Journal of Biomechanics*, 33, 1513-1516.
- Song, X., Ahmadian, M., & Southward, S. (2007). Analysis and strategy for superharmonics with semi-active suspension control systems, *Journal of Dynamic Systems, Measurement, and Control*, 129, 795-803.
- Spencer Jr, B.F., Suhardjo, J. & Sain, M.K. (1994). Frequency domain optimal control strategies for aseismic protection. *Journal of Engineering Mechanics*, 120(1), 135-158.
- Spencer Jr, B.F., Dyke, S.J., Sain, M.K. & Carlson, J.D. (1997). Phenomenological model for magnetorheological dampers, *Journal of Engineering Mechanics*, 123(3), 230-238.
- Spencer Jr., B.F. & Nagarajaiah, S. (2003). State of the art of structural control, *Journal of Structural Engineering*, 129(7), 845-856.
- Spong, M.W. & Tsao, T.C. (1998). *Introduction to Mechatronics*, Lecture Notes, University of Illinois at Urbana-Champaign.

- Soong, T.T., Dargush, G.F. (1999). *Design of Seismic Isolated Structures*, John Wiley & Sons Inc.
- Stein, G.J., Mucka, P., Chmurny, R., Hinz, B., & Blüthner, R. (2007). Measurement and modelling of x-direction apparent mass of the seated human body-cushioned seat system, *Journal of Biomechanics*, 40, 1493-1503.
- Stengel, R. F. (1994). *Optimal Control and Estimation*: Dover Publications.
- Symans, M.D. & Constantinou, M.C. (1997). Seismic testing of a building structure with a semi-active fluid damper control system, *Earthquake Engineering and Structural Dynamics*, 26, 759-777.
- Symans, M.D. & Kelly, S.W. (1999). Fuzzy logic control of bridge structures using intelligent semi-active seismic isolation systems, *Earthquake Engineering and Structural Dynamics*, 28, 37-60.
- The Scalar Kalman Filter, Swarthmore college, [www.swarthmore.edu/NatSci/echeeve1/Ref/Kalman/ScalarKalman.html](http://www.swarthmore.edu/NatSci/echeeve1/Ref/Kalman/ScalarKalman.html), 20.4.2012.
- Şahin, İ., Öz, H.R., Engin, T., İlhan A. & Akpolat, A. (2005). Manyetik sıvılı damperlerin yapısal analizi, *Mühendis ve Makina*, 46 (551),41-50.
- Ogata, K. (2002). *Modern Control Engineering*, Prentice Hall.
- Oh, S.K., Y.H. Yoon, & Krishna, A.B. (2007), A study on the performance characteristics of variable valve for reverse continuous damper," *World Academy of Science, Engineering and Technology*, 32, 123-128.
- Ok, S.-Y., Kim, D.-S., Park, K.-S., & Koh, H.-M. (2007). Semi-active fuzzy control of cable-stayed bridges using magnetorheological dampers, *Engineering Structures*, Vol.29, 776-788.
- Özdemir S. (2008). *System Analysis and Control Lecture Notes*, İYTE Mechanical Engineering Department.
- Turan, G., and Kinay, G., Deprem Simülatorü (Masaüstü), TÜBİTAK Proje Raporu, Proje No:105M015, İzmir, Ekim 2007.
- Turan, G., & Kinay, G. (2009). Control of seismic response of three-dimensional model structure by MRDs, *Proceedings of Kocaeli International Earthquake Symposium*,166-173, KOU, Kocaeli.
- Turan, G. & Kinay, G. (2009). Fuzzy control of seismic behaviour by semi-active magnetorheological dampers, *Proceedings of 1st International Fuzzy Systems Symposium*, TOBB University of Economics and Technology, Ankara.
- Turan, G. & Aydın, E. (2011). Değişken sönümleme katsayılı amortisörlerin deprem simülasyonu ile üç katlı bir yapıya olan etkisinin değerlendirilmesi, *Tübitak Proje Raporu*, Proje no:107M353.

- Turan, G. (2010). Hybrid control of a 3-D structure by using semi-Active dampers, *Proceedings of the 9th International Congress on Advances in Civil Engineering*, Trabzon, Turkey.
- Yang, J.N., Wu, J.C., & Agrawal, A.K. (1995). Sliding mode control for seismically excited linear structures, *Journal of Engineering Mechanics*, 121(12), 1386-1390.
- Yang, J.N., Wu, J.C., & Agrawal, A.K. (1995). Sliding mode control for nonlinear and hysteretic structures, *Journal of Engineering Mechanics*, Vol: 121(12), 1330-1339.
- Yang, J.N., Wu, J.C., Reinhorn, A.M., & Riley, M. (1996). Control of sliding-isolated buildings using sliding-mode control, *Journal of Structural Engineering*, 122(2), 179-186.
- Yang, G., (2001). *Large-scale Magneto-rheological Fluid Damper for Vibration Mitigation: Modeling, Testing and Control*, PhD Thesis, University of Notre Dame, Notre Dame, Indiana.
- Yazıcı, İ., Özdemir, A., Şahin, İ., & Engin, T. (2008). Yarı aktif koltuk süspansiyon sisteminin bilgisayar tabanlı gerçek zaman uygulaması, *Otomatik Kontrol Türk Milli Komitesi Otomatik Kontrol Ulusal Toplantısı 2008 Bildiri Özetleri*, İTÜ, İstanbul.
- Yoon, Y.H., M.J. Choi, & Kim, K.H. (2002). Development of a reverse continuous variable damper for semi-active suspension, *International Journal of Automotive Technology*, 3(1), 27-32.
- Yoshida, O., & Dyke, S.J. (2004). Seismic control of a nonlinear benchmark building using smart dampers, *Journal of engineering Mechanics*, 130(4), 386-392.
- Wang, J., Dong, C., Shen, Y., & Wei, J. (2008). Robust modelling and control of vehicle active suspension with MRD, *Vehicle System Dynamics*, 46, Supplement, 509-520.
- Wang, G.-Q., Zhou, X.-Y., Zhang, P.-Z., & Igel, H. (2002). Characteristics of amplitude and duration for near fault strong ground motion from the 1999 Chi-Chi, Taiwan Earthquake. *Soil Dynamics and Earthquake Engineering*, 22, 73-96.
- Wei, L., & Griffin, J. (1998). The prediction of seat transmissibility from measures of seat impedance, *Journal of Sound and Vibration*, 214(1), 121-137.
- Welch, G., & Bishop, G. (2001). *An Introduction to the Kalman Filter*: ACM SIGGRAPH 2001.
- Wereley, N.M., Kamath, G.M. & V., Madhavan. (1999). Hysteresis modeling of semi-active magnetorheological helicopter dampers, *Journal of Intelligent Material Systems and Structures*, 10, 624-633.
- Williams, R.L. & Lawrence, D.A. (2007). *Linear State-Space Control Systems*, USA: John Wiley & Sons,

- Wilson, C.M.D. (2005). *Fuzzy Control of Magnetorheological Dampers for Vibration Reduction of Seismically Excited Structures*, PhD Dissertation, Florida State University.
- Wilson, C.M.D., Abdullah, M.M. (2005). Fuzzy control of magnetorheological dampers in civil structures, *6th European Conference on Structural Dynamics (EURODYN)*, [www.wheel.eng.fsu.edu/research/cwilson/Wilson-Abdullah\\_EURODYN\\_05.pdf](http://www.wheel.eng.fsu.edu/research/cwilson/Wilson-Abdullah_EURODYN_05.pdf)
- Wood, S.L. (1995, Fall). *Introduction to Structural Dynamics Lecture Notes*, University of Illinois Department of Civil Engineering,
- Yan, P. & Özbay, H. (2007). On switching  $H^\infty$  controllers for a class of linear parameter varying systems. *Systems & Control Letters*, 56, 504-511.
- Yan, P. & Özbay, H. (2008). Stability analysis of switched time delay systems. *SIAM Journal on Control and Optimization*, 47(2), 936-949.
- Yang, F., Sedaghati, R. & Esmailzadeh, E. (2009). Development of LuGre friction model for large-scale magneto-rheological fluid dampers, *Journal of Intelligent Material Systems and Structures*, 20(8), 923-937.
- Yang, G. (2001). *Large-scale Magnetorheological Fluid Damper for Vibration Mitigation: Modeling, Testing and Control*, PhD Thesis, University of Notre Dame, Notre Dame, Indiana.
- Yang, G., Spencer Jr, B.F., Jung, H.J. & Carlson, J.D. (2002). Phenomenological model of large-scale MRD systems. *Advances in Building Technology - Elsevier Science Ltd. 1*, 545-552.
- Yao, G.Z., Yap, F.F., Chen, G., Li, W.H. & Yeo, S.H. (2002). MRD and its application for semi-active control of vehicle suspension system, *Mechatronics*, 12, 963-973, (Technical Note).
- Yoshida, O., Dyke, S.J., Giacomini, L.M. & Truman, K.Z. (2003). Experimental verification of torsional response control of asymmetric buildings using MRDs, *Earthquake Engineering and Structural Dynamics*, 32(13), 2085-2105,
- Yoshida, O. (2003). *Torsionally Coupled Response Control of Earthquake Excited Asymmetric Buildings: Development and Application of Effective Control Systems Using Smart Dampers*, PhD Thesis, Washington University, St.Louis, Missouri.
- Yoshida, O. & Dyke, S.J. (2004). Seismic control of a nonlinear benchmark building using smart dampers, *Journal of Engineering Mechanics*, 130(4), 386-392.
- Yoshida, O. & Dyke, S.J. (2005). Response Control in Full Scale Irregular Buildings Using MRDs, *Journal of Structural Engineering*, 131(5), 734-742.
- Yuen, K., Shi, Y., Beck, J., & Lam, H. (2007). Structural protection using MRDs with clipped robust reliability-based control, *Struct Multidisc Optim*, 34, 431-443.

Zak, S., (2003). *Systems and Control*, Oxford University Press.

Zhou, K. & Doyle, J.C. (1995). *Robust and Optimal Control*, USA: Prentice Hall.

Zhou, B., Zongli, L. & Duan, G. (2010). Robust global stabilization of linear systems with input saturation via gain scheduling. *International Journal of Robust and Nonlinear Control*, 20, 424-447.

Zhu, W.Q., Luo, M. & Dong, L. (2004). Semi-active control of wind excited building structures using MR/ER dampers, *Probabilistic Engineering Mechanics*, 19, 279-285.

## APPENDIX A

### SOLUTION OF THE CONTINUOUS-TIME STATE EQUATION

The homogeneous (unforced) state equation is,

$$\dot{\mathbf{x}}(t) = \mathbf{A}(t)\mathbf{x}(t) \quad (\text{A.1})$$

where the upper dot indicates time derivation and  $\mathbf{x}(t_0)$  is known. Integration results,

$$\mathbf{x}(t) = \mathbf{x}(t_0) + \int_{t_0}^t \mathbf{A}(\tau) \mathbf{x}(\tau) d\tau \quad (\text{A.2})$$

Replacing  $t$  by  $\tau$  yields,

$$\mathbf{x}(\tau) = \mathbf{x}(t_0) + \int_{t_0}^{\tau} \mathbf{A}(\tau) \mathbf{x}(\tau) d\tau \quad (\text{A.3})$$

Substituting Equation (A.3) into Equation (A.2) results in the following expression:

$$\begin{aligned} \mathbf{x}(t) &= \mathbf{x}(t_0) + \int_{t_0}^t \mathbf{A}(\tau) \left[ \mathbf{x}(t_0) + \int_{t_0}^{\tau} \mathbf{A}(\tau) \mathbf{x}(\tau) d\tau \right] d\tau \\ &= \mathbf{x}(t_0) + \int_{t_0}^t \mathbf{A}(\tau) d\tau \mathbf{x}(t_0) + \int_{t_0}^t \mathbf{A}(\tau) \int_{t_0}^{\tau} \mathbf{A}(\tau) \mathbf{x}(\tau) d\tau d\tau \end{aligned}$$

Continuing this process by replacing  $t$  by  $\tau$  and plugging the result into Equation (A.2) yields (Raven, 1995),

$$\mathbf{x}(t) = \left[ \mathbf{I} + \int_{t_0}^t \mathbf{A}(\tau) d\tau + \int_{t_0}^t \mathbf{A}(\tau) \int_{t_0}^{\tau} \mathbf{A}(\tau) d\tau d\tau + \int_{t_0}^t \mathbf{A}(\tau) \int_{t_0}^{\tau} \mathbf{A}(\tau) \int_{t_0}^{\tau} \mathbf{A}(\tau) d\tau d\tau d\tau + \dots \right] \mathbf{x}(t_0)$$

The solution of the homogeneous state equation (A.1) is

$$\mathbf{x}(t) = \Phi(t, t_0) \mathbf{x}(t_0) \quad (\text{A.4})$$

where  $\Phi(t, t_0)$  is the state transition matrix, which transforms any initial state  $\mathbf{x}(t_0)$  of the dynamic system into any state  $\mathbf{x}(t)$  at time  $t$  in the absence of either a forcing function or process noise.

$$\Phi(t, t_0) = \left[ I + \int_{t_0}^t \mathbf{A}(\tau) d\tau + \int_{t_0}^t \mathbf{A}(\tau) \int_{t_0}^{\tau} \mathbf{A}(\tau) d\tau d\tau + \int_{t_0}^t \mathbf{A}(\tau) \int_{t_0}^{\tau} \mathbf{A}(\tau) \int_{t_0}^{\tau} \mathbf{A}(\tau) d\tau d\tau d\tau + \dots \right] \quad (\text{A.5})$$

Similarly, the solution of the state equation  $\dot{\mathbf{x}}(t) = \mathbf{A}(t)\mathbf{x}(t) + \mathbf{B}(t)\mathbf{u}(t) + \mathbf{G}(t)\mathbf{w}(t)$  is

$$\mathbf{x}(t) = \Phi(t, t_0) \mathbf{x}(t_0) + \int_{t_0}^t \Phi(t, \tau) \mathbf{B}(\tau) \mathbf{u}(\tau) d\tau + \int_{t_0}^t \Phi(t, \tau) \mathbf{G}(\tau) \mathbf{w}(\tau) d\tau \quad (\text{A.6})$$

which composes of the homogeneous and forced solutions. The initial state  $\mathbf{x}(t_0)$  is known and  $\Phi(t, t_0)$  is the state transition matrix from  $t_0$  to  $t$ . In general, the transition matrix does not have an explicit form. If the commutativity property in Equation (A.7) is satisfied,

$$\mathbf{A}(t) \int_{t_0}^t \mathbf{A}(\tau) d\tau = \int_{t_0}^t \mathbf{A}(\tau) d\tau \mathbf{A}(t) \quad (\text{A.7})$$

only then the state transition matrix has the form in Equation (A.8) (Shalom et al.).

$$\Phi(t, t_0) = e^{\int_{t_0}^t \mathbf{A}(\tau) d\tau} \quad (\text{A.8})$$

The commutativity property presented by Equation (A.7) is satisfied by time-invariant systems or by systems with diagonal  $\mathbf{A}(t)$  matrices. For a time-invariant system, starting from time step  $t_{j-1}$ , the state transition matrix becomes,

$$\Phi(t_j, t_{j-1}) = \Phi(t_{j-1}) = \Phi_{j-1} = e^{\mathbf{A}(t_j - t_{j-1})} = e^{\mathbf{A}dt} \quad (\text{A.9})$$

where  $dt$  is the time increment. The notation  $\Phi(t_j, t_{j-1})$  indicates the transition from time  $t_{j-1}$  to time  $t_j$ .

## APPENDIX B

### TRANSFORMATION FROM CONTINUOUS TO DISCRETE SYSTEMS

Given the linear, continuous-time differential equation model for a stochastic dynamic system, the evolution of the state vector  $\mathbf{x}$  in time is described by

$$\dot{\mathbf{x}}(t) = \mathbf{A}(t)\mathbf{x}(t) + \mathbf{B}(t)\mathbf{u}(t) + \mathbf{G}(t)\mathbf{w}(t) \quad (\text{B.1})$$

The time-varying measurement model is,

$$\mathbf{y}(t) = \mathbf{D}(t)\mathbf{x}(t) + \mathbf{v}(t) \quad (\text{B.2})$$

Terms in Equation (B.1) and (B.2) are displayed in Table 2. The solution of the system in Equation (B.1) is recalled from Equation (A.6),

$$\mathbf{x}(t) = \boldsymbol{\Phi}(t, t_0) \mathbf{x}(t_0) + \int_{t_0}^t \boldsymbol{\Phi}(t, \tau) \mathbf{B}(\tau) \mathbf{u}(\tau) d\tau + \int_{t_0}^t \boldsymbol{\Phi}(t, \tau) \mathbf{G}(\tau) \mathbf{w}(\tau) d\tau \quad (\text{B.3})$$

with the known initial condition  $\mathbf{x}(t_0)$ .

Zero-order hold (ZOH) assumes that the control inputs and the disturbances are piecewise constant over the sampling period  $dt$ . Applying a ZOH to  $\mathbf{u}(t)$ ,  $\mathbf{u}(t)$  becomes constant throughout the sample interval, that is,  $\mathbf{u}(\tau) = \mathbf{u}(j \cdot dt - dt)$ ,  $j \cdot dt - dt \leq \tau < j \cdot dt$ . ZOH is also applied to the disturbances, resulting in  $\mathbf{w}(\tau) = \mathbf{w}(j \cdot dt - dt)$ . The initial time step is  $t_0 = j \cdot dt - dt = t_{j-1}$ . The next step is  $t = t_0 + dt = t_j$ .

$$\mathbf{x}(t_j) = \boldsymbol{\Phi}(t_j, t_{j-1}) \mathbf{x}(t_{j-1}) + \int_{t_{j-1}}^{t_j} \boldsymbol{\Phi}(t_j, \tau) \mathbf{B}(\tau) d\tau \mathbf{u}(t_{j-1}) + \int_{t_{j-1}}^{t_j} \boldsymbol{\Phi}(t_j, \tau) \mathbf{G}(\tau) d\tau \mathbf{w}(t_{j-1}) \quad (\text{B.4})$$

Equation (B.4) gives the solution  $\mathbf{x}$  at the  $j$ th time step, assuming that input and disturbance are piecewise constant, as the sum of a term consisting of the transition of

the initial state and terms arising from the input and process noise. By a sampling definition as  $\mathbf{x}(t)_{@t=jT} = \mathbf{x}_j$ , Equation (B.4) turns into

$$\mathbf{x}_j = \Phi_{j-1} \mathbf{x}_{j-1} + \Gamma_{j-1} \mathbf{u}_{j-1} + \Lambda_{j-1} \mathbf{w}_{j-1} \quad (\text{B.5})$$

where

$$\Phi_{j-1} = \Phi(t_j, t_{j-1}), \Gamma_{j-1} = \int_{t_{j-1}}^{t_j} \Phi(t_j, \tau) \mathbf{B}(\tau) d\tau, \text{ and } \Lambda_{j-1} = \int_{t_{j-1}}^{t_j} \Phi(t_j, \tau) \mathbf{G}(\tau) d\tau$$

If the system properties are constant throughout the time interval  $dt$ , then the  $\mathbf{B}(\tau)$  and  $\mathbf{G}(\tau)$  terms can be taken out of the integral. Then  $\Gamma_{j-1}$  and  $\Lambda_{j-1}$  turns into Equation (B.6),

$$\begin{aligned} \Gamma_{j-1} &= \int_{t_{j-1}}^{t_j} \Phi(t_j, \tau) d\tau \mathbf{B}_{j-1} \\ \Lambda_{j-1} &= \int_{t_{j-1}}^{t_j} \Phi(t_j, \tau) d\tau \mathbf{G}_{j-1} \end{aligned} \quad (\text{B.6})$$

where  $\mathbf{B}_{j-1} = \mathbf{B}(t_{j-1})$  and  $\mathbf{G}_{j-1} = \mathbf{G}(t_{j-1})$ .

Additionally, details about the state transition matrix are presented in Appendix A. The transformation for the measurement equation is presented by Equation (D.10). The continuous formulation can be obtained from the discrete case, vice versa, by a limiting process (Shalom et al., 2001).

## APPENDIX C

### KALMAN FILTER (DISCRETE-TIME FORMULATION)

A random process is modeled as,

$$\mathbf{x}_j = \Phi_{j-1}\mathbf{x}_{j-1} + \Gamma_{j-1}\mathbf{u}_{j-1} + \Lambda_{j-1}\mathbf{w}_{j-1} \quad (\text{C.1})$$

The measurement of the process is performed at discrete times as,

$$\mathbf{y}_j = \mathbf{H}_j\mathbf{x}_j + \mathbf{v}_j \quad (\text{C.2})$$

The terms in Equations (C.1) and (C.2) are defined in Table 5.3. Equation (C.1) describes the way that a state  $\mathbf{x}_j$  is modeled as a linear combination of the previous state  $\mathbf{x}_{j-1}$ , some input  $\mathbf{u}_{j-1}$ , and some process noise  $\mathbf{w}_{j-1}$ . Similarly, the measurement equation Equation (C.2) shows the relationship between the process state and the measurement as the measurement is a linear combination of the states.

In the formulations, the head  $\hat{\phantom{x}}$  stands for the estimated variables and the super minus indicates a priori estimation case. Derivation of the dynamic estimation algorithm starts with performing a priori state estimate  $\hat{\mathbf{x}}_j^-$ . The *a priori state estimate*  $\hat{\mathbf{x}}_j^-$  is utilized to predict the output  $\hat{\mathbf{y}}_j$ .

The a priori value is the one before the measurement information is taken into account, and the a posteriori value is performed after the measurement information is employed. Alternatively, the a priori value is the predicted one and the a posteriori value is the updated one.

The difference between the estimated output and the measured (actual) output is the *measurement residual* (measurement estimation error). The residual shows the discrepancy between the actual measurement and the a priori measurement estimate.

$$\text{Residual} = \mathbf{y}_j - \hat{\mathbf{y}}_j = \mathbf{y}_j - \mathbf{H}_j\hat{\mathbf{x}}_j^- \quad (\text{C.3})$$

By using this information, the estimated state  $\hat{\mathbf{x}}_j$  is improved as,

$$\hat{\mathbf{x}}_j = \hat{\mathbf{x}}_j^- + \mathbb{L}_j \text{Residual} = \hat{\mathbf{x}}_j^- + \mathbb{L}_j(\mathbf{y}_j - \mathbf{H}_j \hat{\mathbf{x}}_j^-) \quad (\text{C.4})$$

The first term  $\hat{\mathbf{x}}_j^-$  in Equation (C.4) represents the a priori prediction of  $\hat{\mathbf{x}}_j$  without any measurement knowledge of the current step. The second term is a correction term containing the difference between the new measurement and its estimate, namely the residual, weighted by a gain factor  $\mathbb{L}_j$ . The gain  $\mathbb{L}_j$  is the most important part of the Kalman estimator.

In the following lines, the optimal gain  $\mathbb{L}_j$  is obtained to improve the state estimate. First, the predicted state  $\hat{\mathbf{x}}_j^-$  is defined by performing the mathematical expectation to the state equation presented in Equation (C.1),

$$\hat{\mathbf{x}}_j^- = E\{\mathbf{x}_j\} = E\{\Phi_{j-1}\mathbf{x}_{j-1} + \Gamma_{j-1}\mathbf{u}_{j-1} + \Lambda_{j-1}\mathbf{w}_{j-1}\} \quad (\text{C.5})$$

where the operator  $E\{\ \}$  represents the expected, or mean, value. The expected value of a known term is itself. Since the process noise  $\mathbf{w}$  is a white sequence with zero mean, its expected value is zero.

$$\hat{\mathbf{x}}_j^- = \Phi_{j-1}\hat{\mathbf{x}}_{j-1} + \Gamma_{j-1}\mathbf{u}_{j-1} \quad (\text{C.6})$$

The state estimate errors, each of which are the difference between the actual state  $\mathbf{x}_j$  and the estimate, are defined in Equation (C.7),

$$\mathbf{e}_j^- = \mathbf{x}_j - \hat{\mathbf{x}}_j^- = \Phi_{j-1}(\mathbf{x}_{j-1} - \hat{\mathbf{x}}_{j-1}) + \Lambda_{j-1}\mathbf{w}_{j-1}, \quad \mathbf{e}_j = \mathbf{x}_j - \hat{\mathbf{x}}_j \quad (\text{C.7})$$

The input  $\mathbf{u}$  does not appear in the a priori estimate error (Equation (C.7)) meaning that it does not have an effect on the estimation error as long as it is known. Then, an expression for the predicted measurement  $\hat{\mathbf{y}}_j$  is similarly obtained by performing the expectation of the measurement equation Equation (C.2).

$$\hat{\mathbf{y}}_j = E\{\mathbf{y}_j\} = E\{\mathbf{H}_j\mathbf{x}_j + \mathbf{v}_j\} \quad (\text{C.8})$$

Since measurement noise has zero mean, the term  $E\{\mathbf{v}_j\}$  vanishes,

$$\hat{\mathbf{y}}_j = \mathbf{H}_j E\{\mathbf{x}_j\} = \mathbf{H}_j \hat{\mathbf{x}}_j^- \quad (\text{C.9})$$

The a priori error covariance  $\mathbb{P}_j^-$  is as follows

$$\mathbb{P}_j^- = E\{(\mathbf{x}_j - \hat{\mathbf{x}}_j^-)(\mathbf{x}_j - \hat{\mathbf{x}}_j^-)^T\} \quad (\text{C.10})$$

where  $\mathbb{P}_j^-$  is a positive-definite matrix. The expressions for the plant in Equation (C.1) and for the a priori state estimate in Equation (C.6) are plugged into Equation (C.10), resulting in the following expression:

$$\begin{aligned} \mathbb{P}_j^- &= E\{(\boldsymbol{\Phi}_{j-1}\mathbf{x}_{j-1} + \boldsymbol{\Gamma}_{j-1}\mathbf{u}_{j-1} + \boldsymbol{\Lambda}_{j-1}\mathbf{w}_{j-1} - \boldsymbol{\Phi}_{j-1}\hat{\mathbf{x}}_{j-1} - \boldsymbol{\Gamma}_{j-1}\mathbf{u}_{j-1})(\boldsymbol{\Phi}_{j-1}\mathbf{x}_{j-1} \\ &\quad + \boldsymbol{\Gamma}_{j-1}\mathbf{u}_{j-1} + \boldsymbol{\Lambda}_{j-1}\mathbf{w}_{j-1} - \boldsymbol{\Phi}_{j-1}\hat{\mathbf{x}}_{j-1} - \boldsymbol{\Gamma}_{j-1}\mathbf{u}_{j-1})^T\} \\ &= E\{(\boldsymbol{\Phi}_{j-1}(\mathbf{x}_{j-1} - \hat{\mathbf{x}}_{j-1}) + \boldsymbol{\Lambda}_{j-1}\mathbf{w}_{j-1})(\boldsymbol{\Phi}_{j-1}(\mathbf{x}_{j-1} - \hat{\mathbf{x}}_{j-1}) + \boldsymbol{\Lambda}_{j-1}\mathbf{w}_{j-1})^T\} \end{aligned}$$

The process noise is independent of the previous values of either the state or its a priori estimate. Therefore, multiplication of the first and fourth terms in the last expression is zero and multiplication of the second and third terms is zero.

$$\begin{aligned} \mathbb{P}_j^- &= E\{(\boldsymbol{\Phi}_{j-1}(\mathbf{x}_{j-1} - \hat{\mathbf{x}}_{j-1})(\mathbf{x}_{j-1} - \hat{\mathbf{x}}_{j-1})^T \boldsymbol{\Phi}_{j-1}^T + \boldsymbol{\Lambda}_{j-1}\mathbf{w}_{j-1}\mathbf{w}_{j-1}^T \boldsymbol{\Lambda}_{j-1}^T)\} \\ &= \boldsymbol{\Phi}_{j-1} E\{(\mathbf{x}_{j-1} - \hat{\mathbf{x}}_{j-1})(\mathbf{x}_{j-1} - \hat{\mathbf{x}}_{j-1})^T\} \boldsymbol{\Phi}_{j-1}^T + \boldsymbol{\Lambda}_{j-1} E\{\mathbf{w}_{j-1}\mathbf{w}_{j-1}^T\} \boldsymbol{\Lambda}_{j-1}^T \end{aligned}$$

Using the previous definitions for the a posteriori estimate error covariance matrix  $\mathbb{P}_{j-1}$  and for the process noise covariance matrix  $\mathbb{Q}_{j-1}$ , the a priori estimate error covariance matrix  $\mathbb{P}_j^-$  becomes as follows

$$\mathbb{P}_j^- = \boldsymbol{\Phi}_{j-1} \mathbb{P}_{j-1} \boldsymbol{\Phi}_{j-1}^T + \boldsymbol{\Lambda}_{j-1} \mathbb{Q}_{j-1} \boldsymbol{\Lambda}_{j-1}^T \quad (\text{C.11})$$

which gives the a priori error covariance as a function of the previous a posteriori value.

The a posteriori error covariance  $\mathbb{P}_j$  is, as follows

$$\mathbb{P}_j = E\{(\mathbf{x}_j - \hat{\mathbf{x}}_j)(\mathbf{x}_j - \hat{\mathbf{x}}_j)^T\}$$

$$\mathbb{P}_j = E\left\{[\mathbf{x}_j - \hat{\mathbf{x}}_j^- - \mathbb{L}_j(\mathbf{y}_j - \mathbf{H}_j\hat{\mathbf{x}}_j^-)][\mathbf{x}_j - \hat{\mathbf{x}}_j^- - \mathbb{L}_j(\mathbf{y}_j - \mathbf{H}_j\hat{\mathbf{x}}_j^-)]^T\right\}$$

where  $\mathbb{P}_j$  is a positive-definite matrix. The measurement equation (Equation (C.2)) is plugged into the last expression, resulting in

$$\mathbb{P}_j = E\left\{[\mathbf{x}_j - \hat{\mathbf{x}}_j^- - \mathbb{L}_j(\mathbf{H}_j\mathbf{x}_j + \mathbf{v}_j - \mathbf{H}_j\hat{\mathbf{x}}_j^-)][\mathbf{x}_j - \hat{\mathbf{x}}_j^- - \mathbb{L}_j(\mathbf{H}_j\mathbf{x}_j + \mathbf{v}_j - \mathbf{H}_j\hat{\mathbf{x}}_j^-)]^T\right\}$$

The expression is turned into the following one by the fact that the a priori estimation error  $\mathbf{e}_j^-$  is uncorrelated with the measurement noise  $\mathbf{v}_j$ ,  $E\{(\mathbf{x}_j - \hat{\mathbf{x}}_j^-)\mathbf{v}_j\} = E\{\mathbf{e}_j^- \mathbf{v}_j\} = 0$ ,

$$\begin{aligned}\mathbb{P}_j &= E\left\{[(\mathbf{I} - \mathbb{L}_j\mathbf{H}_j)(\mathbf{x}_j - \hat{\mathbf{x}}_j^-)(\mathbf{x}_j - \hat{\mathbf{x}}_j^-)^T(\mathbf{I} - \mathbb{L}_j\mathbf{H}_j)^T + \mathbb{L}_j\mathbf{v}_j\mathbf{v}_j^T\mathbb{L}_j^T]\right\} \\ &= (\mathbf{I} - \mathbb{L}_j\mathbf{H}_j) E\{[\mathbf{e}_j^- \mathbf{e}_j^{-T}]\} (\mathbf{I} - \mathbb{L}_j\mathbf{H}_j)^T + \mathbb{L}_j E\{\mathbf{v}_j\mathbf{v}_j^T\} \mathbb{L}_j^T\end{aligned}$$

Using the previous definitions for the a priori estimate error covariance matrix  $\mathbb{P}_j^-$  and for the measurement noise covariance matrix  $\mathbb{R}_j$ , the a posteriori error covariance matrix becomes as follows

$$\mathbb{P}_j = (\mathbf{I} - \mathbb{L}_j\mathbf{H}_j) \mathbb{P}_j^- (\mathbf{I} - \mathbb{L}_j\mathbf{H}_j)^T + \mathbb{L}_j\mathbb{R}_j\mathbb{L}_j^T \quad (\text{C.12})$$

The estimation error increases as the measurement noise increases (see Equation (C.12)). This is consistent with the intuition that as the measurement becomes noisy, the estimation keeps away from the actual state.

The heart of the Kalman estimator, the gain  $\mathbb{L}_j$ , is determined by optimizing a chosen quadratic cost function. In general, a quadratic cost function has a form of  $\mathbf{q}^T(t)\mathbb{T}\mathbf{q}(t)$ , where  $\mathbf{q}(t)$  is the variable to be optimized and  $\mathbb{T}$  is a symmetric, positive-definite *weighting matrix*. For the current problem, the expected value of the squared state estimation error is chosen to be minimized with a unity weighting matrix. Hence, the cost function to be minimized by choosing the gain  $\mathbb{L}_j$  is

$$\mathbf{J}_j = E\{\mathbf{e}_j \mathbf{e}_j^T\} = \text{tr}(\mathbb{P}_j) \quad (\text{C.13})$$

where  $\text{tr}$  indicates trace of the matrix. The terms along the main diagonal of  $\mathbb{P}_j$  are the variances of state estimation errors. Here, the aim is to minimize the sum of the terms along the main diagonal of  $\mathbb{P}_j$ . The trace is minimized due to the fact that individual mean-squared errors are minimized when the sum of them is minimized. On the other hand, there are various ways for optimization by different choices of cost function (Brown & Hwang, 1992). Thus, an estimate is produced in such a manner that the error is minimized statistically. Consequently, from Equation (C.12),

$$\frac{\partial \mathbf{J}_j}{\partial \mathbb{L}_j} = \frac{\partial \text{tr}(\mathbb{P}_j)}{\partial \mathbb{L}_j} \quad (\text{C.14})$$

It is obvious that the trace of a matrix is equal to the trace of its transpose. Differentiation of the trace is performed by using the following matrix differentiation formulas,

$$\begin{aligned} \frac{\partial \text{tr}(\mathfrak{S}\mathfrak{I})}{\partial \mathfrak{S}} = \mathfrak{I}^T &\Rightarrow \frac{\partial \text{tr}(\mathbb{L}_j \mathbf{H}_j \mathbb{P}_j^-)}{\partial \mathbb{L}_j} = (\mathbf{H}_j \mathbb{P}_j^-)^T \\ \frac{\partial \text{tr}(\mathfrak{S}\mathfrak{S}\mathfrak{S}^T)}{\partial \mathfrak{S}} = 2\mathfrak{S}\mathfrak{S} &\Rightarrow \frac{\partial \text{tr}(\mathbb{L}_j (\mathbf{H}_j \mathbb{P}_j^- \mathbf{H}_j^T + \mathbb{R}_j) \mathbb{L}_j^T)}{\partial \mathbb{L}_j} = 2\mathbb{L}_j (\mathbf{H}_j \mathbb{P}_j^- \mathbf{H}_j^T + \mathbb{R}_j) \end{aligned} \quad (\text{C.15})$$

where matrix  $\mathfrak{S}\mathfrak{I}$  must be square and matrix  $\mathfrak{S}$  must be symmetric.  $\mathbb{P}_j^-$  is independent of the gain  $\mathbb{L}_j$ . Equation (C.12) is rearranged as

$$\mathbb{P}_j = \mathbb{P}_j^- - \mathbb{L}_j \mathbf{H}_j \mathbb{P}_j^- - \mathbb{P}_j^- \mathbf{H}_j^T \mathbb{L}_j^T + \mathbb{L}_j (\mathbf{H}_j \mathbb{P}_j^- \mathbf{H}_j^T + \mathbb{R}_j) \mathbb{L}_j^T \quad (\text{C.16})$$

Differentiation of the trace of  $\mathbb{P}_j$  with respect to  $\mathbb{L}_j$  results as follows

$$\frac{\partial \text{tr}(\mathbb{P}_j)}{\partial \mathbb{L}_j} = -2(\mathbf{H}_j \mathbb{P}_j^-)^T + 2\mathbb{L}_j (\mathbf{H}_j \mathbb{P}_j^- \mathbf{H}_j^T + \mathbb{R}_j) \quad (\text{C.17})$$

The expression in Equation (C.17) is set equal to zero and is solved for the optimal gain, resulting in

$$\mathbb{L}_j = \mathbb{P}_j^- \mathbf{H}_j^T (\mathbf{H}_j \mathbb{P}_j^- \mathbf{H}_j^T + \mathbb{R}_j)^{-1} \quad (\text{C.18})$$

Finally, the optimal Kalman observer gain  $\mathbb{L}_j$ , which minimizes the mean-square estimation error, is obtained for the discrete-time model. An alternative form of the discrete-time gain matrix  $\mathbb{L}_j$  is presented in Equation (D.1).

Additionally, whether the extremum is a minimum or a maximum is determined as follows: The second derivative of the cost function should be positive-definite to provide the sufficient condition for a minimum. This fact can be formulized by the following equation:

$$\frac{\partial^2 \text{tr}(\mathbb{P}_j)}{\partial \mathbb{L}_j^T \partial \mathbb{L}_j} = 2(\mathbf{H}_j \mathbb{P}_j^- \mathbf{H}_j^T + \mathbb{R}_j) > \mathbf{0} \quad (\text{C.19})$$

The extremum obtained by  $\mathbb{L}_j$ , which is defined in Equation (C.18) is a minimum since  $\mathbb{P}_j^-$  and  $\mathbb{R}_j$  are positive-definite (Stengel, 1994). On the hand, the priori error covariance  $\mathbb{P}_j^-$  is a positive-definite matrix since  $\mathbb{P}_j^-$  cannot be a negative-definite matrix (see Equation (C.10)).  $\mathbb{R}_j$  must be positive-definite to guarantee a minimum. In order to obtain a compact expression for the a posteriori error covariance  $\mathbb{P}_j$ , the gain equation (Equation (C.18)) is rearranged as,

$$\mathbb{R}_j = \mathbb{L}_j^{-1} (\mathbf{I} - \mathbb{L}_j \mathbf{H}_j) \mathbb{P}_j^- \mathbf{H}_j^T$$

An expression for posteriori error covariance  $\mathbb{P}_j$ , which do not contain the variable  $\mathbb{R}_j$ , is formed by plugging the expression for  $\mathbb{R}_j$  into Equation (C.12),

$$\begin{aligned} \mathbb{P}_j &= (\mathbf{I} - \mathbb{L}_j \mathbf{H}_j) \mathbb{P}_j^- (\mathbf{I} - \mathbb{L}_j \mathbf{H}_j)^T + \mathbb{L}_j \mathbf{K}_j^{-1} (\mathbf{I} - \mathbb{L}_j \mathbf{H}_j) \mathbb{P}_j^- \mathbf{H}_j^T \mathbb{L}_j^T \\ &= (\mathbf{I} - \mathbb{L}_j \mathbf{H}_j) (\mathbb{P}_j^- (\mathbf{I} - \mathbb{L}_j \mathbf{H}_j)^T + \mathbb{P}_j^- \mathbf{H}_j^T \mathbb{L}_j^T) \end{aligned}$$

Finally, the expression for the a posteriori error covariance  $\mathbb{P}_j$  is obtained as,

$$\mathbb{P}_j = (\mathbf{I} - \mathbb{L}_j \mathbf{H}_j) \mathbb{P}_j^- \quad (\text{C.20})$$

## APPENDIX D

### TRANSFORMATION FROM KALMAN OBSERVER TO KALMAN-BUCY OBSERVER

Transformation from the Kalman observer (discrete-time formulation) to the Kalman-Bucy observer (continuous-time formulation) is just a limiting process as the time increment  $dt$  goes to zero.

Before starting the derivation, expressions for the process noise covariance matrix  $\mathbb{Q}_j$  and for the measurement noise covariance matrix  $\mathbb{R}_j$  in terms of continuous variables are required to eliminate the discrete variables in the formulation. Additionally, an expression for the Kalman filter gain  $\mathbb{L}_j$  containing a single  $\mathbb{R}_j^{-1}$  term is required to eliminate the term  $dt$  during the limiting process.

First, Equation (C.18) is rearranged to obtain an expression for the Kalman filter gain  $\mathbb{L}_j$ . The expression should contain a single  $\mathbb{R}_j^{-1}$  term. Therefore, a term of  $\mathbb{R}_j^{-1}\mathbb{R}_j$  is added at the middle of the expression.

$$\begin{aligned}\mathbb{L}_j &= \mathbb{P}_j^- \mathbf{H}_j^T \mathbb{R}_j^{-1} \mathbb{R}_j (\mathbf{H}_j \mathbb{P}_j^- \mathbf{H}_j^T + \mathbb{R}_j)^{-1} \\ &= \mathbb{P}_j^- \mathbf{H}_j^T \mathbb{R}_j^{-1} ((\mathbf{H}_j \mathbb{P}_j^- \mathbf{H}_j^T + \mathbb{R}_j) \mathbb{R}_j^{-1})^{-1} \\ &= \mathbb{P}_j^- \mathbf{H}_j^T \mathbb{R}_j^{-1} (\mathbf{H}_j \mathbb{P}_j^- \mathbf{H}_j^T \mathbb{R}_j^{-1} + \mathbf{I})^{-1}\end{aligned}$$

The expression on the right-hand side is taken to the left and the multiplications are performed as follows:

$$\begin{aligned}\mathbb{L}_j (\mathbf{H}_j \mathbb{P}_j^- \mathbf{H}_j^T \mathbb{R}_j^{-1} + \mathbf{I}) &= \mathbb{P}_j^- \mathbf{H}_j^T \mathbb{R}_j^{-1} \\ \mathbb{L}_j \mathbf{H}_j \mathbb{P}_j^- \mathbf{H}_j^T \mathbb{R}_j^{-1} + \mathbb{L}_j &= \mathbb{P}_j^- \mathbf{H}_j^T \mathbb{R}_j^{-1}\end{aligned}$$

Then, the term  $\mathbb{L}_j$  is left on the left-hand-side alone,

$$\mathbb{L}_j = -\mathbb{L}_j \mathbf{H}_j \mathbb{P}_j^- \mathbf{H}_j^T \mathbb{R}_j^{-1} + \mathbb{P}_j^- \mathbf{H}_j^T \mathbb{R}_j^{-1}$$

$$\mathbb{L}_j = (\mathbf{I} - \mathbf{L}_j \mathbf{H}_j) \mathbb{P}_j^- \mathbf{H}_j^T \mathbb{R}_j^{-1} \quad (\text{D.1})$$

Equation (C.20) is plugged into Equation (D.1),

$$\mathbb{L}_j = \mathbb{P}_j \mathbf{H}_j^T \mathbb{R}_j^{-1} \quad (\text{D.2})$$

which is the alternative form of the discrete-time Kalman filter gain matrix.

The process noise covariance matrix is presented in Table 5.2 as,

$$E\{\mathbf{w}_j \mathbf{w}_i^T\} = \mathbb{Q}_j \Delta(j - i) \quad (\text{D.3})$$

for discrete-time case and, as,

$$E\{\mathbf{w}(t) \mathbf{w}^T(r)\} = \mathbf{Q}(t) \delta(t - r) \quad (\text{D.4})$$

for continuous-time case, where  $\mathbb{Q}_j$  and  $\mathbf{Q}(t)$  are positive definite covariance matrices.  $\Delta$  and  $\delta$  are Kronecker and Dirac delta functions, respectively. The expression for the discrete-time process noise in Equation (B.5) is as follows

$$\mathbf{A}_j \mathbf{w}_j = \int_{t_j}^{t_{j+1}} \boldsymbol{\Phi}(t_{j+1}, \tau) \mathbf{G}(\tau) \mathbf{w}(\tau) d\tau \quad (\text{D.5})$$

For vanishingly small values of time increment  $dt$ , the state transition matrix  $\boldsymbol{\Phi}(t_j, t_j)$  tends to the identity matrix. Equation (D.5) turns into Equation (D.6) for  $\mathbf{G}(t)$  values constant or slowly varying over the time interval.

$$\mathbf{A}_j \mathbf{w}_j = \mathbf{G}(t_j) \mathbf{w}(t_j) dt \quad (\text{D.6})$$

The covariance of the discrete-time process noise is as,

$$E\{\mathbf{A}_j \mathbf{w}_j \mathbf{w}_j^T \mathbf{A}_j^T\} = \mathbf{A}_j E\{\mathbf{w}_j \mathbf{w}_j^T\} \mathbf{A}_j^T = \mathbf{A}_j \mathbb{Q}_j \mathbf{A}_j^T \quad (\text{D.7})$$

Then, Equation (D.5) is plugged into Equation (D.7),

$$E\{\Lambda_j \mathbf{w}_j \mathbf{w}_j^T \Lambda_j^T\} = E \left\{ \left[ \int_{t_j}^{t_{j+1}} \Phi(t_{j+1}, \tau) \mathbf{G}(\tau) \mathbf{w}(\tau) d\tau \right] \left[ \int_{t_j}^{t_{j+1}} \Phi(t_{j+1}, \alpha) \mathbf{G}(\alpha) \mathbf{w}(\alpha) d\alpha \right]^T \right\}$$

The above expression is rewritten as a double integral as follows

$$E\{\Lambda_j \mathbf{w}_j \mathbf{w}_j^T \Lambda_j^T\} = E \left\{ \iint_{t_j}^{t_{j+1}} \Phi(t_{j+1}, \tau) \mathbf{G}(\tau) \mathbf{w}(\tau) \mathbf{w}^T(\alpha) \mathbf{G}^T(\alpha) \Phi^T(t_{j+1}, \alpha) d\tau d\alpha \right\}$$

Applying the expectation on the integrand yields,

$$E\{\Lambda_j \mathbf{w}_j \mathbf{w}_j^T \Lambda_j^T\} = \iint_{t_j}^{t_{j+1}} \Phi(t_{j+1}, \tau) \mathbf{G}(\tau) E\{\mathbf{w}(\tau) \mathbf{w}^T(\alpha)\} \mathbf{G}^T(\alpha) \Phi^T(t_{j+1}, \alpha) d\tau d\alpha$$

Equation (D.4) is plugged into the last expression,

$$E\{\Lambda_j \mathbf{w}_j \mathbf{w}_j^T \Lambda_j^T\} = \iint_{t_j}^{t_{j+1}} \Phi(t_{j+1}, \tau) \mathbf{G}(\tau) \mathcal{Q}(\tau) \delta(\tau - \alpha) \mathbf{G}^T(\alpha) \Phi^T(t_{j+1}, \alpha) d\tau d\alpha$$

Then, it is integrated over  $\alpha$ ,

$$E\{\Lambda_j \mathbf{w}_j \mathbf{w}_j^T \Lambda_j^T\} = \int_{t_j}^{t_{j+1}} \Phi(t_{j+1}, \tau) \mathbf{G}(\tau) \mathcal{Q}(\tau) \mathbf{G}^T(\alpha) \Phi^T(t_{j+1}, \alpha) d\tau$$

For very small values of time increment, the state transition matrix  $\Phi(t_j, t_j)$  tends into the identity matrix, and the expression becomes as follows for  $\mathbf{G}(t)$  values constant or slowly varying within the time interval.

$$E\{\Lambda_j \mathbf{w}_j \mathbf{w}_j^T \Lambda_j^T\} = \mathbf{G}(t_j) \mathcal{Q}(t_j) \mathbf{G}^T(t_j) dt \quad (\text{D.8})$$

Equations (D.7) and (D.8) are collected together resulting in

$$\Lambda_j \mathbb{Q}_j \Lambda_j^T = \mathbf{G}(t_j) \mathbf{Q}(t_j) \mathbf{G}^T(t_j) dt \quad (\text{D.9})$$

The last term in Equation (C.11) will be replaced with its equivalent in Equation (D.9). Additionally, an expression for the measurement noise covariance matrix  $\mathbb{R}_j$  is obtained as follows. The discrete-time measurement can be thought as a short-term average of the continuous-time measurement, during which the state is assumed to be constant (Bar-Shalom et al., 2001).

$$\begin{aligned} \mathbf{y}_j &= \frac{1}{dt} \int_{t_j-dt}^{t_j} \mathbf{y}(\tau) d\tau \\ &= \frac{1}{dt} \int_{t_j-dt}^{t_j} [\mathbf{D}(\tau) \mathbf{x}(\tau) + \mathbf{v}(\tau)] d\tau \\ &= \mathbf{D}(t_j) \mathbf{x}(t_j) + \frac{1}{dt} \int_{t_j-dt}^{t_j} \mathbf{v}(\tau) d\tau \end{aligned} \quad (\text{D.10})$$

Comparison of the last expression with the discrete-time measurement equation ( $\mathbf{y}_j = \mathbf{H}_j \mathbf{x}_j + \mathbf{v}_j$ ) yields,

$$\mathbf{D}(t_j) = \mathbf{H}_j \quad (\text{D.11})$$

and the discrete-time and continuous-time measurement noises are related as

$$\mathbf{v}_j = \frac{1}{dt} \int_{t_j-dt}^{t_j} \mathbf{v}(\tau) d\tau \quad (\text{D.12})$$

The covariance of the discrete-time measurement noise and the intensity of the continuous-time measurement noise are related as follows

$$\begin{aligned} \mathbb{R}_j &= E\{\mathbf{v}_j \mathbf{v}_j^T\} = E\left\{\frac{1}{dt^2} \iint_{t_j-dt}^{t_j} \mathbf{v}(\tau) \mathbf{v}^T(\alpha) d\tau d\alpha\right\} \\ &= \frac{1}{dt^2} \iint_{t_j-dt}^{t_j} \mathbf{R}(\tau) \delta(\tau - \alpha) d\tau d\alpha \end{aligned}$$

Integration of the Dirac delta function with respect to  $\tau_2$  is equal to the Heaviside (unit step) function, and the expression becomes

$$\mathbb{R}_j = \frac{1}{dt^2} \int_{t_j-dt}^{t_j} \mathcal{R}(\tau) d\tau = \frac{1}{dt} \frac{1}{dt} \int_{t_j-dt}^{t_j} \mathcal{R}(\tau) d\tau$$

The value of the last integration divided by  $dt$  is an average value of the continuous function  $\mathcal{R}$  at the time step  $t_j$ . Finally, the relationship between the covariances of the discrete-time measurement noise and the continuous-time measurement noise is, as follows

$$\mathbb{R}_j = \frac{1}{dt} \mathcal{R}(t_j) \quad (\text{D.13})$$

So far, expressions, which are required during the derivation of the gain matrix and the propagation equation of the state error covariance, have been obtained.

While transforming from discrete to continuous case, as  $dt$  goes to zero, there is not a distinction between the a priori and a posteriori error covariance matrices  $\mathbb{P}_{j-1}^-$  and  $\mathbb{P}_{j-1}$ . Using its alternative form in Equation (D.2), the optimal filter gain takes the form in Equation (D.14) in the limit case,

$$\mathbf{L}(t) = \lim_{dt \rightarrow 0} \left\{ \frac{\mathbb{L}_j}{dt} \right\} = \lim_{dt \rightarrow 0} \left\{ \frac{\mathbb{P}_j \mathbf{H}_j^T \mathbb{R}_j^{-1}}{dt} \right\} \quad (\text{D.14})$$

Equation (D.13) is plugged into Equation (D.14), resulting in

$$\mathbf{L}(t) = \lim_{dt \rightarrow 0} \left\{ \frac{dt \mathbb{P}_j \mathbf{H}_j^T \mathcal{R}^{-1}(t_j)}{dt} \right\}$$

The term  $\mathbf{H}_j$  can be replaced by  $\mathbf{D}(t_j)$  by means of Equation (D.11) for the continuous-time case. Finally,

$$\mathbf{L}(t) = \mathcal{P}(t) \mathbf{D}^T(t) \mathcal{R}^{-1}(t) \quad (\text{D.15})$$

The same limiting procedure is applied to the covariance difference equation,

$$\lim_{dt \rightarrow 0} \left\{ \frac{\mathbb{P}_j^- - \mathbb{P}_{j-1}^-}{dt} \right\} = \frac{d\mathbb{P}(t)}{dt} = \dot{\mathbb{P}}(t) \quad (\text{D.16})$$

The expression for the a priori error covariance matrix  $\mathbb{P}_j^-$  is recalled from Equation (C.11),

$$\mathbb{P}_j^- = \boldsymbol{\Phi}_{j-1} \mathbb{P}_{j-1} \boldsymbol{\Phi}_{j-1}^T + \mathbf{A}_j \mathbb{Q}_j \mathbf{A}_j^T \quad (\text{D.17})$$

An expression for the state transition matrix  $\boldsymbol{\Phi}_{j-1}$  of the time-varying case is required. The expression for  $\boldsymbol{\Phi}(t, t_0)$  is referred from Equation (A.5),

$$\boldsymbol{\Phi}(t, t_0) = \left[ \mathbf{I} + \int_{t_0}^t \mathbf{A}(\tau) d\tau + \int_{t_0}^t \mathbf{A}(\tau) \int_{t_0}^{\tau} \mathbf{A}(\tau) d\tau d\tau + \int_{t_0}^t \mathbf{A}(\tau) \int_{t_0}^{\tau} \mathbf{A}(\tau) \int_{t_0}^{\tau} \mathbf{A}(\tau) d\tau d\tau d\tau + \dots \right] \quad (\text{D.18})$$

$\mathbf{A}(\tau)$  is assumed to be constant over the time interval  $(t, t_0)$ . This assumption is not a contradiction for time-varying systems. The system is still time-varying. Additionally, the higher order terms, which contain powers of  $dt$  equal to or greater than two, will vanish during the limiting procedure. Therefore, the corresponding integrands in Equation (D.18) are not taken into account. Finally,  $\boldsymbol{\Phi}(t, t_0)$  is approximated as, for a time-varying system,

$$\boldsymbol{\Phi}(t, t_0) \approx \mathbf{I} + \mathbf{A}(t)dt \quad (\text{D.19})$$

The initial step  $t_0 = t_{j-1}$  and the next step  $t = t_j$  are inserted to the expression,

$$\boldsymbol{\Phi}(t_j, t_{j-1}) = \boldsymbol{\Phi}(t_{j-1}) = \boldsymbol{\Phi}_{j-1} \approx \mathbf{I} + \mathbf{A}(t_{j-1})dt = \mathbf{I} + \mathbf{A}_{j-1}dt \quad (\text{D.20})$$

Equation (D.17) is referred,

$$\mathbb{P}_j^- = (\mathbf{I} + \mathbf{A}_{j-1}dt)(\mathbb{P}_{j-1}^- - \mathbb{L}_{j-1}\mathbf{H}_{j-1}\mathbb{P}_{j-1}^-)(\mathbf{I} + \mathbf{A}_{j-1}dt)^T + \mathbf{A}_{j-1} \mathbb{Q}_{j-1} \mathbf{A}_{j-1}^T \quad (\text{D.21})$$

The expression (Equation (D.9)) for  $\mathbf{A}_{j-1}\mathbf{Q}_{j-1}\mathbf{A}_{j-1}^T$  is substituted into the last equation,

$$\mathbb{P}_j^- = (\mathbf{I} + \mathbf{A}_{j-1}dt)(\mathbb{P}_{j-1}^- - \mathbb{L}_{j-1}\mathbf{H}_{j-1}\mathbb{P}_{j-1}^-)(\mathbf{I} + \mathbf{A}_{j-1}dt)^T + \mathbf{G}(t_{j-1})\mathbf{Q}(t_{j-1})\mathbf{G}^T(t_{j-1})dt$$

The multiplications and limiting procedure are performed. After this, there is not a distinction between the a priori and a posteriori error covariance matrices.

$$\begin{aligned} \lim_{dt \rightarrow 0} \left\{ \frac{\mathbb{P}_j^- - \mathbb{P}_{j-1}^-}{dt} \right\} = \lim_{dt \rightarrow 0} \left\{ \mathbb{P}_{j-1}^- \mathbf{A}_{j-1}^T - \frac{\mathbb{L}_{j-1}\mathbf{H}_{j-1}\mathbb{P}_{j-1}^-}{dt} - \mathbb{L}_{j-1}\mathbf{H}_{j-1}\mathbb{P}_{j-1}^- \mathbf{A}_{j-1}^T \right. \\ \left. + \mathbf{A}_{j-1}\mathbb{P}_{j-1}^- + \mathbf{A}_{j-1}\mathbb{L}_{j-1}\mathbf{H}_{j-1}\mathbb{P}_{j-1}^- + \mathbf{G}(t_{j-1})\mathbf{Q}(t_{j-1})\mathbf{G}^T(t_{j-1}) \right\} \end{aligned} \quad (\text{D.22})$$

Equation (D.13) is plugged into Equation (D.2),

$$\mathbb{L}_{j-1} = dt \mathbb{P}_{j-1} \mathbf{H}_{j-1}^T \mathcal{R}^{-1}(t_{j-1}) \quad (\text{D.23})$$

The term  $\mathbf{H}_{j-1}$  can be replaced by  $\mathbf{D}(t_{j-1})$  by means of Equation (D.11) for the continuous-time case. Equation (D.23) is inserted into Equation (D.22). Then, the propagation equation of the covariance is formed as follows, namely the matrix Riccati differential equation,

$$\dot{\mathcal{P}}(t) = \mathbf{A}(t)\mathcal{P}(t) + \mathcal{P}(t)\mathbf{A}^T(t) + \mathbf{G}(t)\mathbf{Q}(t)\mathbf{G}^T(t) - \mathcal{P}(t)\mathbf{D}^T(t)\mathcal{R}^{-1}(t)\mathbf{D}(t)\mathcal{P}(t) \quad (\text{D.24})$$

with the initial condition  $\mathcal{P}(t_0)$ .

## APPENDIX E

# MATLAB CODE FOR VOD INCLUDING KALMAN-BUCY OBSERVER

```
%%%%%%%%%%%%%%%%%%%%%%%%%%%%%%%%%%%%%%%%%%%%%%%%%%%%%%%%%%%%%%%%%%%%%%%%%%%%%%  
Gain Scheduled Control of a VOD by LQG %%%%%%%%%  
%%%%%%%%%%%%%%%%%%%%%%%%%%%%%%%%%%%%%%%%%%%%%%%%%%%%%%%%%%%%%%%%%%%%%%%%%%%%%%  
  
%author: Kinay  
%created: january 2010  
%last modified: 27.5.2013  
  
close all; clear; clc;  
  
superstructure %3x3 superstructure  
  
base %base  
  
h1star = ones(dofstar,1); %EQ xdd is applied to all DOFs  
h2star = (1 0 0 0)'; storyD = 1;  
  
eq_  
  
disp_limit_of_base = 0.03; %m  
f_damper_MAX = 5000; %Newton, max damper force  
c_ = (100:100:1000 1500:500:3000 10000:5000:25000); %VOD's  
  
passive_min_max_damping  
  
noise_generation  
  
size_initiation  
  
inner_controller_CORE %CORE  
  
disp('simulation STARTS')  
  
c_opti(1) = min(c_); %simulation starts with min c_  
A_combstar = A_combstar_store(:,:,1);  
C_combstar = C_combstar_store(:,:,1); %capital C: system matrix  
c_combstar = c_combstar_store(:,:,1); %small c: damping matrix  
AbAUG = AbAUG_store(:,:,1);  
CbAUG = CbAUG_store(:,:,1);  
Kb = Kb_store(:,:,1);  
LbAUG = LbAUG_store(:,:,1);  
  
flag = 0; sayt = 0;  
XbAO = zeros(2+2,1); XsOBS = zeros(2*dof,1); XESTI_ = zeros(2*dofstar,1);  
  
for i = 2:length(eq)  
  
Prhs(:,i) = -Mstar * h1star * eq(i);  
xhelper0 = xSTATEstar(:,i-1);
```

```

(x_ , xDot_ , xDdot_ ) = NewmarkLIN(Mstar, Kstar, c_ combstar, Prhs(:,i-1:i), dt, xhelper0);
xSTATEstar(:,i) = (x_(:,2) ; xDot_(:,2)); xDdotstar(:,i) = xDdot_(:,2);

xSTATEb = xSTATEstar(1:4:5,:); xSTATEs = (xSTATEstar(2:4,:) ; xSTATEstar(6:8,:));

fD(:,i) = -c_opti(i-1) * xSTATEstar(dofstar+1,i);
Ymeasured(:,i-1:i) = (xSTATEstar(1:dofstar,i-1:i) + measuNOIS(1:dofstar,i-1:i) ; fD(:,i-1:i) +
measuNOIS(ns,i-1:i));
YBmeasured = Ymeasured(1:4:5,:); YSmeasured = Ymeasured(2:4,:);

%Observer of augmented base
AbAUG_OBS = AbAUG - LbAUG*CbAUG;
BbAUG_OBS = (BbAUG-LbAUG*DbAUG LbAUG);
XbAO = complexanalysis(AbAUG_OBS , BbAUG_OBS , (0 0 ; xSTATEs(1:3:6,i-1:i) ; eqN(i-1:i) ;
YBmeasured(:,i-1:i)) , XbAO);
XbAUG_ESTI(:,i) = XbAO(1:2);

%Observer of diagonalized superstructure
AsOBS = As-Ls*Cssu;
BsOBS = (Gs-Ls*Dd Ls);
XsOBS = complexanalysis(AsOBS , BsOBS , (eqN(i-1:i) ; xSTATEb(:,i-1:i) ; YSmeasured(:,i-1:i)) ,
XsOBS);
XsESTI(:,i) = XsOBS;

XESTI(:,i) = (XbAUG_ESTI(1,i) ; XsESTI(1:3,i) ; XbAUG_ESTI(2,i) ; XsESTI(4:6,i));

velocity_correction

%UPPER CONTROLLER
if abs(XbAUG_ESTI(1,i)) < disp_limit_of_base
    if XbAUG_ESTI(2,i-1) * XbAUG_ESTI(2,i) < 0
        flag=0;
    end %if

else
    flag=1;
end

flag_1_and_0

fD(i) = -c_opti(i) * XbAUG_ESTI(2,i);

restricting_fD

fD(i) = -c_opti(i) * XbAUG_ESTI(2,i);

if abs(fD(i)) > f_damper_MAX
    for jj = 2:length(c_)
        if c_opti(i) == c_(jj);
            c_opti(i) = c_(jj-1);
        end
    end
end
fD(i) = -c_opti(i) * XbAUG_ESTI(2,i);

obtain_A_C_Ab_Cb_cD_Kb_LbAUG

end %end of time loop
plot_

```

## APPENDIX F

### UNFORCED RESPONSE OF SECOND-ORDER MECHANICAL SYSTEM

The unforced equation of motion for a SDOF second-order system is formulated as follows:

$$m\ddot{q}(t) + c\dot{q}(t) + kq(t) = 0 \quad (\text{F.1})$$

A general solution for Equation (F.1) in shape of  $q(t) = e^{pt}$  is searched where  $p$  is a real or complex number (Artem, 2008). The general solution and its derivatives are plugged into Equation (F.1),

$$(mp^2 + cp + k) e^{pt} = 0 \quad (\text{F.2})$$

For a nontrivial solution, the first part in Equation (F.2) should be equal to zero since the second part cannot be zero. By multiplying this equation by  $1/m$ ,

$$p^2 + \frac{c}{m}p + \frac{k}{m} = 0 \quad (\text{F.3})$$

If the damping is assumed to be viscous, then  $c/m = 2\zeta\omega_n$ .  $\zeta$  is the dimensionless damping ratio defined as the fraction of the present damping to the critical damping value. The critical damping value is the damping value representing the boundary between the under-damped and over-damped cases. Hence, Equation (F.3) turns into the following equation since  $\omega_n^2 = k/m$ .

$$p^2 + 2\zeta\omega_n p + \omega_n^2 = 0 \quad (\text{F.4})$$

The roots of Equation (F.4) are as follows

$$p_{1,2} = -\zeta\omega_n \pm \omega_n\sqrt{\zeta^2 - 1} \quad (\text{F.5})$$

Up to that point, there is not a restriction related with the damping ratio  $\zeta$ . For over-damped case ( $\zeta > 1$ ), the roots of Equation (F.4) are real and distinct, leading to a solution as,

$$q(t) = \mathbb{C}_1 e^{(-\zeta + \sqrt{\zeta^2 - 1})\omega_n t} + \mathbb{C}_2 e^{(-\zeta - \sqrt{\zeta^2 - 1})\omega_n t} \quad (\text{F.6})$$

where  $\mathbb{C}_1$  and  $\mathbb{C}_2$  are constants. The motion decays to a reference zero value without oscillations. On the other hand, if  $\zeta = 1$  (critically damped case), then the roots of Equation (F.4) are real and repeated and the solution becomes

$$q(t) = (\mathbb{C}_1 + \mathbb{C}_2 t) e^{-\zeta\omega_n t} \quad (\text{F.7})$$

The motion is similar to the over-damped case. The critically damped response returns to an equilibrium position without performing oscillations and at a faster rate compared to the over-damped case. As damping is added to the system, the system returns to an equilibrium position slower than the critically damped case.

Finally, for the under-damped case ( $\zeta < 1$ ), the roots of Equation (F.4) become complex leading to a oscillatory behavior (coming in conjugate pairs). The response is formulated as:

$$q(t) = \mathbb{C}_1 e^{(-\zeta + \sqrt{\zeta^2 - 1})\omega_n t} + \mathbb{C}_2 e^{(-\zeta - \sqrt{\zeta^2 - 1})\omega_n t} \quad (\text{F.8})$$

By plugging the rearrangement in Equation (F.9),

$$\sqrt{\zeta^2 - 1} = \sqrt{1 - \zeta^2} i \quad (\text{F.9})$$

Equation (F.8) becomes as follows

$$q(t) = (\mathbb{C}_1 e^{i\sqrt{1 - \zeta^2}\omega_n t} + \mathbb{C}_2 e^{-i\sqrt{1 - \zeta^2}\omega_n t}) e^{-\zeta\omega_n t} \quad (\text{F.10})$$

The damped circular frequency is defined as  $\omega_d = \omega_n \sqrt{1 - \zeta^2}$  for under-damped systems. By plugging this definition into Equation (F.10), the following formula is obtained.

$$q(t) = (\mathbb{C}_1 e^{i\omega_d t} + \mathbb{C}_2 e^{-i\omega_d t}) e^{-\zeta\omega_n t} \quad (\text{F.11})$$

The Euler formula ( $e^{-i\omega t} = \cos \omega t \pm i \sin \omega t$ ) is plugged into Equation (F.11) for complex exponential term,

$$\begin{aligned} q(t) &= (\mathbb{C}_1 (\cos \omega_d t + i \sin \omega_d t) + \mathbb{C}_2 (\cos \omega_d t - i \sin \omega_d t)) e^{-\zeta\omega_n t} \\ &= ((\mathbb{C}_1 + \mathbb{C}_2) \cos \omega_d t + i(\mathbb{C}_1 - \mathbb{C}_2) \sin \omega_d t) e^{-\zeta\omega_n t} \\ &= (\mathbb{C}_3 \cos \omega_d t + \mathbb{C}_4 \sin \omega_d t) e^{-\zeta\omega_n t} \end{aligned} \quad (\text{F.12})$$

Finally, the under-damped response  $q(t)$  becomes

$$q(t) = \mathbb{C} \sin(\omega_d t + \phi) e^{-\zeta\omega_n t} \quad (\text{F.13})$$

where  $\mathbb{C}$  is a constant.  $\phi$  is the phase angle.

At this point, the sinusoidal term, which leads to the oscillatory behavior, arises from the imaginary part of the roots  $p_{1,2}$  that only exists in under-damped case. On the other hand, the real part determines how fast the response decays acting as an envelope curve (Özdemir, 2008).

## APPENDIX G

### FINITE-TIME LINEAR QUADRATIC REGULATOR

The formulation of a steady-state (infinite-horizon) LQR consists of three equations: a performance index, its optimum solution (in form of an algebraic Riccati equation (ARE)), and a feedback control law that contains the solution of the ARE. In this subsection, the aim is to answer the questions below:

- Does the linearity of LQR arise from the definition of the system ( $\dot{\mathbf{x}}(t) = \mathbf{A}\mathbf{x}(t) + \mathbf{B}\mathbf{u}(t)$ ), or from the definition of the controller ( $\mathbf{u}(t) = -\mathbf{K}\mathbf{x}(t)$ ) ?
- How is the state feedback form chosen? Is it supplied by the formulation or does it originate from a shape that is assumed at the beginning of the formulation?
- Why is the cost function chosen as  $\tilde{J}(\mathbf{z}) = \frac{1}{2} \int_{t_0}^{\infty} \{\mathbf{x}^T(t)\mathbf{Q}\mathbf{x}(t) + \mathbf{u}^T(t)\mathbf{R}\mathbf{u}(t)\}dt$ ? How can it be modified?
- How is the cost function minimized? What is the Euler-Lagrange equation? What is the Hamiltonian function?

The derivation of LQ-based control algorithms (LQR, LQG,  $H_2$ /LQG) look like an optimization problem rather than a control design due to the minimization of the performance index. The *necessary condition* for a minimum is that the first variation of the related function must vanish. Additionally, the minimality of the extremum is guaranteed by a positive-definite second variation as a *sufficient condition*.

In the literature, the solution of the LQR problem is obtained via the dynamic programming or via a variational approach. The dynamic programming states that an optimal cost function must get the minimum value of the cost function:  $J^* = \min_{\mathbf{u}(t)}\{J\}$ . Hence, the necessary and sufficient conditions for minimality are satisfied simultaneously. The dynamic programming solution leads to the *Hamilton-Jacobi-Bellman (HJB) equation* (Başar et al., 1998; Anderson & Moore, 1989; Bryson & Ho, 1975).

In the variational approach, a certain function is minimized. If this function is the Hamiltonian function  $\mathcal{H}[\mathbf{x}(t), \mathbf{u}(t), \boldsymbol{\lambda}(t), t] = j[\mathbf{x}(t), \mathbf{u}(t), t] + \boldsymbol{\lambda}^T(t)[\mathbf{A}\mathbf{x}(t) + \mathbf{B}\mathbf{u}(t)]$  for a linear time-invariant system, then the approach is named the *minimum*

*principle of Pontryagin* (Stengel, 1994). After minimizing the Hamiltonian function, the well-known Euler-Lagrange equation is formed.

In the current study, the variational approach is utilized. An augmented cost function  $\tilde{J}$  is minimized instead of the Hamiltonian function. First of all, the inner structure of the cost function has to be determined.

The current optimization problem is to determine a control input  $\mathbf{u}^*(t)$  that enforces the system to follow a trajectory  $\mathbf{x}^*(t)$ , while minimizing a scalar cost function  $J(\mathbf{z})$  subjected to the constraints imposed by the state equation and the defined initial state  $\mathbf{x}_0$ . The asterisks \* stands for the optimal case.  $\mathbf{z}(t)$  contains the variables that are desired to be optimized.

The aim is to reflect the magnitude of the function  $J(\mathbf{z}(t), \dot{\mathbf{z}}(t), t)$ , which is a measure of the cost paid along a trajectory. The area under it may be a convenient measure of its cumulative magnitude within a certain time period. For unconstrained minimization, the cost of  $\mathbf{z}(t)$  on the interval  $(t_0, t_f)$  can be defined as the integral of a function reflecting the contribution of the variables to the cost. Here, the derivative  $\dot{\mathbf{z}}(t)$  is assumed to be continuous for the mathematical necessities during minimization. Then, the performance index may take the following form:

$$J(\mathbf{z}) = \int_{t_0}^{t_f} j[\mathbf{z}(t), \dot{\mathbf{z}}(t), t] dt$$

with possible boundary conditions.  $\mathbf{z}^*(t)$  minimizes the objective function  $J(\mathbf{z})$ .

If some constraints exist, they can be imposed via the augmented cost function. Additionally, if the final state is set free, but it is desired to be penalized via a terminal state penalty, then the performance index becomes,

$$\tilde{J}(\mathbf{z}) = \int_{t_0}^{t_f} \{j[\mathbf{z}(t), \dot{\mathbf{z}}(t), t] + \lambda^T(t) c[\mathbf{z}(t), \dot{\mathbf{z}}(t), t]\} dt + \mathbb{Y}(\mathbf{x}(t_f), t_f) \quad (\text{G.1})$$

The constraint is embedded within the function to be minimized by the *Lagrange multiplier* vector  $\lambda(t)$ . In the constrained optimization,  $\mathbf{z}^*(t)$  minimizes  $\tilde{J}(\mathbf{z})$ , while satisfying the given boundary conditions and the constraint  $c[\mathbf{z}(t), \dot{\mathbf{z}}(t), t] = 0$  over the entire interval. Due to mathematical requirements, Lagrange multiplier functions are assumed to be continuously differentiable on the

interval  $(t_0, t_f)$ .  $\mathbb{Y}(\mathbf{x}(t_f), t_f)$  is the terminal state penalty term, by which the system is forced to be as close as possible to reference zero state at time  $t_f$ . The regulator is punished, if it cannot drive the system to zero state at the predefined time  $t_f$ . This is a *free-final-state and fixed-time constraint optimization problem*.

If the attention is turned into the inner structure of the scalar integrand function  $j[\mathbf{z}(t), \dot{\mathbf{z}}(t), t]$ , a scalar quadratic form as  $\mathbf{z}^T(t)\mathbf{z}(t)$  may be a convenient selection, otherwise positive and negative terms may cancel each other leading to a completely wrong result. In the next steps of minimization, differentiation of the integrand function  $j$  will be performed and a constant number of 2 will appear in the formulation. A constant 1/2 is introduced to the cost function in order to get rid of the multiplier 2. Otherwise, it would have been carried out throughout the result. For the current problem, the cost should reflect the penalty paid in terms of the states, control input, and time. The performance index should penalize nonzero states and control inputs. Therefore, the variable  $\mathbf{z}(t)$  in Equation (G.1) takes the following form:

$$\mathbf{z}(t) = \begin{bmatrix} \mathbf{x}(t) \\ \mathbf{u}(t) \end{bmatrix}$$

If total accelerations are desired to be regulated instead of states, then  $\mathbf{z}(t)$  should be arranged in a convenient way including  $\mathbf{u}(t)$  (Turan & Aydın, 2011). One of the fundamental objectives in a control design is to keep the magnitude of the control input bounded, or relatively small. Additionally, for a regulator problem, an arbitrary nonzero initial state has to be moved to a zero state as fast as possible. Therefore, it may be a convenient choice to limit  $\mathbf{x}(t)$  during the event by such a cost as  $\int_{t_0}^{t_f} \{\mathbf{x}^T(t)\mathbf{x}(t)\}dt$  (or  $\int_{t_0}^{t_f} \{\mathbf{x}^T(t)\mathbf{x}(t)\}^{1/2}dt$ ) that represents the accumulated deviation of the state from zero state. A weight can be introduced on the states to exhibit the relative importance among the states and the control. The designer may desire to pay more control input for some of the states that are more important than the others, or vice versa. In the current research, the control of the base response is much more crucial than those of the story responses since the whole structure can be protected by controlling the response of the base. Hence, the function  $j$  becomes  $[\mathbf{x}^T(t) \quad \mathbf{u}^T(t)] \begin{bmatrix} \mathbf{Q} & \mathbf{0} \\ \mathbf{0} & \mathbf{R} \end{bmatrix} \begin{bmatrix} \mathbf{x}(t) \\ \mathbf{u}(t) \end{bmatrix}$ . The zero cross terms in the weighting matrix point out

the uncoupled nature of the variables in the current problem. To this end, the cost function of the constrained minimization is introduced in a weighted quadratic form as:

$$\begin{aligned} \tilde{J}(\mathbf{z}) = & \frac{1}{2} \int_{t_0}^{t_f} \{ \mathbf{x}^T(t) \mathbf{Q} \mathbf{x}(t) + \mathbf{u}^T(t) \mathbf{R} \mathbf{u}(t) + \boldsymbol{\lambda}^T(t) [\mathbf{A} \mathbf{x}(t) + \mathbf{B} \mathbf{u}(t) - \dot{\mathbf{x}}(t)] \} dt \\ & + \frac{1}{2} \mathbf{x}^T(t_f) \mathbf{S} \mathbf{x}(t_f) \end{aligned} \quad (\text{G.2})$$

for the deterministic control design of a linear time-invariant system

$$\dot{\mathbf{x}}(t) = \mathbf{A} \mathbf{x}(t) + \mathbf{B} \mathbf{u}(t) \quad \mathbf{x}(t_0) = \mathbf{x}_0 \quad (\text{G.3})$$

The weights  $\mathbf{Q}$ ,  $\mathbf{R}$ , and  $\mathbf{S}$  are constant vectors for a linear time-invariant system. They may be chosen as constant or time dependent in case of a linear time-variant system (Başar et al., 1998).

The weighting matrix  $\mathbf{Q}$  must be symmetric since the cross weights  $Q_{ij}$  and  $Q_{ji}$ , which denote the relationship between the elements  $x_i$  and  $x_j$ , should be identical. Similarly,  $\mathbf{R}$  and  $\mathbf{S}$  should be symmetric. Additionally, they must be positive-semidefinite since they represent the weights of the related variables. Distinctively,  $\mathbf{R}$  should be strictly positive-definite\*\*. This obligation will appear within the context of the sufficient condition for a minimum of the cost function (Zak, 2003). Williams and Lawrence (2007) defines the cost function as:

*“The cost function serves to capture the fundamental design tradeoff between the conflicting objectives of regulation performance and control effort.”* (p.358). Therefore, the relative values of  $\mathbf{Q}$ ,  $\mathbf{R}$ , and  $\mathbf{S}$  represent the importance of  $\mathbf{x}(t)$ ,  $\mathbf{u}(t)$ , and  $\mathbf{x}(t_f)$  in the control design, respectively. Desired performance specifications are imposed on the controlled system response by proper choice of the weighting matrices as summarized in Table G.1.

---

\*\* A symmetric matrix is *positive-definite*, if all its eigenvalues are positive. It is *positive-semidefinite*, if all its eigenvalues are nonnegative. Hence, its smallest eigenvalue can be zero.

Table G.1. Performance of the controller

$Q$	$R$	Advantage	Disadvantage
High	Low	Good regulation performance	High control energy
Low	High	Inadmissible regulation performance	Low control energy

According to Table G.1, if  $Q$  is chosen relatively high compared to  $R$ , then the contribution of the state to the cost will be higher than that of the control. Thus, the system forces itself to decrease the contribution of the states by keeping the states relatively small. Vice-versa, if  $Q$  is selected relatively small compared to  $R$ , the states will be relatively large. Similarly, as the penalty  $S$  on the final state is increased, the regulation performance gets better in the sense that the final state gets closer to a zero state, and vice versa. In summary, if the weight of any variable is held relatively high, then the system will tend to underspend in terms of the related variable. The weights are generally determined by a trial-and-success procedure. They are tuned until a satisfactory behavior is reached or until the control aims are fulfilled.

The cost function has already been determined. At the current step, the attention is turned into the minimization of the performance index. For a functional  $\tilde{J}$  whose first two derivatives are continuous, the fundamental theorem of calculus of variations states that *for an optimum  $\mathbf{z}^*(t)$  to exist, the (first) variation of  $\tilde{J}(\mathbf{z})$  must vanish*. Physically, this condition indicates that  $\tilde{J}(\mathbf{z})$  is insensitive (stationary) to infinitesimal changes (variations) in  $\mathbf{z}(t)$ . In the current formulation, the necessary condition is fulfilled by satisfying the Euler-Lagrange equation in Equation (G.4). The sufficient condition for a minimum is that the second variation must be a positive-definite matrix for every nonzero variation. In the current study, the minimality is guaranteed by utilizing the Gateaux variation as described by (Williams & Lawrence, 2007).

$$\delta\tilde{J}[\mathbf{z}^*(t), \delta\mathbf{z}(t)] = \mathbf{0}$$

The first variation of the integral function  $\tilde{J}$  is performed. Then, integration by parts is applied to express the relation only in terms of  $\delta\mathbf{z}(t)$  (Naidu, 2003). Finally, the following relation is obtained.

$$\int_{t_0}^{t_f} \left[ \frac{\partial \tilde{J}}{\partial \mathbf{z}^*} - \frac{d}{dt} \left( \frac{\partial \tilde{J}}{\partial \dot{\mathbf{z}}^*} \right) \right] \delta \mathbf{z}(t) dt = \mathbf{0}$$

Since  $\delta \mathbf{z}(t)$  is arbitrary, the only way for the necessary condition to be satisfied is that the coefficient of  $\delta \mathbf{z}(t)$  vanishes. This yields the well-known *Euler-Lagrange equation* as,

$$\frac{\partial \tilde{J}}{\partial \mathbf{z}^*} - \frac{d}{dt} \left( \frac{\partial \tilde{J}}{\partial \dot{\mathbf{z}}^*} \right) = \mathbf{0} \quad (\text{G.4})$$

within the whole interval. For the current constrained minimization problem where the variable is  $\mathbf{z}(t) = [\mathbf{x}^T(t) \quad \mathbf{u}^T(t)]^T$  and the integrand function is as follows

$$\tilde{J}[\mathbf{z}(t), \dot{\mathbf{z}}(t), t] = \frac{1}{2} [\mathbf{x}^T(t) \mathbf{Q} \mathbf{x}(t) + \mathbf{u}^T(t) \mathbf{R} \mathbf{u}(t)] + \lambda^T(t) [\mathbf{A} \mathbf{x}(t) + \mathbf{B} \mathbf{u}(t) - \dot{\mathbf{x}}(t)] \quad (\text{G.5})$$

The Euler-Lagrange equation yields

$$[\mathbf{x}^T(t) \mathbf{Q} + \lambda^T(t) \mathbf{A} \quad \mathbf{u}^T(t) \mathbf{R} + \lambda^T(t) \mathbf{B}]^T = \frac{d}{dt} [-\lambda^T(t) \quad \mathbf{0}]^T$$

in matrix form. The equations are rearranged and transposed, resulting in the following formulas:

$$\dot{\lambda}(t) = -\mathbf{A}^T \lambda^T(t) - \mathbf{Q} \mathbf{x}(t) \quad (\text{G.6})$$

$$\mathbf{u}(t) = -\mathbf{R}^{-1} \mathbf{B}^T \lambda(t) \quad (\text{G.7})$$

At the moment, three equations (Equations (G.3), (G.6), and (G.7)) should be solved simultaneously for the LQR problem. They are rearranged in matrix form as below,

$$\begin{bmatrix} \dot{\mathbf{x}}(t) \\ \dot{\lambda}(t) \end{bmatrix} = \begin{bmatrix} \mathbf{A} & -\mathbf{B} \mathbf{R}^{-1} \mathbf{B}^T \\ -\mathbf{Q} & -\mathbf{A}^T \end{bmatrix} \begin{bmatrix} \mathbf{x}(t) \\ \lambda(t) \end{bmatrix} \quad (\text{G.8})$$

$$\mathbf{u}(t) = -\mathbf{R}^{-1} \mathbf{B}^T \lambda(t) \quad (\text{G.9})$$

with boundary conditions

$$\mathbf{x}(t_0) = \mathbf{x}_0 \quad \lambda(t_f) = \mathbf{S}\mathbf{x}(t_f) \quad (\text{G.10})$$

The second boundary condition arises from the fact that the variation of the cost function vanishes on an optimum trajectory (see (Williams & Lawrence, 2007) for details). But, solution of these ordinary differential equations (ODEs) is not guaranteed due to the contradiction in the definition of boundary conditions since they are introduced at different boundaries. It can be solved by the *sweep method* assuming that the states and the Lagrange multiplier are linearly related by

$$\lambda(t) = \mathbf{P}(t)\mathbf{x}(t) \quad (\text{G.11})$$

(Williams & Lawrence, 2007; Başar et al., 1998; Meirovitch, 1989; Bryson & Ho, 1975). Hence, an expression for control input in form of state feedback is obtained by substituting Equation (G.11) into Equation (G.9) as follows:

$$\mathbf{u}(t) = -\mathbf{R}^{-1}\mathbf{B}^T\mathbf{P}(t)\mathbf{x}(t) = -\mathbf{K}(t)\mathbf{x}(t) \quad (\text{G.12})$$

where the time varying feedback gain matrix is  $\mathbf{K}(t) = \mathbf{R}^{-1}\mathbf{B}^T\mathbf{P}(t)$ . Minimization of the augmented cost function  $\tilde{J}$  yields to a linear feedback law. Choosing a nonquadratic cost would not turn out to a linear feedback law (Anderson & Moore, 1989).

An initial condition  $\lambda(t_0)$  or a terminal condition  $\mathbf{x}(t_f)$  is required to solve Equation (G.8). These can be obtained by the linear relation between the states and the Lagrange multiplier in Equation (G.11) at  $t_0$  and  $t_f$  as follows

$$\lambda(t_0) = \mathbf{P}(t_0)\mathbf{x}_0 \quad \mathbf{P}(t_f) = \mathbf{S}$$

The initial condition for  $\lambda(t)$  is known. Then, the ODEs in Equation (G.8) can be solved forward in time with  $\mathbf{x}(t_0) = \mathbf{x}_0$  and  $\lambda(t_0) = \mathbf{P}(t_0)\mathbf{x}_0$ . Equation (G.11) is differentiated. Then, the first expression in the matrix form of Equation (G.8) is substituted into it. Finally, by equating the differentiated form of Equation (G.11) to the second expression in the matrix form of Equation (G.8), the following differential equation is obtained:

$$-\dot{\mathbf{P}}(t) = \mathbf{A}^T \mathbf{P}(t) + \mathbf{P}(t) \mathbf{A} - \mathbf{P}(t) \mathbf{B} \mathbf{R}^{-1} \mathbf{B}^T \mathbf{P}(t) + \mathbf{Q} \quad \mathbf{P}(t_f) = \mathbf{S} \quad (\text{G.13})$$

This equation is the well-known *differential Riccati equation* (DRE). The solution  $\mathbf{P}(t)$  to this equation must be symmetric for the whole interval since its boundary condition is defined by a symmetric matrix (Williams & Lawrence, 2007).

## APPENDIX H

### DIAGONALIZATION OF A SQUARE MATRIX

In linear algebra, two matrices  $\mathbb{A}$  and  $\bar{\mathbb{A}} = \mathbf{T}^{-1}\mathbb{A}\mathbf{T} \in \mathbb{C}^{n \times n}$  are named *similar*, if an invertible  $\mathbf{T}$  matrix exists. Here,  $\mathbf{T}$  is a *similarity transformation* that is a linear change of coordinates. The eigenvalues of a square matrix remain unchanged under a similarity transformation since similar matrices have identical characteristic polynomials (Juang, 1994).

The behavior of linear dynamical systems is governed by their eigenvalues and eigenvectors. A square matrix  $\mathcal{A}$  acts on a nonzero vector  $\boldsymbol{\psi}$  by  $\mathcal{A}\boldsymbol{\psi} = \lambda\boldsymbol{\psi}$ . If the vector magnitude changes while its direction remains constant or reverse, then the vector is an *eigenvector* of the matrix. The factor  $\lambda$  that changes the magnitude of the eigenvector is the corresponding *eigenvalue* (Sharma, 2012). Here,  $\mathcal{A}$  is a linear transformation. This case can be visualized in two-dimensional space as in Figure H.1.

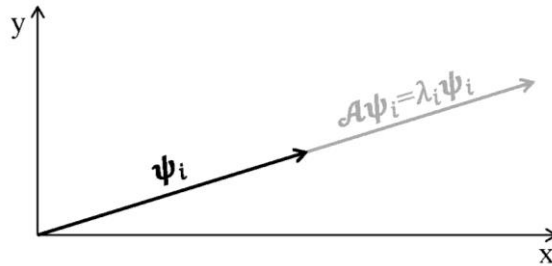


Figure H.1. The  $i$ th eigenvector of the matrix  $\mathcal{A}$  in two-dimensional space (Source: Sharma, 2012)

The standard eigenvalue problem for the  $n \times n$  matrix  $\mathcal{A}$  is as,

$$\mathcal{A}\boldsymbol{\psi}_i = \lambda_i\boldsymbol{\psi}_i, \quad i = 1, 2, \dots, n \quad (\text{H.1})$$

The equations are stacked in a similar manner in (Juang, 1994),

$$\begin{aligned}
\mathcal{A} [\boldsymbol{\psi}_1 \ \boldsymbol{\psi}_2 \ \dots \ \boldsymbol{\psi}_n] &= [\lambda_1 \boldsymbol{\psi}_1 \ \lambda_2 \boldsymbol{\psi}_2 \ \dots \ \lambda_n \boldsymbol{\psi}_n] \\
&= [\boldsymbol{\psi}_1 \ \boldsymbol{\psi}_2 \ \dots \ \boldsymbol{\psi}_n] \begin{bmatrix} \lambda_1 & 0 & \dots & 0 \\ 0 & \lambda_2 & & 0 \\ & \vdots & \ddots & \vdots \\ 0 & 0 & \dots & \lambda_n \end{bmatrix} \quad (\text{H.2})
\end{aligned}$$

in matrix form,

$$\mathcal{A}\boldsymbol{\Psi} = \boldsymbol{\Psi}\boldsymbol{\Lambda} \quad (\text{H.3})$$

where  $\boldsymbol{\Psi}$  is the eigenvector matrix. By postmultiplying Equation (H.3) by  $\boldsymbol{\Psi}^{-1}$ , the eigendecomposition of the matrix  $\mathcal{A}$  is obtained as

$$\mathcal{A} = \boldsymbol{\Psi}\boldsymbol{\Lambda}\boldsymbol{\Psi}^{-1} \quad (\text{H.4})$$

Similarly, by premultiplying Equation (H.3) by  $\boldsymbol{\Psi}^{-1}$ , the diagonalized form of the matrix  $\mathcal{A}$  is as follows

$$\boldsymbol{\Lambda} = \boldsymbol{\Psi}^{-1}\mathcal{A}\boldsymbol{\Psi} \quad (\text{H.5})$$

where  $\boldsymbol{\Lambda}$  contains the eigenvalues of  $\mathcal{A}$  on the main diagonal (see Equation (H.2-b)).

For a square matrix  $\mathcal{A}$ , *diagonalization* is the operation of performing a similarity transformation resulting a diagonal matrix  $\boldsymbol{\Lambda}$ , in which the eigenvalues of  $\mathcal{A}$  are placed on the main diagonal (Williams & Lawrence, 2007).

# APPENDIX I

## SIGNALS AND RELATED SUBJECTS

### Signal Construction:

In the present research, signals were constructed numerically. Then, they were sampled. In the present subsection, the facts that have to be considered while sampling a signal were mentioned.

If an analog signal is sampled twice at every cycle, then the curve obtained by connecting the sample points resembles the continuous signal. There is a risk of sampling at zero values, leading to a meaningless case. Therefore, it is a convenient way to sample more than twice at every cycle (Bores, 1998). The sampling theorem by C.E.Shannon simply states that it is required to sample a signal at a rate at least two times greater than its maximum frequency component in order to represent the signal correctly (Texas Instruments, 2004). For sure, the resulting signal is much more close to the original one as the sampling rate increases.

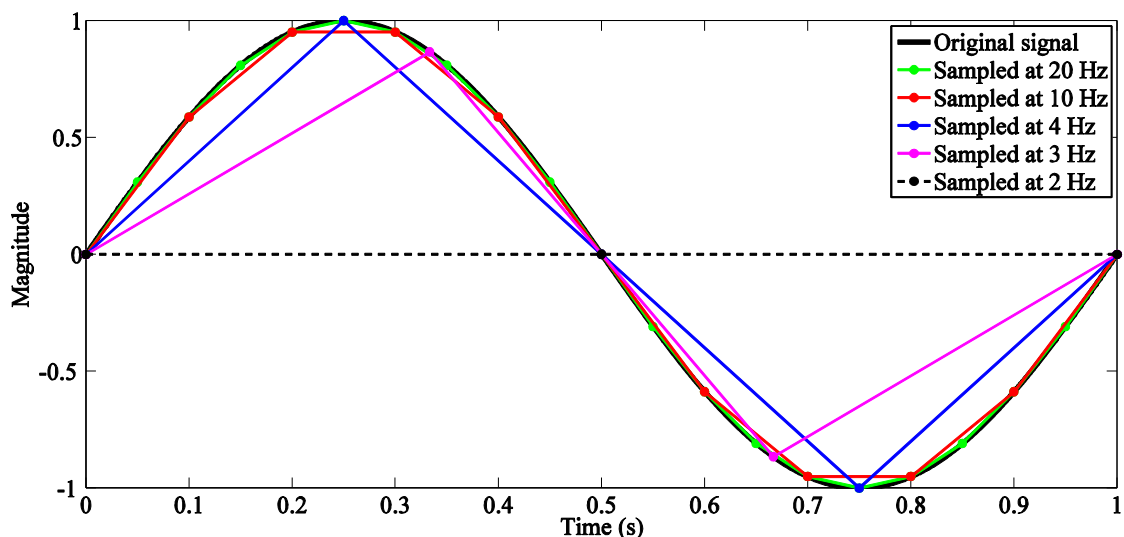


Figure I.1. A signal of 1 Hz is sampled at different frequencies as 2, 3, 4, 10, and 20 Hz (The sampled points and reconstructed signals are indicated by dot and colored lines, respectively)

In Figure I.1, a signal which represented an analog signal of 1 Hz was sampled at different frequencies (2, 3, 4, 10, and 20 Hz). The sampled values were indicated by

colored dots. The sampled signals were reconstructed simply by connecting points by colored lines. There are various signal reconstruction ways (Lathi, 2010; Proakis & Manolakis, 1996).

In Figure I.1, the full period signal was constructed starting from zero. Otherwise, spectral leakage would occur during the FFT transformation and the energy would spread out various frequencies instead of a single frequency in the spectral domain (see the following lines about spectral leakage).

According to the sampling theorem, the signal indicated by the bold black line had to be sampled at least at 2 Hz which came across zero values for the present case (see Figure I.1). Consequently, the sampling frequency was at least 20 times higher than the signal frequency.

### **Fourier Analysis:**

The Fourier analysis is based on the Fourier series and Fourier transform. Its discretized form is present for digital systems. The main idea is that a function periodic in time can be represented as a sum of sinusoids (Ewins, 2000).

The Fourier transform is a reversible mathematical transformation between the time and frequency domains. The discrete Fourier transform is computed via the fast Fourier transform (FFT) that utilizes a specific computational algorithm developed for faster calculations in the 1960s. The number of data is required to be a power of 2 in FFT (Juang, 1994).

The FFT assumes the signal is periodic and symmetric out of the given range of signal. The number of data has to be a power of 2 for FFT. If this is not the case, then zero padding symmetrically to both ends of the data set is recommended. But, at this point, it is important to note that the frequency content is contaminated by the components those come from the sudden drop at both ends of the data set. This impulsive effect may add components similar to white noise, and the components that do not exist in the signal may appear. Therefore, instead of a sudden drop, a smooth transition band to zero value may be applied symmetrically to both ends of the signal.

In the context of the present thesis, the FFT function was coded within MATLAB. The magnitudes of the FFT were obtained from the *fft* functional of MATLAB. The number of data supplied by the *fft* functional of MATLAB was the number of bins. Bins in frequency domain correspond to the samples in time domain.

The *fft* functional of MATLAB gave relative amplitudes of components of the signal. The magnitudes in time-domain were calculated by dividing the absolute value of the *fft* functional by half of the number of samples in time or in frequency domains.

### Spectral Leakage:

In the context of the present research, the FFT of signals were performed several times. Most of these signals were the responses of the systems and the seismic excitation in time domain. They were composed of sine waves with various frequencies. In the present subsection, the effect of improper simulation of a signal on the frequency distribution of the signal was visualized for a pure sine wave. Actually, this fact could not be taken into account in the present research since the signals were composed of sine waves with various frequencies.

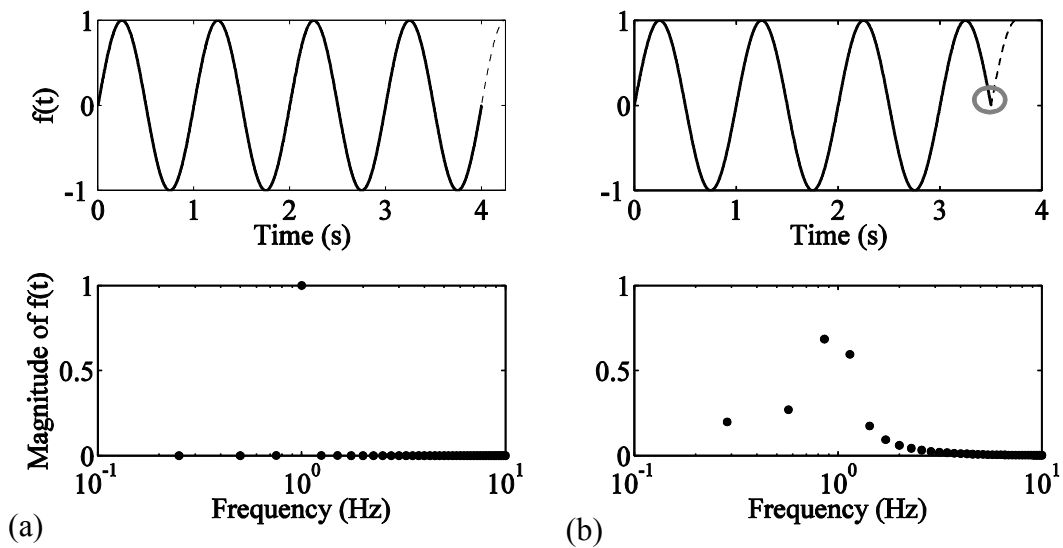


Figure I.2. (a) Proper and (b) improper simulation or measurement of the same sine wave (Source: Ewins, 2000)

Figure I.2 shows a single sine wave of 1 Hz, which is measured properly and improperly. The signal in time- and frequency-domains are presented in Figure I.2(a) and (b), respectively. The signal in Figure I.2(a) is measured till the first 4 seconds which is a full period. On the other hand, the signal in Figure I.2(b) is measured for 3.5 seconds. According to Figure I.2(b), when the measurement is performed inconveniently, the energy of the signal leaks into a number of frequencies instead of a concentrating at a single frequency. The observed phenomenon is known as *spectral*

*leakage*. The Fourier transform assumes that the signal is periodic outside the measurement interval. If this is not the case in reality, then discontinuities at the edges of the measurement interval occur as indicated by a red circle.

In the literature, there exist suggestions to prevent or reduce the effect of leakage for data acquisition (Ewins, 2000; Bores, 1998).

## APPENDIX J

### MATLAB CODES FOR MRD INCLUDING LQR, SMC, $H_2$ /LQG, AND FUZZY CONTROLLERS

```
%%%%%%%%%%%%%%%%%%%%%%%%%%%%%%%%%%%%%%%%%%%%%%%%%%%%%%%%%%%%%%%%%%%%%%%%  
%%  
%% Response of superstructure is controlled by MRD (LQR) %%  
%%%%%%%%%%%%%%%%%%%%%%%%%%%%%%%%%%%%%%%%%%%%%%%%%%%%%%%%%%%%%%%%%%%%%%%%  
%author: Kinay  
%created: 2009, updated: 6.2013
```

```
close all; clear; clc;  
superstructure %3x3 superstructure  
h1 = ones(dof,1); h2 = (1 0 0)'; storyD = 1;  
EQ_;  
global fMRDmax vMAX stepIN  
fMRDmax = 3000 %max MRD force N  
vMAX = 2.25; %max applied voltage V  
stepIN = 100; %chosen, A VERY IMPORTANT CHOICE FOR THE ALGORITHM  
system_;  
size_initiation;  
lqr_;  
  
for i = 2:length(eq)  
  
    P(:,i) = -Mss * h1 * eq(i) - h2 * fMRD(i-1);  
    xhelper0 = xSTATE(:,i-1);  
    (x_ , xDot_ , xDdot_ ) = NewmarkLIN(Mss, Kss, css, P(:,i-1:i), dt, xhelper0);  
    xSTATE(:,i) = (x_(:,2) ; xDot_(:,2)); xDdot(:,i) = xDdot_(:,2);  
  
    uC(i) = -Kgain * xSTATE(:,i);  
    v(i) = MODIclippedCONTR(uC(i), fMRD(i-1));  
  
    (u(i), s(i), y(i), yDot(i), fMRD(i)) = MRDhysteresis(xSTATE(storyD,i-1), xSTATE(dof+storyD,i-1),  
u(i-1), v(i), s(i-1), y(i-1), yDot(i-1));  
  
end %i  
plot_
```

```
%%%%%%%%%%%%%%%%%%%%%%%%%%%%%%%%%%%%%%%%%%%%%%%%%%%%%%%%%%%%%%%%%%%%%%%%  
%%  
%% Response of superstructure is controlled by MRD (SMC) %%  
%%%%%%%%%%%%%%%%%%%%%%%%%%%%%%%%%%%%%%%%%%%%%%%%%%%%%%%%%%%%%%%%%%%%%%%%  
%author: Kinay  
%created: 2009, updated: 6.2013
```

```
close all; clear; clc;  
superstructure %3x3 superstructure  
h1 = ones(dof,1); h2 = (1 0 0)'; storyD = 1;  
EQ_;  
global fMRDmax vMAX stepIN  
fMRDmax = 3000; vMAX = 2.25; stepIN = 100;  
system_;  
size_initiation;
```



```

    (u(i), s(i), y(i), yDot(i), fMRD(i)) = MRDhysteresis(xSTATE(storyD,i-1), xSTATE(dof+storyD,i-1),
u(i-1), v(i), s(i-1), y(i-1), yDot(i-1)));

end %i
plot_

%%%%%%%%%%%%%%%%%%%%%%%%%%%%%%%%%%%%%%%%%%%%%%%%%%%%%%%%%%%%%%%%%%%%%%%%%%%%%%
%           Response of superstructure is controlled by MRD (Fuzzy logic controller)           %
%%%%%%%%%%%%%%%%%%%%%%%%%%%%%%%%%%%%%%%%%%%%%%%%%%%%%%%%%%%%%%%%%%%%%%%%%%%%%%
%author: Kinay
%created: 2009, updated: 6.2013

% input: first floor's displacement and velocity
% output: voltage applied to MRD
% KINAY's membership functions and fuzzy inference rules

close all; clear; clc;
superstructure %3x3 superstructure
h1 = ones(dof,1); h2 = (1 0 0)'; storyD = 1;
EQ_ : %includes some details related with fuzzy logic

global fMRDmax vMAX stepIN
fMRDmax = 3000; vMAX = 2.25; stepIN = 100;
system_;
size_initiation;

(xUNCON, xdUNCON, xddUNCON) = NewmarkLIN(Mss, Kss, css, -Mss * h1 * eq, dt); %uncontrolled
3x3 superstructure
x1 = xUNCON(1,:); x1 = max(abs(x1)) %1st floor's displacement
xd1 = xdUNCON(1,:); xd1 = max(abs(xd1)) %1st floor's velocity

disp('ATTENTION: change the boundaries of inputs x1 & xd1 in fuzzy toolbox')

disp('FOR NORMAL STRUCTURE, if they are different than -0.04<x1<0.04 & -0.55<xd1<0.55 for IMP
eq')
disp('type fuzzy("DUZCE_EQ_fuzzy") or fuzzy("IMPERIAL_VALLEY_EQ_fuzzy") on the command
window to change the boundaries of two input, disp and velo of first floor')

for i = 2:length(eq)

    P(:,i) = -Mss * h1 * eq(i) - h2 * fMRD(i-1);
    xhelper0 = xSTATE(:,i-1);
    (x_, xDot_, xDdot_) = NewmarkLIN(Mss, Kss, css, P(:,i-1:i), dt, xhelper0);
    xSTATE(:,i) = (x_(:,2); xDot_(:,2)); xDdot(:,i) = xDdot_(:,2);

    v(i) = evalfis((xSTATE(1,i) xSTATE(4,i)),fis); %FUZZY CONTROLLER

    (u(i), s(i), y(i), yDot(i), fMRD(i)) = MRDhysteresis(xSTATE(storyD,i-1), xSTATE(dof+storyD,i-1),
u(i-1), v(i), s(i-1), y(i-1), yDot(i-1)));

end %i
%surfview(fis)
plot_

```

## VITA

Gökçe KINAY was born in İzmir, Turkey, on February 12, 1979, the daughter of Gülsüm İmren ERAL and Sinan KINAY. After completing her degree at Karşıyaka Anatolian High School, İzmir, Turkey, in 1997, she entered the Dokuz Eylül University, receiving the degree of Bachelor of Civil Engineering in July, 2001 with honours. She entered the Graduate School in the Department of Civil Engineering at the İzmir Institute of Technology (İYTE) in September, 2001. She received her first Master of Science degree on computational mechanics of materials and structures in COMMAS at University of Stuttgart, Germany in May, 2004. After a professional career, she received her second Master of Science degree on structural mechanics in the Department of Civil Engineering at İYTE in July, 2006. She started PhD studies in the Department of Mechanical Engineering at İYTE in October, 2006. She attended to a one year of scientific orientation program in the Department of Mechanical Engineering at İYTE. She received the degree of Doctor of Philosophy of Mechanical Engineering in August, 2013 with honours. During the PhD studies, she was a scholar of National Scholarship Programme for PhD students by TÜBİTAK Science Fellowships and Grant Programmes Department (BİDEB). She has been a member of Turkish Chamber of Civil Engineers since 2001. Her interest areas are semi-active and hybrid structural control, structural dynamics, structural mechanics, computational mechanics, dynamics, numerical analysis. During the PhD studies, she assisted to the lectures of Computer Science and Programming, Statics, Applied Mathematics for Engineers, Dynamics, Strength of Materials, Numerical Methods in Engineering, System Analysis and Control in the Department of Mechanical Engineering at İYTE. During her PhD studies at İYTE, she founded the Society of Friends of Animals in 2007. She worked in the area of the Gülbahçe Campus to rehabilitate the stray domestic animals for five years. Since 2012, she has left her responsibilities in the society and has been working as the founding chairman of the Society of Friends of Animals at İYTE.

Permanent address: Siraselviler Sitesi No:40 Urla-İzmir, TURKEY

This thesis was typed entirely by the author.